Author:
Cuahtecontzi Delint, Rosalia

Title:
Stem Cell Membrane Re-Engineering for Adhesion to the Extracellular Matrix

Stem Cell Membrane Re-Engineering for Adhesion to the Extracellular Matrix

Rosalia Cuahtecontzi Delint

A dissertation submitted to the University of Bristol in accordance with the requirements for award of the degree of Doctor of Philosophy in the Faculty of Life Sciences, School of Cellular and Molecular Medicine

March 2019

Word count: 31878

Abstract

One of the major challenges within the rapidly growing field of regenerative medicine is the efficient integration of stem cells after transplantation. To address this issue, an artificial cell membrane binding nanobiohybrid was rationally designed to provide donor cells with cartilage tissue adhesion properties. The protein constituent consists of a peptide sequence from placenta growth factor 2 (PlGF-2) fused to a supercharged green fluorescent protein (scGFP), giving [scGFP_PlGF2]. Significantly, PlGF-2 has an extremely high binding affinity for extracellular matrix (ECM) proteins and the supercationic scGFP provides a cell membrane anchor region for anionic polymer surfactant conjugation. Accordingly, the solvent-exposed sites of the protein were electrostatically conjugated with a polymer surfactant, forming [scGFP_PlGF2][S]. This allowed the construct to insert into the membrane of human mesenchymal stems cells (hMSCs), whilst the PlGF2 domain is displayed to provide the cells with affinity for ECM proteins.

The addition of the polymer surfactant did not affect the structure and function of the fusion protein. Moreover, hMSCs modified with [scGFP_PlGF2][S] did not exhibit any signs of cytotoxicity at working concentrations, and there was no impact on the cells ability to proliferate or differentiate. Importantly, there was a significant increase in cellular adherence to collagen II when comparing modified cells to unmodified cells with *in vitro* models. Moreover, the modified cells adhered strongly to bovine ex vivo articular cartilage explants and could be readily observed on the cartilage using confocal and electron microscopy. These findings suggest that re-engineering hMSC membranes with [scGFP_PlGF2] could be a viable approach to improve stem cell therapy outcomes in the regeneration of damaged cartilage tissue.

Acknowledgements

I would like to thank the Bristol Centre for Functional Nanomaterials for accepting me as part of the 2014 cohort, particularly to Dr Annela Seddon and Dr Terry McMaster. I would also like to thank the Consejo Nacional de Ciencia y Tecnología in México for funding this project.

I would like to express my sincere gratitude to my primary supervisor Dr Adam Perriman for this opportunity, his motivation, patience, and vast knowledge, and Dr Wael Kafienah for his input in the last chapter of this project.

I also wish to thank everyone in C74, particularly Karen Still and Vivian Diamanti for all their help with cell culture matters.

I would like to acknowledge to the University of Bristol staff in the histology unit, the Wolfson Bioimaging Facility for their protocols and guidance for sample analysis, and all the technicians on B and C floor for keeping the labs running.

I would like to thank to my BCFN cohort, especially those who became my close friends: Tania Castillo, Omar Gomez, and Sam Pearce.

I would like to express my greatest appreciation to all the Perriman group members, to those that were here when I started my PhD: James Armstrong, Maddy Burke, Rob Deller, Tom Green, Monika Jakimowicz, and Ben Carter, for all their guidance when I ever since I joined the group, the bouldering trips, and for all the Chinese takeaways. To the members that joined about the same time as me: Graham Day, Ioannis Zampetakis, Beth Hickton, and Carl Marsh, thank you for your kindness and for always being a good laugh. I am grateful to Wenjin Xiao, for teaching me everything about stem cell culture, and for the chats during microfluidics experiments. To the group members who joined after me: William Zhang, Thomas Richardson, Jenna Shapiro, Corrigan Hicks, George Klemperer, Peter Johnson,

Runa Begum, Sara Carreira, Agata Jakimowicz, Will Macalester, David Coe, and Li Tao, thank you all for the board game sessions, lunch time conversations, the crosswords, Friday doughnuts, and for making the office and the lab a great place to work. You all have had a good (or bad) influence on me. Also thank you to all those who proof-read this thesis.

I would also like to thank Andrea Brancaccio for the football chats, and the ginger tea.

A very special thanks to my boyfriend, for putting up with my craziness, for his encouragement, for looking after me, and for being my best friend.

Thank you to my house-mates in Bristol: Sam Brooks, Alex Howat, Tania Castillo, and Andy James, for making the house a lovely place to live, and for giving me a family away from home.

Finally, I would like to thank my parents who would always ask how my experiments were going, for spoiling me every time I went back home, and for believing in me. I would also like to express my gratitude to my sisters, who encouraged me to pursue my desire to study a doctorate degree, and for being an excellent role-model.

Author's Declaration

I declare that the work in this dissertation was carried out in accordance with the requirements of the University's Regulations and Code of Practice for Research Degree Programmes and that it has not been submitted for any other academic award. Except where indicated by specific reference in the text, the work is the candidate's own work. Work done in collaboration with, or with the assistance of, others, is indicated as such. Any views expressed in the dissertation are those of the author.

SIGNED: ..... DATE: .....

Table of Contents

List of Figures

List of Tables

Abbreviations

BCA	bicinchoninic acid
BM	bone marrow
BSA	bovine serum albumin
CD	circular dichroism
cDNA	complementary deoxyribonucleic acid
CMC	critical micelle concentration
CPD	critical point dryer
DAB	3'-diaminobenzidine
DALY	disability adjusted life year
dH_2O	deionised water
DLS	dynamic light scattering
DMEM	dulbecco's modified eagle medium
DMSO	dimethyl sulfoxide
DMSO	dimethyl sulfoxide
DNA	deoxyribonucleic acid
DPX	dibutylphthalate polystyrene xylene
E. Coli	escherichia coli
ECM	extracellular matrix
EDTA	ethylendiaminetetraacetic acid
eGFP	enhanced green fluorescent protein
ELISA	enzyme-linked immunosorbent assay
ESCs	embryonic stem cells
FBS	foetal bovine serum
FGF	basic human fibroblast growth factors
FSC-A	forward scatter area
FSC-H	forward scatter height
FTIR	Fourier transformed infrared spectroscopy
GAG	glycosaminoglycan
GFP	green fluorescent protein
HA	hyaluronic acid
HBSS	Hank's buffer
HCl	hydrochloric acid

hMSCs	human mesenchymal stem cells
IL	interleukin
IMAC	immobilised-metal affinity chromatography
IMS	industrial methylated spirit
iPSCs	induced pluripotent stem cells
IPTG	isopropyl β-d-1-thiogalactopyranoside
ITS	insulin transferrin selenium
LB	lysogenic broth
MALDI-TOF	matrix-assisted laser desorption/ionization mass spectrometry time of flight
MSCs	mesenchymal stem cells
MTS	3-(4,5-dimethylthiazol-2-yl)-5-(3-carboxymethoxyphenyl)-2-(4-sulfophenyl)-2h-tetrazolium
Na_2HPO_4	sodium phosphate dibasic
NaBr	sodium bromide
NaCl	sodium chloride
NaClO	sodium hypochlorite
NaH_2PO_4	sodium phosphate monobasic
$NaHCO_3$	sodium bicarbonate
NaOH	sodium hydroxide
NHS	national health services
Ni-NTA	nickel nitrilotriacetic acid
NSAIDs	nonsteroidal anti-inflammatory drugs
OA	osteoarthritis
PBS	phosphate buffered saline
PCR	polymerase chain reaction
PD	population doubling
PDB	protein data bank
PDGF	platelet derived growth factor
PEG	polyethylene glycol
PFA	paraformaldehyde
PI	propidium iodide
PlGF2	placenta growth factor 2

PMSF	phylmethylsulfonyl fluoride
PPI	proton pump inhibitor
qPCR	quantitative polymerase chain reaction
RNA	ribonucleic acid
rpm	revolutions per minute
SAB	sample application buffer
SANS	small angle neutron scattering
SAXS	small angle x-ray scattering
SC	stem cells
scGFP	supercharged green fluorescent protein
sfGFP	superfolder green fluorescent protein
SDS	sodium dodecyl sulphate
SDS-PAGE	sodium dodecyl sulphate polyacrylamide gel electrophoresis
SEC	size exclusion chromatography
SEM	scanning electron microscopy
SOC	super optimal broth with catabolite repression
SRCD	synchrotron radiation circular dichroism
SSC-H	side scatter height
ssDNA	single stranded deoxyribonucleic acid
TBS	tris buffered saline
TEMPO	2,2,6,6 -tetramethylpiperidine 1-oxyl
TGF-β3	transforming growth factor beta three
TNF	tumour necrosis growth factor
UV-vis	ultra-violet visible
VEGF	vascular endothelial growth factor
WR	working reagent
X-gal	X-galactose

Chapter 1

Introduction: Stem Cell Therapies for Osteoarthritis

This chapter outlines the burden of osteoarthritis (OA) and the economic impact of musculoskeletal disorders. These topics are followed by the aetiology and pathogenesis of OA disease, as well as the innate attempt of the human body to repair damaged sites. The advantages and disadvantages of traditional surgeries are also discussed. Significantly, surgery fails to induce repair and tends only to alleviate pain symptoms. As a result, the area of tissue engineering has emerged with regenerative stem cell therapies to overcome these shortfalls. Accordingly, a review of literature that covers recent approaches to treat osteoarthritis is presented, which includes the re-engineering of the stem cell membrane using different materials and approaches.

1.1 The importance of osteoarthritis

1.2.1 Definition of osteoarthritis

The Osteoarthritis research society international (OARSI) has defined osteoarthritis (OA) as “a disorder of the movable joints characterised by extracellular matrix (ECM) degradation and cell stress originated by micro- or macro-injuries that stimulate dysfunctional repair responses, including inflammatory pathways of innate immunity”[1].

OA is the most common disease among older individuals, with half the population aged 65 years or older diagnosed with chronic articular disorders[2]. Pain is the main symptom of this disability, impeding people from performing basic daily activities[3]. OA can develop in the hip, hands or the knee, with the latter one being the most prevalent, accounting for 83% of the total osteoarthritis burden[4] (Figure 1.1).

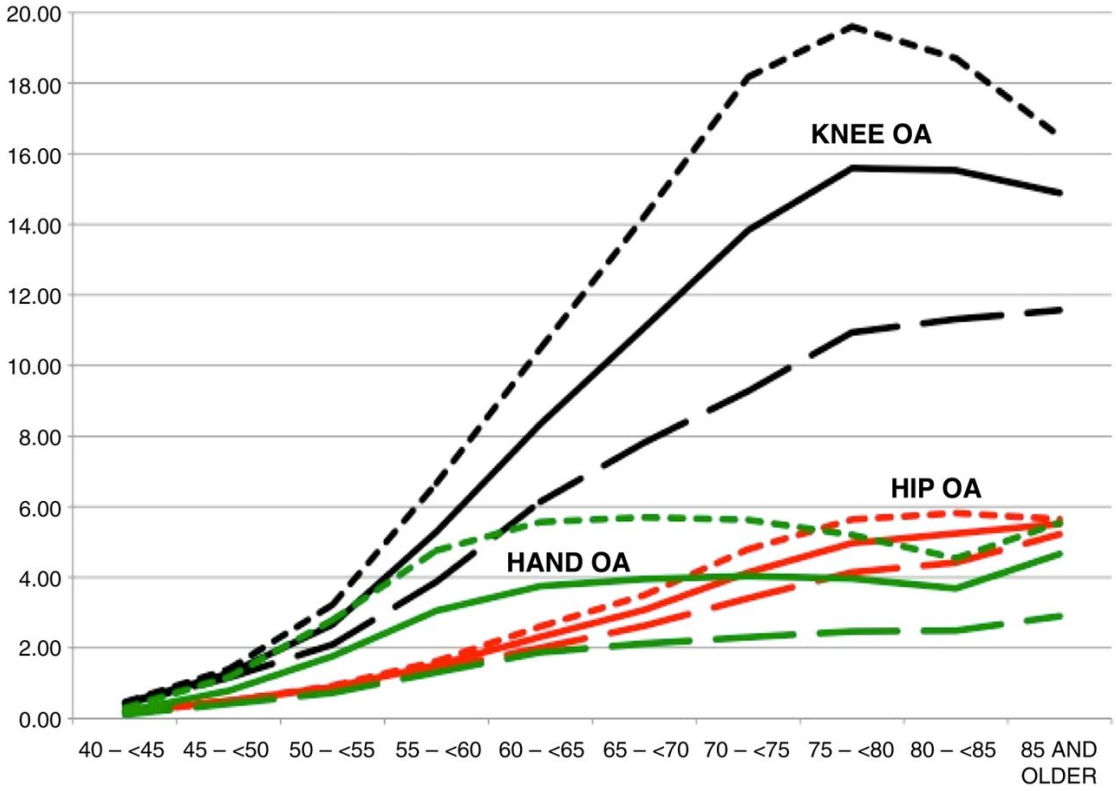

Figure 1.1 Representation of age and gender rates (/1000 person-years) of osteoarthritis (OA). Combined population (solid line), women (short dashed line), and men (long dashed line). Different types of OA are plotted: knee(black), hip (red), and hand (green). Reproduced with permission from Annals of the Rheumatic Diseases[5].

The information from Figure 1.1, from the analysis in Spain, can be extrapolated to other countries. The probability of osteoarthritis of occurring in women is higher, presumably caused by the change in hormones typically around menopause age[5].

1.1.1 The economic impact of osteoarthritis

Given the high occurrence of OA disease, it is necessary to standardise the cost of OA-related expenses per country including direct and indirect costs[6], as these can be substantial. Direct costs include hospital fees, medical visits, prescriptions, surgery, and care services[7]. Indirect costs are linked to the value of loss of productivity owing to illness (i.e. days off work)[7]. Depression, anxiety, and suffering are considered intangible costs[8].

For instance, a study conducted by Le Pen in 2003 highlighted that the direct cost of OA was approximately 1.6 billion euros per year (£1.1 billion), distributed as €820 (£558) million in hospital admissions, €270 (£183) million in physician visits and €520 (£354) million spent in medications[9].

Nevertheless, most of the available data can only be obtained from developed countries, which does not allow for a global estimation. A review by Puig-Junoy and colleagues concluded that the majority of the OA-related studies are conducted in the United States of America, which accounted for 56% of the total publications up to 2015, this was followed by Canada with 8%, Australia and Spain with 5% and France 1%[10].

It has been estimated from the gathered studies so far, that the average amount of money spent per patient suffering from an osteoarthritic knee in a year is €4,257 EUR (£3,108 GBP), ranging from €838 (£612) to €7,675 (£5,603), furthermore, the average incremental cost per year is €4,175 (£3,048), ranging from €528 (£385) to €11,293 (£8,244) from direct costs[10], either in medical visits or medications. The highest end of the cost corresponds to patients undergoing surgery, spending nearly 30 times more than non-hospitalised individuals[9]. These rates were converted from euros to GBP according to the average exchange rate in 2015 provided by the European Central Bank[11].

According to the National Health Service (NHS), in the United Kingdom (UK) the primary treatment for patients with OA is the prescription of painkillers including non-steroidal anti-inflammatory drugs (NSAIDs) and paracetamol[12], with over 50% of the patients taking NSAIDs[8]. Topical and oral NSAIDs incurred a cost of £19.2 million, and £25.65 respectively, in 2010. Furthermore, the cost of proton pump

inhibitors (PPIs) as gastroprotective agents against NSAID, was £11.6 million (Figure 1.2).

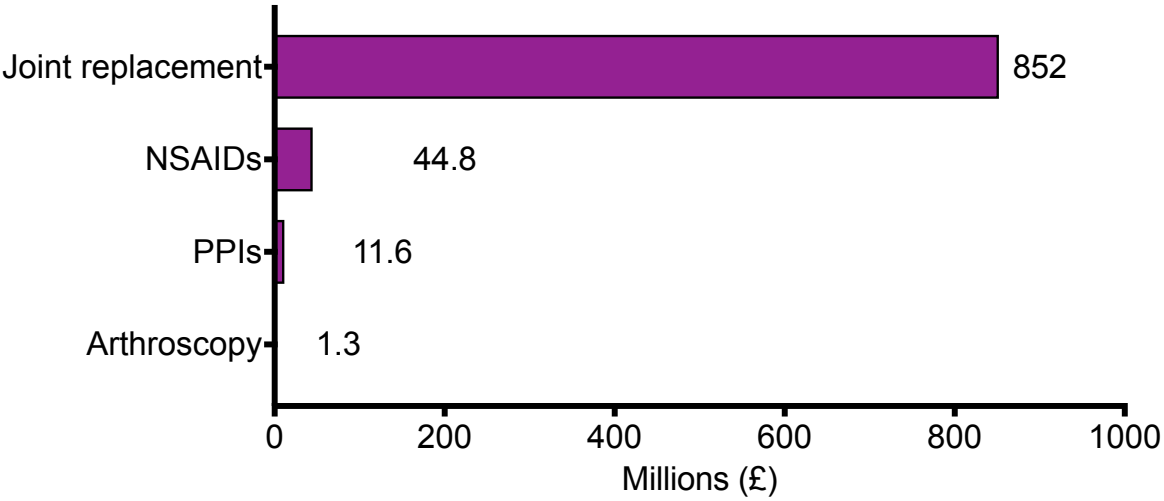

Figure 1.2 The cost of osteoarthritis in the United Kingdom according to the National Health Services. NSAIDs: non-steroidal anti-inflammatory drugs, PPIs: proton pump inhibitors. Adapted from[8].

Other costs are derived from arthroscopy and expensive total joint replacements[8]. Additionally, the costs for patients requiring recurrent medical visits due to OA symptoms are estimated to as high as £36 million a year[13]. Moreover, the indirect costs of OA is reported to have a major effect on the UK economy, since it has been estimated that £3.2 billion are lost in economic production every year[8].

According to Versus Arthritis, the largest research organisation for arthritis in the UK, £1.6 billion pounds were spent by research charities in 2016. Unfortunately, the research funding for musculoskeletal diseases (including hip, back and knee osteoarthritis and rheumatoid arthritis) remains disproportional, as it received only 2.8% of the funding for research in 2014. This is despite a reported 9% of disability adjusted life years (DALYs)[14] attributed to OA. DALYs are a measure of the impact of diseases, for instance, the years of healthy life lost or early death[15] (Figure 1.3).

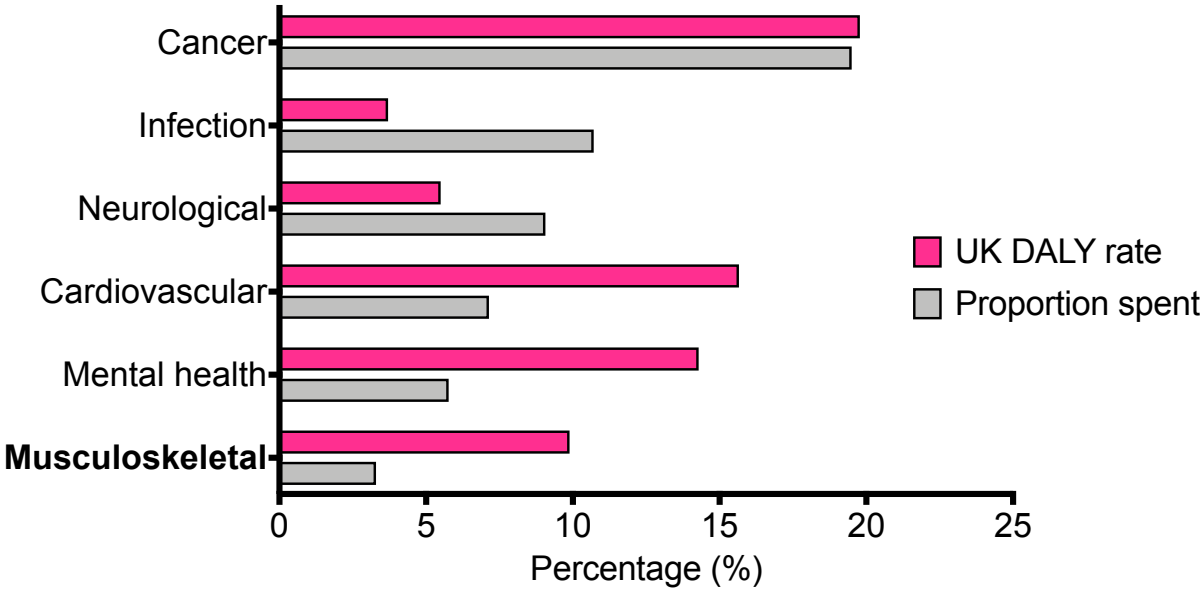

Figure 1.3 Research spend, expressed as a percentage of total research funding (grey), versus burden of disease (pink). The top health research categories are represented. DALY: disability adjusted life year. Adapted from[14].

At present, all commercially available therapies concern the treatment of OA symptoms instead of avoiding the progression of the disease. Importantly, it is crucial to understand the pathology of osteoarthritis.

1.2 Hyaline cartilage

1.2.2 Function and structure of hyaline cartilage

There are three main types of cartilage in the human body: elastic, fibrocartilage, and hyaline cartilage. The first one offers support to structures frequently subjected to deformation such as the epiglottis, larynx, and the external ear. Fibrocartilage is present in intervertebral discs and tendons. It possesses thick collagen fibres, characteristic of dense connective tissue and, like elastic cartilage, is rich in glycosaminoglycans[16].

Hyaline cartilage, also called articular cartilage (AC), serves the key role of providing mechanical support for developing bones and nose. Additionally, this

type of tissue provides a lubricated surface for the diarthroidal joints, and helps in the distribution of loads[17]. The knee joint cavity is also lined by a thin connective tissue that secretes the lubricating synovial fluid. This tissue layer is called the synovium (Figure 1.4). AC is avascular, alymphatic and aneural. It is comprised by a dense extracellular matrix (ECM), which is secreted by a highly specialised type of cells called chondrocytes[18].

The unique structure of the ECM is what confers to this tissue the important function of protecting the joints. Approximately three quarters of the wet weight of AC is water[19]. The water flow transports essential nutrients to the chondrocytes and provides lubrication[17]. From the remaining 25%, most of the dry weight (50–80%) is concentrated in collagen fibres with a triple helical structure[19].

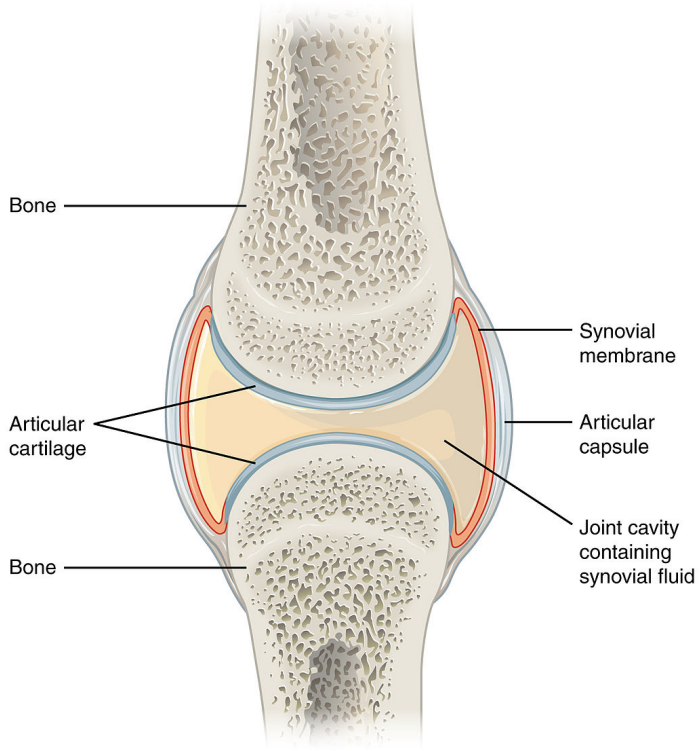

Figure 1.4 Schematic representation of a knee joint. Articular (hyaline) cartilage surrounds the bone to distribute the load. Reproduced from Anatomy & Physiology[20].

Collagen type II constitutes 85–90% of the total extracellular matrix components, along with proteoglycans (10–15%)[21], and specialised glycosaminoglycan hyaluronic acid (HA).

Proteoglycans are proteins containing glycosaminoglycan (GAG) chains covalently attached to a core protein. These anionic chains repel each other by electrostatic repulsion due to the negative charge[17]. Proteoglycans provide the ECM the ability to resist compressional forces due to its osmotic properties[22]. GAGs are categorised into keratan sulphate, heparan sulphate, chondroitin sulphate, dermatan sulphate, and HA, depending on the repeating disaccharide. HA surrounds migrating and proliferating cells and has a large number of anionic residues that interact with water, forming a hydrated gel. It also keeps cells separated from one another, providing them with freedom to move and proliferate[23]. HA binds to aggrecan, the most abundant proteoglycan which contains over 100 GAG polysaccharides in its protein core[23] (Figure 1.5).

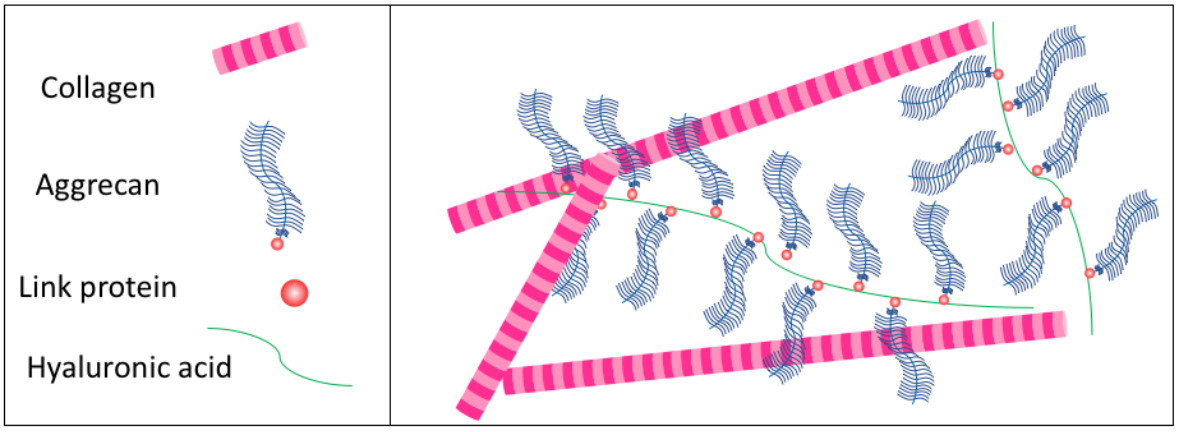

Figure 1.5 Schematic representation of articular cartilage extracellular matrix. Aggrecan is bound to hyaluronic acid in a collagen network.

The ECM, along with chondrocytes, is arranged into four different zones within the cartilage, characterised by their organisation and arrangement of collagen fibres (Figure 1.6).

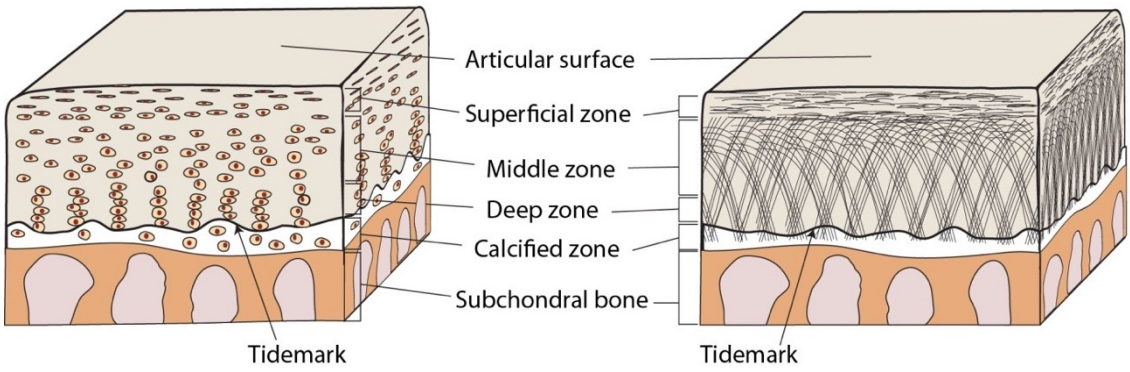

Figure 1.6 Schematic representation of articular cartilage zones in the knee joint. The left image depicts the orientation of the chondrocytes while the right image represents the collagen fibres. Reproduced from Zhang et al.[24]

The superficial layer is the most exposed to the synovial fluid, it contains a high density of flattened chondrocytes and the collagen fibres are aligned parallel to the articular surface. The stability of this area is crucial for the deeper layers of cartilage, as it protects them from shear stress[17].

Adjacent to the superficial zone is the transitional or middle zone. In this layer, the collagen fibres are wider and are ordered in oblique positions. The chondrocytes present a spherical shape and exist at lower densities than the superficial zone[17].

The deep zone contains the largest collagen fibres in diameter, arranged, along with chondrocytes, in a perpendicular fashion to articular surface. This layer is characterised by having the highest proteoglycan content and the least water concentration. Importantly, it resists the greatest amount of compression[17]. Chondrocytes in the deep zone can undergo terminal differentiation and produce collagen X[25].

Finally, the calcified cartilage is divided from upper uncalcified zones by the tidemark. The calcified zone has the key role to anchor the collagen fibrils onto the subchondral bone[17]. AC is further divided into three regions (Figure 1.7).

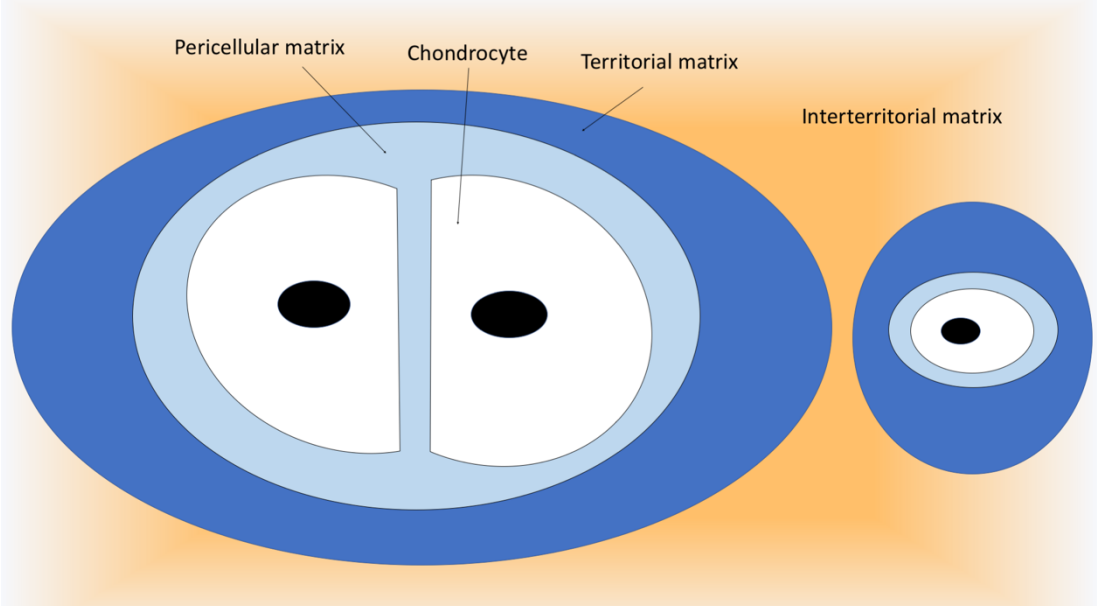

Figure 1.7 Schematic representation of cartilage regions. The pericellular matrix surrounds the chondrocytes, and it is in turn enclosed by the territorial matrix. Interterritorial space is the area between chondrocytes.

The pericellular matrix, or chondron, surrounds the chondrocytes and it is rich in proteoglycans and glycoproteins[26]. Next is the territorial matrix, which contains collagen fibrils and protects the cells from the load-bearing stress[17]. The interterritorial region is the largest and contains the collagen fibrils arranged in different positions depending on the zone[17].

1.2.3 Damaged cartilage and osteoarthritis

The severe stress affecting hyaline cartilage due to biomechanical pressure can lead to wear and tear[27]. Injuries in the cartilage can lead to progressive joint degeneration due to the poor capacity of endogenous tissue healing. This is owed to the absence of progenitor cells, blood vessels, nerves, and the low proliferation rate of chondrocytes. Damage in cartilage has been associated with a number of traumatic injuries due to sports, and musculoskeletal disorders, such as osteoarthritis (OA)[28].

1.2.1.1 Osteoarthritis disease

Chondrocytes are the only cell type that reside in cartilage. They are responsible for synthesising a number of compounds such as collagen, proteoglycans, glycoproteins and hyaluronan, to form the ECM[29]. The metabolic activity of these cells can be disrupted by the presence of pro-inflammatory cytokines and growth factors[25]. Amongst the collagens secreted by chondrocytes, the expression of collagen type X also results in the production and release of proteolytic enzymes. These enzymes cause clearance of the ECM and aid in the undesirable formation of bone and vascularisation[29].

A frail balance between synthesis and degradation of ECM must be achieved to maintain homeostasis[25]. Injuries in the AC can lead to loss of ECM, which in turn can trigger the chondrocytes' natural function to secrete more ECM components. However, the turnover rate of these components is intrinsically unbalanced, i.e., proteoglycan renewal rate is approximately 25 years, while the half-life of collagen fibres varies from decades to 400 years[30]. As a consequence, the damage of ECM can slowly degrade AC, this is in part, because it is not possible to detect OA in its early stages.

Degradation of the cartilage also occurs because the number of chondrocytes decreases with age. As a result, the chondrocytes situated in the superficial layer migrate to the deeper layers, resulting in poor hydration and elevated compressive stiffness on the matrix joint[25].

1.2.3.1 Osteoarthritis pathogenic mechanisms

A unique mechanism for the aetiology of osteoarthritis (OA) has not yet been found[31], although it is thought to be the combination of various changes occurring in the cartilage simultaneously. In healthy ECM, the phosphorylation of ALK5 and

Smad3 proteins play an important role as receptors for TGF-β, and transduction of the TGF-β signal into the cell, respectively[32,33]. The function of TGF-β1 is to actively block the hypertrophic changes of chondrocytes[33,34]. Furthermore, fibroblast growth factor 2 (FGF-2), cooperates with TGF-β2 to inhibit hypertrophy[35]. The active phosphorylation of ALK5 and Smad3 is decreased with age[31], thus initiating hypertrophy in the remaining cells (Figure 1.8).

Hypertrophic chondrocytes secrete HtrA1[36], a potent protease involved in the blocking of TGF-β[31], causing terminal differentiation in chondrocytes. Additionally, hypertrophic chondrocytes, often referred to as activated chondrocytes, gradually start to proliferate[35], form chondrocyte clusters[37], and secrete collagen type X.

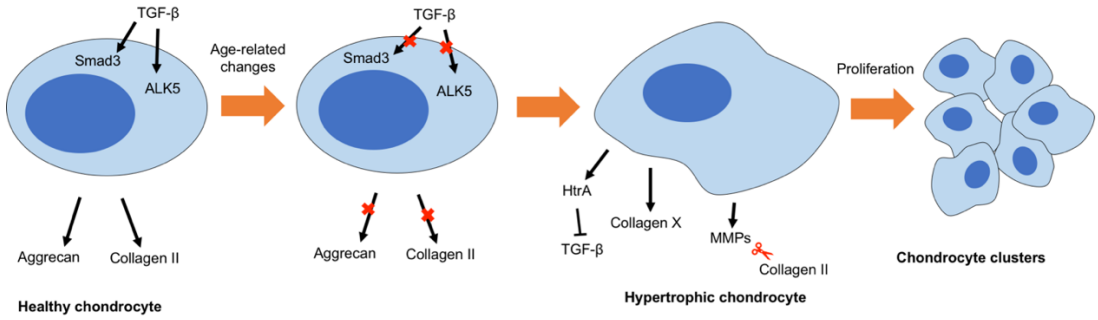

Figure 1.8 Schematic representation of chondrocyte hypertrophy. Transforming growth factor (TGF-β) phosphorylation by Smad3 and ALK5 is reduced with age, downregulating the production of aggrecan and collagen II. This event causes hypertrophic chondrocytes as they start the production of HtrA (blocking TGF- β), collagen X, and metalloproteinases (MMPs) which cleave collagen II. Hypertrophic chondrocytes proliferate and form chondrocyte clusters.

Activated chondrocytes initiate the synthesis of various proteolytic enzymes, including matrix metalloproteinases (MMPs), which cleave the collagen and proteoglycan fibres[25], disrupting the crosslinked network. Here, MMP13 plays a critical role in the cleavage and denaturation of collagen II[38], the main component of cartilage ECM. MMP13 upregulation increases 40-fold in damaged cartilage

compared to non-osteoarthritic cartilage[39], hence it is commonly used as a biomarker for OA[40].

Although the exact mechanism that drives chondrocytes to secrete HrtA1 and MMPs is still unclear[41,42], it has been proposed that their expression is a resultant of mechanical stress and inflammation[43]. In the progression state of OA, the overexpression of HtrA1 and MMPs is followed by denaturation of the pericellular and intracellular matrix. As a consequence, the biomechanical microenvironment of the chondrocytes is altered, promoting chondrocyte hypertrophy[31].

Furthermore, signalling cascades coming from inflammatory cytokines, interleukins, and tumour necrosis factor, including IL-1β, IL-6, and TNF-α, are present during OA development (Figure 1.9). Such inflammatory cytokines are secreted by synoviocytes and chondrocytes. They play a key role in cell metabolism by upregulating the expression of MMPs and preventing the production of MMPs inhibitors[44], such as tissue inhibitor of metalloproteinases 1 (TIMP-1)[45].

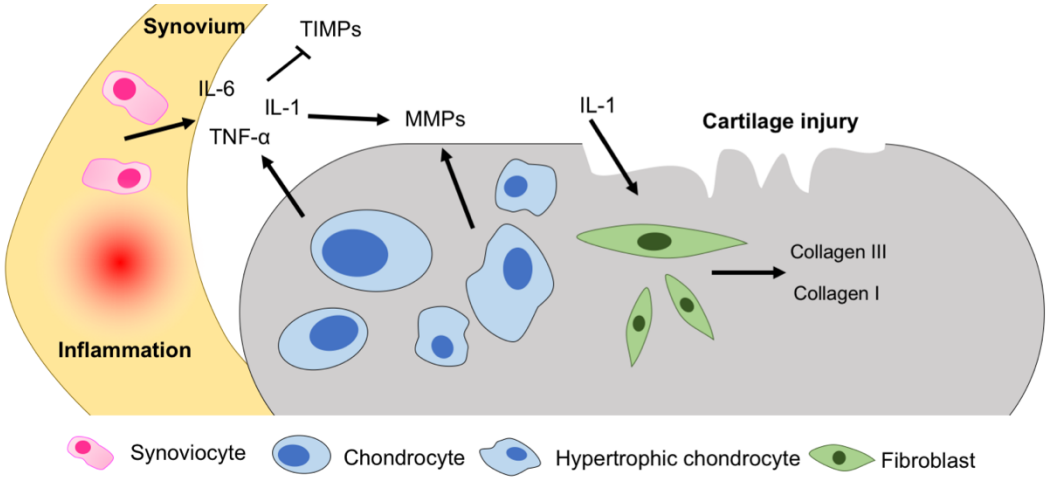

Figure 1.9 Schematic representation of osteoarthritis pathogenesis. Synoviocytes and chondrocytes secrete cytokines, interleukins and tumor necrosis factor (IL-1β, IL-6, and TNF-α, respectively), which prevents tissue inhibitor metalloproteinases to counteract the degradative metalloproteinases (MMPs). Interleukins cause chondrocytes to dedifferentiate into fibroblast cells, secreting collagen I and III.

The presence of TNF-α in the cartilage ECM can be recognised by receptors in nerve terminals and activate high threshold ion channels, which propagate pain signals from surrounding tissues to the central nervous system[46].

Cytokines such as IL-1 can induce dedifferentiation. In this scenario, the chondrocyte phenotype is altered to a fibroblast-like cell. Dedifferentiated chondrocytes cease the synthesis of collagen II and aggrecans, and instead they secrete collagen I and III[37].

After the loss of ECM, healthy chondrocytes actively start the production of collagen II and proteoglycans; however, the disparity of production of collagen II versus proteolytic enzymes results in the in eventual loss of AC.

In addition, mechanical and humoral factors stimulate the formation of osteophytes[37] and fibrosis[47]. Osteophytes are a bony outgrowth containing fibrocartilage on their top surface[48]. In an attempt to repair and stabilise the joint[37], stem cells from the bone marrow are recruited to the injured area from the bone surface (i.e. periosteum), however, these cells, and hypertrophic chondrocytes[25], often differentiate into aberrant osteoblast-like cells[25], forming osteophytes. Nevertheless, studies have found that in larger osteophytes, some hyaline cartilage has formed on the surface, and the new ECM fibres seem to have a high content of collagen II and TGF-β[49].

In summary, the early stages of OA begin with age and the loss of chondrocyte population, followed by a cascade of reactions leading to cell hypertrophy and degeneration of the ECM and erosion of the cartilage. These factors induce the formation of osteophytes and fibrosis in the cartilage, compromising motility and causing pain. Conversely, the mixture of damaged fibrillated cartilage and calcified osteophytes marks the end stage of OA[31].

1.2.3.2 Articular cartilage injuries

Injuries of the cartilage are divided into matrix disruption, partial thickness, and full thickness defects[28] (Figure 1.10). Matrix disruption is often caused by a mild trauma injury, in this case, the remaining chondrocytes would increase their metabolic activity in order to restore the damaged matrix[28].

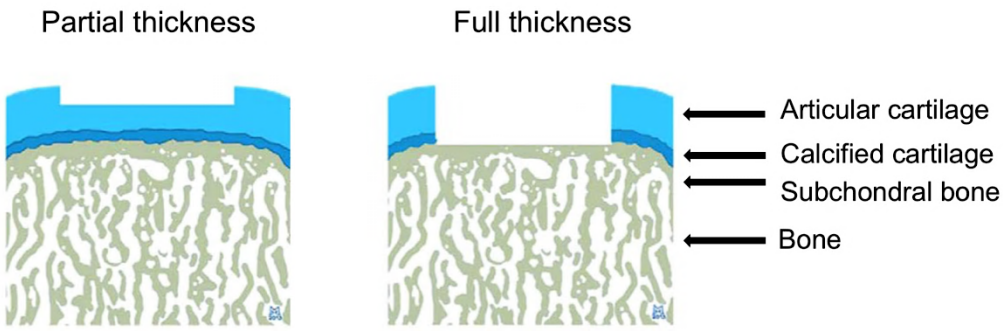

Figure 1.10 Schematic representation of cartilage defects. Partial thickness affects only the cartilage while full thickness injury reaches the bone. Adapted from[50].

Partial thickness damage in articular cartilage is often the result of a fissure on the superficial zone. In order to repair the damage, neighbouring cells initiate proliferation, however, the attempted restoration by the cells concludes before healing completion[28].

Full thickness defects develop from acute injuries going deep into the subchondral bone, damaging blood vessels, where a spontaneous repair response occurs. Blood, growth factors, and progenitor cells are simultaneously released from the bone marrow, and migrate to the injured site[51]. First, a spontaneous blood clot is created consisting primarily of a fibrin matrix containing proteins, red and white blood cells, and growth factors[52]. This clot is only capable of adhering to the surface of the bone and rarely to cartilage[52]. However, the clot is only able to fill small defects (1–2 mm deep), and larger lesions (6 mm) may not be completely filled[53].

Subsequently, mesenchymal stem cells (MSCs) replace the blood clot with a vascularised scar-like tissue[54]. Following this, endochondral ossification is generally started from the sides and floor of the injury towards the joint fissure, growing bone and new cartilage at the surface[52]. This new form of cartilage is indeed more similar to fibrocartilage than hyaline cartilage[55]. Fibrocartilage presents a more permeable matrix, but its mechanical competence is inferior to hyaline cartilage[56] and these two types of tissue do not integrate. Therefore, the new formed fibrocartilage begins to degenerate after formation.

1.2.3.3 Surgical treatments for osteoarthritis

At the present, several surgical methods have been developed in order to treat osteoarthritis, such as arthroscopy, drilling, and osteotomy, to name a few.

(i) Arthroscopy and lavage

The lavage of the knee is the irrigation and rinsing of the joint with saline solution to remove debris or loose AC fragments[52]. Despite this approach being merely empirical, it has been proved to alleviate pain in OA patients[57]. It has been postulated that, through lavage, some pain-signalling molecules may be removed[52]. However, other studies suggest that pain relief is owed to a placebo effect of the surgical intervention[58].

(ii) Pridie drilling

Pioneered by Kenneth Pridie in 1959, this surgery follows the premise of spontaneous repair by drilling therapeutic holes in the subchondral bone[59] (Figure 1.11). Patients have demonstrated that the benefit from this surgery as that pain is diminished, however, there is no long-term advantage to it, since the newly-formed fibrocartilage is deteriorated in time.

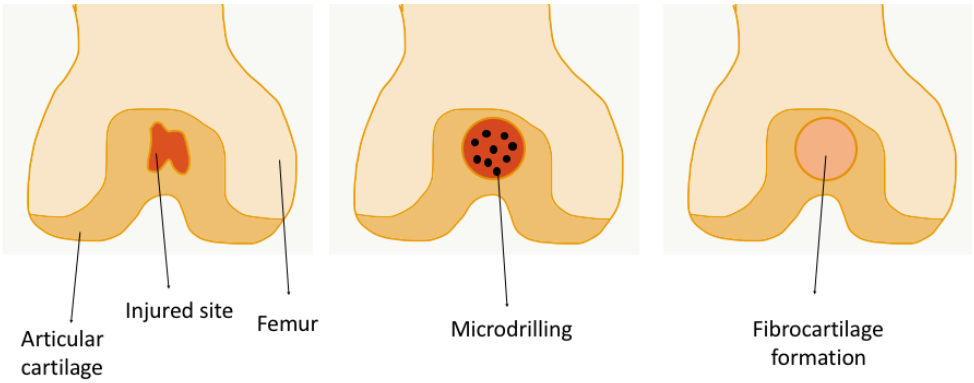

Figure 1.11 Schematic representation of Pridie drilling. First, the injured site area is homogenised, and small holes are drilled into the bone. Then, fibrocartilage is formed due to the endogenous immune response.

An extreme approach to this technique is spongialisation, whereby the whole subchondral bone is removed to expose the remaining cartilage to the cancellous bone or spongiosa zone. This technique has not gained popularity and the approach is still questionable[52].

(iii) Osteotomy

High tibial osteotomy is one of the most frequent surgeries to relieve pain from patients with severe joint deformities due to OA. This consists in the reshaping of the bone to distribute load more evenly. Osteotomy is often combined with a micro-drilling procedure[60].

(iv) Osteochondral transplantation

This approach, also called mosaicplasty, is achieved by transferring one or more cylindrical osteochondral autografts or allografts from a low weight-bearing area of the knee to the injured site[61] (Figure 1.12). This should be the last resort in surgery. In order to successfully complete the procedure, a correct alignment of the inserted discs is needed. The results from some studies have shown to be favourable for the majority of patients where the new matrix successfully integrated with the injured site[62].

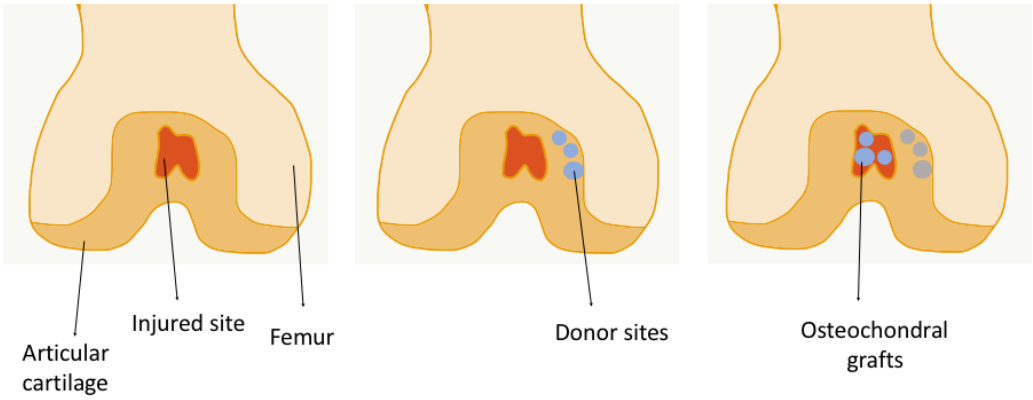

Figure 1.12 Schematic representation of mosaicplasty. Autografts are harvested from a low weight-bearing area of the knee to the injured site.

However, deterioration of the donor site can result in complications, and cartilage grafts often disintegrate as their biomechanical properties are inferior[63], since they are harvested from a low weight-bearing area in the knee joint.

(v) Total knee replacement

This has shown to be a durable approach compared to the previously discussed surgeries, lasting for 15 years[64]. The total knee replacement involves the removal of bone from the femur and tibia to insert a prothesis. The metallic femoral and tibial components possess a polyethylene disc shape that to resembles a natural joint[64].

Overall, the strategies discussed above are able to help alleviate pain and improve joint motility, however, they do not provide the properties of native and mechanical cartilage. For this reason, new approaches are being developed using tissue engineering techniques, for example, with hydrogels.

1.3 The emergence of regenerative cell therapies

Autologous chondrocyte implantation (ACI) is the first and most popular cell-based therapy for articular cartilage (AC) repair[65]. This technique was clinically initiated by Peterson and Brittberg in 1987[66,67]. Here, a cartilage sample is taken from a low-weight bearing part of the cartilage, followed by isolation of the chondrocytes and *in vitro* monolayer expansion, before being injected into the patients defect site. In order to lock the chondrocytes in place, a periosteal flap is placed and sewed over the injury site[67] (Figure 1.13).

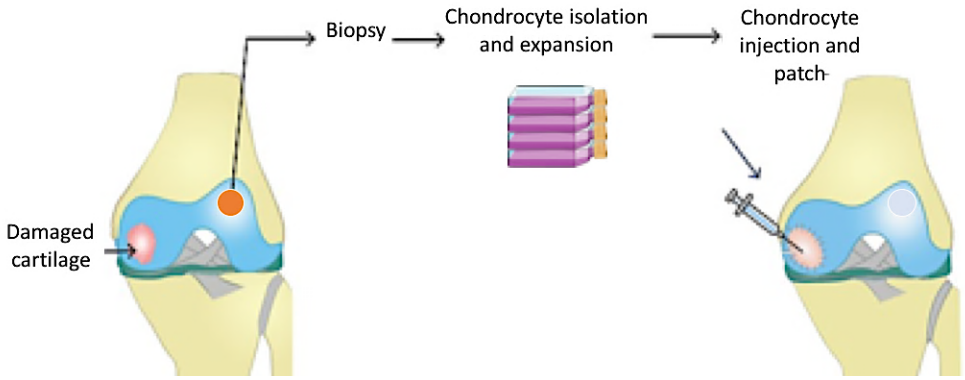

Figure 1.13 Schematic representation of autologous chondrocyte injection. First, chondrocytes are harvested and isolated from a healthy cartilage biopsy. Then, chondrocytes are expanded and injected into the damaged site. Adapted from[68].

The majority of the patients submitted to this treatment had a satisfactory outcome in the first years[69]. Nevertheless, a follow-up from patients after five years revealed that the repair was not homogeneous[67].

ACI still encounters limitations, including cost and complications resulting from the two surgical procedures: flap graft failure, donor site morbidity, and chondrogenic phenotype loss of chondrocytes during *in vitro* expansion[70,71]. Dedifferentiated chondrocytes are more prone to generate fibrous cartilage than hyaline cartilage. A proposed solution has been to administer cells that are able to fabricate any type of tissue with the adequate biological signalling[72], such as stem cells. Accordingly,

the clinical trend in cell therapies has moved from the use of cartilage cells to bone marrow derived cells[73].

1.2.4 Stem cells overview

Stem cells (SCs) are defined as cells having the capacity for self-renewal and the ability to differentiate into multiple cell types. SC can be further categorised owed to their origin as embryonic, adult, or genetically induced pluripotent stem cells (iPSCs).

Embryonic stem cells (ESCs) are derived from the inner cell mass of pre-implantation embryos, when the blastocyst is formed five days after fertilisation[74]. ESCs are pluripotent, as they have the capacity to undergo differentiation into all somatic cell lines *in vitro*. They are able to undergo extensive proliferation. However, the use of ESCs remains controversial due to the moral value of the embryo and the harvesting of oocytes[75]; which remains restricted in several countries[76]. Furthermore, the transplantation of ESCs has been associated with the formation of teratomas[77].

An alternative to ESCs are induced pluripotent stem cells (iPSCs) and adult stem cells, which could overcome the ethical issues associated with ESCs. iPSCs were generated by Takahashi and Yamanaka in 2006[78]. In order to create them, mature cells were reprogrammed *in vitro* with genes to dedifferentiate them into a pluripotent state[74]. iPSCs are believed to possess the same characteristics of embryonic stem cells including pluripotent differentiation, and a number of different reprogramming techniques have been established, including integrating systems such as viral transfection, or non-integrating methods such as plasmid DNA transfer[79].

Adult stem cells are rare populations of undifferentiated cells located inside the body. They contribute to homeostasis of organs and tissues and are responsible for regenerating cells that are lost due to tissue turnover, injury or pathological processes[80]. These cells include haematopoietic stem cells, found in the umbilical cord and bone marrow, as well as mesenchymal stem cells, predominantly located in the bone marrow.

Bone marrow (BM) is the major source for adult human mesenchymal stem cells (hMSCs). BM derived stem cells can undergo multilineage differentiation into a range of cell types, including adipocytes, osteoblasts, and myocytes (Figure 1.14). This type of cells is characterised for being plastic-adherent *in vitro.* Unlike ESCs, the pluripotency of hMSCs is limited and can only undergo population doubling 20 to 40 times before reaching senescence[81].

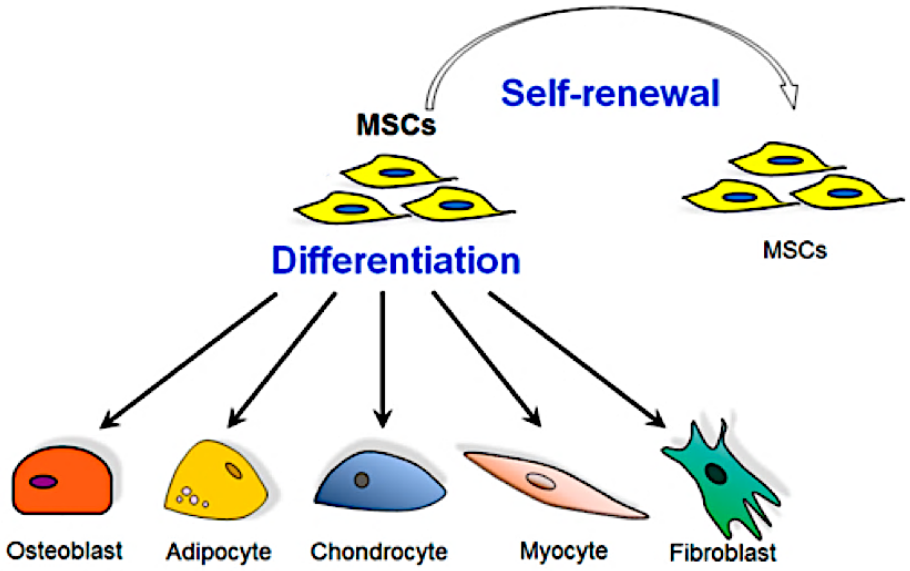

Figure 1.14 Human mesenchymal stem cells (hMSCs). hMSCs are able to either self-replicate or differentiate into various cell types such as osteoblasts, adipocytes, chondrocytes, myocytes, and fibroblasts. Adapted from[83].

In order to comply with clinical standards, the harvested cells should be effectively isolated and expanded *in vitro* while maintaining their multipotency[70]. Nevertheless, a universal protocol for scalable expansion or isolation has not been established

for hMSCs[82]. Besides bone marrow, hMSCs can be isolated from adipose tissue, synovium, and muscle.

1.2.5 Biology of mesenchymal stem cells

Besides their inherent adherence to plastic, human mesenchymal stem cells (hMSCs) are identified by the expression of surface markers such as CD44, CD90, CD105, CD106, CD166, and stro-1; and by the lack of hematopoietic markers CD14, CD34, and CD45, and endothelial cell markers (CD31)[84,85], depending on the source[86].

Since stem cells are maintained quiescent in their specialised niches until they are recruited, it is imperative that they are protected from immune response[87]. hMSCS are considered to have immunosuppressive properties via cell-cell contact and interactions with innate (e.g. neutrophils, dendritic cells, macrophages) and adaptive immune cells (T and B lymphocytes)[87].

Studies have suggested that stem cells are also capable of expressing chemokine receptors, demonstrating their potential to home and to decrease inflammation[88]. For instance, hMSCs secrete IL-6, which can reduce the respiratory processes of neutrophils, in turn inhibiting production of reactive oxygen species[89]. Additionally, MSCs have been shown to supress lymphocyte proliferation[90].

Due to these characteristics: multipotent differentiation, immunosuppression, and secretion of pro-inflammatory cytokines[91], human MSCs (hMSCs) have been the main focus of study in the development stem cell therapies.

1.2.6 Immune response to mesenchymal stem cells

Severe tissue damage is followed by inflammation[92]. The diffusion of macrophages and neutrophils is mediated by the release of the components of

necrotic cells[93]. It is the phagocytosis of necrotic cells leads to the secretion of pro-inflammatory factors including tumour necrosis factor (TNF-α) and free radicals[94]. After tissue damage, hMSCs are recruited in response to pro-inflammatory factors[95,96]. This initiates a complex signalling pathway for the mobilisation of hMSCs after injury[97]. It has been proposed that hMSC homing follows a similar pathway that have been described for leukocyte homing. In this process, cell migration to the damaged vicinity occurs as a consequence of the release of cytokines by the vascular endothelium and platelets. Then, a number of molecules, through coordinated expression, are implicated in hMSCs rolling and adhesion. This results in deceleration of the cells in the blood flow, followed by endothelial transmigration and movement into the extracellular space[98,99].

The mechanism by which stem cells contribute to tissue repair has not yet been elucidated. Besides hMSCs ability to differentiate and integrate into existing tissue[98,100] it has been proposed that hMSCs can impact the injury site microenvironment with the release of trophic factors that modulate paracrine signals[101] or the secretion extracellular vesicles (EVs), which contain active signalling molecules[102]. For instance, mesenchymal stem cell EVs have been used to treat AC defects in murine models[102,103].

MSCs have also been isolated from the synovium fluid[104], where they contribute to cartilage repair in small animals[105]; however, it has been suggested that due to the large size of human joints, it is improbable that these cells can migrate the long distances to injury sites[106]. Furthermore, two sub-populations of senescent MSC-like progenitor cells were found inhabiting knee articular cartilage in OA patients, which could be an indication of attempted cartilage repair leading to replicative

exhaustion and loss of proliferation[107]. This suggests that the MSC senescence and loss of replication capability leads to the progression of OA[106].

Due to the rare population of hMSCs in the human body (1 in 10,000 BM cells[108]) it is not surprising that research has endeavoured to enhance the recruitment of resident stem cells onto the injury sites. This includes the exploitation of the natural mechanisms of cell homing, such as the artificial administration of the growth factors TGF-β and platelet derived growth factor from blood plasma, which are present when wounds initiate[109]. Furthermore, the local injection of chemokine stromal derived factor (SDF-1α)[110] and adhesion molecule E-selectin has exhibited an increase in the recruitment BM-MSCs[111]. The excess of cytokines on the damaged site might reduce endogenous stem cell response by saturating the cell receptors, which are unable to sense difference in chemokine levels and inhibit migration[110]. Other approaches include the modification of the site with DNA peptides before injection[112].

1.2.7 Stem cell therapies

Considering the ability of stem cells to differentiate, they are a promising tool for tissue repair and gene therapies. Stem cell therapy involves the injection of stem cells into the damaged site (Figure 1.15). Stem cells can be harvested from the same person (autologous) or from a donor (allogenic) before being administered to the patient. Stem cell therapies are currently being used to treat a variety of diseases, including cancer[113], heart disease (strokes)[114], osteogenesis imperfecta[115], immune diseases[116], and lately, osteoarthritis[117].

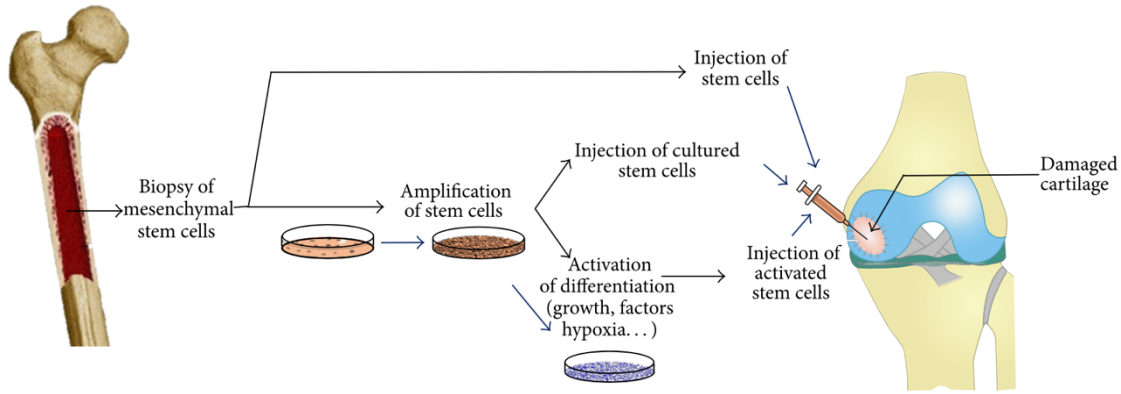

Figure 1.15 Schematic representation of mesenchymal stem cell transplantation. Cells are harvested from the bone marrow, isolated, and expanded *in vitro.* Stem cells can be treated or not before injection into the damaged site. Reproduces from[68].

After *in vivo* transplantation into the patient, common findings have been inhibition of innate inflammatory response, survival of existing cells, and fibrosis decrease[118]. Importantly, bone marrow (BM) derived stem cells have been the most popular type of SC for research after a PUBMED research involving the use of stem cell in cartilage regeneration, from 2000 to 2019. This is primarily because of their availability and regeneration capabilities. For example, Sacchetti et al. demonstrated that BM resident hMSCs are the only type of MSCs capable of forming a whole ectopic ossicle (very small bone) containing bone and hematopoietic cells[119]. Despite this bone ossicle assay not being translatable to the clinic, it demonstrates the ability of BM-derived MSCs to differentiate into two complimentary tissues[106]. Additionally, tissues created using autologous stem cells do not induce an immune response[74].

1.2.7.1 Stem cell therapies in osteoarthritis of the knee

The use of human mesenchymal stem cells (hMSCs) to treat osteoarthritis (OA) has increased over the past years, encouraged by successful pre-clinical trials in large animals, which demonstrated a decrease in the progress of OA[120]. Furthermore, the administration via local intra-articular cavity injection in the knee

has been demonstrated to be the safest and optimum approach[121,122] and as such, has been used in all clinical trials.

At the present, there are 7067 clinical trials active or completed involving the use of stem cells in regenerative therapies (world-wide search in clinicaltrials.gov), however, only 20 of these are focussed on treating knee osteoarthritis. There is no published data about the outcomes of these studies at present.

In 2016 a systematic review of the available data demonstrated that implantation of hMSCs could successfully alleviate pain symptoms and improve joint motility in the knee by forming new hyaline-like cartilage, compared to the control[123,124]. A meta-analysis in 2017[125], designed to summarise previous reviews for hMSCs therapies in knee defects, was conducted by Yubo, et al. Only articles with a sufficient number of candidates submitted to treatment and with an established control were used. The results are summarised in Table 1.1.

Table 1.1 Available publications of clinical trials for mesenchymal stem cell injection therapies, adapted from[125] and [126]. CT=clinical trial, ACI= autologous chondrocyte injection, HA= hyaluronic acid.

Year (country)	CT Phase	Patients (male); control	Age mean; control	Follow up (months)	Control arm	Dose of hMSCs
2010 (Singapore) [127]	III	36(20); 36(18)	44.0; 42.5	25	ACI	$1–1.5\times10^7$
2014 (USA)[128]	II	18; 19	46	24	Placebo	5×10^7
2014 (USA)[128]	II	18; 19	46	24	Placebo	15×10^7
2015 (China)[125]	III	40(14); 40(13)	55.9; 55.1	12	HA	11.5×10^7
2015 (Spain)[129]	II	15(6); 15(5)	56.6; 57.3	12	HA	4×10^7

Other clinical trials, where adipose-derived stem cells were injected with or without growth factors, or osteotomy, have also proven to be successful[125]. More recently, a phase II trial was carried out whereby freshly harvested cells from bone marrow

were isolated and administered by intra-articular injection during the same surgery with positive results[130].

Importantly, stem cell therapies hold substantial benefits for patients suffering from osteoarthritic knee. Nevertheless, there are still limitations regarding clinical trials as, for instance, clinical trials for AC repair have scarcely been conducted in different countries[73], there are no multinational large samples to analyse stem cell therapies for OA, and some negative results remain unpublished[125]. To overcome these issues, a greater patient population is needed for a more robust analysis.

1.2.8 Challenges in stem cell therapies

One of the main barriers for the clinical translation of stem cell therapies is the lack of cell engraftment. Less than 1% of *in vitro* expanded stem cells can home to the damaged tissue. Poor attachment is, in part, because MSCs lose their *in vivo* homing receptors on the cell surface[131]. Additionally, MSCs cease to produce *in vivo* markers in artificial *in vitro* expansion culture and, consequently, markers for stem cell identification may be different for newly isolated cells than for *in vitro* expanded cultures[86].

The appropriate interaction between hMSCs and ECM is crucial to permit cell viability and engraftment. Failure to accomplish MSC-ECM interactions result in anoikis (homelessness) and apoptosis[132]. Cell adhesion is crucial for cell communication, and the maintenance and development of tissue. Adhesion is implicated in the differentiation, survival, migration, and cycle of the cell. *In vivo*, cells communicate through extracellular and intracellular stimuli by cell-cell adhesion or cell-ECM adhesion (focal adhesion) through integrins[132]. Integrins are a subclass of transmembrane adhesion-receptors, which facilitate cell-to-matrix adhesion by forming a bridge between the cell cytoskeleton and ECM[133]. It has

been demonstrated that focal adhesions and cell spreading increase with integrin binding and clustering[134]. In musculoskeletal diseases, the effective cell-ECM interactions are impeded by the inflammatory toxic environment on the damaged site[132] (Figure 1.16).

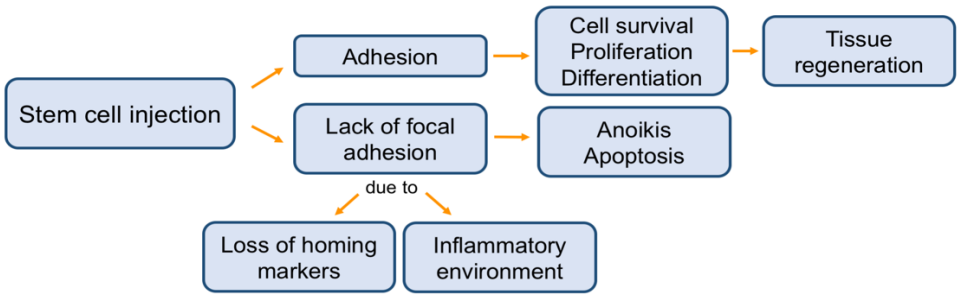

Figure 1.16 Consequences of adhesion and lack of adhesion of stem cells after injection.

Peripheral vein injection or local injection are the two methods used for stem cell transplantation into large organs such as heart and lungs. Both techniques have demonstrated the ability of MSCs to engraft into the damaged site, the latter being superior for stem cell retention[135]. In some cases, peripheral intra-artery administration leads to MSCs distribution to other healthy tissues such as the lungs and small blood vessels (i.e. microvasculature)[136].

A limited number of cells are retained when they are injected in a saline suspension, leading to cell death and clearance. Lan et al., found that less than 5% of the administered MSCs were retained in the injured lungs site after seven days[137]. Due to this low engraftment rate, large numbers of cells are needed for a beneficial effect after transplantation. On average, 10^7–10^8 cells are transplanted, as seen in the previous section form the clinical trials. This means that a population of 10^5 cells should undergo at least 17 doublings, which may lead to the cells reaching senescence, although, this effect might be reversible[81].

Regardless the type of targeted tissue or disease, the survival and engraftment of MSCs in injured or healthy tissue are crucial for successful tissue repair, and low

engraftment might limit tissue regeneration and reduce paracrine activity[138]. Optimal delivery and engraftment could result in the need of fewer cells.

In order to improve adhesion and viability of stem cells in the inflamed aggressive environment, a variety of techniques have been employed. For instance, it has been suggested that the encapsulation of cells in biomaterials might protect them from mechanical stress and at the same time, allow them to access nutrients such as oxygen and growth factors, and avoid cell displacement[139].

Another factor to consider in the administration of stem cells is the injection itself. The shear force produced by the needle while the injection is carried out might have a significant impact in the viability of the cells as it can cause rupture of the cell membrane[140]. Therefore encapsulation of cells in hydrogels before delivery is ideal to prevent membrane damage, as these materials can also have growth factors and proteins embedded in their fibres to improve the cell environment[141]. Hydrogels have proven their ability to retain cells in the damaged site and are discussed below in section 1.4.

The lack of *in vivo* stem cell retention after transplantation is hampering experimental progress and clinical implementation of stem cell therapies. In light of this, new methods to condition the stem cells for transplantation are necessary.

1.4 Tissue engineering based approaches for osteoarthritis

The inefficient endogenous repair of damaged ECM has led to the progress of tissue engineering, mainly utilizing scaffolding materials. The aim of these novel materials is to mimic the cartilage ECM environment by supporting cell viability, proliferation, and matrix secretion while substituting the function of the missing matrix until new articular cartilage (AC) is formed[142]. For instance, inserted collagen scaffolds act as a mesh to enhance the spontaneous healing response, this expands the blood clot created after a deep injury in the AC[52].

In order to recreate the ECM microenvironment, scaffolds must be biodegradable without exuding toxic by-products. They must be porous to allow circulation of nutrients, integrate with existing tissue, and give mechanical support[142].

Over the past years, many of the materials utilised for scaffolds are hydrogels. These scaffolds contain a three-dimensional network, allowing for high water retention[143]. They are made by crosslinking polymer chains through covalent bonds or sustained by intermolecular interactions (i.e. electrostatic interactions), to provide them with elastic and osmotic properties[144]. Hydrogels can be administered with minimal invasion surgery, are injectable and, because of their nature, can fill any shape of defect site[145] (Figure 1.17).

Hydrogel-based scaffolds are being created using natural and synthetic polymers. Natural polymers include alginate[147], chitosan[148], collagen[149], and fibrin[150], which can be degraded by natural enzymes. Polyethylene glycol (PEG) is the most studied synthetic polymer due to its biocompatibility[151], the same is true for its derivatives polyethylene glycol methacrylate (PEGMA), polyethylene glycol diacrylate (PEGDA)[152], followed by polyvinyl alcohol (PVA)[153]. A mixture of natural

and synthetic polymers is often used to attune the material to the desired properties[154].

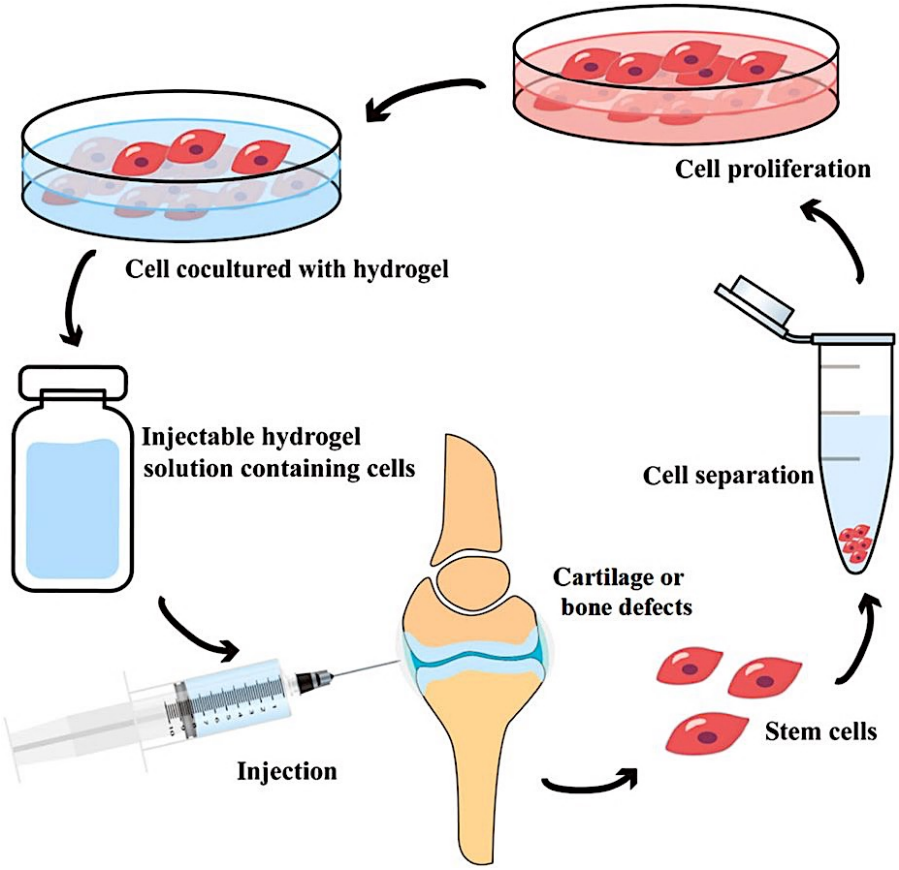

Figure 1.17 Schematic representation of the preparation of hydrogels for tissue regeneration. Image reproduced from[146].

Moreover, hydrogels can be produced with a variety of methods, including emulsification[155], lyophilisation[156], electrospinning[157], solvent casting[158], lithography[159], and cutting-edge 3D printing technology[160,161].

Importantly, injectable hydrogels can be employed as carriers for medications[162], growth factors[157], or combinations of these[163]. More recently, hydrogels have been used as a cell delivery vehicle. For instance, Smerglio et al. developed a hydrogel scaffold containing chondrocytes where the cells were able to survive for up to three weeks[164]. In another study, Chen et al., seeded chondrocytes in an alginate

matrix for delivery to *in vivo* rabbit osteochondral defect model, with an observed improvement in knee wound healing[165].

As mentioned above, another functional characteristic of hydrogels is that they can be rationally designed to exhibit a wide portfolio of properties. Scaffolds can be decorated with different molecules such as the integrin binding tripeptide Arginine-Glycine-Aspartic Acid (RGD)[166]. RGD is the minimal sequence within fibronectin type III that can be recognised by cell integrins to induce adhesion[23], although, this affinity is less than that of native fibronectin. Growth factors, fibronectin[167], and collagen[168] have also been used to enhance cell adhesion or to attract cells to the injured site. A few studies have revealed the use of hydrogels as a vehicle to deliver genes via non-viral vectors (i.e. transfection), with the release of DNA before the scaffold is degraded[169]. Needham reported polymeric scaffolds loaded with transcription factors typical for skeletal development and improved the healing of osteochondral defects in rats[170]. However, a significant restriction of these scaffolds is the rapid diffusion of DNA content *in vivo,* low DNA content, and the tendency of DNA for aggregation[171]. At the present, a number of hydrogel-based scaffolds with one or more of the aforementioned properties are commercially available[172].

Despite biodegradability being the most attractive property of hydrogel-based scaffolds, this characteristic also makes them susceptible to mechanical failure, since most hydrogels undergo bulk erosion[151]. For instance, when hydrogels are used for AC regeneration, there is a trade-off between stiffness to bare the loads and degradability due to compression.

Regardless of the technique and materials used to create hydrogel-based scaffolds, porosity is an essential characteristic to maintain biocompatibility. Pore

density and size are crucial to guarantee that cells are at the optimal distance from their nutrient source[173], and accordingly so that cells can migrate and penetrate the full scaffold depth. Pores should be big enough to surround the cells and retain them, but not too small to prevent migration.

Another concern for *in vivo* compatibility of hydrogel-scaffolds is the toxic remnant chemicals that are used for polymerisation or cross-linking precursors[146]. Unreacted monomers, organic solvents and other materials utilised for the manufacture of hydrogels may be present even after extensive washing, causing cytotoxic and detrimental effects to the implanted site[146]. Hydrogel scaffolds may also instigate foreign body reaction in sensitive patients, leading to the release of oxygen free radicals and degradative enzymes[174].

1.2.9 Stem cell conditioning

Cell resistance to hostile microenvironments has been the focus of many investigations to improve stem cell delivery. It has been proposed that the amount of oxygen stem cells were exposed to during *in vitro* expansion has an effect on their proliferation, differentiation capacities, and ability to secrete paracrine soluble factors[175]. After injection, MSCs are subjected to sudden stress in a low oxygen environment within the tissue defect. Therefore preconditioning within hypoxic conditions (1% oxygen) before transplantation has been practised, providing an enhancement in the survival rates and engraftment of hMSCs in a pulmonary fibrotic mice model[137]. Adipose-derived MSCs have been treated with hypoxia and SDF-1$^{\alpha}$, which enhanced their retention after administration[176]. The use of small molecule antioxidants, such as curcumin, to treat BM-MSCs prevents oxidative-stress-induced-apoptosis[177], and preconditioning with growth factors have also been studied[178].

The combination of various techniques has been studied in an attempt to achieve superior tissue engineering. Cai et al. demonstrated that MSCs delivered in a hydrogel matrix can increase the number of attached cells in a mouse model[140]. In a similar manner, hydrogel nanofibers containing growth factors and seeded muscle stem cells proved to enhance cell engraftment and, therefore, tissue repair[179]. The fibres are also able to degrade in parallel with tissue regeneration[179]. Another approach is to treat the target tissue prior to cell transplantation[180].

Regulatory requirements must be complied with when designing new materials, such as toxicity, scalability, and cost-effective commercialisation[181]. In light of all of this, there is a vast window of opportunity to improve stem cell therapies by employing stem cell membrane engineering strategies.

1.2.10 Stem cell membrane reengineering

The engineering or modification of the cell membrane can be achieved by different strategies, such as the addition of antibodies, synthetic or natural molecules, as well as genetic modification. The introduction of genetic materials into MSCs can be accomplished using viral or non-viral vectors. Viral vector modification enables long term stable transgene expression. For instance, transfection using a lenti-virus enhanced the survival rates of rat MSCs and increased resistance to cell apoptosis in a hypoxic environment in rat ischaemia model[182].

In the same manner, genetic modification has enabled MSCs to induce overexpression of antiapoptotic signalling[183,184] and cell adhesion enhancement[183]. However, the use of these viral vectors is accompanied by high levels of pressure in the gene regulation[185], as overexpression of a gene could cause detrimental secondary effects in the long term.

The engineering of cell membranes can also be achieved via surface chemistry. Hao Cheng et al., engineered the membranes of human MSCs in a two-step reaction. First, the amine groups on the cell membrane proteins were functionalised with a maleimide containing group, which was subsequently reacted with a cystein-cotaining peptide K, a known E-selectin binding peptide to enhance cell adhesion into the injured site[186]. In the innate wound healing mechanism, P-selectin plays a key role in the recruitment of leukocytes to the injured site and in healthy tissue remains dormant inside of endothelial cells as granules. After endothelial cells are activated during inflammation by histamine or thrombin, P-selectin is transported to the endothelial cell surface. E-selectin has a similar purpose, however, it is secreted by endothelial cells in response to the influence of cytokines such as TNF-a[187]. Inspired by this naturally occurring process, Sarkar et. al. modified the cell membrane surface of MSCs with cell adhesion molecules. Sialyl Lewix X (SLE^x), the active site of P-selectin glycoprotein ligand in leukocytes, was covalently attached on the surface of the cell membrane with a biotin-streptavidin bridge. These cells showed superior rolling capacity and attachment compared to unmodified cells[188]. Two years later, the same group used biotinylated unilamellar vesicles that integrated into the cell membrane of MSCs. Subsequently, SLE^x was immobilised on the cell surface with a streptavidin linker. The inserted biotinylated lipids were internalised after 8 hours[189].

Another approach has exploited the hydrophobic nature of the cell membrane to enhance the adhesion properties of the cells. DNA origami technology was used to assemble modified-cell arrays onto chemically functionalised surfaces with complimentary DNA sequences[190]. Akbari et al., used hydrophobic anchors to attach DNA self-assembled origami nano-structures to primary cells. Cholesterol

conjugated oligonucleotides were used for amphiphilic insertion into the membrane, which subsequently bound ssDNA with an incorporated self-assembled nano-platform that served as a tuneable “breadboard” for specific cell-cell binding[191].

Artificial membrane-binding proteins have been used to reduce necrosis in MSC-seeded scaffolds by creating a myoglobin-polymer surfactant complex. This complex was created by electrostatic conjugation of the anionic polymer surfactant to solvent-exposed positively charges on chemically cationized myoglobin. Significantly, when introduced to the cell, the polymer surfactant corona surrounding the protein reconfigured to spontaneously insert into the plasma membrane, effectively anchoring the construct to the cell at extremely high loadings. Pre-treating MSCs with these complexes imparted an oxygen reservoir, which under hypoxia, released oxygen when levels were significantly low. The synthesis of polymer-protein complexes or conjugates has been utilised not only to modify stem cell surfaces, but also to give proteins enhanced solubility characteristics[192].

As an alternative to chemically induced cationization during the synthesis of these electrostatic conjugates, the use of genetically modified proteins that exhibit a high level of positive charge, such as supercharged GFP[193] (scGFP) could be employed. Indeed, this is core to this thesis and will be discussed below.

1.5 The green fluorescent protein

The green fluorescent protein (GFP) is an inherent protein found in the jellyfish *Aequorea victoria*, and was cloned by Douglas Prasher in 1992[194]. The GFP gene has been used as a marker for gene expression[195], as a mutagenesis biosensor[196], as a probe to detect localisation into cell compartments, and as a non-invasive marker for living cells. Wild type GFP is a 21 kDa protein, consisted of 238 residues, which defines its primary structure[197]. GFP has a β-barrel structure, formed by β-turns, 11 β-sheets and five α-helices, which constitute the secondary structure[198,199], held by the hydrogen bonds between amino acids (Figure 1.18).

A segment folded into an α-helix creates a spiral, holding the backbone in a straight position where the residues point outwards. The β-strands are short, almost completely extended polypeptide segments. Packed β-strands form a β-sheet. The U-shaped β-turns produce the reverse direction of the protein chain (anti-parallel β-sheets), and also helps proteins fold into compact structures[23]. GFP tertiary structure is stable due to the hydrophobic non-covalent interactions.

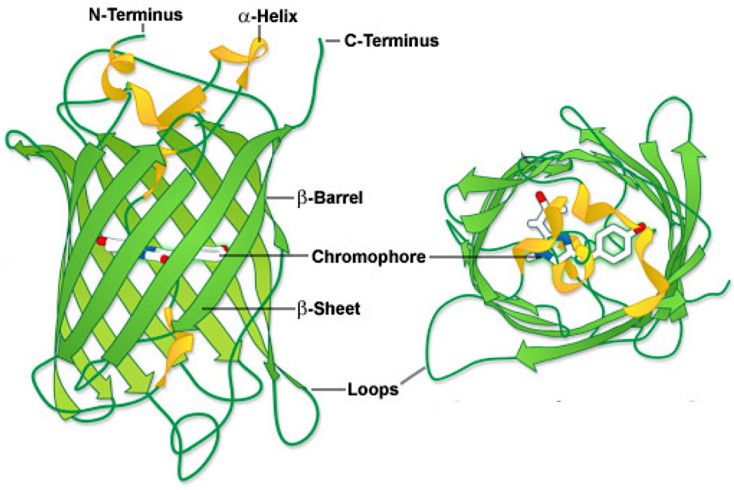

Figure 1.18 Schematic representation of the green fluorescent protein (GFP). GFP is comprised by a β-barrel structure and α-helices. Adapter from[200].

Correct folding of the GFP structure is necessary to observe the fluorescent properties of the fluorophore, as the resulting tertiary structure provides shielding, which prevents quenching in the aqueous environment. The native protein has a quaternary structure, it forms a dimer, although this has been knocked out of laboratory grade GFP.

The GFP fluorophore is an α-helix with the covalently bound 4-(*p*-hydroxybenzylidene) imidazolidine-5-one or HBI. It has been suggested that the formation of the chromophore is due to a nucleophilic attack of the amino group in glycine 67 (Gly67) on the carbonyl group of serine 65 (Ser65), leading to the creation of imidazoline-5-one, which is subsequently dehydrated[201]. This results in the chromophore maturation, which is the formation of a cyclic group with the amino group in tyrosine 66 (Tyr66)[201].

Multiple variants of wild-type green fluorescent protein (GFP) have been synthesised in order to improve protein folding or to change the emission and excitation spectra, the latter resulting in yellow, blue, or cyan fluorescent proteins[202]. Superfolder GFP (sfGFP) was created to enhance folding robustness[203]. This protein was based in the previously modified enhanced GFP (eGFP) and Cycle3 GFP, containing 12 mutations in total with respect to the wild-GFP[204]. sfGFP remains well folded regardless the stability of the fused protein partner[203].

Recently, sfGFP was radically reengineered such that 29 of the solvent-exposed amino acids were altered to the positively charged amino acids lysine and arginine This novel protein, called supercharged GFP (scGFP), has a theoretical net charge of +36 (Figure 1.19).

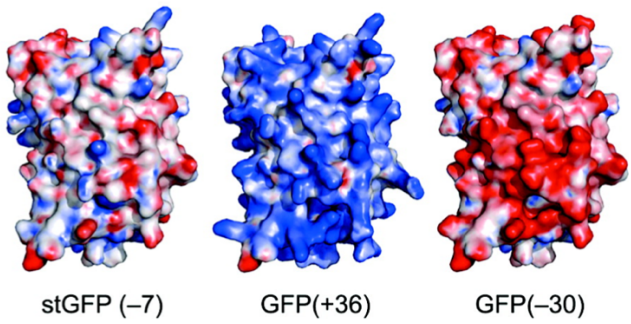

Figure 1.19 Surface representation of supercharged green fluorescent proteins variants. Blue: positive charge, red: negative charge. Reproduced from[193].

This scGFP is resistant to aggregation and remains soluble when heated to 100°C. Furthermore, scGFP has the ability to interact with mammalian cells in an electrostatic fashion with the negatively charged proteoglycans on the cell membrane surface[205] with low toxicity upon internalisation[206]. Significantly, this new highly cationic globular fluorescent protein presents an exciting new opportunity to extend on the work of Armstrong et al.[207] to develop a completely new class of cell membrane binding proteins. Accordingly, the synthesis of novel scGFP-polymer surfactant hybrid constructs is a central to this thesis.

1.6 Adhesion to the extracellular matrix

Martino et al. screened the most predominant proteins in the extracellular matrix (ECM): fibronectin, vitronectin, tenascin C, osteopontin, fibrinogen and collagen I; against 25 growth factors from three different families[208]. After an enzyme-linked immunosorbent assay (ELISA), it was found that placenta growth factor 2 (PlGF2) exhibited high affinity for the six ECM proteins. In contrast, placenta growth factor 1 (PlGF1) did not display significant affinity towards any of the screened proteins. The only difference between PlGF1 and PlGF2 is a 21-aminoacid peptide in PlGF2 with the sequence RRPKGRGKRRREKQRPTDCHL in between amino acids 123 and 144, subsequently named PlGF2_123−144.

Accordingly, the peptide was genetically fused to growth factors platelet derived growth factor (PDGF-BB), to produce PDGF-BB/PlGF2_123−144, and to vascular endothelial growth factor (VEGF-A165), producing VEGF-A165/PlGF2_123−144. These were then administered into a mouse skin would model. The engineered growth factors displayed strong binding and retention in endogenous ECM, which was attributed to the insertion of the peptide. Moreover, the addition of the PlGF2_123−144 domain did not interfere with the growth factors biological activity In addition, a significant difference in the number of cells recruited to the damaged site was detected when wounds were treated with the modified growth factors compared to the wild type due to their persistence on the ECM.

In light of these findings, it was reasoned that the supercharged GFP could be recombinantly expressed fused with the peptide PlGF2_123−144. The new construct [scGFP_PlGF2] would have an increased affinity for ECM proteins.

1.7 Project design and aims

In light of the discussion of the literature above, it is becoming clear that one of the major challenges in regenerative therapies involving stem cells injection, is the efficiency of prompt and firm adhesion for subsequent engraftment of the transplanted cells onto the target site. Accordingly, this project is focused on the modification of human mesenchymal stem cells (hMSCs) surface membrane using protein-polymer surfactant nanobiohybrids, in order to increase the cell adhesion number. This can be accomplished by the expression of rational design and the synthesis of a fusion protein formed by supercharged green fluorescent protein (scGFP) and a placenta growth factor 2 domain (PlGF2_123–144), the expressed protein was named [scGFP_PlGF2]. The positively charged scGFP moiety is electrostatically bound to the anionic oxidised IGEPAL co-890 polymer surfactant, while the PlGF2 domain is free to interact and associate with the ECM surface, creating [scGFP_PlGF2][S]. The hydrophobic tail of the polymer surfactant serves as an anchor to associate with the cell membrane (Figure 1.20). This nanobiohybrid can be used to reengineer the surface of hMSCs to instil enhanced ECM binding properties to regulate cell adhesion to natural scaffold might provide great benefits for injectable regenerative therapies.

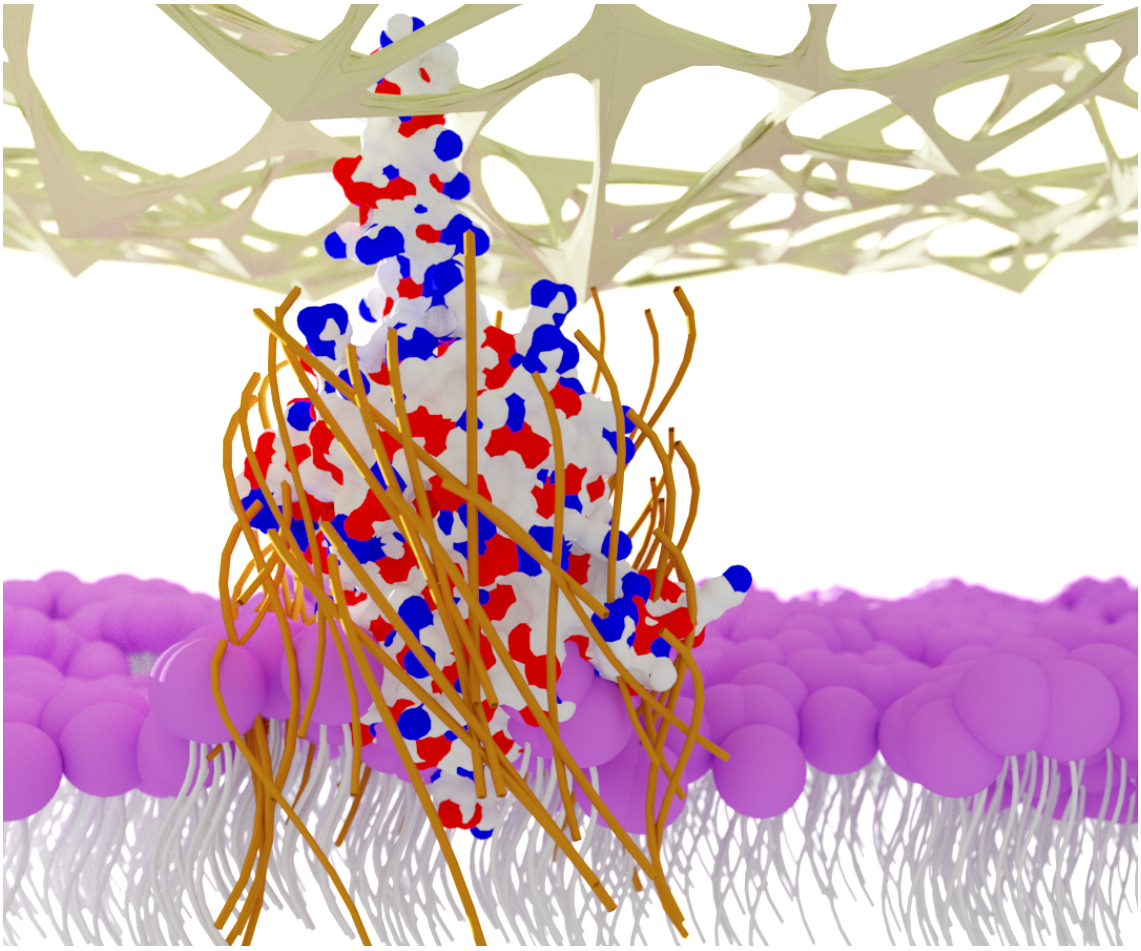

Figure 1.20 Schematic representation of nanobiohybrid interaction. The supercharged GFP barrel is electrostatically conjugated with the surfactant (yellow), which anchors onto the cell membrane (purple), leaving the PlGF2 domain free to interact with the extracellular matrix.

1.8 Thesis structure

This thesis consists of one materials and methods chapter, followed by three chapters of results, and a general conclusions chapter. All techniques used to perform the research are described in Chapter 2: Materials and methods. In the first chapter of results, Chapter 3, the synthesis and characterisation of the electrostatically formed nanobiohybrid construct is detailed, including structural and biophysical analyses. Chapter 4 describes the interaction of the novel nanobiohybrids [scGFP_PlGF2], and [scGFP_PlGF2][S] with human mesenchymal stem cells (hMSCs), utilising microscopy, as wells as *in vitro* cytotoxicity, proliferation, and differentiation assays. The final data chapter (Chapter 5) explores the ability of the modified hMSCs to interact with proteins from the cartilage extracellular matrix (ECM), both in vitro, and via bovine ex vivo explants.

1.9 Bibliography

1. Kraus, V. B., Blanco, F. J., Englund, M., Karsdal, M. A. & Lohmander, L. S. Call for standardized definitions of osteoarthritis and risk stratification for clinical trials and clinical use. *Osteoarthr. Cartil.* **23**, 1233–1241 (2015).

2. Xing, D. *et al.* Osteoarthritis and all-cause mortality in worldwide populations: Grading the evidence from a meta-analysis. *Sci. Rep.* **6**, 24393 (2016).

3. Song, J., Chang, R. W. & Dunlop, D. D. Population impact of arthritis on disability in older adults. *Arthritis Care Res.* **55**, 248–255 (2006).

4. Vos, T. *et al.* Years lived with disability (YLDs) for 1160 sequelae of 289 diseases and injuries 1990–2010: a systematic analysis for the Global Burden of Disease Study 2010. *Lancet* **380**, 2163–2196 (2012).

5. Prieto-Alhambra, D. *et al.* Incidence and risk factors for clinically diagnosed knee, hip and hand osteoarthritis: Influences of age, gender and osteoarthritis affecting other joints. *Ann. Rheum. Dis.* **73**, 1659–1664 (2014).

6. Xie, F., Thumboo, J. & Li, S. C. True Difference or Something Else? Problems in Cost of Osteoarthritis Studies. *Semin. Arthritis Rheum.* **37**, 127–132 (2007).

7. March, L. M. & Bachmeier, C. J. M. Economics of osteoarthritis: A global perspective. *Bailliere's Clinical Rheumatology* **11**, 817–834 (1997).

8. Chen, A., Gupte, C., Akhtar, K., Smith, P. & Cobb, J. The Global Economic Cost of Osteoarthritis: How the UK Compares. *Arthritis* **2012**, 1–6 (2012).

9. Le Pen, C., Reygrobellet, C. & Gérentes, I. Financial cost of osteoarthritis in France: The 'COART' France study. *Jt. Bone Spine* **72**, 567–570 (2005).

10. Puig-Junoy, J. & Ruiz Zamora, A. Socio-economic costs of osteoarthritis: A systematic review of cost-of-illness studies. *Semin. Arthritis Rheum.* **44**, 531–541 (2015).

11. Markets, F. Statista. *2019* Available at: https://www.statista.com/statistics/412806/euro-to-gbp-average-annual-exchange-rate/.

12. No Title. Available at: http://www.nhs.uk/conditions/vaccinations/pages/the-history-of-vaccination.aspx.

13. Curtis, L. Unit Costs of Health and Social Care 2005 compiled by Lesley Curtis and Ann Netten. *Technology* (2005).

14. Arthritis Research UK. *State of Musculoskeletal Health 2018*. *Arthritisresearchuk.Org* (2018). doi:10.2214/AJR.16.17742

15. WHO. WHO | Metrics: Disability-Adjusted Life Year (DALY). *Metrics: Disability-Adjusted Life Year (DALY). Quantifying the burden of disease from mortality and morbidity* (2014). doi:10.1109/ICASSP.2016.7472899

16. Fowler, K. Connective Tissues. in *Cell Biology* **3**, 555–570 (Elsevier, 2017).

17. Sophia Fox, A. J., Bedi, A. & Rodeo, S. A. The basic science of articular cartilage: structure, composition, and function. *Sports Health* **1**, 461–8 (2009).

18. Alford, J. W. & Cole, B. J. Cartilage restoration, part 1: Basic science, historical perspective, patient evaluation, and treatment options. *Am. J. Sports Med.* **33**, 295–306 (2005).

19. Mow, V. C., Ratcliffe, A. & Poole, A. R. Cartilage and diarthrodial joints as paradigms for hierarchical materials and structures. *Biomaterials* **13**, 67–97 (1992).

20. OpenStax. Introduction - Anatomy & Physiology - OpenStax CNX. *Mar 6* (2013). Available at: https://cnx.org/contents/FPtK1zmh@6.27:zMTtFGyH@4/Introduction. (Accessed: 22nd February 2019)

21. Riesle, J., Hollander, A. P., Langer, R., Freed, L. E. & Vunjak-Novakovic, G. Collagen in tissue-engineered cartilage: Types, structure, and crosslinks. *J. Cell. Biochem.* **71**, 313–327 (1998).

22. Roughley, P. J. & Lee, E. R. Cartilage proteoglycans: Structure and potential functions. *Microsc. Res. Tech.* **28**, 385–397 (1994).

23. Lodish, H. *et al. Molecular Biology*. (Sara Tenney, 2008).

24. Zhang, X., Blalock, D. & Wang, J. Classifications and Definitions of Normal Joints. in *Osteoarthritis - Progress in Basic Research and Treatment* (InTech, 2015). doi:10.5772/59977

25. Akkiraju, H. & Nohe, A. Role of Chondrocytes in Cartilage Formation, Progression of Osteoarthritis and Cartilage Regeneration. *J. Dev. Biol.* **3**, 177–192 (2015).

26. Poole, C. A. Articular cartilage chondrons: Form, function and failure. *J. Anat.* **191**, 1–13 (1997).

27. Barnett, C. H. Wear and tear in joints. *J Bone Jt. Surg [Br]* **38**, 567–575 (1956).

28. Temenoff, J. S. & Mikos, A. G. Review: Tissue engineering for regeneration of articular cartilage. *Biomaterials* **21**, 431–440 (2000).

29. Archer, C. W. & Francis-West, P. The chondrocyte. *Int. J. Biochem. Cell Biol.* **35**, 401–404 (2003).

30. Verzijl, N. *et al.* Effect of collagen turnover on the accumulation of advanced glycation end products. *J. Biol. Chem.* **275**, 39027–39031 (2000).

31. van der Kraan, P. M. & van den Berg, W. B. Chondrocyte hypertrophy and osteoarthritis: role in initiation and progression of cartilage degeneration? *Osteoarthr. Cartil.* **20**, 223–232 (2012).

32. NCBI. TGFBR1 transforming growth factor beta receptor 1 [Homo sapiens (human)]. (2019). Available at: https://www.ncbi.nlm.nih.gov/gene?Db=gene&Cmd=ShowDetailView&TermToSearch=7046. (Accessed: 9th January 2019)

33. Liu, L. *et al.* Smad2 and Smad3 have differential sensitivity in relaying TGFβ signaling and inversely regulate early lineage specification. *Sci. Rep.* **6**, 21602 (2016).

34. Yang, X. *et al.* TGF-β/Smad3 signals repress chondrocyte hypertrophic differentiation and are required for maintaining articular cartilage. *J. Cell Biol.* **153**, 35–46 (2001).

35. Dreier, R. Hypertrophic differentiation of chondrocytes in osteoarthritis: The developmental aspect of degenerative joint disorders. *Arthritis Res. Ther.* **12**, 216 (2010).

36. Tsuchiya, A. *et al.* Expression of mouse HtrA1 serine protease in normal bone and cartilage and its upregulation in joint cartilage damaged by experimental arthritis. *Bone* **37**, 323–336 (2005).

37. Sandell, L. J. & Aigner, T. Articular cartilage and changes in arthritis. An introduction: cell biology of osteoarthritis. *Arthritis Res.* **3**, 107–13 (2001).

38. Billinghurst R Clarke; Dahlberg, Leif; Lonescu, Mirela; Reimer, Agnes; Bourne, Robert; Rorabeck, Cecil; Mitchell, John Hambor; Diekmann, Oliver; Tschesche, Harald; Chen, Jeffrey; Wart, Hal Van; Poole, A. R. Enhanced Cleavage of Type II collagen by Collagenases in Osteoarthritic Articular Cartilage. *J. Virol.* **86**, 4129–4138 (2012).

39. Fukui, N. *et al.* Zonal gene expression of chondrocytes in osteoarthritic cartilage. *Arthritis Rheum.* **58**, 3843–3853 (2008).

40. Rose, B. J. & Kooyman, D. L. A Tale of Two Joints: The Role of Matrix Metalloproteases in Cartilage Biology. *Dis. Markers* **2016**, 4895050 (2016).

41. Lin, P. M., Chen, C. T. C. & Torzilli, P. A. Increased stromelysin-1 (MMP-3), proteoglycan degradation (3B3- and 7D4) and collagen damage in cyclically load-injured articular cartilage. *Osteoarthr. Cartil.* **12**, 485–496 (2004).

42. Polur, I., Lee, P. L., Servais, J. M., Xu, L. & Li, Y. Role of HTRA1, a serine protease, in the progression of articular cartilage degeneration. *Histol. Histopathol.* **25**, 599–608 (2010).

43. Loeser, R. F. Age-Related Changes in the Musculoskeletal System and the Development of Osteoarthritis. (2010). doi:10.1016/j.cger.2010.03.002

44. Kostoulas, G., Lang, A., Nagase, H. & Baici, A. Stimulation of angiogenesis through cathepsin B inactivation of the tissue inhibitors of matrix metalloproteinases. *FEBS Lett.* **455**, 286–290 (1999).

45. Dean, D. D., Muniz, O. E. & Howell, D. S. Association of collagenase and tissue inhibitor of metalloproteinases (TIMP) with hypertrophic cell enlargement in the growth plate. *Matrix* **9**, 366–75 (1989).

46. Mease, P. J., Hanna, S., Frakes, E. P. & Altman, R. D. Pain mechanisms in osteoarthritis: Understanding the role of central pain and current approaches to its treatment. *J. Rheumatol.* **38**, 1546–1551 (2011).

47. Remst, D. F. G., Davidson, E. N. B. & Van Der Kraan, P. M. Unravelling osteoarthritis-related synovial fibrosis: a step closer to solving joint stiffness. doi:10.1093/rheumatology/kev228

48. van der Kraan, P. M. & van den Berg, W. B. Osteophytes: relevance and biology. *Osteoarthr. Cartil.* **15**, 237–244 (2007).

49. Aigner, T., Dietz, U., Stöss, H. & von der Mark, K. Differential expression of collagen types I, II, III, and X in human osteophytes. *Lab. Invest.* **73**, 236–43 (1995).

50. Cucchiarini, M. *et al.* A vision on the future of articular cartilage repair. *Eur. Cell. Mater.* **27**, 12–6 (2014).

51. Buckwalter, J. A. Articular Cartilage: Injuries and Potential for Healing. *J. Orthop. Sport. Phys. Ther.* **28**, 192–202 (1998).

52. Hunziker, E. B. Articular cartilage repair: basic science and clinical progress. A review of the current status and prospects. *Osteoarthr. Cartil.* **10**, 432–463 (2002).

53. Jackson, D. W., Lalor, P. A., Aberman, H. M. & Simon, T. M. Spontaneous repair of full-thickness defects of articular cartilage in a goat model. A preliminary study. *J. Bone Joint Surg. Am.* **83-A**, 53–64 (2001).

54. Shapiro, F., Koide, S. & Glimcher, M. J. Cell origin and differentiation in the repair of full-thickness defects of articular cartilage. *J. Bone Joint Surg. Am.* **75**, 532–53 (1993).

55. Moyad, T. F. Cartilage injuries in the adult knee: Evaluation and management. *Cartilage* **2**, 226–236 (2011).

56. Heath, C. A. & Magari, S. R. Mini-review: Mechanical factors affecting cartilage regeneration in vitro. *Biotechnol. Bioeng.* **50**, 430–437 (2000).

57. Livesley, P. J., Doherty, M., Needoff, M. & Moulton, A. Arthroscopic lavage of osteoarthritic knees. *J. Bone Joint Surg. Br.* **73**, 922–6 (1991).

58. Moseley, J. B., Wray, N. P., Kuykendall, D., Willis, K. & Landon, G. Arthroscopic treatment of osteoarthritis of the knee: A prospective, randomized, placebo-controlled trial. Results of a pilot study. *Am. J. Sports Med.* **24**, 28–34 (1996).

59. Mirza, M. Z., Swenson, R. D. & Lynch, S. A. Knee cartilage defect: marrow stimulating techniques. *Curr. Rev. Musculoskelet. Med.* **8**, 451–6 (2015).

60. Jackson, J. P. & Waugh, W. Tibial osteotomy for osteoarthritis of the knee. *J Bone Jt. Surg Br* **43**, 746–751 (1961).

61. Robert, H. Chondral repair of the knee joint using mosaicplasty. *Orthop.*

Traumatol. Surg. Res. **97**, 418–429 (2011).

62. Hangody, L. *et al.* Autologous osteochondral grafting—Technique and long-term results. *Injury* **39**, 32–39 (2008).

63. Bentley, G. *et al.* A prospective, randomised comparison of autologous chondrocyte implantation versus mosaicplasty for osteochondral defects in the knee. *J. Bone Joint Surg. Br.* **85**, 223–30 (2003).

64. Ahmed, T. A. E. & Hincke, M. T. Strategies for Articular Cartilage Lesion Repair and Functional Restoration. *Tissue Eng. Part B Rev.* **16**, 305–329 (2010).

65. Huang, B. J., Hu, J. C. & Athanasiou, K. A. Cell-based tissue engineering strategies used in the clinical repair of articular cartilage. *Biomaterials* **98**, 1–22 (2016).

66. Peterson, L., Brittberg, M., Kiviranta, I., Åkerlund, E. L. & Lindahl, A. Autologous chondrocyte transplantation: Biomechanics and long-term durability. *Am. J. Sports Med.* **30**, 2–12 (2002).

67. Brittberg, M. *et al.* Treatment of Deep Cartilage Defects in the Knee with Autologous Chondrocyte Transplantation. *N. Engl. J. Med.* **331**, 889–895 (1994).

68. Baugé, C. & Boumédiene, K. Use of Adult Stem Cells for Cartilage Tissue Engineering: Current Status and Future Developments. *Stem Cells Int.* **2015**, 1–14 (2015).

69. Ogura, T., Bryant, T. & Minas, T. Long-term Outcomes of Autologous Chondrocyte Implantation in Adolescent Patients. *Am. J. Sports Med.* **45**, 1066–1074 (2017).

70. Mobasheri, A., Kalamegam, G., Musumeci, G. & Batt, M. E. Chondrocyte and mesenchymal stem cell-based therapies for cartilage repair in osteoarthritis and related orthopaedic conditions. *Maturitas* **78**, 188–198 (2014).

71. Schulze-Tanzil, G. *et al.* Redifferentiation of dedifferentiated human chondrocytes in high-density cultures. *Cell Tissue Res.* **308**, 371–379 (2002).

72. Reinke, J. M. & Sorg, H. Wound repair and regeneration. *Eur. Surg. Res.* **49**, 35–43 (2012).

73. Negoro, T., Takagaki, Y., Okura, H. & Matsuyama, A. Trends in clinical trials for articular cartilage repair by cell therapy. *npj Regen. Med.* **3**, 17 (2018).

74. Chagastelles, P. C. & Nardi, N. B. Biology of stem cells: An overview. *Kidney Int. Suppl.* **1**, 63–67 (2011).

75. Robertson, J. A. Human embryonic stem cell research: Ethical and legal issues. *Nat. Rev. Genet.* **2**, 74–78 (2001).

76. McLaren, A. *Ethical and social considerations of stem cell research*. *Nature*

414, (2001).

77. Denker, H. W. Potentiality of embryonic stem cell: An ethical problem even with alternative stem cell sources. *J. Med. Ethics* **32**, 665–671 (2006).

78. Takahashi, K. & Yamanaka, S. Induction of Pluripotent Stem Cells from Mouse Embryonic and Adult Fibroblast Cultures by Defined Factors. *Cell* **126**, 663–676 (2006).

79. Singh, V. K., Kalsan, M., Kumar, N., Saini, A. & Chandra, R. Induced pluripotent stem cells: applications in regenerative medicine, disease modeling, and drug discovery. *Front. Cell Dev. Biol.* **3**, 2 (2015).

80. Ermolaeva, M., Neri, F., Ori, A. & Rudolph, K. L. Cellular and epigenetic drivers of stem cell ageing. *Nat. Rev. Mol. Cell Biol.* **19**, 594–610 (2018).

81. Li, Y. *et al.* Senescence of mesenchymal stem cells (Review). *Int. J. Mol. Med.* **39**, 775–782 (2017).

82. Hu, L. *et al.* Mesenchymal Stem Cells: Cell Fate Decision to Osteoblast or Adipocyte and Application in Osteoporosis Treatment. *Int. J. Mol. Sci.* **19**, 360 (2018).

83. Ma, J. *et al.* Concise Review: Cell-Based Strategies in Bone Tissue Engineering and Regenerative Medicine. *Stem Cells Transl. Med.* **3**, 98–107 (2014).

84. Maleki, M., Ghanbarvand, F., Behvarz, M. R., Ejtemaei, M. & Ghadirkhomi, E. Comparison of mesenchymal stem cell markers in multiple human adult stem cells. *Int. J. Stem Cells* **7**, 118–126 (2014).

85. Dominici, M. *et al.* Minimal criteria for defining multipotent mesenchymal stromal cells. The International Society for Cellular Therapy position statement. *Cytotherapy* **8**, 315–317 (2006).

86. Boxall, S. A. & Jones, E. Markers for characterization of bone marrow multipotential stromal cells. *Stem Cells Int.* **2012**, (2012).

87. Ichiryu, N. & Fairchild, P. J. Immune Privilege of Stem Cells. 1–16 (2013). doi:10.1007/978-1-62703-478-4_1

88. Chamberlain, G., Fox, J., Ashton, B. & Middleton, J. Concise Review: Mesenchymal Stem Cells: Their Phenotype, Differentiation Capacity, Immunological Features, and Potential for Homing. *Stem Cells* **25**, 2739–2749 (2007).

89. Williams, A. R. & Hare, J. M. Mesenchymal stem cells: Biology, pathophysiology, translational findings, and therapeutic implications for cardiac disease. *Circ. Res.* **109**, 923–940 (2011).

90. Bartholomew, A. *et al.* Mesenchymal stem cells suppress lymphocyte proliferation in vitro and prolong skin graft survival in vivo. *Exp. Hematol.* **30**, 42–48 (2002).

91. Uccelli, A., Moretta, L. & Pistoia, V. Mesenchymal stem cells in health and disease. *Nat. Rev. Immunol.* **8**, 726–736 (2008).

92. Medzhitov, R. Origin and physiological roles of inflammation. *Nature* **454**, 428–435 (2008).

93. Luster, A. D., Alon, R. & Von Andrian, U. H. Immune cell migration in inflammation: present and future therapeutic targets. *Nat. Immunol.* **6**, (2005).

94. Krysko, D. V *et al.* Macrophages use different internalization mechanisms to clear apoptotic and necrotic cells. *Cell Death Differ.* **13**, 2011–2022 (2006).

95. Shi, Y. *et al.* How mesenchymal stem cells interact with tissue immune responses. *Trends Immunol.* **33**, 136–143 (2012).

96. Chen, Y. *et al.* Recruitment of endogenous bone marrow mesenchymal stem cells towards injured liver. *J. Cell. Mol. Med.* **14**, 1494–1508 (2010).

97. Kavanagh, D. P. J. & Kalia, N. Hematopoietic Stem Cell Homing to Injured Tissues. *Stem Cell Rev. Reports* **7**, 672–682 (2011).

98. Rennert, R. C., Sorkin, M., Garg, R. K. & Gurtner, G. C. Stem cell recruitment after injury: lessons for regenerative medicine. *Regen. Med.* **7**, 833–50 (2012).

99. Butcher, E. C. & Picker, L. J. Lymphocyte Homing and Homeostasis. *Science (80-.).* **272**, 60–66 (1996).

100. Ankrum, J. & Karp, J. M. Mesenchymal stem cell therapy: Two steps forward, one step back. *Trends Mol. Med.* **16**, 203–209 (2010).

101. Chen, L., Tredget, E. E., Wu, P. Y. G., Wu, Y. & Wu, Y. Paracrine factors of mesenchymal stem cells recruit macrophages and endothelial lineage cells and enhance wound healing. *PLoS One* **3**, e1886 (2008).

102. Zhang, S. *et al.* Exosomes derived from human embryonic mesenchymal stem cells promote osteochondral regeneration. *Osteoarthr. Cartil.* **24**, 2135–2140 (2016).

103. Cosenza, S., Ruiz, M., Toupet, K., Jorgensen, C. & Noël, D. Mesenchymal stem cells derived exosomes and microparticles protect cartilage and bone from degradation in osteoarthritis. *Sci. Rep.* **7**, 16214 (2017).

104. Jorgenson, K. D., Hart, D. A., Krawetz, R. & Sen, A. Production of adult human synovial fluid-derived mesenchymal stem cells in stirred-suspension culture. *Stem Cells Int.* **2018**, 8431053 (2018).

105. Hunziker, E. B. & Rosenberg, L. C. Repair of partial-thickness defects in articular cartilage: cell recruitment from the synovial membrane. *J. Bone Joint Surg. Am.* **78**, 721–33 (1996).

106. McGonagle, D., Baboolal, T. G. & Jones, E. Native joint-resident mesenchymal stem cells for cartilage repair in osteoarthritis. *Nat. Rev.*

Rheumatol. **13**, 719–730 (2017).

107. Fellows, C. R. *et al.* Characterisation of a divergent progenitor cell sub-populations in human osteoarthritic cartilage: The role of telomere erosion and replicative senescence. *Sci. Rep.* **7**, 41421 (2017).

108. Ng, Y. Y., Baert, M. R. M., de Haas, E. F. E., Pike-Overzet, K. & Staal, F. J. T. Isolation of human and mouse hematopoietic stem cells. *Methods Mol Biol* **506**, 13–21 (2009).

109. Civinini, R. *et al.* Growth factors in the treatment of early osteoarthritis. *Clin. Cases Miner. Bone Metab.* **10**, 26–9 (2013).

110. Cross, D. P. & Wang, C. Stromal-derived factor-1 alpha-loaded PLGA microspheres for stem cell recruitment. *Pharm. Res.* **28**, 2477–2489 (2011).

111. Oh, I. Y. *et al.* Involvement of E-selectin in recruitment of endothelial progenitor cells and angiogenesis in ischemic muscle. *Blood* **110**, 3891–3899 (2007).

112. Freeman, R. *et al.* Instructing cells with programmable peptide DNA hybrids. *Nat. Commun.* **8**, 15982 (2017).

113. Zhang, C.-L., Huang, T., Wu, B.-L., He, W.-X. & Liu, D. Stem cells in cancer therapy: opportunities and challenges. *Oncotarget* **8**, 75756–75766 (2017).

114. Wei, L., Wei, Z. Z., Jiang, M. Q., Mohamad, O. & Yu, S. P. Stem cell transplantation therapy for multifaceted therapeutic benefits after stroke. *Prog. Neurobiol.* **157**, 49–78 (2017).

115. Chan, J. K. Y. & Götherström, C. Prenatal transplantation of mesenchymal stem cells to treat osteogenesis imperfecta. *Front. Pharmacol.* **5**, 223 (2014).

116. Leyendecker, A., Pinheiro, C. C. G., Amano, M. T. & Bueno, D. F. The use of human mesenchymal stem cells as therapeutic agents for the in vivo treatment of immune-related diseases: A systematic review. *Front. Immunol.* **9**, 2056 (2018).

117. Freitag, J. *et al.* Mesenchymal stem cell therapy in the treatment of osteoarthritis: Reparative pathways, safety and efficacy - A review. *BMC Musculoskelet. Disord.* **17**, 230 (2016).

118. Poll, D., Parekkadan, B., Borel Rinkes, I. H. M., Tilles, A. W. & Yarmush, M. L. Mesenchymal Stem Cell Therapy for Protection and Repair of Injured Vital Organs. *Cell. Mol. Bioeng.* **1**, 42–50 (2008).

119. Sacchetti, B. *et al.* Self-Renewing Osteoprogenitors in Bone Marrow Sinusoids Can Organize a Hematopoietic Microenvironment. *Cell* **131**, 324–336 (2007).

120. Murphy, J. M., Fink, D. J., Hunziker, E. B. & Barry, F. P. Stem Cell Therapy in a Caprine Model of Osteoarthritis. *Arthritis Rheum.* **48**, 3464–3474 (2003).

121. Shen, W. *et al.* Osteoarthritis Prevention Through Meniscal Regeneration

Induced by Intra-Articular Injection of Meniscus Stem Cells. *Stem Cells Dev.* **22**, 2071–2082 (2013).

122. Duscher, D. *et al.* Stem Cells in Wound Healing: The Future of Regenerative Medicine? A Mini-Review. *Gerontology* **62**, 216–225 (2016).

123. McIntyre, J. A., Jones, I. A., Han, B. & Vangsness, C. T. Intra-articular Mesenchymal Stem Cell Therapy for the Human Joint: A Systematic Review. *Am. J. Sports Med.* **46**, 036354651773584 (2017).

124. Chahla, J. *et al.* Intra-articular cellular therapy for osteoarthritis and focal cartilage defects of the knee: A systematic review of the literature and study quality analysis. *J. Bone Jt. Surg. - Am. Vol.* **98**, 1511–1521 (2016).

125. Yubo, M. *et al.* Clinical efficacy and safety of mesenchymal stem cell transplantation for osteoarthritis treatment: A meta-analysis. *PLoS One* **12**, (2017).

126. Kristjánsson, B. & Honsawek, S. Mesenchymal stem cells for cartilage regeneration in osteoarthritis. *World J. Orthop.* **8**, 674–680 (2017).

127. Nejadnik, H., Hui, J. H., Choong, E. P. F., Tai, B. C. & Eng Hin Lee. Autologous bone marrow-derived mesenchymal stem cells versus autologous chondrocyte implantation: An observational cohort study. *Am. J. Sports Med.* **38**, 1110–1116 (2010).

128. Vangsness, C. T. *et al.* Adult Human Mesenchymal Stem Cells Delivered via Intra-Articular Injection to the Knee Following Partial Medial Meniscectomy. *J. Bone Jt. Surgery-American Vol.* **96**, 90–98 (2014).

129. Vega, A. *et al.* Treatment of Knee Osteoarthritis With Allogeneic Bone Marrow Mesenchymal Stem Cells: A Randomized Controlled Trial. *Transplantation* **99**, 1681–90 (2015).

130. Shapiro, S. A., Kazmerchak, S. E., Heckman, M. G., Zubair, A. C. & O'Connor, M. I. A Prospective, Single-Blind, Placebo-Controlled Trial of Bone Marrow Aspirate Concentrate for Knee Osteoarthritis. *Am. J. Sports Med.* **45**, 82–90 (2017).

131. Jones, E. A. *et al.* Isolation and characterization of bone marrow multipotential mesenchymal progenitor cells. *Arthritis Rheum.* **46**, 3349–3360 (2002).

132. Giancotti, F. G. & Ruoslahti, E. Integrin signaling. *Science* **285**, 1028–32 (1999).

133. Khalili, A. A. & Ahmad, M. R. A Review of Cell Adhesion Studies for Biomedical and Biological Applications. *Int. J. Mol. Sci.* **16**, 18149–84 (2015).

134. Chen, C. S., Alonso, J. L., Ostuni, E., Whitesides, G. M. & Ingber, D. E. Cell shape provides global control of focal adhesion assembly. *Biochem. Biophys. Res. Commun.* **307**, 355–361 (2003).

135. Wei, X. *et al.* Mesenchymal stem cells: a new trend for cell therapy. *Acta*

Pharmacol. Sin. **34**, 747–754 (2013).

136. Von Bahr, L. *et al.* Analysis of tissues following mesenchymal stromal cell therapy in humans indicates limited long-term engraftment and no ectopic tissue formation. *Stem Cells* **30**, 1575–1578 (2012).

137. Lan, Y. W. *et al.* Hypoxia-preconditioned mesenchymal stem cells attenuate bleomycin-induced pulmonary fibrosis. *Stem Cell Res. Ther.* **6**, 97 (2015).

138. Chavakis, E. & Urbich, C. Homing and engraftment of progenitor cells: A prerequisite for cell therapy. *J. Mol. Cell. Cardiol.* **45**, 514–522 (2008).

139. Vinatier, C., Mrugala, D., Jorgensen, C., Guicheux, J. & Noël, D. Cartilage engineering: a crucial combination of cells, biomaterials and biofactors. *Trends in Biotechnology* **27**, 307–314 (2009).

140. Cai, L., Dewi, R. E. & Heilshorn, S. C. Injectable hydrogels with in situ double network formation enhance retention of transplanted stem cells. *Adv. Funct. Mater.* **25**, 1344–1351 (2015).

141. Aguado, B. A., Mulyasasmita, W., Su, J., Lampe, K. J. & Heilshorn, S. C. Improving Viability of Stem Cells During Syringe Needle Flow Through the Design of Hydrogel Cell Carriers. *Tissue Eng. Part A* **18**, 806–815 (2012).

142. Kock, L., Van Donkelaar, C. C. & Ito, K. Tissue engineering of functional articular cartilage: The current status. *Cell Tissue Res.* **347**, 613–627 (2012).

143. He, Z., Wang, B., Hu, C. & Zhao, J. An overview of hydrogel-based intra-articular drug delivery for the treatment of osteoarthritis. *Colloids Surfaces B Biointerfaces* **154**, 33–39 (2017).

144. Zhao, W., Jin, X., Cong, Y., Liu, Y. & Fu, J. Degradable natural polymer hydrogels for articular cartilage tissue engineering. *J. Chem. Technol. Biotechnol.* **88**, 327–339 (2013).

145. Liu, M. *et al.* Injectable hydrogels for cartilage and bone tissue engineering. *Bone Res.* **5**, 17014 (2017).

146. Lee, K. Y. & Mooney, D. J. Alginate: Properties and biomedical applications. *Prog. Polym. Sci.* **37**, 106–126 (2012).

147. Ahmadi, F., Oveisi, Z., Samani, S. M. & Amoozgar, Z. Chitosan based hydrogels: characteristics and pharmaceutical applications. *Res. Pharm. Sci.* **10**, 1–16 (2015).

148. Antoine, E. E., Vlachos, P. P. & Rylander, M. N. Review of Collagen I Hydrogels for Bioengineered Tissue Microenvironments: Characterization of Mechanics, Structure, and Transport. *Tissue Eng. Part B Rev.* **20**, 683–696 (2014).

149. Patel, B., Xu, Z., Pinnock, C. B., Kabbani, L. S. & Lam, M. T. Self-assembled Collagen-Fibrin Hydrogel Reinforces Tissue Engineered Adventitia Vessels Seeded with Human Fibroblasts. *Sci. Rep.* **8**, 3294 (2018).

150. Parlato, M., Reichert, S., Barney, N. & Murphy, W. L. Poly(ethylene glycol) hydrogels with adaptable mechanical and degradation properties for use in biomedical applications. *Macromol. Biosci.* **14**, 687–98 (2014).

151. Gibas, I. & Janik, H. Review: Synthetic polymer hydrogels for biomedical applications. *Chem. Chem. Technol.* **4**, 297–305 (2010).

152. Ma, S. *et al.* A Novel Method for Preparing Poly(vinyl alcohol) Hydrogels: Preparation, Characterization, and Application. *Ind. Eng. Chem. Res.* **56**, 7971–7976 (2017).

153. Patenaude, M. & Hoare, T. Injectable, mixed natural-synthetic polymer hydrogels with modular properties. *Biomacromolecules* **13**, 369–378 (2012).

154. El-Sherbiny, I. M. & Yacoub, M. H. Hydrogel scaffolds for tissue engineering: Progress and challenges. *Glob. Cardiol. Sci. Pract.* **2013**, 316–42 (2013).

155. Belyaeva, E., Valle, D. Della, Neufeld, R. J. & Poncelet, D. New approach to the formulation of hydrogel beads by emulsification/ thermal gelation using a static mixer. *Chem. Eng. Sci.* **59**, 2913–2920 (2004).

156. Rich, M. H. *et al.* Water-Hydrogel Binding Affinity Modulates Freeze-Drying-Induced Micropore Architecture and Skeletal Myotube Formation. *Biomacromolecules* **16**, 2255–2264 (2015).

157. Bruggeman, K. F., Williams, R. J. & Nisbet, D. R. Dynamic and Responsive Growth Factor Delivery from Electrospun and Hydrogel Tissue Engineering Materials. *Adv. Healthc. Mater.* **7**, 1700836 (2018).

158. Annabi, N. *et al.* Controlling the Porosity and Microarchitecture of Hydrogels for Tissue Engineering. *Tissue Eng. Part B Rev.* **16**, 371–383 (2010).

159. Ozawa, F., Ino, K., Shiku, H. & Matsue, T. Electrochemical hydrogel lithography of calcium-alginate hydrogels for cell culture. *Materials (Basel).* **9**, (2016).

160. Li, H., Tan, C. & Li, L. Review of 3D printable hydrogels and constructs. *Mater. Des.* **159**, 20–38 (2018).

161. Armstrong, J. P. K., Burke, M., Carter, B. M., Davis, S. A. & Perriman, A. W. 3D Bioprinting Using a Templated Porous Bioink. *Adv. Healthc. Mater.* **5**, 1724–1730 (2016).

162. Hoare, T. R. & Kohane, D. S. Hydrogels in drug delivery: Progress and challenges. *Polymer (Guildf).* **49**, 1993–2007 (2008).

163. Kontturi, L. S. *et al.* An injectable, in situ forming type II collagen/hyaluronic acid hydrogel vehicle for chondrocyte delivery in cartilage tissue engineering. *Drug Deliv. Transl. Res.* **4**, 149–158 (2014).

164. Smeriglio, P., Lai, J. H., Yang, F. & Bhutani, N. 3D Hydrogel Scaffolds for Articular Chondrocyte Culture and Cartilage Generation. *J. Vis. Exp.* (2015). doi:10.3791/53085

165. Chen, W. *et al.* Autologous nasal chondrocytes delivered by injectable hydrogel for in vivo articular cartilage regeneration. *Cell Tissue Bank.* **19**, 35–46 (2018).

166. Kim, H. D. *et al.* Extracellular-Matrix-Based and Arg-Gly-Asp–Modified Photopolymerizing Hydrogels for Cartilage Tissue Engineering. *Tissue Eng. Part A* **21**, 757–766 (2015).

167. Charles, R. N., Derek, J. M., Scott, M. H. & Kristi, S. A. Attachment of fibronectin to poly(vinyl alcohol) hydrogels promotes NIH3T3 cell adhesion, proliferation, and migration. *J. Biomed. Mater. Res.* **57**, 217–223 (2001).

168. Zhang, X., Yang, Y., Yao, J., Shao, Z. & Chen, X. Strong collagen hydrogels by oxidized dextran modification. *ACS Sustain. Chem. Eng.* **2**, 1318–1324 (2014).

169. Eliaz, R. E. & Szoka, F. C. Robust and prolonged gene expression from injectable polymeric implants. *Gene Ther.* **9**, 1230–1237 (2002).

170. Needham, C. J. *et al.* Osteochondral tissue regeneration through polymeric delivery of DNA encoding for the SOX trio and RUNX2. *Acta Biomater.* **10**, 4103–4112 (2014).

171. Rey-Rico, A., Madry, H. & Cucchiarini, M. Hydrogel-Based Controlled Delivery Systems for Articular Cartilage Repair. *Biomed Res. Int.* **2016**, 1215263 (2016).

172. Spiller, K. L., Maher, S. A. & Lowman, A. M. Hydrogels for the Repair of Articular Cartilage Defects. *Tissue Eng. Part B Rev.* **17**, 281–299 (2011).

173. Salgado, A. J., Coutinho, O. P. & Reis, R. L. Bone Tissue Engineering: State of the Art and Future Trends. *Macromol. Biosci.* **4**, 743–765 (2004).

174. Anderson, J. M., Rodriguez, A. & Chang, D. T. Foreign body reaction to biomaterials. *Semin. Immunol.* **20**, 86–100 (2008).

175. Ejtehadifar, M. *et al.* The effect of hypoxia on mesenchymal stem cell biology. *Adv. Pharm. Bull.* **5**, 141–149 (2015).

176. Naderi-Meshkin, H. *et al.* Injectable hydrogel delivery plus preconditioning of mesenchymal stem cells: exploitation of SDF-1/CXCR4 axis toward enhancing the efficacy of stem cells' homing. *Cell Biol. Int.* **40**, 730–741 (2016).

177. Barzegar, A. & Moosavi-Movahedi, A. A. Intracellular ROS protection efficiency and free radical-scavenging activity of curcumin. *PLoS One* **6**, e26012 (2011).

178. Toh, W. S., Foldager, C. B., Pei, M. & Hui, J. H. P. Advances in Mesenchymal Stem Cell-based Strategies for Cartilage Repair and Regeneration. *Stem Cell Rev. Reports* **10**, 686–696 (2014).

179. Sleep, E. *et al.* Injectable biomimetic liquid crystalline scaffolds enhance muscle stem cell transplantation. *Proc. Natl. Acad. Sci.* **114**, 201708142

(2017).

180. Ezquer, F. E., Ezquer, M. E., Vicencio, J. M. & Calligaris, S. D. Two complementary strategies to improve cell engraftment in mesenchymal stem cell-based therapy: Increasing transplanted cell resistance and increasing tissue receptivity. *Cell Adh. Migr.* **11**, 110–119 (2017).

181. Madl, C. M., Heilshorn, S. C. & Blau, H. M. Bioengineering strategies to accelerate stem cell therapeutics. *Nature* **557**, 335–342 (2018).

182. McGinley, L. *et al.* Lentiviral vector mediated modification of mesenchymal stem cells & enhanced survival in an in vitro model of ischaemia. *Stem Cell Res. Ther.* **2**, 12 (2011).

183. Lee, S., Choi, E., Cha, M. J. & Hwang, K. C. Cell adhesion and long-term survival of transplanted mesenchymal stem cells: *Oxid. Med. Cell. Longev.* **2015**, 1–9 (2015).

184. Nowakowski, A., Walczak, P., Lukomska, B. & Janowski, M. Genetic Engineering of Mesenchymal Stem Cells to Induce Their Migration and Survival. *Stem Cells Int.* **2016**, 1–9 (2016).

185. Devetzi, M. *et al.* Genetically-modified stem cells in treatment of human diseases: Tissue kallikrein (KLK1)-based targeted therapy (Review). *Int. J. Mol. Med.* **41**, 1177–1186 (2018).

186. Cheng, H. *et al.* Stem cell membrane engineering for cell rolling using peptide conjugation and tuning of cell-selectin interaction kinetics. *Biomaterials* **33**, 5004–5012 (2012).

187. Koch, A. E., Halloran, M. M., Haskell, C. J., Shah, M. R. & Polverini, P. J. Angiogenesis mediated by soluble forms of E-selectin and vascular cell adhesion molecule-1. *Nature* **376**, 517–519 (1995).

188. Sarkar, D. *et al.* Chemical engineering of mesenchymal stem cells to induce a cell rolling response. *Bioconjug. Chem.* **19**, 2105–2109 (2008).

189. Sarkar, D. *et al.* Engineered mesenchymal stem cells with self-assembled vesicles for systemic cell targeting. *Biomaterials* **31**, 5266–5274 (2010).

190. Todhunter, M. E. *et al.* Programmed synthesis of three-dimensional tissues. *Nat. Methods* **12**, 975–981 (2015).

191. Akbari, E. *et al.* Engineering Cell Surface Function with DNA Origami. *Adv. Mater.* **29**, 1–9 (2017).

192. Pérez, B. *et al.* Insight into the molecular mechanism behind PEG-mediated stabilization of biofluid lipases. *Sci. Rep.* **8**, 12293 (2018).

193. Lawrence, M. S., Phillips, K. J. & Liu, D. R. Supercharging proteins can impart unusual resilience. *J. Am. Chem. Soc.* **129**, 10110–2 (2007).

194. Prasher, D. C., Eckenrode, V. K., Ward, W. W., Prendergast, F. G. & Cormier, M. J. Primary structure of the Aequorea victoria green-fluorescent

protein. *Gene* **111**, 229–33 (1992).

195. Yeh, E., Gustafson, K. & Boulianne, G. L. Green fluorescent protein as a vital marker and reporter of gene expression in Drosophila. *Proc. Natl. Acad. Sci.* **92**, 7036–7040 (1995).

196. Tak, Y. K., Naoghare, P. K., Lee, K. H., Park, S. S. & Song, J. M. Green fluorescent protein (GFP) as a direct biosensor for mutation detection: Elimination of false-negative errors in target gene expression. *Anal. Biochem.* **380**, 91–98 (2008).

197. Kauzmann, W. The Three Dimensional Structures of Proteins. *Biophys. J.* **4**, 43–54 (1964).

198. Richardson, J. S. β-Sheet topology and the relatedness of proteins. *Nature* **268**, 495–500 (1977).

199. Yang, F., Moss, L. G. & Phillips, G. N. The Molecular Structure of Green Fluorescent Protein The Molecular Structure of Green Fluorescent Protein. *Structure* 1–14 (2010).

200. Day, R. N. & Davidson, M. W. The fluorescent protein palette: tools for cellular imaging. *Chem. Soc. Rev.* **38**, 2887–921 (2009).

201. Reid, B. G. & Flynn, G. C. Chromophore formation in green fluorescent protein. *Biochemistry* **36**, 6786–6791 (1997).

202. Davidson, M. W., Gilbert, S. G., Cranfill, P. J., Piston, D. W. & Kremers, G.-J. Fluorescent proteins at a glance. *J. Cell Sci.* **124**, 2676–2676 (2011).

203. Pédelacq, J. D., Cabantous, S., Tran, T., Terwilliger, T. C. & Waldo, G. S. Engineering and characterization of a superfolder green fluorescent protein. *Nat. Biotechnol.* **24**, 79–88 (2006).

204. Andrews, B. T., Schoenfish, A. R., Roy, M., Waldo, G. & Jennings, P. A. The Rough Energy Landscape of Superfolder GFP Is Linked to the Chromophore. *J. Mol. Biol.* **373**, 476–490 (2007).

205. Cronican, J. J. *et al.* Potent delivery of functional proteins into Mammalian cells in vitro and in vivo using a supercharged protein. *ACS Chem. Biol.* **5**, 747–52 (2010).

206. McNaughton, B. R., Cronican, J. J., Thompson, D. B. & Liu, D. R. Mammalian cell penetration, siRNA transfection, and DNA transfection by supercharged proteins. *Proc. Natl. Acad. Sci.* **106**, 6111–6116 (2009).

207. Armstrong, J. P. K. *et al.* Artificial membrane-binding proteins stimulate oxygenation of stem cells during engineering of large cartilage tissue. *Nat. Commun.* **6**, 7405 (2015).

208. Martino, M. M. *et al.* Growth Factors Engineered for Super-Affinity to the Extracellular Matrix Enhance Tissue Healing. *Science (80-.).* **343**, 885–888 (2014).

Chapter 2

Materials and Methods

All chemicals were purchased from Sigma, UK, and used without further treatment unless stated otherwise. Deionised water (dH_2O) was obtained with a resistivity of 18.2 MΩ·cm using a Millipore Milli-Q Reference Water purification system with a Quantum TX polishing cartridge.

2.1 Designing the plasmid

2.1.1 Plasmid construction

A multi histidine tag (His6-tag) was placed on the N terminal of the supercharged green fluorescent protein (scGFP), and the sequence for peptide PlGF2_123–144 was placed on the C terminal.

The plasmid with sequence N-His6-scGFP-PlGF2_123–144-C was designed for pOPIN F vector[1], which is enhanced for multi-histidine tag purification under control of the lac-operon. This vector was also designed for ampicillin resistance. This will be referred as *scgfp-plgf2_123-144* (Appendix A).

2.1.2 Gene amplification

Polymerase chain reaction (PCR) was used to amplify the gene sequence. In 200 µL PCR Eppendorf, the following mix was added: 1 µL template *scgfp-plgf2_123–144*, 1 µL of reverse primer, 1 µL of forward primer, 1 µL polymerase LabTAQ (LabTech, UK) and 10 µL of buffer 5x (LabTech, UK), plus 36 µL of DNase free water to make a final volume of 50 µL.

This was submitted for PCR in a thermocycler (Thermo Fisher Scientific, UK) with the following settings: 95°C for 5 minutes, 95°C 30 seconds for denaturation at the beginning of each cycle, 62°C 30 seconds, 72°C 3 minutes, 90°C to 2°C 30 times, 72°C for 10 minutes, and finally cooled at 4°C (Table 2.1)

Table 2.1 Settings on thermocycler for gene amplification on PCR.

Step	Temperature	Time	Process
1	95°C	5 minutes	Initialisation
2	95°C	30 seconds	Denaturation
3	62°C	30 seconds	Annealing
4	72°C	3 minutes	Replication
5		30 times	Step 2 to 4
6	72°C	10 minutes	
7	4°C	∞	

A 1.5% w/v gel was made by mixing 0.75 g of agarose DNA grade in 50 mL of TAE buffer (Tris base, acetic acid and EDTA). The mixture was boiled in a microwave at 800 W (Tesco, UK) and 10 µL of SYBR safe stain (Invitrogen, UK) was added to the mixture after cooling down to 40°C. The gel blend was placed into a cast and allowed to set for approximately 30 minutes.

The solid gel was placed in an electrophoresis tank, and enough TAE buffer was used to cover the gel. An aliquot of 16 µL of PCR sample was mixed with 4 µL of 5× DNA loading buffer (Qiagen, UK), and the 20 µL were carefully placed into the wells of the gel in duplicate. Hyper ladder (New England BioLabs, UK) was placed in the edges of the gel as a reference for molecular weight. A power source of high voltage was used to apply 100 V to the electrophoresis system for 40 minutes. The band was identified by screening in UV light, and the fluorescent band was carefully cut with a razor. For extraction, a QIAquick gel extraction kit was used as indicated by the manufacturer. Briefly, the gel was dissolved with buffer provided QG, the solution was placed in a column to bind DNA and washed several times with buffer PE. The DNA was eluted with 50 µL of buffer EB (10 mM Tris HCl, pH 8.5).

2.1.3 pOPIN F linearization

The pOPIN F vector was acquired from the Oxford Protein Production Facility (Addgene plasmid # 26042). For linearization, 100 µL of the vector (80 $mg \cdot mL^{-1}$) were added in a 500 µL reaction tube together with 20 µL of 1× cut smart buffer, 2 µL restriction enzyme Hind III, 2 µL of Kpn I (New England BioLabs, UK) and 76 µL of nuclease-free water. The mixture was left to react overnight at 37°C. The sample mixture was then treated with a NucleoSpin Gel and PCR clean-up kit following the instruction of the manufacturer (Gmbg & Co. KG, Germany) to remove enzyme excess.

2.1.4 Plasmid ligation

The In-Fusion cloning method[2] was used to insert genes into the linearized plasmid. 2 µL of infusion 5×-In-Fusion mix (Clontech, USA), 4 µL of purified DNA insert *scgfp-plgf2_123-144*, 2 µL of double despaired pOPIN F, and 2 µL of dH_2O were placed in a 200 µL reaction tube before equilibration on ice for 20 minutes. This tube was then placed in a water bath for 15 minutes at 50°C, and then returned into the ice bath.

2.1.5 Transformation in competent Cells

Transformation in Competent Stellar Cells (Clontech, UK) was performed according to the manufacturer's instructions. In summary, 2 µL of In-Fusion mixture were added to 30 µL of Stellar Competent Cells, and gently mixed. The mixture was then submitted to heat shock transformation for 45 seconds at 42°C and then placed in an ice bath for equilibration. Subsequently, 1 mL of Super Optimal broth with Catabolite repression (SOC) medium was added before the cell suspension was incubated for one hour at 37°C. The cell suspension was then

centrifuged at 13000 rpm for 10 minutes; the supernatant was discarded, and the cell pellet was resuspended in 50 µL of SOC medium.

2.1.5.1 Lysogenic Broth (LB) agar plates

LB agar plates were made by autoclaving a mixture of 2.5 grams of LB (Fisher scientific, UK) and 1.25 grams of Agar No1 bacteriological (Thermo Fisher Scientific, UK). Approximately 25 mL of LB-agar, mixed with carbenicillin (5 $\mu g \cdot mL^{-1}$) were placed in a 9 cm petri dish under sterile conditions, and left to solidify at room temperature for 30 minutes.

2.1.5.2 Blue-white screen

The blue-white screening is a method that allows the detection of successfully transformed bacteria. It relies on the ability of the bacteria to metabolise X-galactose (X-gal) and generate a white metabolite.

Under sterile conditions, 40 µL of isopropyl β-D-1-thiogalactopyranoside (IPTG) from a 1 M stock in dH_2O, as well as 40 µL of X-gal (4 $mg \cdot mL^{-1}$ in dimethyl sulfoxide DMSO) were added to one LB agar plate containing carbenicillin, and homogeneously distributed with a cell spreader. The transformed cell suspension was carefully dripped on the surface of the agar plate and dispersed with a cell spreader. The plate was placed in an incubator at 37°C overnight.

A single white colony was carefully taken from the LB agar plate and placed in 10 mL of starter culture (Lysogenic broth with added carbenicillin 5 $\mu g \cdot mL^{-1}$), and left in rotating motion incubator at 200 rpm over night at 37°C.

For plasmid DNA purification, a QIAgen Spin Miniprep kit was used according to the manufacturer's instructions, whereby the cells were first lysed in the presence of an alkaline buffer, then neutralised in the presence of a high salt buffer to ensure binding onto the silica membrane column. The column was washed to remove cell

debris and contaminants before the DNA was eluted in a low salt buffer by centrifugation[3].

2.2 Expression of scGFP_PlGF2

2.2.1 Transformation on BL21 cells

An aliquot of 2 µL of purified plasmid *scgfp-plgf2_123–144* was added to a 1.5 mL Eppendorf tube containing 50 µL of Competent BL21 *Escherichia coli* (*E. coli*) cells (New England BioLabs, UK) and equilibrated on ice for 30 minutes. Heat shock was performed in a water bath at 42°C for exactly 10 seconds. The cell suspension was then equilibrated on ice for 5 minutes before the addition of 950 µL of SOC media. The cell suspension was incubated for 60 minutes in shaking incubator at 200 rpm at 37°C. The resulting mixture was centrifuged at 1300 rpm for 5 minutes, and the supernatant was discarded. The cell pellet was resuspended in 50 µL of SOC medium and this cell suspension was used to inoculate freshly made LB agar plates in duplicate, and incubated overnight at 37°C.

2.2.2 Protein expression

The *lac* operon in the gene plasmid was used to control protein expression and ensure that only bacteria containing the gene *scgfp-plgf2_123–144* was produced. The gene sequence *scgfp-plgf2_123–144* was expressed using competent BL21(DE3) *Escherichia coli* cells, as established in section 2.2.1. A single colony was chosen to inoculate 10 mL of LB broth, containing carbenicillin (5 $\mu g \cdot mL^{-1}$) and incubated overnight at 37°C rotating at 200 rpm. The next day, the cell suspension was added to 1 L of autoclaved LB medium with 5 $\mu g \cdot mL^{-1}$ carbenicillin and stirred at 200 rpm at 37°C for approximately 4 hours, until the optical density reached 0.6–0.8 at a wavelength of 600 nm. Protein expression was induced using

10 mM of IPTG (Apollo Scientific, Japan). The cell suspension was incubated and agitated overnight at 200 rpm at 37°C. The bacteria culture was centrifuged at 4000 g for 35 minutes at 4°C using Sorval RC6 centrifuge (Thermo Fisher Scientific, UK). Then, the supernatant was discarded, and the sediment was resuspended in 40 mL of lysis buffer (20mM Tris HCl, 1 M NaCl and 20 mM imidazole at pH 7.5). Cells were transferred to a 50 mL falcon tube before being lysed using sonication alternating 1 second on and 1 second off using a Vibra Cell VCX 1500 (Sonics & Materials, USA) at a 63% amplitude for 5 minutes in an ice bath. An aliquot of 50µL of phylmethylsulfonyl fluoride (PMSF) solution (100 mM PMSF in dimethyl sulfoxide DMSO) was added before and after sonication, along with a sufficient amount of lyophilised DNase I from bovine pancreas.

The lysed sample was centrifuged at 20,000 g for 30 minutes, the supernatant was collected and filtered through a 0.22 µm cellulose membrane syringe filter and purified by immobilised metal affinity chromatography using nickel nitrilotriacetic acid (Ni-NTA) as the immobile phase.

2.3 Purification of scGFP_PlGF2

2.3.1 Immobilised Metal Affinity Chromatography

The idea of immobilised-metal affinity chromatography (IMAC) was first introduced in 1975 by Porath et al., based on the observed affinity of positively charged transition metals such as nickel, copper, cobalt and zinc to cysteine and histidine in solutions[4]. The purification of proteins using this technique was accelerated by Hochuli et al. with the invention of an enhanced chelating agent, nitrilitriaceticacid, (NTA) in 1987 and the fast growth of gene design for proteins to be able to express oligo-histidine terminus[5].

The Ni-NTA ligand strongly coordinates the nickel ions with four valences to form a complex. Then the resin is washed with low imidazole to remove unbound proteins. The elution is done via competitive elution by increasing the ionic strength of the imidazole buffer to chelate with the nickel[6].

2.3.1.1 Method

An XK 16 column (GE healthcare life sciences, UK) containing 25 mL of Ni-NTA (Qiagen, UK) was washed with at least 5 column volumes of dH_2O and equilibrated with the same amount of lysis buffer before the lysate was loaded into the column. The column was washed with lysis buffer and different gradients of imidazole using ÄKTA purifier (GE Healthcare, UK) until eluted with high imidazole buffer (500 mM Tris HCl, 1 M NaCl and 20 mM Imidazole adjusted to pH 7.5 with concentrated HCl). All eluted fractions were collected in 2 mL Eppendorf tubes.

The resulting purified protein was buffer exchanged into working buffer (400 mM NaCl, 20 mM Tris HCl, pH 7.5) using a 14000 MWCO cellulose dialysis tubing, (Fisher scientific, US) at 4°C. The purified protein, named [scGFP_PlGF2], was analysed using SDS-PAGE and UV-vis spectroscopy to determine purity, yield and concentration. The same method was used to purify [scGFP].

2.4 Characterisation Techniques

2.4.1 Polyacrylamide gel electrophoresis (SDS-PAGE)

To assess the purity of the protein, [scGFP_PlGF2] was summited to SDS-PAGE. Electrophoresis is a technique widely used to separate macromolecules based on their molecular weight making use of an electric field. This requires a gel support as well as sodium dodecyl sulphate (SDS) to induce protein denaturation. Native proteins are able to keep their tertiary structure due to non-covalent forces i.e.

hydrogen bonds, ionic and hydrophobic forces. SDS disrupts the non-covalent interactions, whilst β-mercaptoethanol is also added to disturb the disulphide bonds in the molecule giving them a linear structure and a homogeneous distribution of a net negative charge[7], making the charge of the protein relative to the molecular mass.

When applying electric current, proteins move through the gel depending on their mass, leaving heavier proteins on the top of the gel and smaller molecules moving faster through the gel pores.

2.4.1.1 Method

For this analysis,10 µL aliquot of the sample was denatured at 95°C for 5 minutes with 10 µL of sample application buffer (SAB) containing 100 mL stock made of 400 mM glycerol, 5% SDS, 50 mM ethylendiaminetetraacetic acid (EDTA), 0.5 mM Tris, 7 mM β-mercaptoethanol, and bromophenol was added until dark blue, to make them visible. A 4-20% bis-tris gel (Invitrogen, USA) was submerged into an X-Cell Surelock electrophoresis chamber (Thermo Fisher, UK) containing running buffer (50 mM Tris base, 38.5 mM glycine and 7 mM SDS). 10 µL of the denatured sample was added to each well, using a PageRuler Plus Prestained ladder (Thermo Fisher, UK) as reference. A power source of high voltage was used to apply 200 V to the system for 60 minutes. The gel was removed from the cast and distained using dH_2O overnight in a shaking motion at 120 rpm at room temperature, or with distaining solution (20% ethanol and 5% acetic acid) for up to two hours.

2.4.2 Bicinchoninic acid (BCA)

BCA is an assay used to determine total protein concentration in a sample. The concentration is dependent on the colour change of the sample solution from

blue/green to purple caused by the reduction of Cu^{2+} to Cu^{1+} ions. The reduction is produced by the peptide bonds present in the protein. The amount of Cu^{1+} is proportional to the amount of protein in the sample. First, the copper in copper sulphate $CuSO_4$ forms a complex with the protein in the sample solution. Then two bicinchoninic acid molecules coordinate with each copper ion to form a purple complex that absorbs light at 562 nm[8]. The spectrum is compared with protein solutions of known concentration.

The reaction that leads to BCA colour formation is strongly influenced by four amino acid residues (cysteine or cystine, tyrosine, and tryptophan) in the amino acid sequence of the protein.

2.4.2.1 Method

A Pierce BCA Protein Assay kit (Thermo Fisher scientific, UK) was used for this process. Enough solution for working reagent (WR) was prepared according to the number of samples (200 µL of WR in a 96 well plate). This was prepared by mixing reagent A ([2,2'-Biquinoline]-4,4'-dicarboxylic acid, sodium salt) and B (Copper II sulphate pentahydrate) in a 50 to 1 ratio.

An aliquot of 25 µL of [scGFP_PlGF2] in solution was added to a 96 well plate (Costar, UK), followed by the addition of 200 µL of WR to the same well. The plate was incubated at 37°C for 30 minutes and the absorption was measured at 562 nm with a multi-mode plate reader Synergy neo2 (BioTek, USA). This was also performed with known concentrations of bovine serum albumin (BSA) as a control. The slope of the linear regression equation line from the plotted graph from absorbance at 562 nm against concentration was taken to produce a standard curve.

2.4.3 Matrix-assisted laser desorption/ionization mass spectrometry time of flight (MALDI-TOF)

MALDI-TOF is a technique generally employed to analyse the mass of a biomolecule. The mass to charge ratio is calculated by the time of flight, which is dependent on the size of the molecule, shorter TOF is characteristic for small molecules and longer time of flight for larger molecules[9].

First, the sample is embedded in a crystalline structure (matrix) and it is then deposited on a conductive plate. Then, the sample is irradiated with a pulsed laser beam, causing structural fragmentation. The resulting particles form a cloud and the ions are attracted by an electric field, finally, they reach a detector to produce a signal plot[10].

2.4.3.1 Method

The average molecular weight of the expressed protein, or surfactant were obtained using a Bruker MALDI mass spectrometer (Applied Biosystems, UK) running FLEX control software (Bruker, USA). The sample was prepared using 1:1 ratio of cinnamic acid matrix (50:50 solution of acetonitrile and 0.1% TFA and saturate with α-Cyano-4-hydroxycinnamic acid), spotted 1 µL sample on rough steel plate and let dry at room temperature for 10 minutes before loading into the machine. Spectra were taken between 10 and 55 kDa for proteins and 0 to 5 kDa for surfactants.

2.4.4 Synchrotron Radiation Circular Dichroism

Circular dichroism (CD) is used to analyse the secondary structure and folding properties of biomolecules[11]. A beam of light is circularly polarised and can rotate in a clockwise or counter clockwise direction. The enantiomeric properties of the

sample determine the absorbance or diffraction of the circularly polarised light in different amounts[12]. After reaching the detector, a single graph is formed specifically for that protein.

2.4.4.1 Method

Protein samples were used at a concentration between 3 and 3.6 $mg \cdot mL^{-1}$ in 20 mM sodium phosphate buffer (100 mM 3.1 g of Na_2HPO_4, 10.9 g of NaH_2PO_4 in dH_2O, pH adjusted with phosphoric acid). Synchrotron radiation circular dichroism (SRCD) was performed in Diamond Light Source (Oxford, UK) at the B23 beamline. Spectra were measured from 180 to 260 nm, using a cylindrical cell with a 200 µm pathlength in a Linkam System. The beam current was 300 mAmps, the slit width was 1 mm, and the integration time was two seconds. The CD spectra was obtained in a temperature ramp from 24 to 90°C with a measurement every 3 degrees, equilibrating the sample for one minute every time. The collected data was analysed using BestSel Software[13].

2.4.5 Ultraviolet-visible UV-vis spectroscopy

The most popular technique to quantitative determine the concentration of an aqueous substance is UV-visible spectroscopy. This method makes use of the electronic transitions of molecules when irradiated with ultraviolet and visible light. The wavelength would be absorbed if it emits the exact amount of energy to make a transition. Electrons are excited from the ground state into the excited state. A spectrum is acquired when the absorption is measured as a function of the wavelength[14]. This also allows to explore chemical structure of some molecules[15].

2.4.5.1 Method

UV-vis spectroscopy was used to calculate the concentration in aqueous buffer of the protein. The absorbance was measured using a Cary 60 UV-Vis spectrometer (Agilent Technologies, USA) over the wavelength range 200–600 nm. Concentration (C) was worked out using the Beer-Lambert law (Equation 2.1) where L is the cuvette path length, A is the absorbance at a wavelength of 280 nm and ε is the extinction coefficient, 17330 M-1cm-1 at 280 nm (Protein Calculator, RCSB Protein Data Bank).

$$A = \varepsilon \times C \times L \qquad \textbf{\textit{Equation 2.1}}$$

2.4.6 Fluorescence Spectroscopy

Fluorescence spectroscopy is a kind of electromagnetic spectroscopy which analyses the fluorescence emitted from a given sample. The electrons in the molecule are excited with an incident photon source, usually UV or visible light. When vibrational relaxation occurs, the photons are released with lower energy and higher wavelength in the form of emission light.

Usually, two types of spectrum can be achieved with this technique. An emission spectrum can be obtained when the sample is irradiated with a fixed excitation wavelength and the emission intensity is recorded as a function of the emission wavelength. An excitation spectrum is produced when the emission light is held at a constant wavelength and excitation changes are detected[16].

2.4.6.1 Method

This method was predominantly used to measure fluorescence emission. Samples were analysed using a fluorescence spectrometer in Cary Eclipse fluorometer (Agilent Technologies, USA) using Cary Scan (Agilent Technologies, USA)

software. Excitation and emission scans were performed at room temperature. Emission spectra were taken at a different range of temperatures from 350 to 600 nm, with a high emission peak at 511 nm.

2.4.7 Dynamic Light Scattering

Dynamic light scattering (DLS) is a technique used to determine the size distribution of particles at micro and sub-micro molecular level. A light monochromator is shot into the sample through a polariser, as a result, the incident wavelength is scattered in different directions. The scattering can cause constructive or destructive interference, leading to a time-dependent fluctuation in the scattered light, this pattern is then analysed by the detector[17].

2.4.7.1 Method

DLS was performed using a UV-micro disposable plastic cuvette with ZetaSizer Nano ZS (Malvern Instruments, UK) and ZetaSizer software (Malvern Instruments, UK). Samples were filtered with a syringe filter (0.22 µm pore size) before measurement, the parameters selected were 3 runs with 10 measurements each with 120 seconds of equilibration time at 25 and 37°C.

2.4.8 Zeta Potential

Zeta potential is the electric potential in an interfacial double layer in a colloidal system. It allows to measure the charge present in molecule surfaces.

2.4.8.1 Method

These measurements were taken with ZetaSizer Nano ZS (Malvern Instruments, UK) and ZetaSizer software (Malvern Instruments, UK) using a plastic cuvette, the parameters selected were from 10 to 100 runs with 120 seconds of equilibration time at 25 and 37°C.

2.4.9 Small angle X-ray scattering

SAXS can provide structural information about biomolecules in an aqueous solution. A collimated monochromatic beam is irradiated on a sample, generating a pattern from the scattered waves, which is the average of the scatter produced in all possible orientations. This means that the 2D collector will interpret the scattering as a magnitude and not as scattering intensity[18]. The Diamond beamline B21 is dedicated to measure SAXS for samples in aqueous solution.

2.4.9.1 Method

Sample measurements were carried out by the mail-in service provided by Diamond Light Source (Oxford, UK) in beamline B21. This beamline uses a bending magnet source and delivers approximately 3×10^{12} photons per second directly to the sample. These photons are then dispersed over a cross-section of 0.8 mm by 2 mm to enhance the particle signal while minimising radiation damage. The detector (Eiger 4M) measures with a scattering vector (q) range from 0.0032 to 0.38 $Å^{-1}$ The beam size was <75 μm, operating with a fixed camera length at 4.014 metres at 12.4 keV. SAXS measurements were coupled with size exclusion chromatography (SEC-SAXS) using a superdex 200 column (GE Healthcare). The data was collected in 30 successive frames, each with a one second exposure time.

The 60 μL samples were prepared by concentrating the purified construct [scGFP_PlGF2], [scGFP] and [scGFP_PlGF2][S] with a 10 MWCO spin concentrator (Merck, USA) until the desired concentration was achieved, and verified with NanoDrop ND-1000 (Thermo Scientific, USA). The buffer was subtracted from the sample before the data was analysed using ScÅtter software

with ATSAS plugins[19] following the instructions from www.bioisis.net tutorial website.

2.4.9.2 Data representation and interpretation

The three main plots that can be obtained to give an idea of the studied protein are: the raw scattering data, the Kratky plot, and the P(r) distribution plot.

The obtained scattering data can be presented as a log I(q) vs log q($Å^{-1}$). The log I(q) axis emphasises the high q data, and the log q ($Å^{-1}$) highlights the data at the low angle which carries the strongest signal. A monodisperse sample (i.e. no aggregates, or interparticle repulsion) would show a flat line at small angles[20] (Figure 2.1 a).

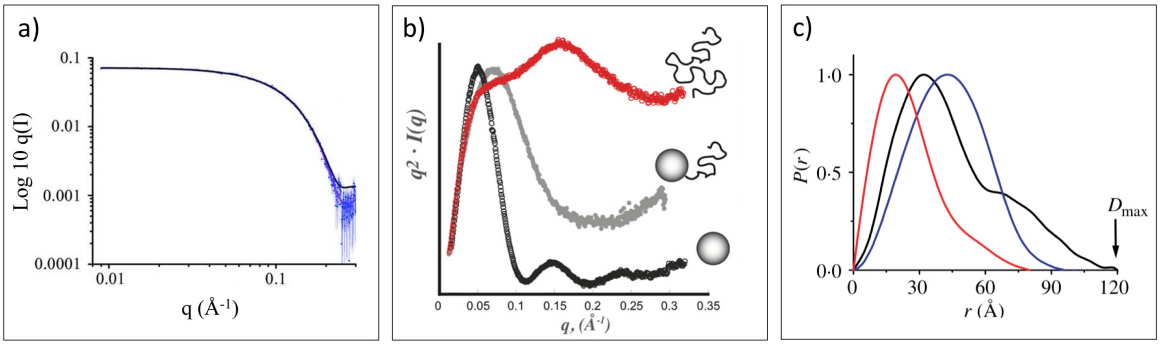

Figure 2.1 Representative curves from data obtained with Scåtter. a) scattering data plotted as from log q(I) versus q($Å^{-1}$). The raw data (blue dots) and fitted data (magenta) display a flat line on the low q region, suggesting no aggregations or interparticle repulsion. Note the black line was a bead model fit. Adapted from[20]. b) representation of different Kratky plots of scattering data. Folded globular protein (black), a partially folded protein with a random coil, or flexible protein (grey), and a fully unfolded protein (red). Adapted from[19]. c) Representation of P(r) distribution plots. A globular protein (blue) displaying uniform distribution. Proteins with an elongated feature (red) display a longer tail at larger r. The different features in a multi-domain protein produce multiple peaks (black). Adapted from[21].

The Kratky plot (q^2×I(q) vs q $Å^{-1}$) of the scattering data is indicative of globularity of the studied protein. The curve for a globular protein would appear as a bell shape, whereas a partially folded flexible protein would have a bell shape with a

tail that does not return to 0 at high q, and an unfolded structure would display a plateau at higher q values (Figure 2.1 b)

The P(r) distribution function plot is a representation of the distribution of the distances between the atoms in the protein in real space. For instance, a protein with a high aspect ratio would display a longer tail approaching to zero at larger r, while a globular protein would show a single uniform peak[21]. A protein with multiple domains would exhibit multiple peaks (Figure 2.1 c).

The produced file from ScÅtter was submitted to EMBL DAMMIF online service[22] in order to obtain a dummy atom bead model. Subsequently, the available structure for superfolder green fluorescent protein (sfGFP) (PDB ID 2b3p) was modified by adding a hexa-histidine tag, and the sequence for PlGF2_123−144 on the N and C terminal, respectively. This was done utilising the build and fusion functions in PyMOL. Finally, these two models were superimposed on the obtained DAMMIF .pdb file.

2.5 Oxidation of IGEPAL co-890

Following previous methods[23], the oxidised IGEPAL co-890 surfactant [S] was synthesised by the oxidation of the hydroxyl groups of polyoxyethylene (n=40) nonylphenyl ether to yield a carboxylic acid terminus. First, 2 g of IGEPAL co-890 were dissolved in 50 mL of dH_2O. The solution was then mixed with 30 mg of 2,2,6,6–Tetramethylpiperidine 1-oxyl (TEMPO), 50 mg of sodium bromide (NaBr), and 5 mL of sodium hypochlorite (NaClO) containing 10-15% available chlorine. The solution was continually adjusted with sodium hydroxide (NaOH) until pH 11 was reached and stirred for 24 h inside a safety fume hood. 10 mL of ethanol were added to the reaction to quench it, and the pH was adjusted to 1 with concentrated HCl.

To purify the oxidised surfactant, solvent extraction was performed by washing with three aliquots of 80 mL of chloroform and with the same amount of dH_2O at pH 1. The chloroform was evaporated from the organic phase under reduced pressure at 40°C. The resulting solid was dissolved in 40 mL of ethanol at 65°C and recrystallized overnight at -20°C. The ethanol was decanted, and the solid product re-dissolved in 20 mL of ethanol at 65°C and dried under reduced pressure at 40°C. The resulting product was a waxy white/yellow solid.

2.5.1 Fourier Transformed Infrared Spectroscopy (FTIR)

FTIR is used to obtain the vibrational spectrum of a molecule and is a unique to a defined molecule. When a sample absorbs infrared radiation, a vibrational excitation is induced in the covalent bonds in the molecule. The vibrational modes, such as rocking, twisting, wagging, scissoring symmetric or asymmetric stretching, depend on the strength and mass of the bonds. The raw data is then analysed by the system using the mathematical process Fourier transform to obtain the spectrum[24].

2.5.1.1 Method

The native IGEPAL co-890 and the oxidised resultant polymer were analysed using Fourier Transform Infra-Red spectrometer (Perkin Elmer, USA). A small amount was carefully deposited onto the sample compartment before spectrum acquisition. The data was obtained as the result of 15 accumulations scanning from wavenumber 550 to 4000 cm^{-1}.

2.5.2 Purity of oxidised IGEPAL co-890

A solution of 2.5 mM oxidised surfactant was needed to perform an acid-base titration. 4.5 mL of the solution were titrated with 2.5 mM NaOH and the pH was

recorded after every addition and plotted as a function of the added volume. The resulting graph was used to determine the concentration of carboxylic acid in the oxidised surfactant. The ratio NaOH mol / COOH mol was used to know how many molecules of carboxylic acid had been neutralised by sodium hydroxide.

2.5.3 Extinction coefficient of oxidised IGEPAL co-890

A solution of 2.5 mg·mL^{-1} was used to measure absorbance at 280 nm with UV-vis spectroscopy. A linear equation was used to fit absorbance as a function of concentration. The extinction coefficient (ε) was calculated using the gradient (m) and the path length of the cuvette (L = 1 cm).

$$\frac{A}{C} = m = \varepsilon \times L \qquad \textbf{\textit{Equation 2.2}}$$

2.6 Synthesis of scGFP_PlGF2 conjugate

To form the nanobiohybrid conjugate [scGFP_PlGF2][S], the concentration of protein expressed [scGFP_PlGF2] was known by measuring UV-vis light absorbance at 280 and 487 nm. The number of positive sites was counted as 39 lysine and 27 arginine molecules, giving a total of 66 positive residues (Appendix B). The surfactant amount to be added was calculated with Equation 2.3.

$$S = P_m \times C_n \times S_w \times 1.4 \qquad \textbf{\textit{Equation 2.3}}$$

Where S is the surfactant to be added in mg, P_m is the number of moles calculated for [scGFP_PlGF2] C_n is the number of cationic residues present in [scGFP_PlGF2], 66, S_w surfactant molecular weight, and since the surfactant is added in excess, it is multiplied by 1.4. The solution was stirred overnight at 200 rpm and it was then dialysed in a 14000 MWCO cellulose bag into 400 mM NaCl and 20 mM Tris at pH 7.5.

2.6.1 Calculating the amount of bound surfactant

A UV-vis spectrum from [scGFP_PlGF2][S] before and after conjugation was taken from 200 to 600 nm. The difference in absorbance between the two peaks at 280 nm was used to determine the surfactant to protein ratio after conjugation (Sr) using Equation 2.4.

$$Sr = \frac{P_n \times 66}{C_n - P_n} \qquad \textit{Equation 2.4}$$

C_n is the number of molecules calculated for [scGFP_PlGF2][S] whilst P_n is the number of molecules calculated for [scGFP_PlGF2], multiplied by the number of positive residues in the protein (66).

2.7 General cell culture techniques

2.7.1 Human mesenchymal stem cell culture

For optimal cell growth and viability, there are several conditions that must be fulfilled by the culture medium. A buffering, such as sodium bicarbonate ($NaHCO_3$), is necessary to maintain the cell surroundings at a constant and optimal pH. Phenol red is also used as a pH indicator for the system, which turns yellow under acidic environments and pink in alkaline environments. Furthermore, sodium pyruvate is in the medium as a carbon source for the cells to metabolise. Foetal bovine serum (FBS) is added to the media in order to constantly feed the cells with growth factors, sugars and lipids. To prevent and control bacterial growth, penicillin and streptomycin are supplemented into the medium. L-glutamine is supplemented into the media to provide essential nucleotides and energy to improve cell metabolism[25].

In this case, Dulbecco's Modified Eagle Medium (DMEM) low-glucose medium, containing sodium pyruvate and $NaHCO_3$, with or without phenol red, was chosen for all cell culture.

Human mesenchymal stem cells (hMSCs) were isolated from the proximal femur bone marrow of patients undergoing total hip replacement surgery, according with the Bristol Southmead Hospital Research Ethics Committee guidelines (reference #078/01). All cell culture work was executed in SAFE 2020 laminar flow hoods (Thermo Fisher Scientific, UK), and incubated in Hera cell 150 (Thermo Fisher Scientific, UK) at 37°C under a 5% carbon dioxide atmosphere. hMSCs were expanded in monolayer using T25, T75 or T175 flasks (Fisher Scientific, UK) using 5, 12, or 25 mL of culture medium respectively. The media was changed every 2 days.

The culture medium to expand the collected hMSCs: DMEM containing $NaHCO_3$, supplemented with 100 units mL^{-1} penicillin, 100 µg mL streptomycin, 2 mM GlutaMAX supplement (Invitrogen, USA), 10% v/v foetal bovine serum (FBS), and 5 $ng{\cdot}mL^{-1}$ of freshly added basic human fibroblast growth factors (FGF) (Peprotech, USA).

2.7.2 Cell trypsinisation

After cells reached 90% confluency, they were passaged. Culture medium was aspirated, and the cell monolayer was washed twice with 10 mL of Dulbecco's phosphate buffered saline (PBS) without calcium and magnesium, then an aliquot of 5–6 mL of trypsin/EDTA solution (Sigma, UK) was added. The flask was placed inside the incubator for 5 minutes at 37°C. The flask was gently tapped to ensure cell detachment. To inactivate the trypsin, 10 to 12 mL of culture medium were added into the flask, and the resuspended cells were transferred into a 50 mL

falcon tube (Fisher Scientific, UK) for centrifugation at 1500 rpm for 5 minutes, Sorvall Legend RT centrifuge (Thermo Scientific, UK). The supernatant was discarded, and the cell pellet was resuspended in culture medium by gently pipetting up and down. The cells were counted by adding 10 µL of the cell suspension into an AC1000 improved Neubauer haemocytometer (Hawksley, UK). The resuspended hMSCs were either passaged to another flask to continue culture or treated for experiments.

2.8 Stem cell modification with nanobiohybrids

Human mesenchymal stem cells were seeded in well plates at desired density, and after adhesion to the plate, they were incubated for 15 and 30 minutes with 2 mL of [scGFP_PlGF2] or [scGFP_PlGF2][S], and observed with a widefield fluorescent microscope (Leica LASX). There was no observable difference in the fluorescence intensity between the cells treated for 15 or 30 minutes, therefore an incubation time for 15 minutes was chosen.

hMSCs were also treated in suspension. After trypsinisation and resuspension in phenol-free DMEM (without supplements), cells were treated for 15 minutes at 37°C with 2 mL of 4 µM of either [scGFP], [scGFP_PlGF2] or [scGFP_PlGF2][S] in shaking motion at 50 rpm. The hMSCs suspension was centrifuged at 1500 rpm for 5 minutes to remove unbound proteins and resuspended in phenol-free DMEM without supplements at desired density.

2.8.1 Cytotoxicity

MTS is a colorimetric assay used to measure the metabolic rate of the cells to give an indication of viability. It is based on the ability of the cell to reduce 3-(4,5-dimethylthiazol-2-yl)-5-(3-carboxymethoxyphenyl)-2-(4-sulfophenyl)-2H-

tetrazolium (MTS) into formazan. This reduction is performed by NAD(P)H-dependent dehydrogenase enzymes presents in the metabolic functioning cells.

2.8.1.1 Method

Mesenchymal stem cells from different patients were seeded in a 48 well plate (20,000 cells per well). In order to build a standard curve, 0, 500, 1000, 2000, 5000, 10,000, 14,000 and 20,000 cells per well were seeded in duplicate. The wells containing 20,000 hMSCs were exposed to a range of different concentrations of [scGFP_PlGF2] and [scGFP_PlGF2][S] (2, 4, 6, 12 and 18 µM) in triplicate for 15 minutes at 37°C. Cells were rinsed twice with 0.5 mL of PBS and 300 µL of DMEM phenol-free culture media (low glucose 1 $mg \cdot mL^{-1}$) DMEM containing pyridoxine-HCL and $NaHCO_3$, supplemented with 100 $units \cdot mL^{-1}$ penicillin, 100 $\mu g \cdot mL^{-1}$ streptomycin, 2 mM GlutaMAX supplement (Invitrogen, USA), 10% v/v FBS and 5 $ng \cdot mL^{-1}$ freshly added basic human fibroblast growth factors, FGF (Peprotech, USA) and placed in incubator overnight at 37°C in 5% CO_2.

The next day, the media was replaced with 300 µL of phenol-free culture media containing 60 µL of CellTiter 96 solution (Promega, USA), containing 3-(4,5-dimethylthiazol-2-yl)-5-(3-carboxymethoxyphenyl)-2-(4-sulfophenyl)-2H-tetrazolium (MTS) and placed in incubator at 37°C in 5% CO_2 atmosphere. After two hours, 100 µL of each well were transferred to a 96 well plate (Corning, UK) in triplicate and the absorbance was measured at 490 nm using microplate Mithras LB 140 (Berthold technologies, Germany).

2.8.2 Cell proliferation

After resuspending hMSCs in phenol-free DMEM (without supplements), they were treated for 15 minutes at 37°C with 2 mL of 4 µM of [scGFP_PlGF2] and

[scGFP_PlGF2][S] in shaking motion at 50 rpm. Cells were spun at 1500 rpm for 5 minutes to remove unbound proteins and resuspended in phenol-free DMEM without supplements and counted. 100,000 cells were seeded in a T25 flask with 5 mL of culture medium containing FGF. The medium was changed every two days. After seven days, cells were harvested as previously described, counted and seeded at the initial density. Population doubling rate (PD) was calculated from the number of cells seeded (ns) and harvested (nh), these numbers where then normalised to the untreated cells used as a control.

$$PD = \frac{\log\left(\frac{nh}{ns}\right)}{\log(2)} \qquad \textbf{\textit{Equation 2.5}}$$

2.8.3 Flow cytometry

Flow cytometry is used to analyse and/or sort cells in a population according to its internal and external characteristics. First, cells are arranged to individually pass through an interrogation point containing a laser beam. The light scattered from the irradiated cells is collected by detectors located parallel to the beam, forward scattering, or in a perpendicularly, side scattering. Additional detectors are placed to collect fluorescent emission.

2.8.3.1 Method

hMscs were expanded in a T175 flask (Fisher Scientific, UK) until 95% confluency. The cells were trypsinised (section 2.7.2) and resuspended in DMEM phenol-free medium before they were exposed to 2 mL of 4 µM [scGFP_PlGF2] or [scGFP_PlGF2][S] for 15 minutes inside cell culture incubator at 37°C in shaking motion 50 rpm. The cell suspension was centrifuged at 1500 rpm for 5 minutes and the pellet was resuspended in suitable buffer for flow cytometry, containing 2% v/v FBS, 2.5 mM EDTA in PBS, at 1×10^6 cells per mL with 0.004 mg·mL^{-1}

propidium iodide (PI). The cell suspension was transferred to flow cytometry tubes (VWR, UK). Samples were analysed with NovoCyte flow cytometer (ACEA Biosciences, USA) and analysed using NovoExpress software (ACEA Biosciences, USA). Parameters were set to 100-300 events per second with 20,000 events accumulated for gate analysis. Untreated cells were used to define the four gates as follows: whole cells by forward scatter height (FSC-H) vs side scatter height (SSC-H), single cells by forward scatter area (FSC-A) vs (FSC-H), PI negative living cells by FSC-A vs Qdot605A and positively labelled cells with GFP were defined by FITC-A vs FSC-A.

2.8.4 Calculating constructs per cell

hMSCs were seeded at a density of 20,000 cell per well and treated with 0.25, 0.5, 2, 4 and 6 μM solutions of [scGFP_PlGF2] or [scGFP_PlGF2][S] for 15 minutes at 37°C under CO_2 atmosphere. The supernatant was aspirated and collected for UV-vis analysis, taking a full spectrum from 200 to 600 nm. The absorption intensity at 487 nm was compared to the known initial absorption and the number of nanobiohybrid constructs on the surface of hMSCs was calculated using Equation 2.6.

$$Constructs\ per\ cell = \frac{C_0 - C_s}{N} N_A \qquad \textbf{\textit{Equation 2.6}}$$

C_0 refers to the initial concentration in moles, C_s is the concentration of the supernatant in moles, N is the seeded cells per plate, and N_A is Avogadro's constant.

2.9 Fluorescent microscopy

2.9.1 Confocal fluorescent microscopy

Confocal microscopy is largely use for the detailed resolution images that can be obtained. It makes use of a focused laser beam able to focus on a specific spot and depth in a sample to emit light at precisely this area. A pinhole within the microscope prevents light that is out of focus to reach the detector to avoid background. This creates images of a particular optical plane. In order to make 3D representations, different optical planes in the sample are scanned. These images are then stacked on the z-axis with a suitable software[26].

2.9.1.1 Method

hMSCs were seeded in glass bottom micro well dishes 35 mm (40,000 hMSCs per dish) (MatTek, USA) with culture media and let to adhere overnight. The nucleus was stained with 1 µL of Hoechst 33342 (Fisher scientific H3570) and the cytoplasm with 1 µL of cell tracker red CMTPX dye (Life technologies C34552) for 30 minutes at 37°C under 5% CO_2 atmosphere. This media was then aspirated and replaced with 2 mL of 4 µM of sample [scGFP_PlGF2] or [scGFP_PlGF2][S]. Cells were incubated for 15 minutes, then washed twice with 1 mL of PBS. Finally, 2 mL of complete phenol-free medium (low glucose 1 mg·mL^{-1} DMEM containing pyridoxine-HCL and $NaHCO_3$ with 100 units·mL^{-1} penicillin, 100 µg·mL^{-1} streptomycin, 2 mM GlutaMAX supplement, 10% v/v foetal bovine serum FBS and 5 ng·mL^{-1} FGF) was added. The cells were analysed using confocal fluorescent microscopy in a Leica DM I6000 inverted epifluorescent microscope in a chamber at 37°C under CO_2 atmosphere.

2.10 Widefield fluorescence microscopy

Wide field microscopy is a type of light microscopy used to image a fluorescent specimen within a sample. The light emitted illuminates at the excitation wavelength specific for the fluorophore and it is collected and interpreted by the detector as an image. In this case, the complete sample is illuminated and signals from all the optical and focal planes are detected[27].

2.10.1 Time lapse microscopy

hMSCs were seeded at a density of 20,000 cells per well, in tissue cultured treated 6 well plate 34.8 mm (Corning, UK) with supplemented culture media 24 hours previous to the experiment. The nucleus was stained with 1 µL Hoechst 33342 (Fisher scientific H3570) for 20 minutes at 37°C under 5% CO_2 atmosphere. This media was then aspirated and replaced with 2 mL of 4 µM of sample [scGFP_PlGF2] and [scGFP_PlGF2][S]. Cells were incubated for 15 minutes, then washed twice with 1 mL of PBS. Finally, 2 mL of supplemented phenol-free medium DMEM (low glucose 1 $mg{\cdot}mL^{-1}$) was added. The cells were analysed using inverted microscope (Leica LASX) with a 20× lens at 37°C under CO_2 atmosphere for 12 hours taking one image every 15 minutes.

2.11 Differentiation assays

2.11.1 Osteogenesis

Mesenchymal stem cells from two patients were harvested and 20,000 hMSCs were seeded in a 12 well plate. The cells were exposed to 300 µL of [scGFP_PlGF2] or [scGFP_PlGF2][S], and cultured in StemPro Osteogenesis differentiation medium (Thermo Fisher Scientific, UK), or complete hMSC culture medium, with media changes every two days. Antifungal water (100 units of

penicillin, 100 µg streptomycin and 2.5 µg of amphotericin in autoclaved dH_2O) was added to fill the remaining wells of the plate.

For osteocyte detection, sample wells were gently washed with 500 µL pf PBS twice, then cells were fixed with 4% paraformaldehyde (PFA) (BioLegend, USA) for 30 minutes at room temperature. The cell monolayer was washed with 500 µL of autoclaved dH_2O before adding 500 µL of filtered solution of Alizarin Red S (2% w/v Alizarin Red S, pH adjusted to 4.1 with HCl). The plate was covered with tin foil to protect it from the light and incubated for 30 minutes at room temperature. The sample wells were washed four times with 1 mL of autoclaved dH_2O, and PBS was added. The samples were immediately imaged with a widefield inverted microscope and analysed with Fiji software (NIH, USA). All images were converted into a 16-bit image and a mean threshold was applied. Then, each image was submitted to particle analysis, using 0 to infinity size and 0 to 1 circularity for the total area covered by the stained monolayer.

2.11.2 Adipogenesis

Cells from one patient were harvested and 20,000 hMSCs were seeded in a 12 well plate. The cells were exposed to 300 µL of [scGFP_PlGF2] or [scGFP_PlGF2][S] for 15 minutes and rinsed twice with PBS. The cells were cultured in StemPro Adipogenesis cell medium (Thermo Fisher Scientific, UK), or complete hMSC culture medium, with media changes every two days. Antifungal water (100 units of penicillin, 100 µg streptomycin and 2.5 µg of amphotericin in autoclaved dH2O) was added to fill the remaining wells of the plate.

After 21 days, the medium was removed by pipetting and the sample wells were washed twice with 500 µL of PBS. 500 µL of neutral buffered formalin 10% (10% of 37-40 formaldehyde, 90% dH2O, 33.5 mM sodium phosphate monobasic

NaH_2PO_4, and 45.5 mM sodium phosphate dibasic Na_2HPO_4) to cover the cell monolayer, this was incubated at room temperature. After 45 minutes, fixation buffer was aspirated, and the wells were washed with 500 µL of autoclaved dH_2O followed by the addition of 500 µL of 60% isopropanol solution and incubated at room temperature for 5 minutes. To stain the cell monolayer, the isopropanol was aspirated and Oil Red O staining solution (stock 0.3% Oil Red O in isopropanol, 3 parts diluted in 2 parts of autoclaved dH2O) was added to fill the wells, filtering the solution right before staining. Cells were incubated for 30 minutes and the wells were washed several times with dH2O. Images were taking using wide field inverted microscope.

2.11.3 Chondrogenesis

Cells from three different patients were plated in a 24 well plate at a density of 50,000 cells per cm^2. Cells were exposed to 1 mL of 4 µM of [scGFP_PlGF2] or [scGFP_PlGF2][S] for 15 minutes in incubator at 37 degrees. The wells were gently rinsed twice with 1 mL of PBS and then 1 mL of chondrogenesis media (4500 $mg{\cdot}mL^{-1}$ glucose) phenol-free DMEM (pyridoxine-HCl and $NaHCO_3$, supplemented with 100 units·mL penicillin and 100 µg·mL streptomycin, 2 mM GlutaMAX, 1 mM sodium pyruvate and 1% v/v insulin transferrin selenium ITS solution), freshly supplemented 0.01 % v/v dexamethasone, 80 nM L-ascorbic acid 2-phosphate, and 10 $ng{\cdot}mL^{-1}$ of TGF-β3 (R&D Systems, USA). This was done in triplicate, with unmodified cells as a control kept in hMSC culture medium, changing media every two days. After three weeks, the cells were lysed to extract RNA for qPCR analysis.

2.11.3.1 RNA extraction

A Qiagen micro RNasy kit was used to extract RNA from the differentiated cells according to manufacturer's instructions. Briefly, the cells were harvested with provided lysis buffer and processed immediately or stored at -80°C for later analysis.

The cells were summited to homogenisation with a 21 G 1½ inch needle. Ethanol was added and then loaded into a column to bind RNA and washed to remove DNA. The purified RNA was then eluted with DNase free water. The samples were kept at -80°C or immediately processed for complementary DNA (cDNA).

For cDNA preparation, a Takara PrimeScript RT reagent kit (Takara, Japan) was used according to the instructions provided by the manufacturer. This was performed in 200 µL RNase free PCR tubes, and the resulting mix was summited to PCR at 37°C for 15 minutes, 85°C 5 seconds and 4°C for cooling. The resulting DNA was immediately used or stored at -80°C for future analysis.

2.11.3.2 qPCR

For this technique, a MicroAmp Fast Optical 96-well reaction plate (Applied biosystems, UK) was used. On each well, 5.5 µL of a mixture containing 5 µL of Taqman master mix and 0.5 µL of the gene set were deposited on the left wall of the well. Followed by the addition of 1 µL cDNA of the sample (section 2.11.3.1) with 3.5 µL of DNase-free water. The 96 well plate was covered with adhesive PCR plate film (Thermo Fisher Scientific, UK). qPCR was carried out using a QuantStudio™ 3D Digital PCR System (Life Technologies). The data obtained was analysed using the double delta Ct analysis method.

2.12 Measuring stem cell affinity

2.12.1 Static affinity assay

A non-tissue culture treated 96 well plate (Fisher, UK) was used to assess adhesion of treated cells to different proteins (fibronectin 10 $\mu g \cdot mL^{-1}$, collagen I 0.2 $mg \cdot mL^{-1}$, collagen II 0.2 $mg \cdot mL^{-1}$ and BSA 10 $mg \cdot mL^{-1}$ was used as a control).100 µL was added to each well in triplicate and left at 4°C overnight. The next day, wells were rinsed twice with 100 µL of PBS and unspecific binding sites were blocked with BSA solution for a minimum of one hour.

hMSCs were counted and treated as mentioned in previous method (2.8) with either [scGFP], [scGFP_PlGF2] or [scGFP_PlGF2][S]. 10,000 cells per well were seeded in each well with 100 µL of DMEM phenol-free medium with no additives and incubated at 37°C in a 5% CO_2 atmosphere. A standard curve was also made with different cell densities (250, 500, 1,000, 2500, 5,000, 7,500 and 10,000 cells per well in duplicate), adding DMEM medium with all supplements in a tissue-culture treatet plate. After four hours, the media was aspirated, and the wells were rinsed with 100 µL of PBS twice to remove non-attached cells and debris. DNA quantification assay (CyQUANT NF cell proliferation assay kit, Invitrogen) was performed to assess cell adhesion to proteins. The solution was prepared diluting HBSS buffer 5 times with DNase free water and adding the corresponding dye. 100 µL of solution was added to each well and the plate was incubated for 60 minutes. The fluorescence was measured with microplate reader with excitation at 485 nm and emission at 530 nm.

2.12.2 Dynamic affinity assay

Dynamic cell adhesion experiments were carried out with a Microfluidic pump ExiGo (Cellix Ltd, UK), with a shear stress precision of ±0.5%. Vena8 Fluoro+ biochips were used to perform this experiment. It contains a total of 8 channels (400 µm in width, 100 µm in depth, and 20 mm long), and a reservoir on each end (Figure 2.2). The biochip is marked with five equally distributed points, which are marked on the top pf each channel. The measurements were performed at each of these five positions.

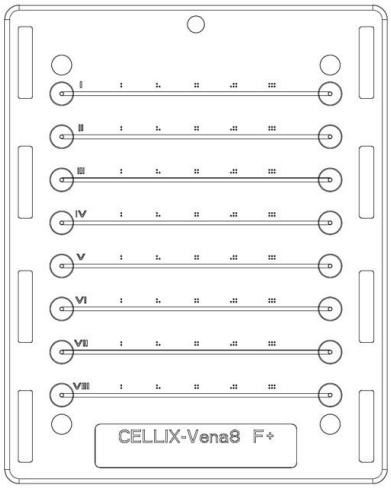

Figure 2.2 Schematic representation of a Vena8 Fluoro+ biochip. Each biochip contains eight channels 400 µm × 100 µm × 20 mm. Each channel is marked with five equally distribuited points, which were used for measurements. Image taken from wearecellix.com.

All channels of the Vena8 Fluoro+ biochip (Cellix Ltd, UK) were coated with 0.1 $mg \cdot mL^{-1}$ collagen II from bovine trachea and left overnight at 4°C in a humidified chamber. Unspecific sites were blocked with 10 $\mu g \cdot mL^{-1}$ BSA. The channel was washed with DMEM phenol-free medium with no additives for 30 seconds at 40 $\mu L \cdot min^{-1}$. Cells were modified and resuspended at a density of 1×10^6 cells per mL in DMEM phenol-free medium without additives. A 50 µL aliquot of cells modified with [scGFP_PlGF2] and [scGFP_PlGF2][S] or unmodified, was added into the channel reservoir every time, and the suspension was withdrawn with a flow rate

of 6, 4 and 3 $mL \cdot min^{-1}$. This was performed with hMSCs from three different patients. In the same way, Vena8 Fluoro+ biochip (Cellix Ltd, UK) was coated with 10 $\mu g \cdot mL^{-1}$ BSA to be used as a negative control.

2.13 Bovine ex vivo explants harvest

Cartilage explants were harvested form the lateral and patellar groove of 6–8-week-old calves, obtained 6–8 hours after death from abattoir F Drury and Sons Ltd in Swindon, UK. The legs were carefully washed and disinfected with Rely+On Virkon (Dupont, UK) and warm dH_2O. The skin from the legs was cautiously removed with 22-size surgical blades (Swann-Morton, UK) until the coronet to reveal the joint area. The hoofs and the top side of the leg were covered in aluminium foil and the exposed surface of the leg was sprayed with 70% ethanol in dH_2O and placed inside a laminar hood (Figure 2.3 a-c).

The outer layer was carefully cut to expose the articular cartilage, lateral and medial meniscus and to cut the anterior cruciate ligament. The cartilage was taken from the lateral and patellar grove. The explant disks were delimited with an 8 mm biopsy punch (Stiefel, Germany) and carefully detached with a 22-size surgical scalpel (Swann-Morton, UK) and collected with tweezers (Figure 2.3 d-h). The discs were added into a falcon tube in PBS containing 1% penicillin/streptomycin solution. After dissection, the pieces were placed in individual wells in a 48 well plate (Corning, UK) and kept in phenol-free medium fully supplemented with antibiotics.

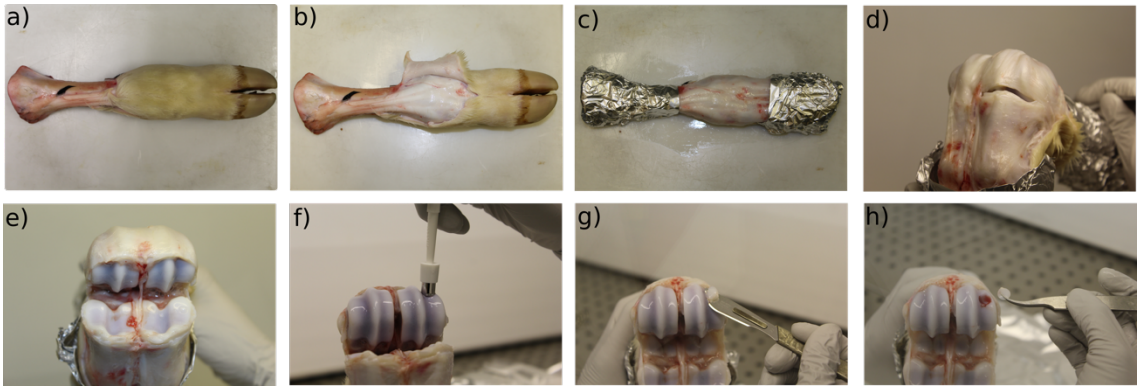

Figure 2.3 Cow leg dissection methodology. The legs were washed before removing the skin (a-b). Then, the sides were covered with aluminium foil and sprayed with 70% ethanol before being placed inside the laminar sterile hood (c). The layer was dissected to expose the articular cartilage (d-e). Finally, the cartilage discs were delimited with an 8 mm biopsy punch and detached with a scalpel and tweezers (f-h).

2.13.1 Stem cell affinity assays in ex vivo explants

Cartilage discs were washed twice in PBS before being cut to 6 mm diameter with a biopsy punch (Stiefel, Germany) and placed in a non-tissue culture treated 96 well plate (Fisher, UK) with 200 µL of DMEM phenol-free medium without supplements. Tissue discs were then stained with Hoechst nuclei stain for five minutes. hMSCs were treated with [scGFP_PlGF2][S], and resuspended in DMEM phenol-free medium, using untreated cells as a control. hMSCs were counted and added onto the cartilage surface (20,000 cells) and placed in incubator at 37°C with 5% CO_2 for four hours. The samples were then used for confocal analysis, fixed for scanning electron microscopy SEM imaging or histology analysis.

2.13.2 Scanning Electron Microscopy

All tissue samples were fixed with 2.5% glutaraldehyde for one hour. To remove excess of fixing agent, the samples were rinsed three times for 10 minutes with 100 mM sodium phosphate buffer pH 7.4. Cartilage samples were then placed in 1% osmium tetroxide for one hour and washed three times for 10 minutes with 100 mM sodium phosphate buffer and washed with dH_2O for 10 minutes. Dehydrations

steps were made with 25, 50, 70, 80, 90, 96, 100% ethanol before being processed with critical point dryer (CPD) Leica EM CPD300, set for 15 cycles of 15°C for cooling and slow heating at 35°C, with slow CO_2 exchange. The samples were carefully removed from the CPD machine and mounted on a SEM specimen stub (Ted Pella, USA) with a conductive carbon mount grip on top. The dry samples were placed in a high-resolution sputter coater (Agar Scientific, UK) and coated with 15 nm from palladium or chromium filament. All samples imaged on Quanta 200 FEI field emission scanning electron microscopy (Thermo Fisher Scientific, UK).

2.13.3 Histology

After hMSCs were seeded on ex vivo explants, the samples were fixed in 10% neutral buffered formalin overnight at room temperature. The tissue pieces were then bathed in 30% sucrose for cryo-sectioning or 70% ethanol.

2.13.4 Stem cell affinity quantification in ex vivo explants

Three-dimensional Z-stack images from cartilage with seeded hMSCs were flattened to 2D using the Z-project function from the Fiji software package (NIH, USA). Then, a median intensity threshold was applied to the images and the resulting image was changed into binary with a watershed segmentation. Finally, the number of cells were counted excluding sizes smaller than 10 μm.

2.13.5 Differentiation on ex vivo explants

Mesenchymal stem cells from three different patients were resuspended and treated in suspension with 2 mL of 4 μM [scGFP_PlGF2][S], and seeded in a 6 mm bovine cartilage explant at a density of 20,000 cells per well in a 96 well plate. A control was made with untreated cells. After four hours, the cartilage was

transferred into a 24 well plate. The wells were gently rinsed twice with 1 mL of PBS and then 1 mL of chondrogenesis media (4500 $mg \cdot mL^{-1}$ glucose) phenol-free DMEM (pyridoxine-HCl and $NaHCO_3$, supplemented with 100 units·mL penicillin and 100 µg·mL streptomycin, 2 mM GlutaMAX, 1 mM sodium pyruvate and 1% v/v insulin transferrin selenium ITS solution), freshly supplemented 0.01 % v/v dexamethasone, 80 nM L-ascorbic acid 2-phosphate, and 10 $ng \cdot mL^{-1}$ of TGF-β3 (R&D Systems, USA), changing media every two days. A control was made where no TGF-β3 was added, for a total of 12 samples. After three weeks, the samples were fixed and sent to the Histology Unit at University of Bristol for sectioning.

2.13.5.1 Immunohistochemistry

After fixation in 10% neutral buffered formalin, cartilage samples were submitted to the Histology Services Unit (University of Bristol), where samples were embedded in paraffin wax to prepare for cutting with a diamond knife. Sections were 10 µM thick with 10 µM space between them. Sections were dried in a microscope slide (VWR, UK) and stored for analysis.

Slices were baked for 1 hour at 56 degrees to prevent detachment and dewaxed by submerging for 30 minutes in Histoclear solution (National Diagnostics, USA). All slices were then rehydrated in three gradients of IMS, starting with 5 minutes in 100%, 90% and 70%, before they were put in a Coplin slide jar filled with tap water. Slices were rinsed with PBS and a wax pen ImmEdge PAP (Vector Laboratories, UK) was used to draw a hydrophobic barrier around each section.

Proteinase K Ready-to-use (Dako, USA) was used for enzymatic retrieval. Sufficient amount of Proteinase K was used to cover the sample, and it was incubated at room temperature. After 10 minutes, slices were washed twice with PBS for 2 minutes to remove enzyme excess. To inhibit endogenous peroxidase

activity was quenched with the addition of 3% H_2O_2 for 10 minutes, and excess was removed with two PBS washes for 2 minutes.

For the next steps, a Novolink polymer detection kit (Leica, UK) was used. To block non-specific proteins, a drop from Novolink Protein Block (0.4% Casein in phosphate-buffered saline, with stabilizers, surfactant, and 0.2% Bronidox L as a preservative) was placed on each sample for 5 minutes at room temperature, and the excess was washed by quickly submerging the slides in PBS.

For collagen I detection, a Collagen I ab234466 primary antibody (Abcam, UK) was used. This was prepared in tris buffer saline TBS (15.2 mM Tris HCl, 4.6 mM tris and 150 mM NaCl) containing 1% goat serum, plus concentration matched isotope IgG as control Abcam isotype ab170190 Mouse IgG1 kappa monoclonal (Abcam, UK). Incubated overnight at 4°C in humidified chamber to avoid dehydration of samples. Unbounded antibody was removed by washing with TBS 3 times for at least 3 minutes. One drop of Novolink post primary (Rabbit anti mouse IgG (<10 µg/mL) in 10% (v/v) animal serum in tris-buffered saline/0.09% ProClinTM 950) was placed on each sample and incubated for 30 minutes, followed by three washes with TBS to prepare for the addition of Novolink polymer (Anti-rabbit Poly-HRP-IgG (<25µg.mL^{-1}) containing 10% (v/v) animal serum in tris-buffered saline/0.09% ProClinTM). Finally, 200 µL of DAB substrate was added to all sections and incubated for 3 minutes. Incubation with DAB (1.74% w/v 3,3' -diaminobenzidine, in a stabilizer solution) was necessary to make antigens visible. For background, a drop of <0.1% Hematoxylin was used and incubated for 3 minutes and rinsed with tap water to remove excess solution.

All slides were dehydrated by 2 minutes immersions in graded IMS 70%, 90% and 100%, followed by three 5-minute immersions in xylene. Slides were left to air dry

for 10 minutes and mounted by adding DPX (mixture of distyrene, a plasticizer, and xylene) and sealed with a coverslip on top. Slices were imaged using widefield fluorescence microscopy.

2.14 Surface functionalisation of bovine cartilage explants

The 6 mm cartilage bovine ex vivo explants were first stained with Hoechst to identify the chondrocyte population. Then, cartilage discs were submerged in a 1 µM solution of either [scGFP]. [scGFP_PlGF2] or [scGFP_PlGF2][S] with 1% BSA in 1.5 mL Nalgene tubes for 24 hours in a CO_2 atmosphere at 37°C. The next day, the supernatant was collected and submitted to UV-vis analysis taking a spectrum of each solution from 200 to 600 nm. The analysis of the 487 nm absorbance peak was used to quantify the protein deposited on the cartilage. This method was taken from Krishnan et al.[28].

All discs were then fixed in 4% paraformaldehyde (PFA) overnight. A vertical cross section of the discs was cut and analysed using confocal microscopy.

2.15 Statistical analysis

All the data obtained was statistically analysed using a student T-test with two-tailed unpaired samples in Microsoft Excel. Differences between the experimental and control groups were compared. The data was expressed as a mean of three biological repeats ± standard deviation. A value of $p < 0.05$ was considered statistically significant.

2.16 Bibliography

1. Berrow, N. S. *et al.* A versatile ligation-independent cloning method suitable for high-throughput expression screening applications. *Nucleic Acids Res.* **35**, e45–e45 (2007).

2. Benoit, R. M., Wilhelm, R. N., Scherer-Becker, D. & Ostermeier, C. An improved method for fast, robust, and seamless integration of DNA fragments into multiple plasmids. *Protein Expr. Purif.* **45**, 66–71 (2006).

3. Qiagen. *QIAprep Miniprep Handbook*. *QIAprep Miniprep Handbook* (2012). doi:10.1111/j.1468-1331.2009.02749.x

4. Porath, J., Carlsson, J., Olsson, I. & Belfrage, G. Metal chelate affinity chromatography, a new approach to protein fractionation. *Nature* **258**, 598–599 (1975).

5. Hochuli, E., Döbeli, H. & Schacher, A. New metal chelate adsorbent selective for proteins and peptides containing neighbouring histidine residues. *J. Chromatogr. A* **411**, 177–184 (1987).

6. Block, H. *et al.* Chapter 27 Immobilized-Metal Affinity Chromatography (IMAC). in *Methods in Enzymology* **463**, 439–473 (2009).

7. Saraswathy, N. & Ramalingam, P. Introduction to proteomics. in *Concepts and Techniques in Genomics and Proteomics* 147–158 (Elsevier, 2011). doi:10.1533/9781908818058.147

8. Smith, P. K. *et al.* Measurement of protein using bicinchoninic acid. *Anal. Biochem.* **150**, 76–85 (1985).

9. Jurinke, C., Oeth, P. & van den Boom, D. MALDI-TOF Mass Spectrometry : A Versatile Tool for High-Performance DNA Analysis. *Mol. Biotechnol.* **26**, 147–164 (2004).

10. Hillenkamp, F., Karas, M., Beavis, R. C. & Chait, B. T. Matrix-Assisted Laser Desorption/Ionization Mass Spectrometry of Biopolymers. *Anal. Chem.* **63**, 31 (1991).

11. Clarke, D. T. Circular dichroism and its use in protein-folding studies. *Methods Mol. Biol.* **752**, 59–72 (2011).

12. Greenfield, N. J. Using circular dichroism spectra to estimate protein secondary structure. *Nat. Protoc.* **1**, 2876–2890 (2006).

13. Micsonai, A. *et al.* Accurate secondary structure prediction and fold recognition for circular dichroism spectroscopy. *PNAS* **112**, E3095–E3103 (2015).

14. Schmid, F. Biological Macromolecules: UV-visible Spectrophotometry. in *Encyclopedia of Life Sciences* 1–4 (John Wiley & Sons, Ltd, 2001). doi:10.1038/npg.els.0003142

15. Tajmir-Riahi, H. -a., N'soukpoe-Kosi, C. N. & Joly, D. Structural analysis of protein – DNA and protein – RNA interactions by FTIR , UV-visible and CD spectroscopic methods. *Spectroscopy* **23**, 81–101 (2009).

16. Karoui, R. *Methodologies for the Characterization of the Quality of Dairy Products*. (Elsevier, 2017). doi:10.1016/bs.afnr.2016.12.007

17. Thomas, S., Thomas, R., K. Zachariah, A. & Mishra, R. K. *Thermal and Rheological Measurement Techniques for Nanomaterials Characterization*. *Thermal and Rheological Measurement Techniques for Nanomaterials Characterization* **3**, (2017).

18. Skou, S., Gillilan, R. E. & Ando, N. Synchrotron-based small-angle X-ray scattering of proteins in solution. *Nat. Protoc.* **9**, 1727–1739 (2014).

19. Rambo, R. P. & Tainer, J. A. Characterizing flexible and intrinsically unstructured biological macromolecules by SAS using the Porod-Debye law. *Biopolymers* **95**, 559–571 (2011).

20. Jacques, D. A., Guss, J. M., Svergun, D. I. & Trewhella, J. Publication guidelines for structural modelling of small-angle scattering data from biomolecules in solution. *Acta Crystallogr. Sect. D Biol. Crystallogr.* **68**, 620–626 (2012).

21. Putnam, C. D., Hammel, M., Hura, G. L. & Tainer, J. A. X-ray solution scattering (SAXS) combined with crystallography and computation: defining accurate macromolecular structures, conformations and assemblies in solution. *Q. Rev. Biophys.* **40**, 191–285 (2007).

22. Franke, D. & Svergun, D. I. DAMMIF, a program for rapid ab-initio shape determination in small-angle scattering. *J. Appl. Crystallogr.* **42**, 342–346 (2009).

23. Armstrong, J. P. K. *et al.* Artificial membrane-binding proteins stimulate oxygenation of stem cells during engineering of large cartilage tissue. *Nat. Commun.* **6**, 7405 (2015).

24. Weyer, L. G. Near-infrared spectroscopy of organic substances. *Appl. Spectrosc. Rev.* **21**, 1–43 (1985).

25. Arora, M. Cell Culture Media: A Review. *Mater. Methods* **3**, (2013).

26. Peterson, D. A. Confocal Microscopy. in *Encyclopedia of Movement Disorders* 250–252 (Academic Press, 2010). doi:10.1016/B978-0-12-374105-9.00230-6

27. Ibidi. Microscopy Techniques and Culture Surfaces: Find the Perfect Match. (2018). Available at: https://ibidi.com/content/215-widefield-fluorescence. (Accessed: 5th October 2018)

28. Krishnan, Y. *et al.* Green fluorescent proteins engineered for cartilage-targeted drug delivery: Insights for transport into highly charged avascular tissues. *Biomaterials* **183**, 218–233 (2018).

Chapter 3

Expression and Characterisation of an Adhesive Protein-polymer Surfactant Construct

3.1 Introduction

Polymer surfactants have been successfully conjugated with proteins to confer beneficial properties such as improved solubility in organic solvents[1,2], and increased proteolytic resistance[3], allowing for the activity of the biological molecule to be retained. The formation of these protein-surfactant conjugates can be via electrostatic and hydrophobic forces[4], where anionic surfactants bind to positive residues such as lysine, arginine and histidine, whilst cationic surfactants bind to negatively charged residues, such as aspartic acid and glutamic acid; and alkyl chains are likely to interact with hydrophobic sites[5].

The formation of these surfactant-conjugates are facilitated by homogenizing the surface charge through chemical cationization, as described by Armstrong et al., who chemically cationized myoglobin and enhanced green fluorescent protein (eGFP) to make it suitable for electrostatic conjugation with anionic polymer surfactants[6]. Here, the team were able to show that the resulting polymer surfactant corona reconfigured at the plasma membrane of human mesenchymal stem cells, promoting spontaneous and persistent adhesion of the complex[6]. This itself was built upon the pioneering work done by Perriman et al., who cationized proteins in order to electrostatically conjugate them with polymer surfactants, allowing the conjugates to be dehydrated to create solvent-free liquid proteins[7–10]. Significantly, these protein-polymer surfactant conjugates were folded, exhibited high levels of thermal stability and maintained their biological functions, under almost completely anhydrous conditions[7–10].

The two-step synthesis described above has shown that it can be used to create artificial membrane binding proteins, nevertheless, the cationization step is non-discriminative, i.e. it might potentially modify all acid sidechains. Although this did

not prove to be a problem for oxygen delivery (myoglobin) and fluorescence (eGFP) at the cell membrane, amino acid sequences associated with hitting specific binding targets on the cell surface or extracellular matrix (ECM) need to be highly conserved and not chemically modified. Accordingly, to impart artificial ECM binding properties to cells, a supercationic mutant of green fluorescent protein, supercharged GFP (scGFP), with a fused peptide from placenta growth factor 2 (PlGF2_123–144) was expressed and purified, termed [scGFP_PlGF2]. This protein was characterised to ensure the peptide-fusion protein did not affect the properties of the native scGFP. This was followed by the synthesis and characterisation of an anionic surfactant derived from IGEPAL co-890. Finally, as some ionic surfactants are known to be protein denaturants when added at concentrations near or above their critical micellar concentration (CMC)[5,11], the properties of the protein-surfactant conjugate were explored to ensure that the structural integrity and function of the protein was not affected.

3.2 Results and discussion

3.2.1 Characterisation of scGFP_PlGF2

3.2.1.1 Analysis of the primary structure of scGFP_PlGF2

The transformed *E. coli* containing *scgfp-plgf2_123-144* gene or *scgfp*, was cultured until the optical density reached 0.8 at 600 nm before protein expression was induced using IPTG (see Materials and Methods 2.2.1 and 2.2.2). The resulting cell suspension was lysed and purified using immobilised metal affinity chromatography, whereby the histidine tag in the protein formed a complex with the Ni-NTA, and it was then eluted by competitive elution with high imidazole gradients. The protein solution obtained yielded approximately 3–5 $mg \cdot L^{-1}$ of culture.

The collected fractions of scGFP fused PlGF2_123–144-peptide protein, [scGFP_PlGF2], were analysed for purity and molecular weight using polyacrylamide gel electrophoresis (SDS-PAGE). Analysis of the SDS-PAGE gel with the image analysis software FIJI (NIH, USA) showed a single band at approximately 32 kDa, which is close to the theoretical molecular weight, 32.118 kDa obtained with online tool Protein Calculator v3.4 (Appendix B) (Figure 3.1). MALDI-TOF mass spectrometry determined the average molecular weight to be 32.110 kDa (Figure 3.2).

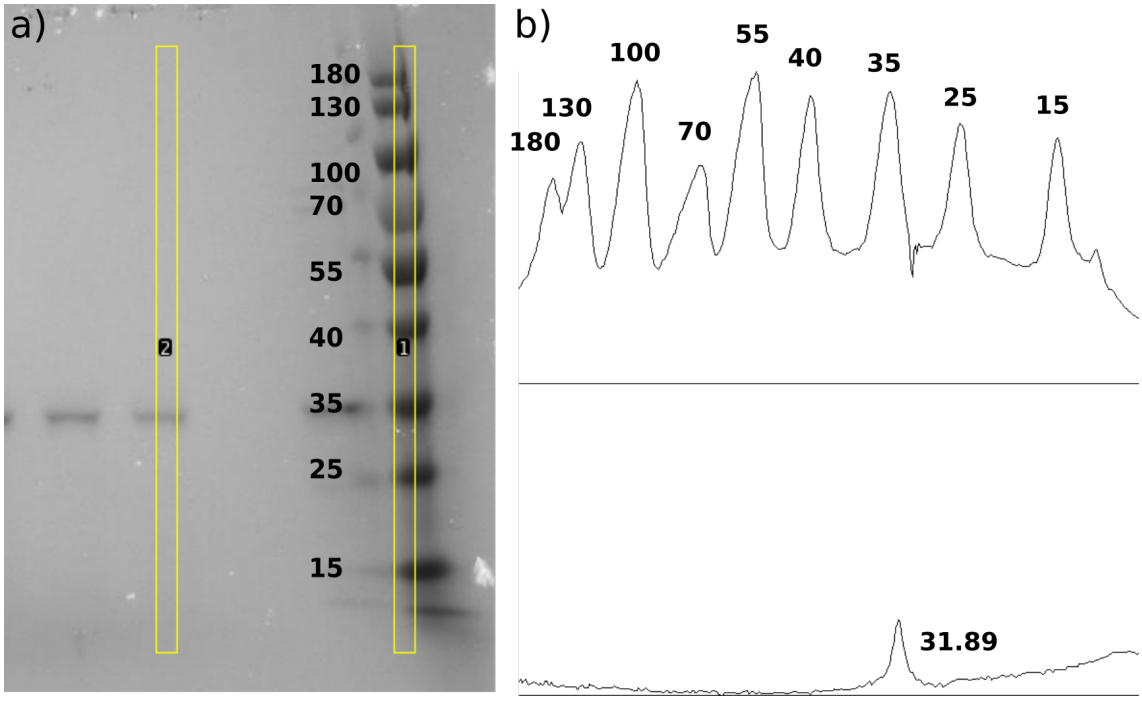

Figure 3.1 Polyacrylamide gel (SDS-PAGE) analysis in Fiji software. a) Polyacrylamide gel (SDS-PAGE) of purified protein with ladder (right), b) image analysis with Fiji software calculated mass to be approximately 32 kDa.

The extinction coefficients for [scGFP_PlGF2] were determined using the BCA assay (see section 2.4.2) with ε=30900 M^{-1} cm^{-1} at 487 nm and ε=17391 M^{-1} cm^{-1} for 280 nm. These values were used to calculate subsequent protein concentrations and are approximate to the values obtained with the protein calculator tool (Appendix B). The ratio of absorbance at 280 and 487 nm was used to analyse the protein purity, as contaminant proteins would contribute to absorbance at 280 nm but not at 487 nm.

Similar expression and purification methods were used to obtain scGFP alone, [scGFP], to use as a control to determine any changes in the properties caused by the fused peptide PlGF2_123–144. Both samples were analysed using MALDI-TOF mass spectrometry and the peaks were found using mMass software. A summary of the mass:charge ratios is found on Table 3.1. The molecular weight of [scGFP] was 29275 Da (Figure 3.2), whereas the molecular weight of

[scGFP_PlGF2] was 32110 Da (Figure 3.3). The difference in molecular weight between [scGFP] and [scGFP_PlGF2] was 2835 Da, which was close to the predicted molecular weight of the peptide sequence for PlGF2_123–144, calculated to be 2988 Da. This difference could have been be due to the calibration of the instrument at the time the molecular weight was determined or potential fragmentation of amino acids (Appendix C).

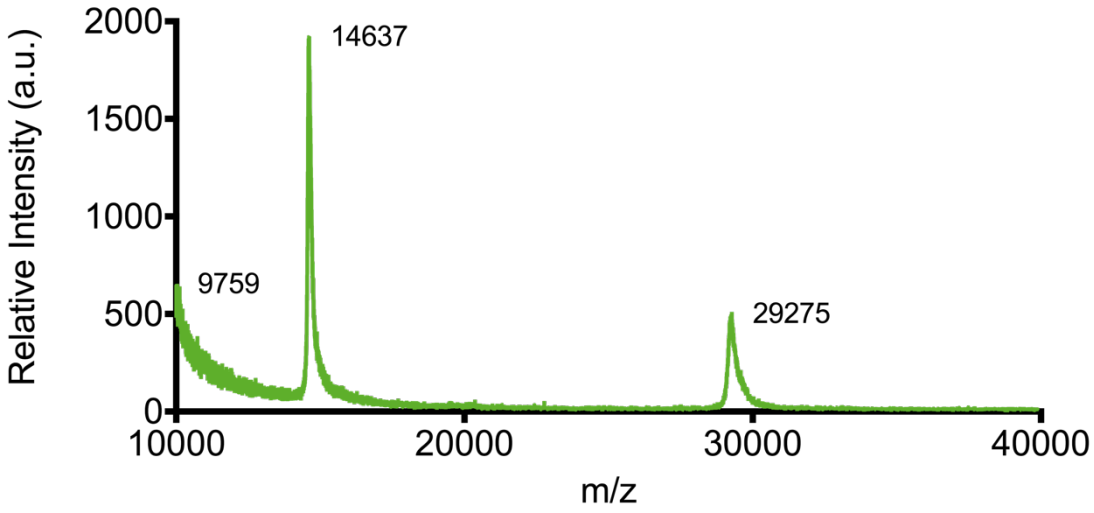

Figure 3.2 Mass spectrometry spectrum from [scGFP]. The mass of the construct was 29275 Da. The protein sample [scGFP] was mixed with sinapinic acid matrix in a 1:1 ratio.

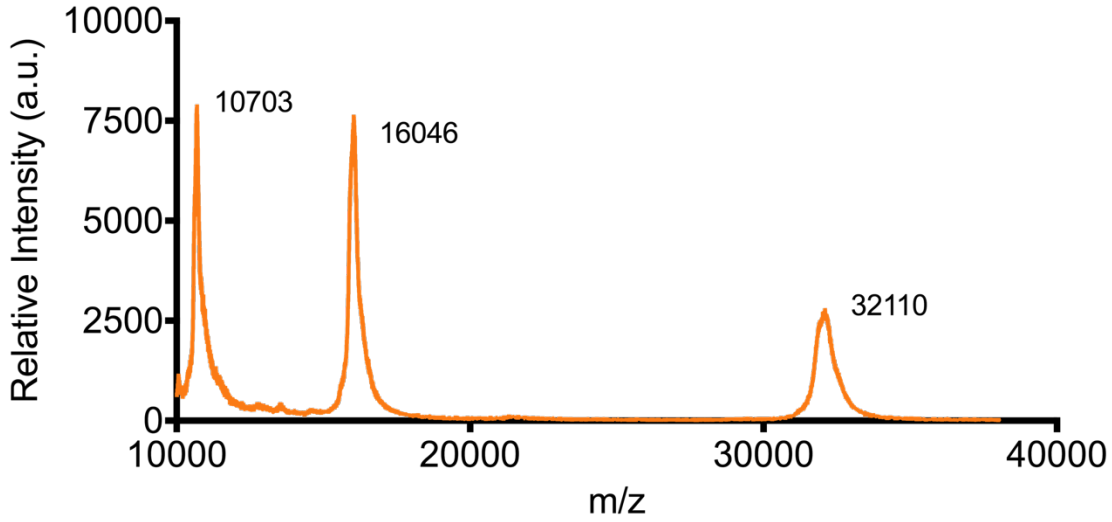

Figure 3.3 Mass spectrometry spectrum from [scGFP_PlGF2]. The mass of the construct was 32110 Da. The protein sample [scGFP_PlGF2] was mixed with sinapinic acid matrix in a 1:1 ratio.

Table 3.1 The three peaks of MALDI-TOF mass spectrum with corresponding mass divided by charge.

	m/z	
Charge	**[scGFP]**	**[scGFP_PlGF2]**
1	29275	32110
2	14637	16046
3	9759	10703

3.2.1.2 Analysis of the secondary structure of scGFP_PlGF2

Synchrotron radiation circular dichroism (SRCD) was used to determine the secondary structure and thermal stability of [scGFP] and [scGFP_PlGF2]. All obtained data was deconvoluted and converted from millidegrees to delta epsilon values using the beta-structure selection algorithm (BeStSel)[12]. In particular, this software considers the existing twist in beta-structures and can differentiate between parallel and antiparallel beta sheets reliably to accurately predict the secondary structure over a wide range of proteins and is optimised for spectra obtained from SRCD. Definitions of the analysed parameters can be found in Table 3.2.

Table 3.2 Secondary structure elements identified by BeStSel.

BeStSel	Protein structure
Helix 1 – regular α-helix	The middle part of α-helices
Helix 2 – distorted α-helix	2-2 residues at the ends of α-helices
Anti 1 – left-twisted β-strand	Left-hand twisted antiparallel β-sheet
Anti 2 – relaxed β-strand	Relaxed (slightly right-handed twisted) antiparallel β-sheet
Anti 3 – right-twisted β-strand	Right-hand twisted antiparallel β-sheet
Parallel β-strand	Parallel β-sheet
Turn	Turns
Others	3,10 helix, π-helix, β-bridge, bend, loop/irregular and invisible regions.

The resulting spectra for [scGFP] and [scGFP_PlGF2] have negative peaks at 218 nm and positive peaks at 195 nm[13] (Figure 3.4 a,b). These features are typical for the antiparallel β-sheets present in the β-barrel structure of scGFP[14], and other GFP variants[15]. In contrast, disordered proteins yield negative peaks near 195 nm[16], which are not present in the spectra obtained. Furthermore, the negative features at 222 and 208 nm, and the positive value for 194 nm correspond to the literature values for α-helical structures in proteins[17]. These peaks are more pronounced in the experimental data than the beta features as alpha-helices absorb more intensely, since the number of residue-residue contacts is higher than strands, making it a more robust structure[18]. The fitting with BeStSel was able to clearly define the beta peaks, where protein concentration and the amino acid count were considered.

The right-twisted β-sheets comprise 10–20 % of folding and left-hand twisted β-sheets are maintained in lower proportions, 1–6%, in both [scGFP] and [scGFP_PlGF2] (Figure 3.4 c,d). This was not surprising, given that right-hand twisted β-sheet have been found to be more stable than left-hand twisted β-sheet, since the right-twist has a lower free-energy[19]. The greater helical structure in [scGFP_PlGF2] is likely due to the addition of the PlGF2 peptide.

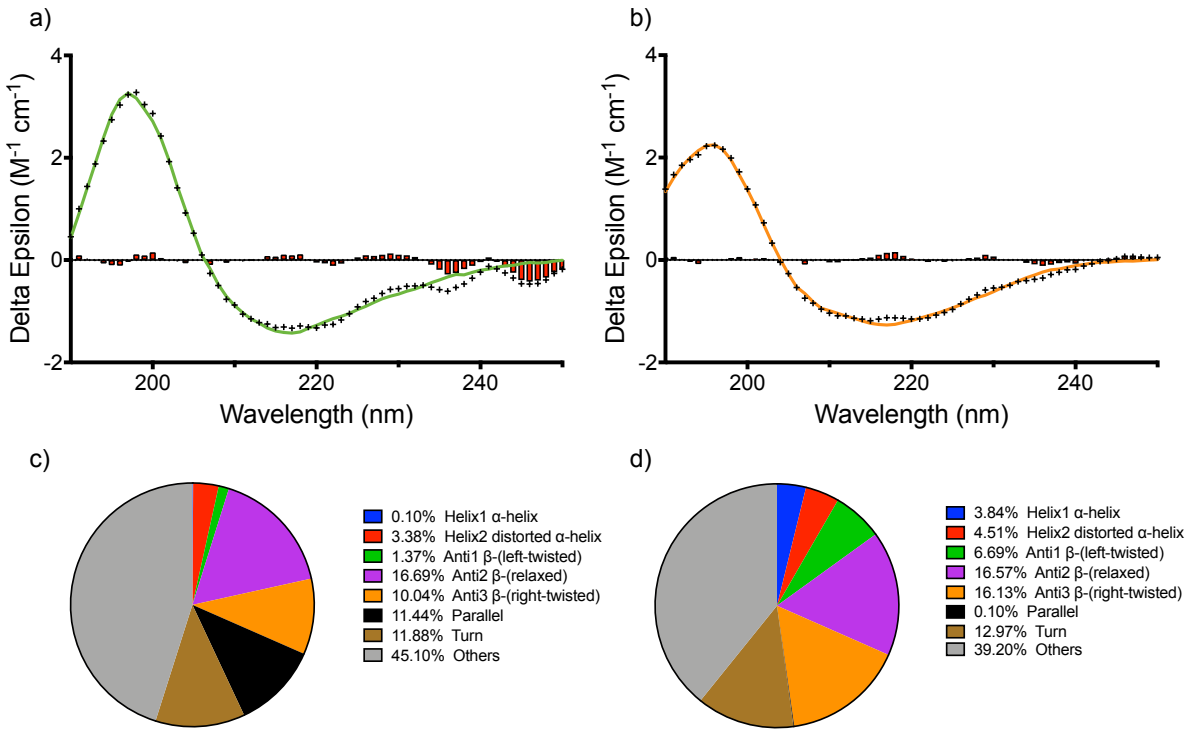

Figure 3.4 Synchrotron radiation circular dichroism spectra. All data was fitted and deconvoluted with BeStSel software. a) Fitted spectrum from [scGFP] (green) and experimental data (black crosses) and residuals (red bars). b) Fitted spectrum and experimental data from [scGFP_PlGF2] (orange) with experimental data (black crosses) and residuals (red bars). c) Secondary structure composition of the [scGFP] CD spectrum deconvoluted. d) Secondary structure composition of the [scGFP_PlGF2] CD spectrum. Measurements were taken at 36°C, at a concentration of 0.35 mg·mL^{-1}.

Lui et al. created +36 scGFP by mutating 29 solvent exposed amino acids on superfolder green fluorescent protein (sfGFP) to cationic lysines and arginines[20]. For this reason, sfGFP was used as a standard to compare with the obtained SRCD spectra of [scGFP] and [scGFP_PlGF2]. The structural composition for sfGFP was calculated from the protein data bank (PDB), accession number 2B3P[21] with BeStSel online tool. However, it should be noted that the data from PDB has been analysed using a defined crystal structure at room temperature, whereas the data obtained was using a liquid protein [scGFP] and [scGFP_PlGF2] at 36°C, with the supercharged proteins containing the multi-histidine tag (Table 3.3).

Table 3.3 Summary of secondary structure for modified green fluorescent proteins. The composition of [scGFP] and [scGFP_PIGF2] are compared to a standard superfolder GFP.

	Predicted %	Measured %	
	sfGFP	scGFP	scGFP_PIGF2
Helix 1 – regular α-helix	0.0	0.1	3.8
Helix 2 – distorted α-helix	1.7	3.4	4.5
Anti 1 – left-twisted β-strand	2.0	1.4	6.7
Anti 2 – relaxed β-strand	27.0	16.7	16.6
Anti 3 – right-twisted β-strand	13.3	10	16.1
Parallel β-strand	4.6	11.4	0.1
Turn	12.3	11.9	13
Others	39.1	45	39.2

No crystal structure of [scGFP] exists, but by comparing the crystal structure of sfGFP with the predicted secondary structure from the PDB[21] and primary sequence of [scGFP], it was found that 5 of the 29 cationic mutations fall into 3_{10}-helix structures. The sfGFP has six of these helices. Thus, the observed increase in the 'others' category, where 3_{10}-helix content is placed, could derive from these mutations disrupting the 3_{10}-helix structures in [scGFP]. Although there are studies that show that the 3_{10}-helix structure can be observed in SCRD with data from 173–260 nm[22], there are also studies that dispute this claim, as truncated data from 185–240 is still able to elucidate the 3_{10}-helix structure[23]. This area of CD still needs to be explored.

The supercharged proteins [scGFP] and [scGFP_PIGF2] were further examined at a range of temperatures to investigate their thermal stability. This was done by taking a measurement at 3-degree intervals from 24 to 90°C, which was the highest possible temperature allowed by the solvent (Figure 3.5).

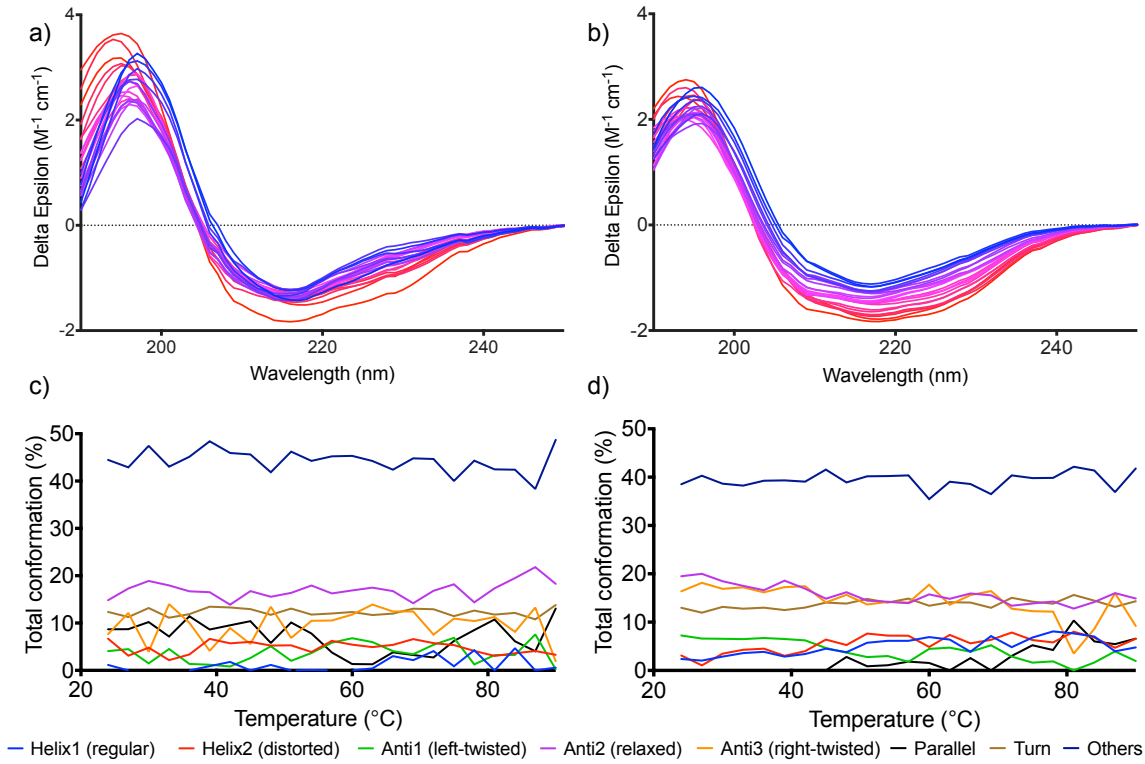

Figure 3.5 Temperature ramp synchrotron radiation circular dichroism spectra. a) Fitted spectra from [scGFP] and b) [scGFP_PlGF2] coloured with a gradient from blue for lower temperatures from 24 to red for temperatures approaching to 90°C. Total conformation percentages across the temperature range are shown for each protein, c) [scGFP] and d) [scGFP_PlGF2]. Data deconvoluted with the BeStSel web service. Measurements were taken at a concentration of 0.35 mg·mL^{-1}.

There was no observable protein denaturation at 90°C or a change in the overall protein structure of [scGFP] compared to [scGFP_PlGF2]. The right-twisted β-sheets comprise 10–20% of folding and left-hand twisted β-sheets are maintained in lower proportions, 5–8%, in both [scGFP] and [scGFP_PlGF2] (Figure 3.5 c,d).

3.2.1.3 Analysis of the tertiary structure of scGFP_PlGF2

UV-vis spectrometry revealed two absorbance peaks in the proteins. The absorbance peak at 280 nm is due to the aromatic amino acids tryptophan and tyrosine in the sequence[24], whereas the peak at 487 nm corresponds to the correct folding of the chromophore present in both [scGFP] and [scGFP_PlGF2], a

tripeptide consisting of the residues threonine (Thr65)[25], tyrosine (Tyr66) and glycine(Gly67)[15] (Figure 3.6).

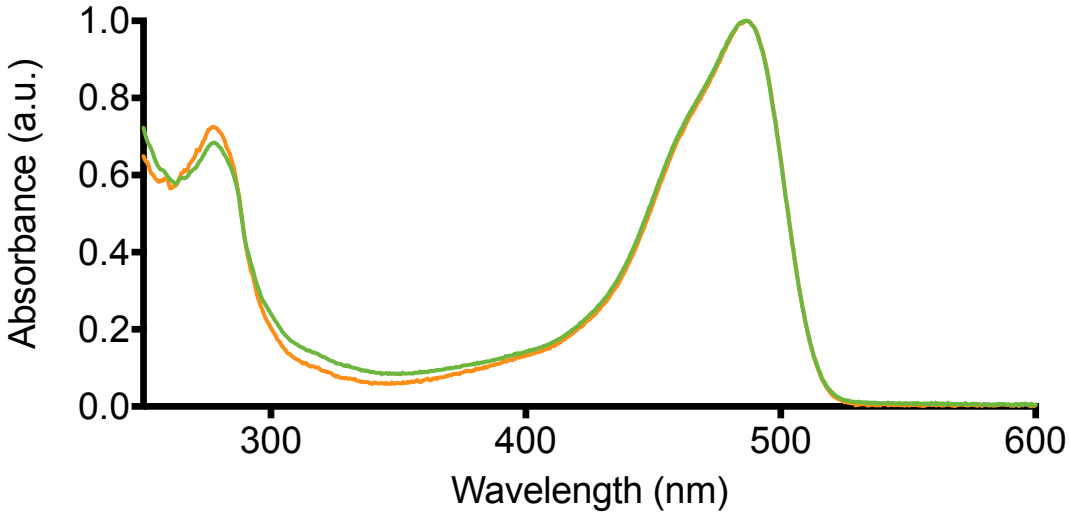

Figure 3.6 UV-vis spectrum of purified [scGFP] (green) and [scGFP_PlGF2] (orange). Measurements were taken in buffer 400 mM sodium chloride, 20 mM Tris.HCl at pH 7.5.

There was no observable difference between the two different protein constructs at 487 nm, indicating that the folding and maturation of the fluorophore remained unchanged when the GFP is expressed with the fused PlGF2-123–144-peptide on the C terminus. A small increase in the 280 nm region is observed for [scGFP_PlGF2], this might be due to the presence of small traces of imidazole (which also absorbs at 280) in the buffer, small amounts of protein aggregates at the time of measurement, or the due to the presence of lysine or glutamic acid in the peptide PlGF2_123-144[26].

A key benefit of using GFP is that it fluoresces when it is correctly folded, and it is excited with blue light. Both [scGFP] and [scGFP_PlGF2] absorbed 487 nm light, and emit light at 511 nm, which is consistent with previous Stokes shift values reported in the literature for scGFP[14] (Figure 3.7). This is evidence that when expressing the protein with the fused peptide, [scGFP_PlGF2], the fluorescent properties of [scGFP] remain unchanged.

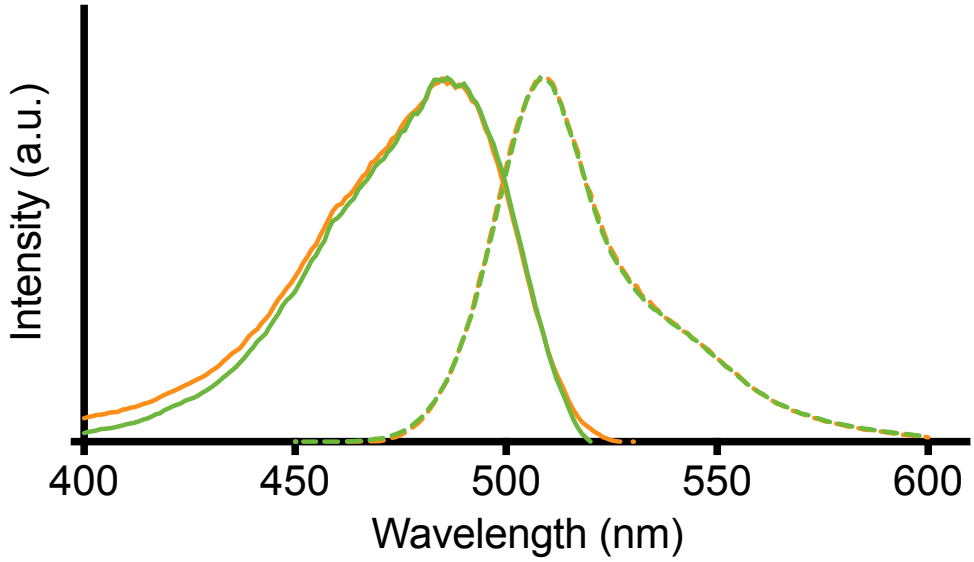

Figure 3.7 Fluorescence emission and excitation peaks at 10 µM concentration. [scGFP] (green solid trace) and [scGFP_PlGF2] (orange solid trace) both peak at 487 nm for excitation and at 511 nm for emission (dashed lines). Measurements were taken in buffer 400 mM NaCl and 20 mM Tris.HCl pH 7.5.

Dynamic light scattering (DLS) measurements were carried out in triplicate to determine the hydrodynamic diameter of the purified proteins (Figure 3.8). The average hydrodynamic diameter of [scGFP] was 4.6±0.3 nm, whilst [scGFP_PlGF2] resulted in an average hydrodynamic diameter of 5.6±0.7 nm. Size and errors were calculated by fitting a non-linear gaussian function and combining the standard deviation of the fit and the measurements. The diameter of [scGFP] and [scGFP_PlGF2] are within error of the green fluorescent protein barrel structure, which is known to be 4.2 nm × 2.4 nm[27], although values of 4 nm × 2.5 nm have also been reported[15]. The difference in size between [scGFP_PlGF2] and [scGFP] of approximately 1 nm is most likely due to the presence of the 21 amino acid peptide chain. DLS particle sizing for number distribution measurements assume that all particles are spherical and that the refractive index of the particles are known[28].

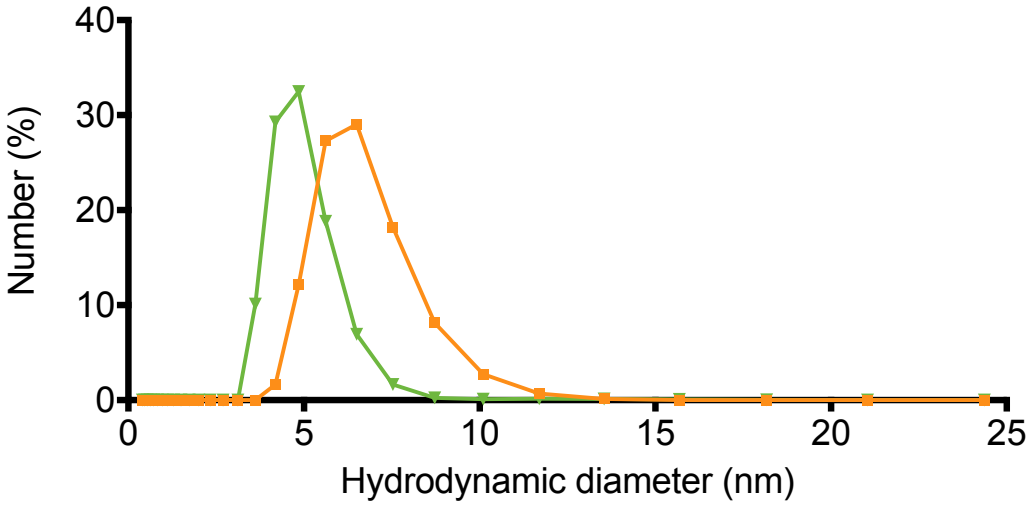

Figure 3.8 Hydrodynamic diameter size distribution obtained with dynamic light scattering. The number percentage measurement was averaged for [scGFP] (green trace) [scGFP_PlGF2] (orange trace). Three successive measurements were taken at a 37°C.

Small angle x-ray scattering (SAXS) was used to understand the conformational tertiary structure in space of [scGFP] (Figure 3.9) and [scGFP_PlGF2] (Figure 3.10). This was performed using in-line size exclusion chromatography at Diamond Light Source on the B21 beamline. For details about the SAXS experiment, please refer to section 2.4.9. The obtained structural parameters are summarised in Table 3.4.

Table 3.4 Summarised parameters obtained from small angle x-ray scattering for [scGFP] and [scGFP_PlGF2].

Structural parameters	[scGFP]	[scGFP_PlGF2]
R_g (Å) [from P(r)]	25.2	28.1
Molecular mass M_r [from I(0)]	24 kDa	35 kDa

The size data was consistent with the values obtained from DLS, with an increase of approximately 6 angstroms in diameter which might be the contribution from the PlGF2 peptide in [scGFP_PlGF2]. The calculated molecular mass for the proteins was also within 10% of the previously obtained value with MALDI-TOF. The

difference in the mass could be due to the quality of the data obtained and the software analysis.

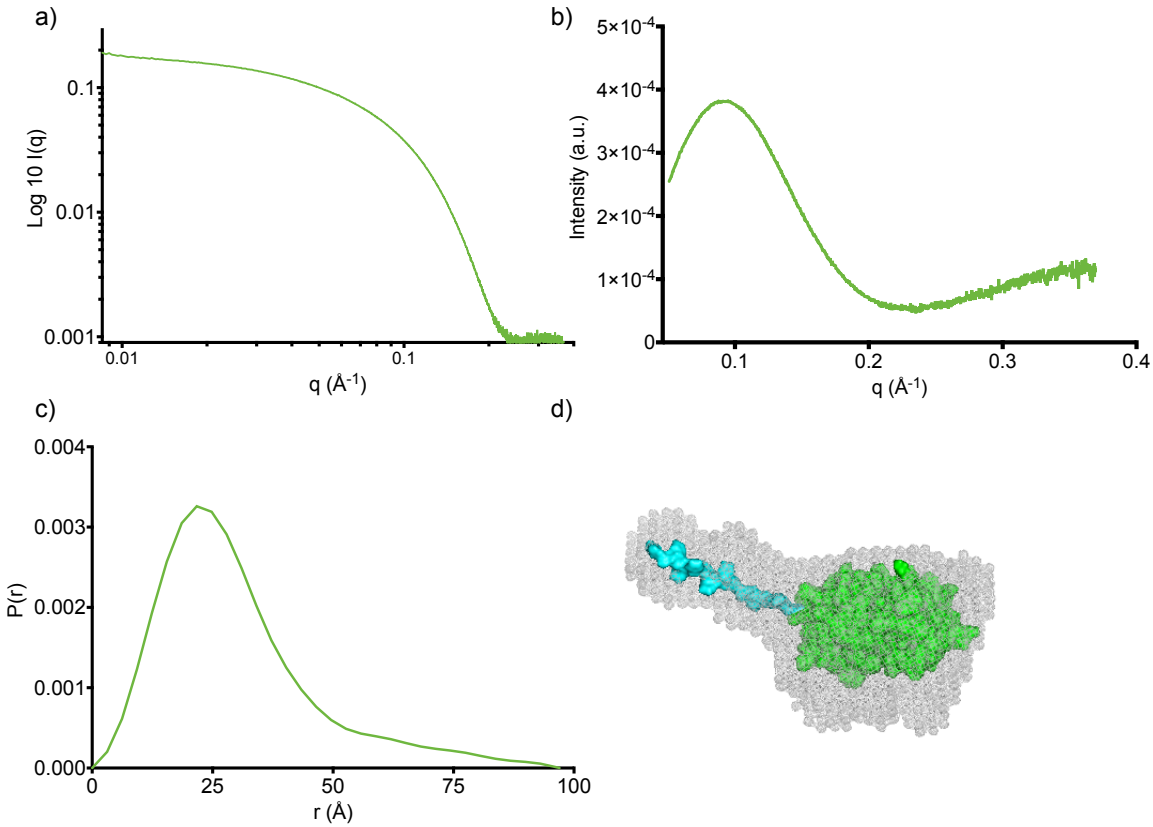

Figure 3.9 Small angle scattering (SAXS) data obtained for [scGFP]. a) SAXS scattering curve after buffer subtraction. b) Kratky plot demonstrated flexibility in the construct. c) The radial probability distribution of the protein. d) PyMOL bead model obtained for [scGFP] compared to crystal structure from superfolder GFP 2b2p and manually added multi-histidine tag in blue.

The Kratky plot indicates a compact protein containing a flexible component[29], which could be attributed to the multi-histidine tag fused to the protein for purification. The Porod exponent is used as an indication of the flexibility of structures: a Porod exponent of 2 corresponds to a highly flexible structure, whereas a value of 4 is indicative of inflexibility[30]. In this case, the resulting Porod exponent was calculated to be 2.4, indication of the presence of a flexible molecule. Additionally, a bead model obtained with EMBL DAMMIF online service[31] showed an overlap with the sfGFP crystal structure (Figure 3.9 d) and added hexa-histidine

tag. This was done by manually editing the primary sequence in PyMOL to obtain the desired chain.

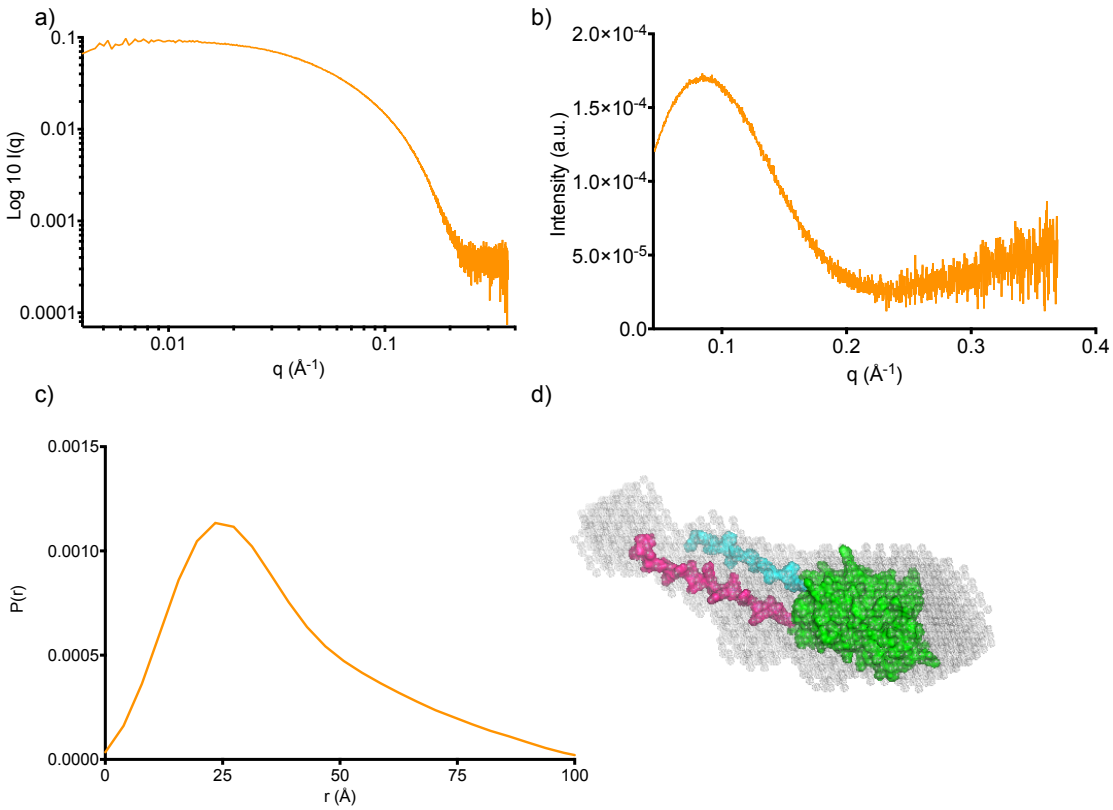

Figure 3.10 Small angle scattering (SAXS) data obtained for [scGFP_PIGF2]. a) SAXS scattering curve after buffer subtraction. b) Kratky plot demonstrating flexibility in the construct. c) The radial probability distribution of the protein. d) PyMOL bead model obtained for [scGFP_PIGF2] compared to crystal structure from superfolder GFP 2b3p and manually added multi-histidine tag in blue.

The results for [scGFP_PIGF2] did not differ considerably from [scGFP]. It did show a larger radius of gyration, which is likely due to the presence of the peptide. This construct was also shown to be flexible, according to the Kratky plot shape. However, the Porod exponent for [scGFP_PIGF2] was calculated to 2.6, which could be indicative of increased rigidity from the fused peptide. The resulting bead model correlated well with the adapted sfGFP structure with the manually added peptide chain and histidine tag (Figure 3.10 d). This was done by manually editing the sequence in PyMOL to obtain the desired chains.

3.2.2 Synthesis of the protein-polymer surfactant nanobiohybrid [scGFP_PlGF2][S]

An oxidised form of IGEPAL co-890 ([S]) was synthesised in order to create an anionic surfactant that could electrostatically conjugate with the positive residues present on the surface of [scGFP_PlGF2] (Figure 3.11). The hydrophilic head group is followed by an amphiphilic polyethylene glycol (n=39) and a hydrophobic nonyl phenyl tail Figure 3.11). For detailed information about the surfactant synthesis and characterisation, please refer to Appendix D.

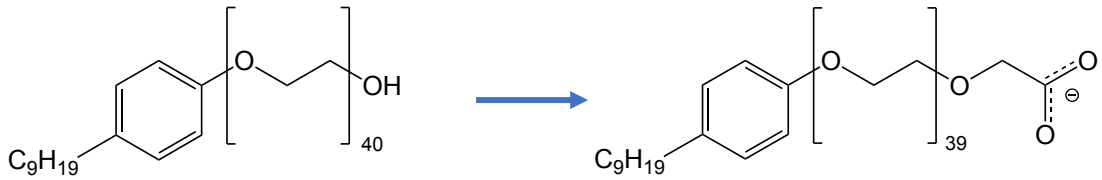

Figure 3.11 Representation of IGEPAL co-890 change after oxidation. The native surfactant IGEPAL co-890 (left) is oxidised to obtain the oxidised version presenting a carboxylic acid at the end (right).

The [scGFP_PlGF2], was conjugated with oxidised IGEPAL co-890 to form [scGFP_PlGF2][S]. This was facilitated by electrostatic interactions between the anionic carboxylic acid of the oxidised IGEPAL co-890 and the 66 cationic residues in [scGFP_PlGF2] to form a stable conjugate. Spectroscopic characterisation was carried out to determine the nature of the secondary and tertiary structure of [scGFP_PlGF2][S].

To quantify the stoichiometry of the oxidised surfactant with [scGFP_PlGF2] to form [scGFP_PlGF2][S], a UV-vis spectrum was taken before and after conjugation (Figure 3.12).

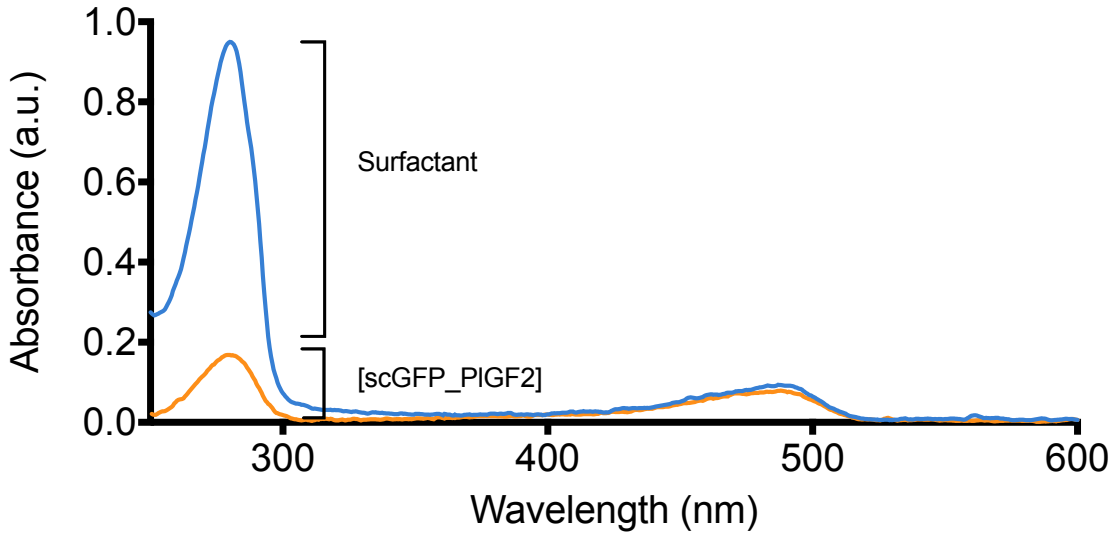

Figure 3.12 UV-vis spectrum of [scGFP_PIGF2] before surfactant addition (orange) and [scGFP_PIGF2][S] (blue). The increased absorption at 280 nm is contribution of the surfactant IGEPAL co-890. Measurements were taken in buffer 400 mM sodium chloride, 20 mM Tris.HCl in pH 7.5.

The difference in absorbance between the two peaks was used to calculate the amount of surfactant bound to each positive residue present in the protein (Sr) using Equation 2.4 (section 2.6.1).

$$Sr = \frac{P_n \times 66}{C_n - P_n} \qquad \textit{Equation 2.4}$$

Where C_n is the number of molecules calculated for [scGFP_PIGF2[S] and P_n is the number of molecules calculated for [scGFP_PIGF2], multiplied by the number of positive residues present in [scGFP_PIGF2], 66. The ratio was determined to be 1.27 surfactant molecules per positive residue, which implied the presence of hydrophobically-driven interactions (in addition to electrostatic) at the surface of the protein, as the dynamic surfactant tail could be interacting with hydrophobic amino acids in the scGFP domain.

3.2.2.1 Analysis of the secondary structure of [scGFP_PlGF2][S]

Some surfactants have the ability to disrupt tertiary and secondary structure of proteins[32]. Therefore, it was necessary to fully characterise the structure of this new hybrid structure to assess the maintenance of structural properties.

To confirm that the secondary structure of [scGFP_PlGF2] was not affected by the addition of the synthetic polymer surfactant, SRCD analysis was performed at Diamond light source on the B23 beamline. The obtained data was deconvoluted and converted from millidegrees to delta epsilon values using the beta-structure selection algorithm (BeStSel)[12] with the same parameters used for [scGFP] and [scGFP_PlGF2] as above section 3.2.1.2 (Table 3.2). From these data (Figure 3.13) it can be observed that there was no significant protein denaturation, as the secondary structure parameters were maintained, as described in section 3.2.1.2. However, there was some evidence of beta to alpha structuration, which may result from changes in the local dielectric constant, which is brought about by the amphiphilic polymer surfactant corona. The deconvoluted values for [scGFP_PlGF2] and [scGFP_PlGF2][S] structures were compared to the DSSP values of sfGFP[20] (Table 3.5).

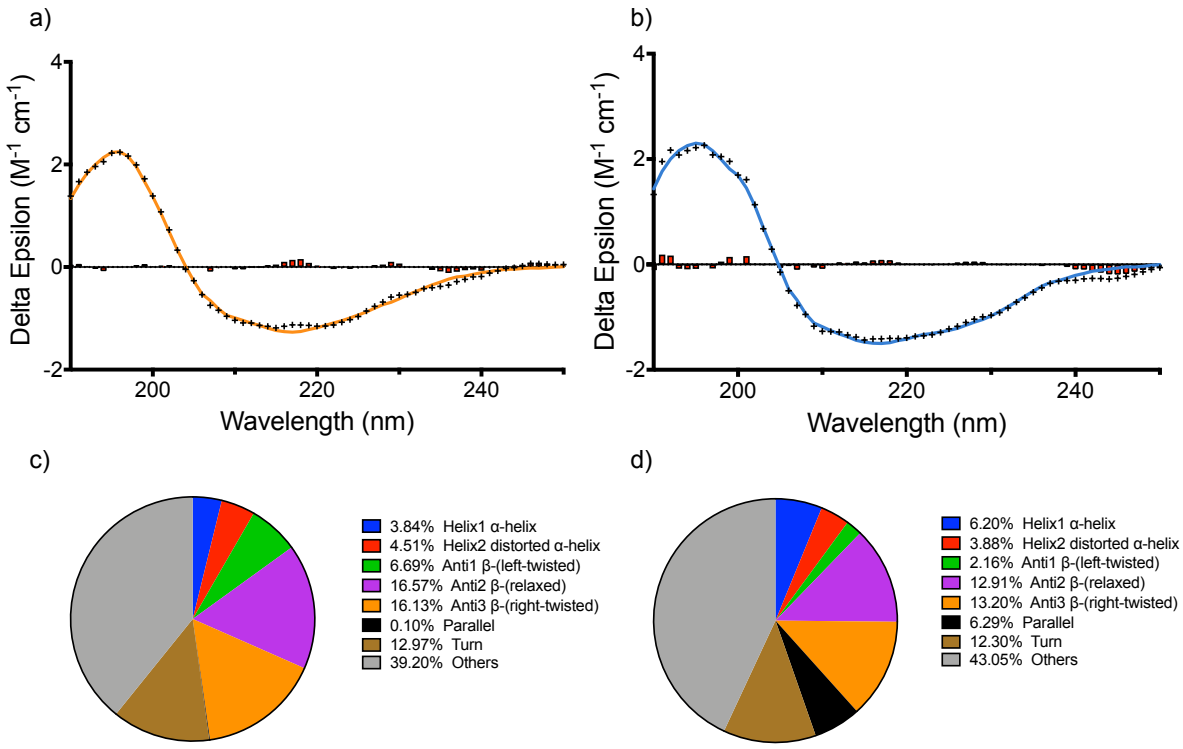

Figure 3.13 Synchrotron radiation circular dichroism spectra. All data was fitted and deconvoluted with BeStSel software. a) Fitted spectrum from [scGFP_PIGF2] (orange) with experimental data (black crosses) and residuals (red bars). b) Fitted spectrum from [scGFP_PIGF2][S] (blue) with experimental data (black crosses) and residuals (red bars). c) Secondary structure composition of the [scGFP_PIGF2] CD spectrum deconvoluted, d) Secondary structure composition of the [scGFP_PIGF2][S] CD spectrum deconvoluted. Measurements were taken at 36°C at a concentration of 0.35 mg·mL^{-1}.

Table 3.5 Summary of secondary structure for modified green fluorescent proteins. The composition of [scGFP_PIGF2] and [scGFP_PIGF2][S] are compared to a standard superfolder GFP.

	Predicted %	Measured %	
	Superfolder GFP	[scGFP_PIGF2]	[scGFP_PIGF2][S]
α-helix	10	8.3	10.1
β-strand	47	39.4	34.6
Turn	12	13	12.3
Others	31	39.2	43

The [scGFP_PIGF2] and [scGFP_PIGF2][S] proteins were examined at increasing temperatures from 24 to 90°C, to elucidate whether the addition of the polymer surfactant compromised the protein structure at high temperatures (Figure 3.14).

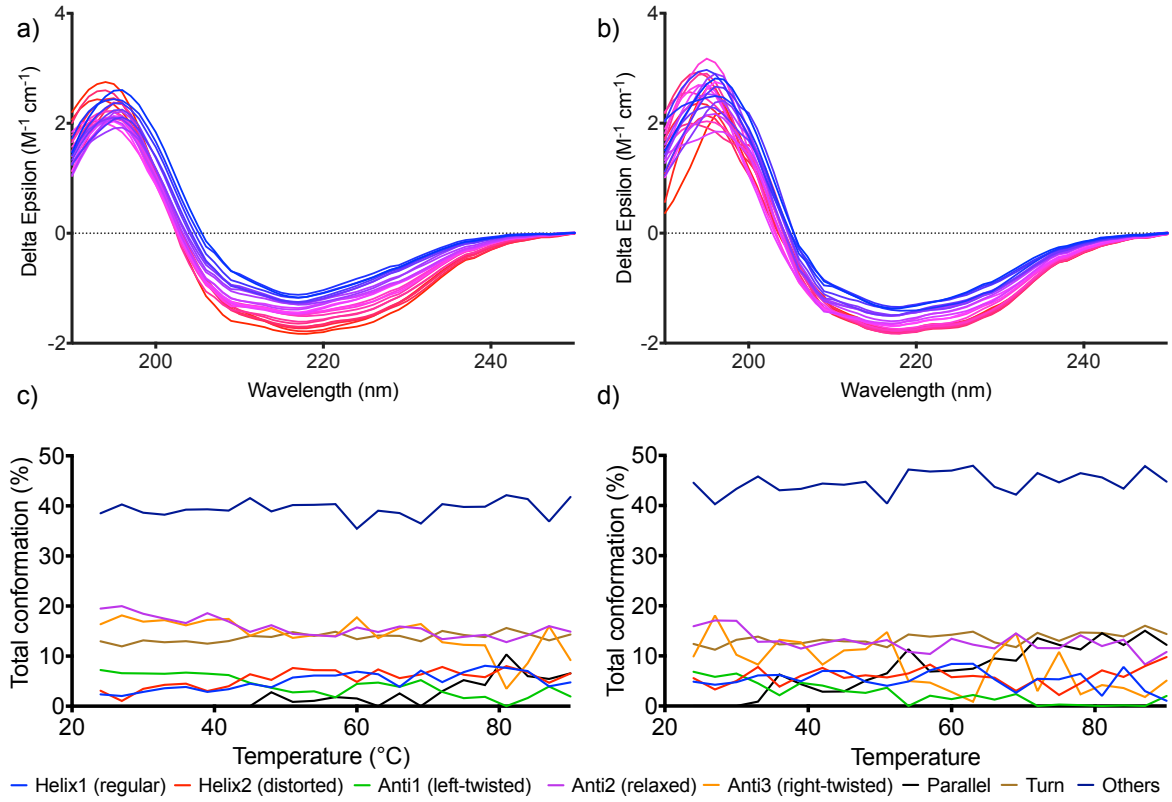

Figure 3.14 Temperature ramp synchrotron radiation circular dichroism spectra. a) Fitted spectra from [scGFP_PlGF2] and b) [scGFP_PlGF2][S] coloured with a gradient from blue for lower temperatures from 24 to red for temperatures approaching to 90°C. Total conformation percentages across the temperature range are shown for each construct, c) [scGFP_PlGF2] and d) [scGFP_PlGF2][S]. Data deconvoluted with the BeStSel web service. Measurements were taken at a concentration of 0.35 mg·mL^{-1}.

There was no observable protein denaturation at 90°C or significant change in the overall protein structure between [scGFP_PlGF2] and [scGFP_PlGF2][S]. This confirms that the polymer surfactant does not affect the thermal stability of [scGFP_PlGF2].

The preservation of the secondary structure and function of [scGFP_PlGF2][S] could be explained with the 39 PEG chains present in the oxidised surfactant[33], since surfactants containing alkyl chains alone tend to promote protein denaturation by disrupting non-covalent protein bonds and binding to the most hydrophobic side of the protein[34,35]. In this case, the PEG units act to bury the

hydrophobic chain[6], preventing denaturation making [scGFP_PlGF2][S] soluble in aqueous solvents. These findings also suggest that this anionic surfactant has the ability to form compact monolayers around proteins as predicted before by molecular dynamics[36].

3.2.2.2 Analysis of the tertiary structure of [scGFP_PlGF2][S]

To assess the effect of the conjugation on the folding of the tertiary structure, [scGFP_PlGF2] and [scGFP_PlGF2][S] were submitted to fluorescence spectroscopy. The absorption of both constructs was observed at 487 nm and the emission peak was at 511 nm, which is consistent with previous stokes shift values related to scGFP[14] and the experimentally derived values obtained above (section 3.2.1.3). The only observable difference is an increase in the fluorescence intensity of [scGFP_PlGF2][S], which could be due to the presence of the surfactant.

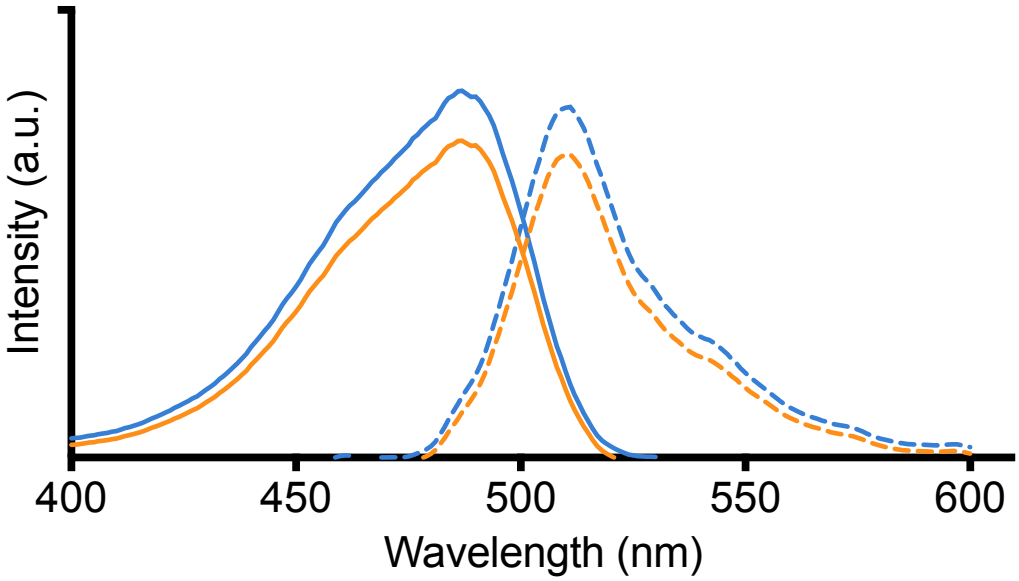

Figure 3.15 Fluorescence emission and excitation spectra. The excitation of [scGFP_PIGF2] (orange solid trace) and [scGFP_PIGF2][S] (blue solid trace) both peak at 487 nm, and the emission peak at 511 nm respectively (dashed lines). Measurements were taken in buffer 400 mM NaCl and 20 mM Tris.HCl pH 7.5.

The average hydrodynamic diameter increased from 5.6±0.7 nm to 8.3±0.3 nm after addition of [S]. This corresponds to a polymer surfactant corona of approximately 1.35 nm encapsulating the protein, which is consistent with dimensions reported for cationized protein-polymer surfactant analogous[33] (Figure 3.16). All measurements were done in triplicate. Size and errors were calculated by fitting a non-linear gaussian function and combining the standard deviation of the fit and the measurements.

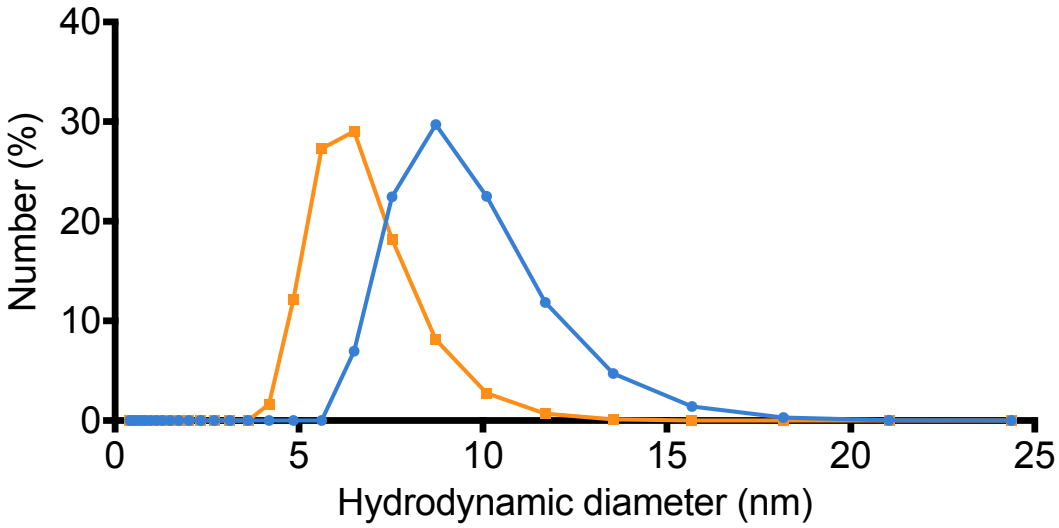

Figure 3.16 Hydrodynamic diameter size distribution obtained with dynamic light scattering. The number percentage measurement was averaged for [scGFP_PlGF2] (orange trace) and [scGFP_PlGF2][S] (blue trace). Three successive measurements were taken at a 37°C.

Zeta potentiometry was used to determine the electric potential for the native [scGFP_PlGF2] and conjugated [scGFP_PlGF2][S] at pH 7.5, which had an average surface charge of 21±0.8 mV and -0.5±0.5 mV, respectively. The positive charge is expected due to the positive charge of the solvent exposed cationic residues in [scGFP_PlGF2] sequence, lysine and arginine[14]. It is also important to state that the protein is in a pH lower than the previously calculated isoelectric point, 10.63 with the online tool Protein Calculator v3.4 (Appendix B). The neutral charge in [scGFP_PlGF2][S] was indication that oxidised IGEPAL co-890 was electrostatically bound to the [scGFP_PlGF2] positive sites, making the overall charge close to zero.

3.3 Chapter conclusions

In this chapter, the synthesis and characterisation of a novel biohybrid was discussed. Crucially, CD, DLS and SAXS analysis showed that the recombinant attachment of the PIGF2 peptide sequence to supercharged GFP did not have a detrimental effect upon protein folding conformation or optical properties. Furthermore, fluorescence spectrophotometry and CD showed no observable change between [scGFP_PlGF2] and the surfactant conjugate [scGFP_PlGF2][S], while DLS analysis showed an increase in the radius consistent with the presence of a compact polymer surfactant corona.

3.4 Further work

Small angle neutron scattering (SANS) could be performed to [scGFP_PlGF2] and [scGFP_PlGF2][S], to gain an understanding of the distribution of the surfactant corona around the protein by contrast. Here contrast variation SANS experiments could be performed using deuterated surfactants to provide more detailed structural information of the polymer surfactant corona.

Obtaining the crystal structure of supercharged proteins, although ambitious (supercharged proteins are difficult to crystallise due to their inherent resistance to aggregation), would give a better understanding of the effects of mutations carried out on superfolder GFP. This could determine if the helices that are mutated are still correctly folded in the structure. The sfGFP has also been mutated to change the most solvent exposed residues to negative amino acids. It could be interesting to explore if a negatively-supercharged protein is able to form conjugates with a cationic surfactant and if its structure is retained.

3.5 Bibliography

1. Brochette, P., Petit, / C & Pileni, P. Cytochrome c in Sodium Bis(2-ethylhexyl) Sulfosuccinate Reverse Micelles: Structure and Reactivity. J. Phys. Chem **92,** (1988).

2. Zhang, Y., Patil, A. J., Perriman, A. W. & Mann, S. Enhanced catalytic activity in organic solvents using molecularly dispersed haemoglobin-polymer surfactant constructs. Chem. Commun. **49,** 9561–9563 (2013).

3. Caliceti, P. & Veronese, F. M. Pharmacokinetic and biodistribution properties of poly(ethylene glycol)-protein conjugates. Adv. Drug Deliv. Rev. **55,** 1261–1277 (2003).

4. Jones, M. N. Surfactant interactions with biomembranes and proteins. Chem. Soc. Rev. **21,** 127 (1992).

5. Yonath, A., Sielecki, A., Moult, J., Podjarny, A. & Traub, W. Crystallographic Studies of Protein Denaturation and Renaturation. 1. Effects of Denaturants on Volume and X-ray Pattern of Cross-Linked Triclinic Lysozyme Crystals. Biochemistry **16,** 1413–1417 (1977).

6. Armstrong, J. P. K. et al. Artificial membrane-binding proteins stimulate oxygenation of stem cells during engineering of large cartilage tissue. Nat. Commun. **6,** 7405 (2015).

7. Brogan, A. P. S., Siligardi, G., Hussain, R., Perriman, A. W. & Mann, S. Hyper-thermal stability and unprecedented re-folding of solvent-free liquid myoglobin. Chem. Sci. **3,** 1839 (2012).

8. Pérez, B. et al. Insight into the molecular mechanism behind PEG-mediated stabilization of biofluid lipases. Sci. Rep. **8,** 12293 (2018).

9. Gallat, F.-X. et al. A polymer surfactant corona dynamically replaces water in solvent-free protein liquids and ensures macromolecular flexibility and activity. J. Am. Chem. Soc. **134,** 13168–71 (2012).

10. Perriman, A. W., Cölfen, H., Hughes, R. W., Barrie, C. L. & Mann, S. Solvent-Free Protein Liquids and Liquid Crystals. Angew. Chemie **121,** 6360–6364 (2009).

11. Otzen, D. E. & Oliveberg, M. Burst-phase expansion of native protein prior to global unfolding in SDS. J. Mol. Biol. **315,** 1231–1240 (2002).

12. Micsonai, A. et al. Accurate secondary structure prediction and fold recognition for circular dichroism spectroscopy. PNAS **112,** E3095–E3103 (2015).

13. Greenfield, N. J. & Fasman, G. D. Computed Circular Dichroism Spectra for the Evaluation of Protein Conformation. Biochemistry **8,** 4108 (1969).

14. Lawrence, M. S., Phillips, K. J. & Liu, D. R. Supercharging proteins can impart unusual resilience. J. Am. Chem. Soc. **129,** 10110–2 (2007).

15. Day, R. N. & Davidson, M. W. The fluorescent protein palette: tools for cellular imaging. Chem. Soc. Rev. **38,** 2887–921 (2009).

16. Chang, C. T., Wu, C. S. C. & Yang, J. T. Circular dichroic analysis of protein conformation: Inclusion of the β-turns. Anal. Biochem. **91,** 13–31 (1978).

17. Holzwarth, G. & Doty, P. The Ultraviolet Circular Dichroism of Polypeptides. J. Am. Chem. Soc. **87,** 218–228 (1965).

18. Abrusán, G. & Marsh, J. A. Alpha Helices Are More Robust to Mutations than Beta Strands. PLoS Comput. Biol. **12,** e1005242 (2016).

19. Chothia, C. Conformation of twisted β-pleated sheets in proteins. J. Mol. Biol. **75,** 295–302 (1973).

20. Pédelacq, J. D., Cabantous, S., Tran, T., Terwilliger, T. C. & Waldo, G. S. Engineering and characterization of a superfolder green fluorescent protein. Nat. Biotechnol. **24,** 79–88 (2006).

21. Kabsch, W. & Sander, C. Dictionary of protein secondary structure: Pattern recognition of hydrogen-bonded and geometrical features. Biopolymers **22,** 2577–2637 (1983).

22. Venyaminov, S. Y., Baikalov, I. A., Wu, C. S. C. & Yang, J. T. Some problems of CD analyses of protein conformation. Anal. Biochem. **198,** 250–255 (1991).

23. Sreerama, N., Venyaminov, S. Y. U. & Woody, R. W. Estimation of the number of α-helical and β-strand segments in proteins using circular dichroism spectroscopy. Protein Sci. **8,** 370–380 (2008).

24. Schmid, F. in Encyclopedia of Life Sciences 1–4 (John Wiley & Sons, Ltd, 2001). doi:10.1038/npg.els.0003142

25. Heim, R., Cubitt, A. B. & Tsien, R. Y. Improved green fluorescence. Nature **373,** 663–664 (1995).

26. Prasad, S. et al. Near UV-Visible electronic absorption originating from charged amino acids in a monomeric protein. Chem. Sci. **8,** 5416–5433 (2017).

27. Orm, M. et al. Crystal Structure of the Aequorea victoria Green Fluorescent Protein. Science (80-.). **273,** 1392–1395 (1996).

28. Stetefeld, J., McKenna, S. A. & Patel, T. R. Dynamic light scattering: a practical guide and applications in biomedical sciences. Biophysical Reviews **8,** 409–427 (2016).

29. Skou, S., Gillilan, R. E. & Ando, N. Synchrotron-based small-angle X-ray scattering of proteins in solution. Nat. Protoc. **9,** 1727–1739 (2014).

30. Reyes, F. E., Schwartz, C. R., Tainer, J. A. & Rambo, R. P. Methods for using new conceptual tools and parameters to assess RNA structure by small-angle X-ray scattering. Methods Enzymol. **549,** 235–263 (2014).

31. Franke, D. & Svergun, D. I. DAMMIF, a program for rapid ab-initio shape determination in small-angle scattering. J. Appl. Crystallogr. **42,** 342–346 (2009).

32. Loo, R. R. O., Dales, N. & Andrews, P. C. Surfactant effects on protein structure examined by electrospray ionization mass spectrometry. Protein Sci. **3,** 1975–1983 (1994).

33. Perriman, A. W. et al. Reversible dioxygen binding in solvent-free liquid myoglobin. Nat. Chem. **2,** 622–626 (2010).

34. Andersen, K. K. et al. The Role of Decorated SDS Micelles in Sub-CMC Protein Denaturation and Association. J. Mol. Biol. **391,** 207–226 (2009).

35. Bhuyan, A. K. On the mechanism of SDS-induced protein denaturation. Biopolymers **93,** 186–199 (2010).

36. Brogan, A. P. S., Sessions, R. B., Perriman, A. W. & Mann, S. Molecular dynamics simulations reveal a dielectric-responsive coronal structure in protein-polymer surfactant hybrid nanoconstructs. J. Am. Chem. Soc. **136,** 16824–16831 (2014).

Chapter 4

Stem Cell Surface Functionalisation

4.1 Introduction

4.1.1 The cell membrane

The cell membrane has long been an important focus of study. It is the barrier that separates the cell from its environment, allowing the transport of nutrients essential for cell survival, and at the same time preventing it from any damage that can be caused by exogenous materials. The cell membrane has been characterised as a lipid structure[1]. In 1972 Singer and Nicholson made the most iconic representation to interpret the cell membrane, the fluid mosaic model[2], which has since served as a platform to interpret the lipid bilayer. This model takes into account the most predominant force that holds the membrane together: hydrophobic interactions[3] (Figure 4.1).

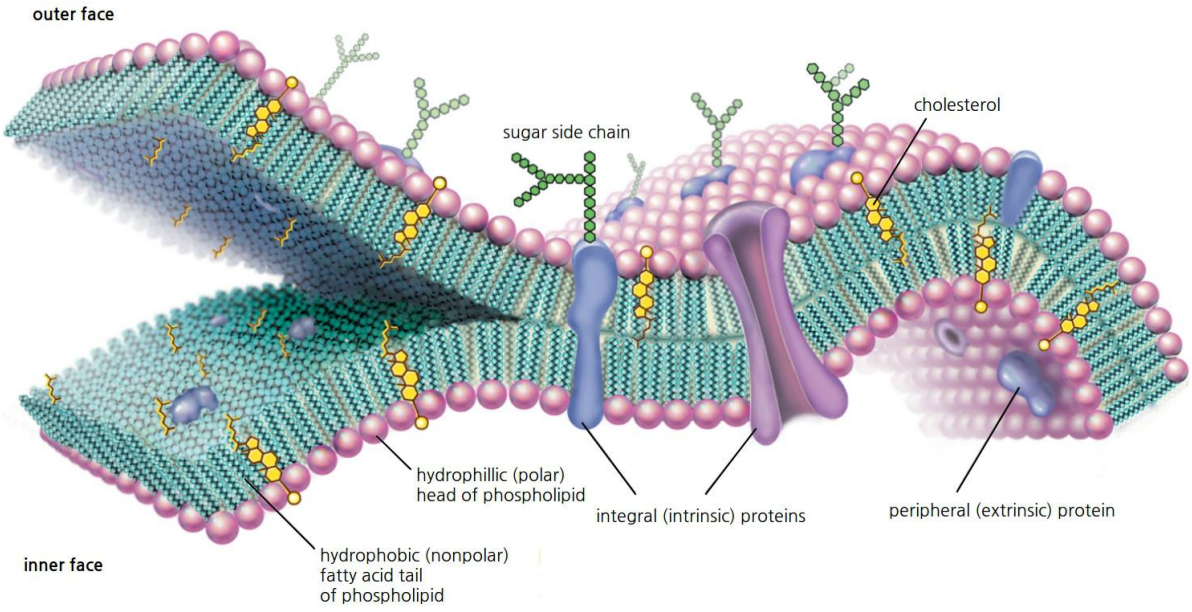

Figure 4.1 Adaptation from the lipid-globular mosaic fluid membrane model. In this cross-sectional image, the lipids are shown in a variety of colours representing the hydrophobic heads towards the outside while the hydrophilic tails face the inside, with globular integral proteins and fatty acid chains and glycoproteins. Reproduced from Encyclopaedia Britannica[4]

The study of the interactions between the cell membrane and its environment, such as cell-cell, cell substrate, and cell-environment are of high importance. These interactions can be exploited in order to further improve cell therapies. Presently, it has been estimated that there are 500–1000 different proteins on the cell surface[5]. These lipids and proteins have a direct effect on the function of the membrane, and also inside of the cell. Additionally, the cell membrane possesses a layer of glycoproteins (mainly sulphated) on the outer layer called the glycocalyx, which allows the cell to interact with the external environment changing cell permeability[6]. Importantly, the glycocalyx has a negative charge.

The bilayer is a very dynamic interface containing a large amount of proteins, lipids, polysaccharides, and fatty acids, interacting with the environment in different manners, and modification of it may have an impact in cell behaviour, viscosity, stiffness, elasticity, and dynamics.

4.1.2 Stem cell modification

Mesenchymal stem cells have broad utility due to their multilineage potential, ability to proliferate *in vitro,* and their relative facile accessibility[7]. However, there are a number of issues that need to be addressed to enhance stem cell therapies and tissue engineering, such as adhesion, rapid proliferation and differentiation, which may require the modification of cells.

One of the approaches carried out to enhance cell properties is gene modification, which consists on transfecting the cells with new genetic material using, for example, viral vectors[8] or lipofection[8]. However, this requires extensive experimentation and handling. Furthermore, cultured stem cells tend to mutate if they are cultured for long periods of time[9].

Another technique is functionalisation of the cell membrane which, in contrast, offers a less invasive approach which may lead to a faster translation for *in vivo* therapies. Different methods have been explored to functionalise cells with lipids[10], amino acids[11], cytokines[12], antibodies[13], and nanoparticles[14], to mention a few. Cell wall turnover, which is the enzymatic process for removal of fragments from the lipidic bilayer structure[15] should be taken into consideration when modifying membranes.

In order to decorate the outside of the cell, covalent modifications have been made to the membrane to attach functional groups that can subsequently interact with other particles or antibodies[13]. Cationic species added in the surrounding media to electrostatically bind molecules to the negatively charged cell membrane have also been studied. Another strategy is to make use of the hydrophobic interactions to anchor lipid tails bound to exogenous particles into the phospholipid bilayer[16].

For instance, in 1991 Kim and Peacock[17] used palmitate-conjugate protein A to anchor antibodies onto the membrane lipidic bilayer. This technique has been further use to anchor and target specific antibodies for chondrogenic cells in cartilage[18] and to provoke anti-tumour responses[19].

Regardless of the technique used, there needs to be a compromise between modifying the surface enough to have a positive effect, but without having an impact on the natural properties of the cell. The main factors that need to be maintained in the design of surface modification of stem cells are viability, proliferation, and differentiation.

In this chapter, the effects of modifying stem cell membranes with proteins and protein–surfactant conjugates are assessed, including cytotoxicity, proliferation and differentiation. Furthermore, the affinity of the constructs for cell membranes,

and their localisation over time is determined with light microscopy and flow cytometry.

4.2 Results and discussion

4.2.1 Measuring the viability of stem cells

Modifying the membrane of human mesenchymal stem cells (hMSCs) with proteins and protein–surfactant conjugates could lead to cell damage or death due to disruption of membrane structure or function. Cell metabolism has been widely used as a marker for viable cells[20]. Accordingly, the viability of functionalised cells was assessed using the 3-(4,5-dimethylthiazol-2-yl)-5-(3-carboxymethoxyphenyl)-2-(4-sulfophenyl)-2H-tetrazolium (MTS) colorimetric assay, which measures the rate of metabolism of MTS into formazan by breaking a nitrogen-nitrogen bond. The cytotoxicity of [scGFP_PlGF2] and [scGFP_PlGF2][S] was shown to be dependent on the incubation concentration for either construct (Figure 4.2). In this experiment, the viability was normalised to the negative control as a 100% rate survival.

The results showed that after 15-minute incubation, concentrations of 12 μM and above, for both native protein and the conjugate, were linked to a significant decrease on cell viability. Accordingly, all subsequent experiments were carried out using a 4 μM protein concentration for both [scGFP_PlGF2] and [scGFP_PlGF2][S]. Studies have revealed that cationic polyplexes might interfere with the regular cell metabolism[21], however, the exact mechanism has not yet been determined[22].

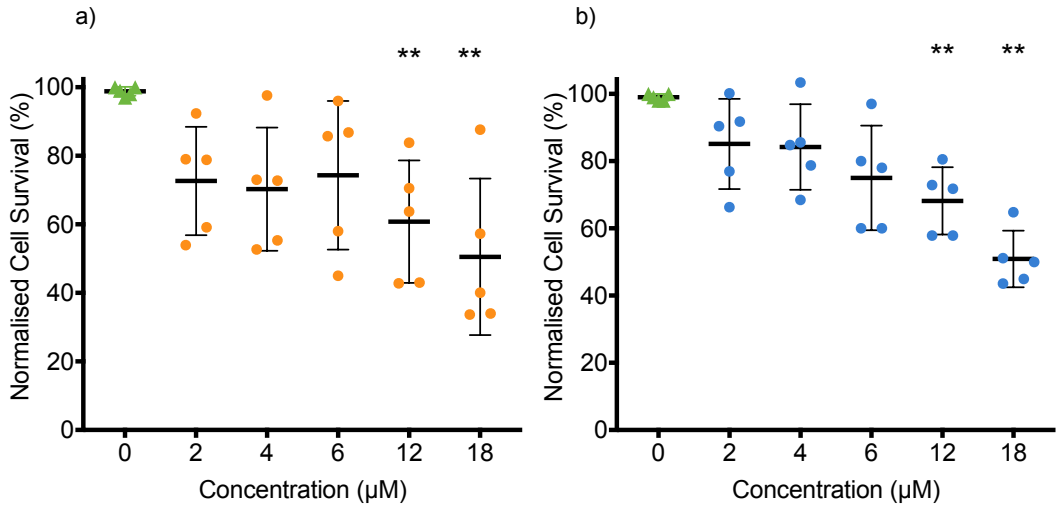

Figure 4.2 Cytotoxicity effects of [scGFP_PlGF2] and [scGFP_PlGF2][S] on human mesenchymal stem cells (hMSCs). The viability of hMSCs was measured by assessing the cell metabolism of MTS into formazan. The data was normalised with respect to the survival of the untreated hMSCs used as control (green). hMSCs were exposed for 15 minutes to a different range of concentrations of a) [scGFP_PlGF2] (orange) and b) [scGFP_PlGF2][S] (blue); measurements were taken 24 hours after exposure. N=5 different patients hMSCs. Individual values, mean, and standard deviation are reported; *: p<0.05.

Another reason for the observed decrease in metabolic rate in the modified cells could be due to the presence of unbound exogenous polymer surfactant. In fact, it has been reported that detergents can disrupt the cell membrane by forming mixed micelles with phospholipids on the surface membrane, which cause cell solubilisation[23]. In order to explore potential surfactant cytotoxicity, a viability assay was carried out on hMSCs with solutions containing the free oxidised IGEPAL co-890 over a range of concentrations that were equivalent to the conjugated surfactant concentration in [scGFP_PlGF2][S] (Figure 4.3), e.g., for a protein concentration of 2.75 μM, 0.5 $mg \cdot mL^{-1}$ of surfactant was added in solution. Interestingly, the cell survival was not significantly affected by the oxidised IGEPAL co-890 until added at 2 $mg \cdot mL^{-1}$, equivalent to a concentration of 8 μM of [scGFP_PlGF2][S], indicating that the toxicity of [scGFP_PlGF2][S] was not caused by unbound polymer surfactant molecules. Instead, cell death could be

linked to protein distributed on the cell membrane, preventing the cell from interacting with necessary nutrients and growth factors present in the cell medium. +36 scGFP has been used as a DNA delivery agent for mammalian cells, however, the concentrations used for such experiments were in the nanomolar range[24]. In contrast, the large amount of exogenous protein or conjugate could also have caused membrane disruption or bind to intracellular components, causing cell death.

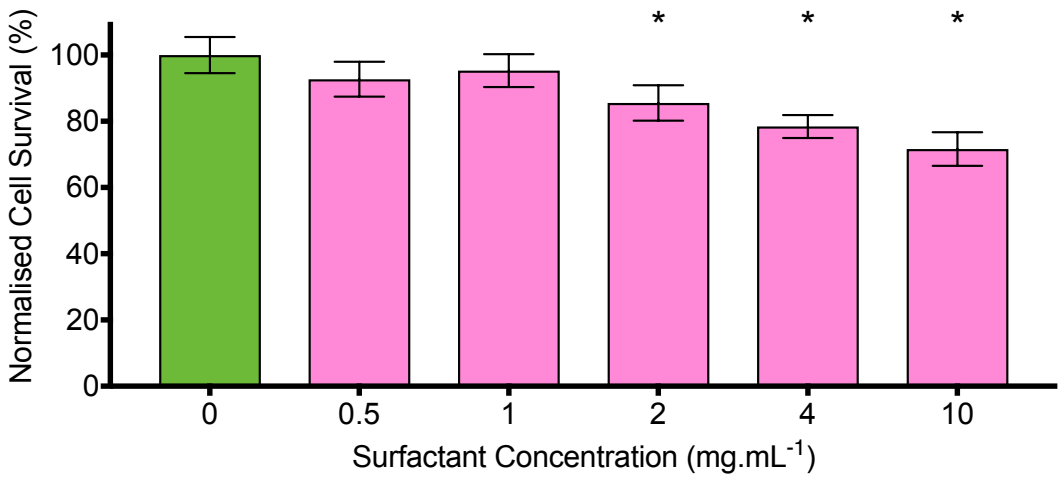

Figure 4.3 Cytotoxicity effects of oxidised IGEPAL co-890 on human mesenchymal stem cells (hMSCs). The metabolism of human mesenchymal stem cells (hMSCs) was measured by assessing the cell metabolism of MTS into formazan. hMSCs were exposed for 15 minutes to a different range of concentrations of polymer surfactant, and measurements were taken 24 hours after exposure. The data was normalised with respect to the survival of the untreated hMSCs used as control. N=2 different patients hMSCs. Mean and standard deviation are reported; *: p<0.05.

To evaluate the expansion rate of modified hMSCs, a proliferation assay was developed by counting the cells 7 and 14 days after exposure to [scGFP_PlGF2] or [scGFP_PlGF2][S] at a concentration of 4 µM (Figure 4.4 and Equation 2.5). After one week, the treated cells appeared to show a minor decrease in cell growth when compared to untreated cells, however, this change was not significant. The result could be due to short-term stress induced by the blocking of cell receptors by the modification[25], which may prevent the exchange of nutrients and growth

factors between the cells and the medium. Importantly, the cells did not lose their ability to proliferate after a further 7 days, indicating that there were no long-term side effects on exposing cells to [scGFP_PIGF2] or the conjugate [scGFP_PIGF2][S] (Figure 4.4). One possibility for this resistance, could be clearance of the constructs from the membrane by excision or endocytosis. The persistence of the conjugate on the membrane will be discussed in section 4.2.3.

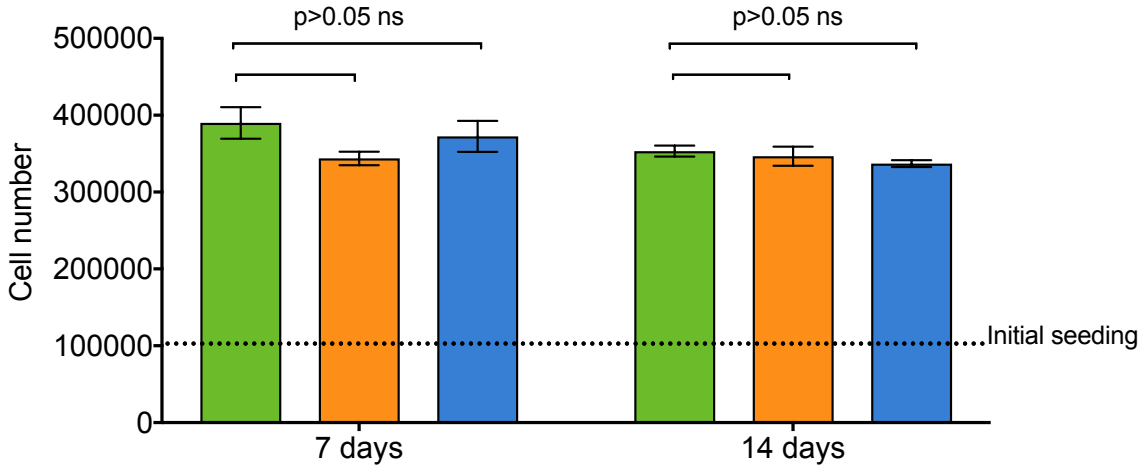

Figure 4.4 Proliferation of human mesenchymal stem cells (hMSCs). hMSCs were exposed to 4 μM of [scGFP_PIGF2] (orange) and [scGFP_PIGF2][S] (blue), compared with untreated cells (green) as a control. Proliferation was evaluated by manual count of the cells every seven days for two weeks. N=3 different patients hMSCs. Mean and standard deviation are reported; *: p<0.05.

The average population doubling time (PD) for each modification was evaluated using Equation 2.5, and then normalised to untreated control hMSCs.

$$PD = \frac{\log\left(\frac{nh}{ns}\right)}{\log(2)} \qquad \textit{Equation 2.5}$$

Where *nh* is number of cells harvested, and *ns* corresponds to the initial seeded cells. The results from two passages were normalised to the untreated cells, summarised in Table 4.1. The difference between modified and unmodified populations were not significant.

Table 4.1 Normalised population doubling rate for cells treated with [scGFP_PlGF2] and [scGFP_PlGF2][S]. The data was normalised to the population doubling rate of the control over seven days.

Time/Construct	Control	[scGFP_PlGF2]	[scGFP_PlGF2][S]
Day 7	1	0.82±0.08	0.94±0.02
Day 14	1	0.95±0.02	0.95±0.03

4.2.2 Measuring the cell membrane affinity for the new constructs

Flow cytometry was used to evaluate the cell membrane-nanobiohybrid interaction. The cells were labelled by resuspension in a solution of 4 μM of either [scGFP_PlGF2] or [scGFP_PlGF2][S] (Figure 4.5).

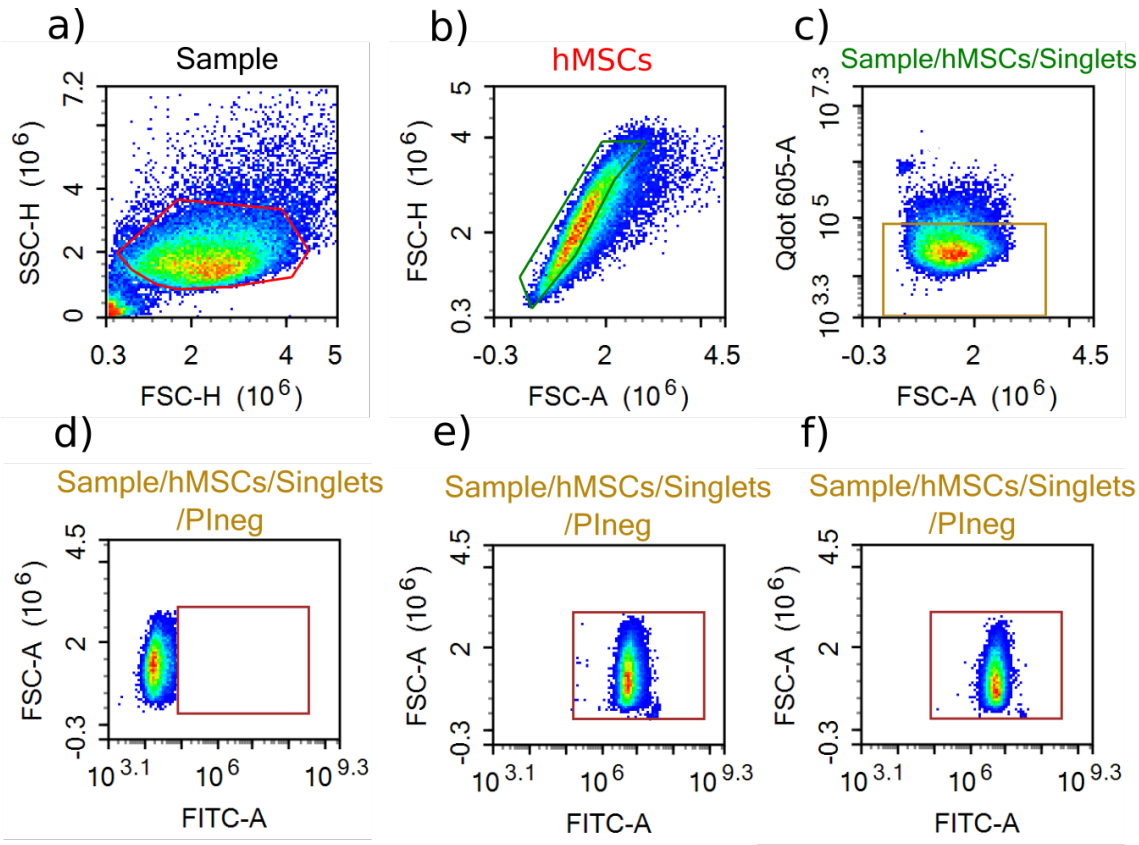

Figure 4.5 Two-dimensional flow cytometry with enclosed gates using a density map from red to blue. Non-labelled human mensenchynal stem cells (hMSCs) were used to define four gates based on granularity, size, viability, and fluorescence. a) Size and granularity parameters forward scattered-height vs side scattering-height (FSC-H vs SSC-H) were used to identify the population of hMSCs to exclude debris. b) This gate was next used to select the single cell population comparing it with forward scatter-area (FSC-A vs FSC-H). c) Selected cells were sorted for their viability as determined by a negative staining with a propidium iodide gate (FSC-A vs Qdot 605-A). The living cell population was measured with FITC-A channel to separate labelled and non-labelled cells within the given sample d) untreated cells, e) [scGFP_PlGF2] or f) [scGFP_PlGF2][S] conjugated with surfactant in individual runs. Representative of three samples.

Untreated hMSCs were used as a control to outline the gates for cell type, according to their size and granularity using forward scattered (FSC-H) and side scattered light (SSC-H) respectively. A red fluorescent Qdot 605-A gate was necessary to identify and exclude unviable cells stained with propidium iodide (PI). This was followed by a FITC channel to detect hMSCs labelled with [scGFP_PlGF2] or [scGFP_PlGF2][S] (Figure 4.5). This gating was designed to evaluate the extent of cell affinity for the protein [scGFP_PlGF2] and corresponding surfactant conjugate. A 100% of the treated cells with [scGFP_PlGF2] and [scGFP_PlGF2][S] were positively labelled with the nanobiohybrids, compared to 0.02% fluorescence in untreated cells, confirming the affinity of these constructs for the cell membrane. However, when comparing the fluorescent intensity of the cells labelled with [scGFP_PlGF2] or [scGFP_PlGF2][S], the intensity was higher for cells modified with [scGFP_PlGF2] (Figure 4.6). It was hypothesised that there was a difference in the number of constructs per cell, depending on whether or not surfactant is present. In order to test this, the amount of [scGFP_PlGF2] and [scGFP_PlGF2][S] distributed on the cell membrane was quantified using UV-vis spectroscopy.

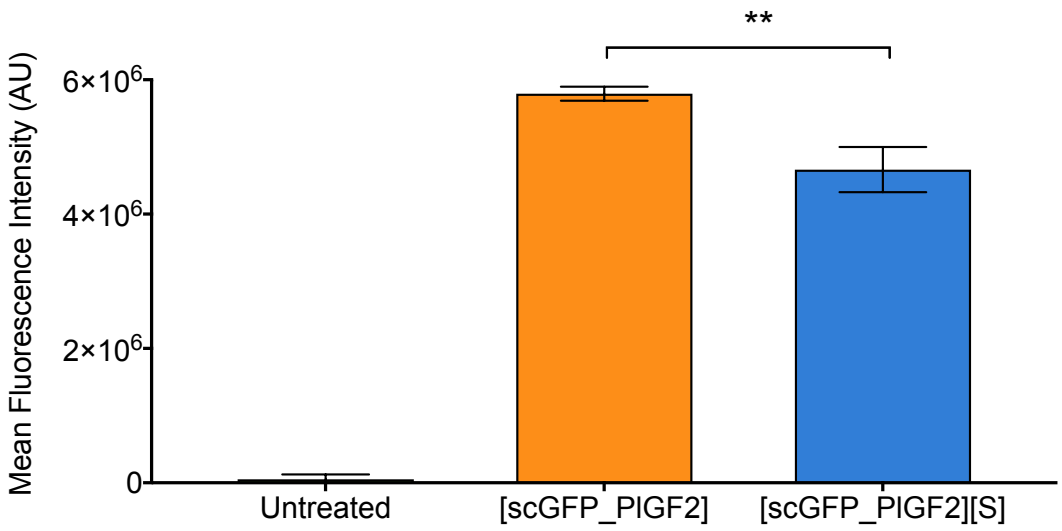

Figure 4.6 Mean fluorescence intensity of cells. Human mesenchymal stem cells (hMSCs) were treated with 4 μM of [scGFP_PlGF2] (orange) or [scGFP_PlGF2][S] (blue) for 15 minutes, compared to untreated cells (green). Mean fluorescence intensity was obtained by comparing whole living cells with a green fluorescent channel. N=3 different patients hMSCs. Mean and standard deviation are reported; *: p<0.05, **: p<0.01.

hMSCs were seeded at a density of 20,000 cell per well and treated with known concentrations of [scGFP_PlGF2] or [scGFP_PlGF2][S] for 15 minutes, the supernatant was collected and analysed by measuring the absorption peak at 487 nm. The absorption intensity was compared to the known initial absorption. The number of nanobiohybrid constructs on the membrane was calculated using Equation 2.6.

$$Constructs\ per\ cell = \frac{C_0 - C_s}{N} N_A \qquad \textbf{\textit{Equation 2.6}}$$

Where C_0 is initial concentration in moles, C_s is the concentration of the supernatant in moles, N is the seeded cell number, and N_A is Avogadro's constant. The resulting constructs per cell were plotted as a function of the concentration (Figure 4.7).

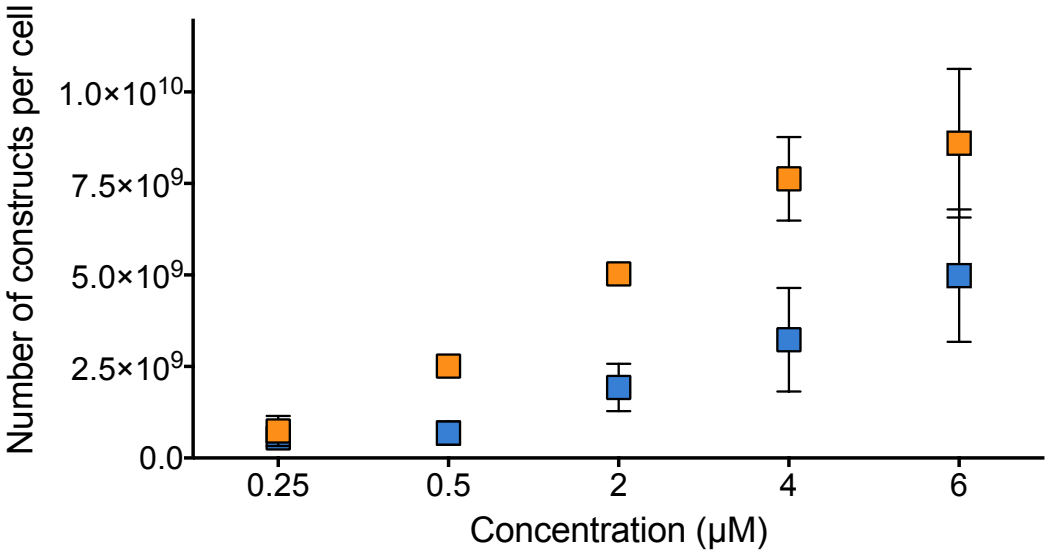

Figure 4.7 UV-vis spectroscopy was used to analyse the number of constructs deposited onto human mesenchymal stem cells (hMSCs). The absorption of the remnant supernatant after cell exposure for 15 minutes was measured to assess the number of [scGFP_PlGF2] (orange) and [scGFP_PlGF2][S] (blue) constructs per cell. Mean and standard deviation are reported. N=2 different patients hMSCs.

The cell membrane appeared to be saturated after 2 μM for [scGFP_PlGF2][S] and 4 μM for [scGFP_PlGF2] as at this point the data suggests that there is no significant difference on the number of constructs per cell when treated at higher concentrations. The number of nanobiohybrids per cell was calculated according to the protein concentration added, giving on average 7.6×10^9 and 3.5×10^9 constructs for [scGFP_PlGF2] and [scGFP_PlGF2][S] respectively, when treated at 4 μM working concentration. This result may explain the fluorescent data from the flow cytometry experiment in (Figure 4.6), whereby the increased mean fluorescence intensity of [scGFP_PlGF2] corresponds to a greater number of construct bound relative to the conjugate [scGFP_PlGF2][S].

The difference in the amount of protein binding to the cell membrane could be due to the high positive charge of [scGFP_PlGF2] protein, as previous studies have revealed that positively charged molecules, such as liposomes or polyplexes (formed by charged proteins and nucleic acids), have higher binding capacity for

cells compared to neutral polyplexes due to the negative charge on the cell membrane[26]. There is also the possibility that [scGFP_PIGF2] is being internalised by the cells. Indeed, supercharged proteins have been used as transfection agents because of their ability to undergo rapid endocytosis in mammalian cells[24]. In the same manner, it has been demonstrated that surfactants can shield the positive charge on polyplexes to decrease internalisation rates[27].

The size of the nanobiohybrids could also be playing a role in this matter, since the protein with the surfactant corona increases the hydrodynamic diameter, as seen in section 3.2.2.2, limiting the number of constructs cells can accommodate compared to [scGFP_PIGF2]. Another possibility is that the deposited nanobiohybrids could be forming multiple layers on the surface of the cell for [scGFP_PIGF2][S]. Changes in absorption and fluorescence of the constructs due to denaturation of the fluorophore were considered to be negligible since supercharged GFP has exhibited significant protease resistance[24]. Due to the nature of the experiments it is difficult to tell where the protein has been localised after exposure, methods such as imaging flow cytometry which allows to take images of individual cells, could be used for further experiments.

4.2.3 Live cell imaging

To observe the interaction between the nanobiohybrid and hMSC membrane in greater detail, live cell confocal microscopy was performed. The images were taken after exposing the cells to 4 μM of [scGFP_PIGF2] or [scGFP_PIGF2][S] for 15 minutes (Figure 4.8). In both cases, it is possible to observe the association of the constructs on the surface of the cell membrane. The images appear to show green dots in the background, which is due to the tendency of the protein to stick

to the surface of the substrate even after two wash steps with PBS, and software background subtraction.

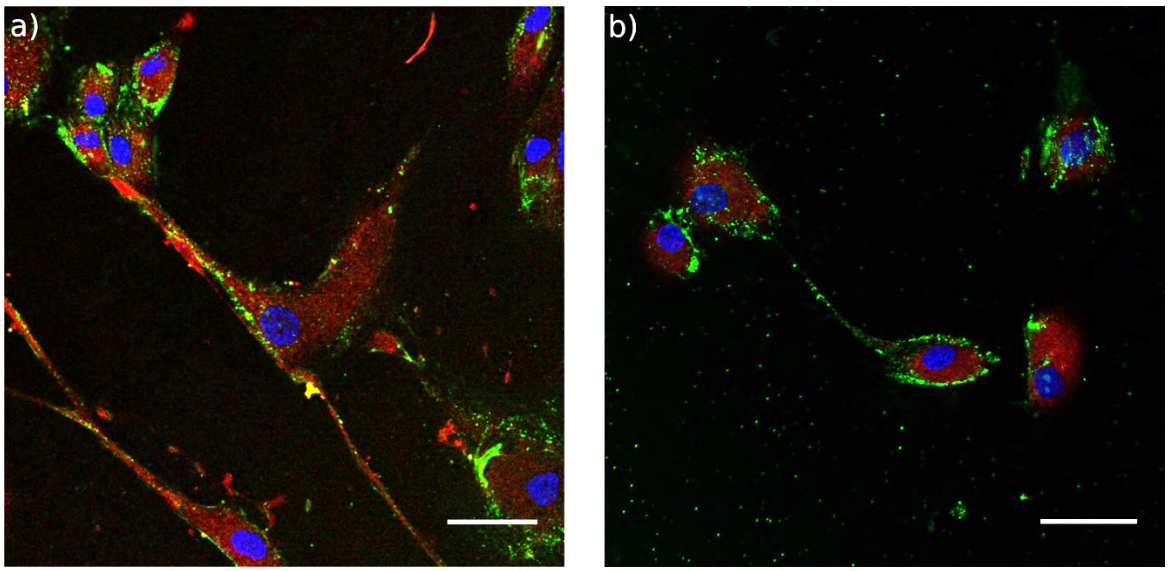

Figure 4.8 Confocal images from hMSCs exposed to the constructs for 15 minutes at 37°C. a) [scGFP_PlGF2] and b) corresponding conjugate [scGFP_PlGF2][S]. Blue: Hoechst nuclei stain, green: [scGFP_PlGF2] or [scGFP_PlGF2][S], red: cell tracker cytoplasm stain. Scale bar: 50 µm.

Time-lapse microscopy was performed to observe the interaction between [scGFP_PlGF2] or [scGFP_PlGF2][S] with the hMSCs membranes over 12 hours (

Figure **4.9**). The images taken showed that [scGFP_PlGF2] was completely internalised by the cells within the first hour, whilst the conjugate was visibly retained on the cell surface for up to 12 hours. This suggests that the distinct intrinsic physicochemical properties of [scGFP_PlGF2] and [scGFP_PlGF2][S] have an impact on their interaction with the cell membrane. The [scGFP_PlGF2] likely associated via electrostatic interactions with sulphated proteoglycans, whereas [scGFP_PlGF2][S] may interact through a hydrophobic manner with lipids in the membrane bilayer. After 24 hours, however, both [scGFP_PlGF2] and the conjugate were fully internalised into the cytoplasm (Figure 4.9 e, f).

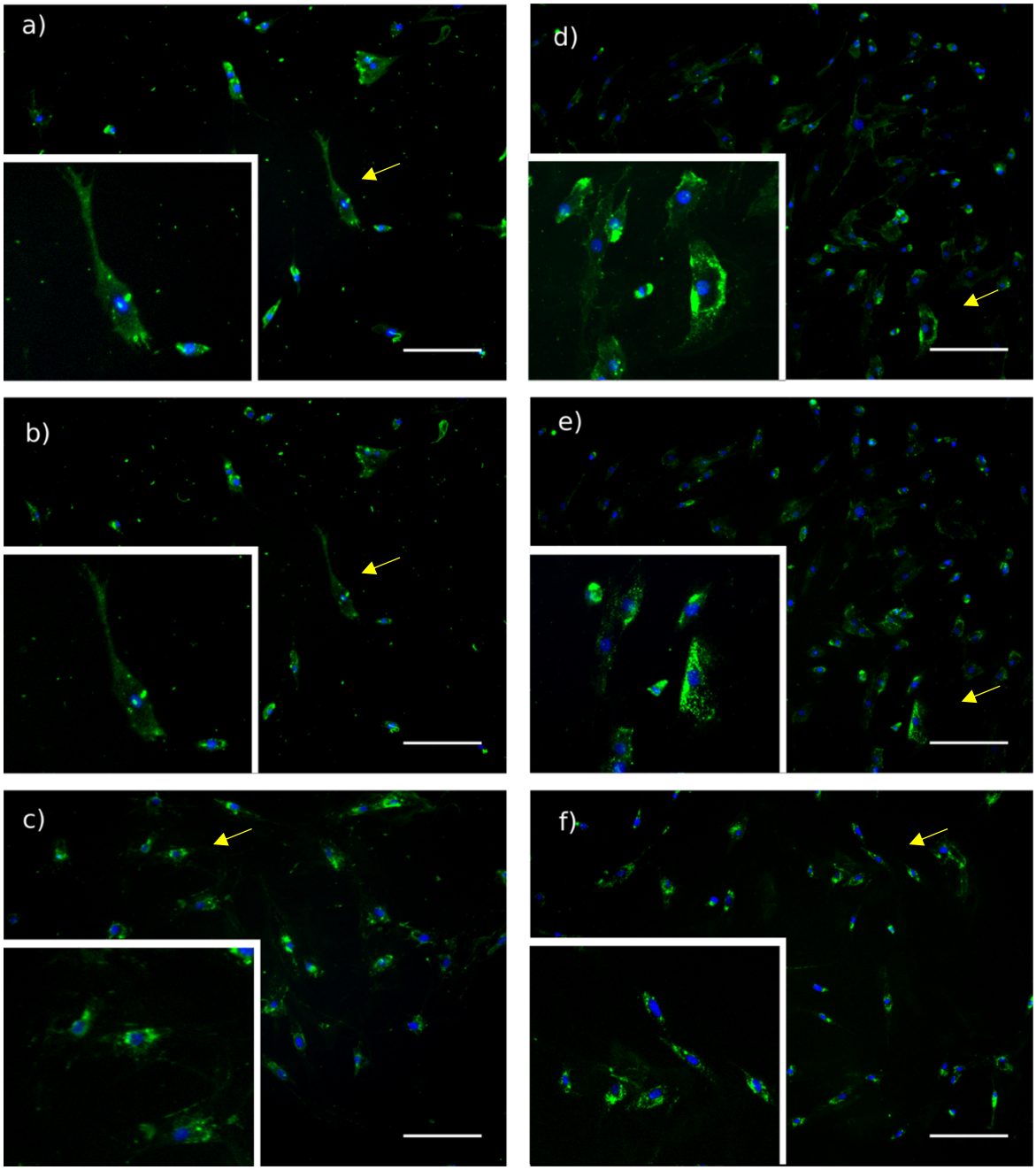

Figure 4.9 Widefield microscopy time-lapse. Human mesenchymal stem cells (hMSCs) were treated for 15 minutes with [scGFP_PlGF2] or [scGFP_PlGF2][S]. a) hMSCs treated with [scGFP_PlGF2][S] T=0, and b) one hour after treatment. d) hMSCs treated with [scGFP_PlGF2] at T=0, and e) T=1. The same samples were analysed after 24h exposure to [scGFP_PlGF2] (c), or conjugate [scGFP_PlGF2][S] (f). Images were taken every 15 minutes with an inverted microscope using a 20× lens under a 5% CO_2 atmosphere at 37°C. Blue: Hoechst nuclei stain, green: [scGFP_PlGF2] or [scGFP_PlGF2][S]. Scale bar: 200 µm.

The observation that the [scGFP_PlGF2] was quickly internalised by hMSCs is consistent with a previous report, which shows that positively charged biomolecules have a higher rate of association and endocytosis[28]. This energy-dependent endocytosis of the protein is due to the electrostatic binding that occurs between the positively charged protein and the negatively charged sulphated proteoglycans on the cell membrane[29]. Indeed, such positively charged molecules have been used as transfection agents due to their efficacy for delivery of biomolecules inside plasma membrane[21].

In contrast, [scGFP_PlGF2][S] was retained on the cell membrane for longer due to the presence of oxidised IGEPAL co-890, which alters the charge of the molecule making it neutral. Previously, it has been demonstrated that when cells are pre-treated with sodium chlorate, which inhibits the formation of the cell negatively charged proteoglycans, did not influence the affinity for surfactant conjugated protein with the cell membrane[30]. This suggests that the nonylphenyl tail of the surfactant inserts into the plasma membrane of hMSCs.

Mechanistic studies where cells were treated with chlorpromazine, a known inhibitor of clathrin formation have demonstrated a decrease in the endocytosis of +36 scGFP[31], cationized enhanced GFP, and cationized enhanced GFP conjugated with oxidised IGEPAL co-890[30], although +36 scGFP cellular internalisation was still dependent on the presence of anionic sulphated proteoglycans[31]. This energy-dependent process is fully shown after 24 hours of exposure.

Following endocytosis, it was considered important to understand when the constructs would be completely removed from the cells. To achieve this, the cells were treated as explained in section 4.2.2, and submitted for flow cytometry

analysis. The reduction in fluorescence intensity on day two may be a sign of denaturation or degradation of [scGFP_PlGF2] and [scGFP_PlGF2][S]. Alternatively, cell proliferation and membrane turnover could play a role in the dilution of nanoconstructs across the cell population. Additionally, after 12 days of treatment, modified hMSCs have lost all exogenous fluorescence (Figure 4.10).

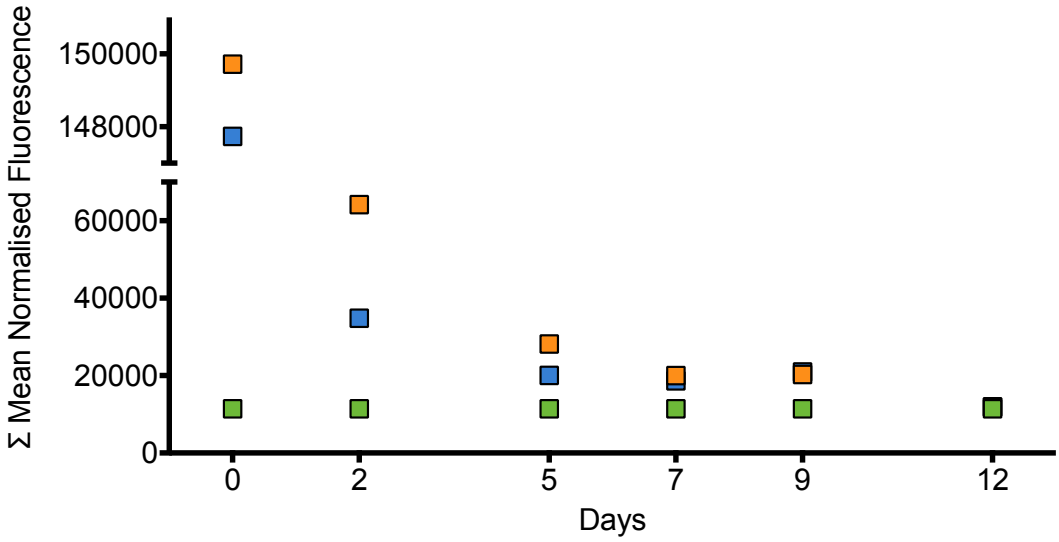

Figure 4.10 Cell fluorescence intensity over the course of 12 days. Human mesenchymal stem cells (hMSCs) were modified in suspension with 4 µM of [scGFP_PlGF2] (orange) or [scGFP_PlGF2][S] (blue). Untreated hMSCSs were used as a control (green). Fluorescence was measured every 2–3 days using flow cytometry, with a FITC gate. N=3 different patients hMSCs. Mean and standard deviation are reported. Standard deviation bars are smaller than the symbol.

4.2.4 Differentiation

Human mesenchymal stem cells (hMSCs) are known for their ability to differentiate into a variety of tissues, including bone, muscle, cartilage, ligament, and adipose[32]. Differentiation studies were performed on the modified cells to assess their capacity to maintain their multipotency. hMSCs cultivated in a monolayer were treated with 4 µM of [scGFP_PlGF2] or [scGFP_PlGF2][S], washed and then exposed to distinct differentiation environments by replacing the basal culture

medium with osteogenic, adipogenic or chondrogenic differentiation medium. There was no visible difference when comparing the modified cells with the control cells, indicating that the cell membrane modification does not impede the ability of the cells to undergo multilineage differentiation (Figure 4.11 and Figure 4.12).

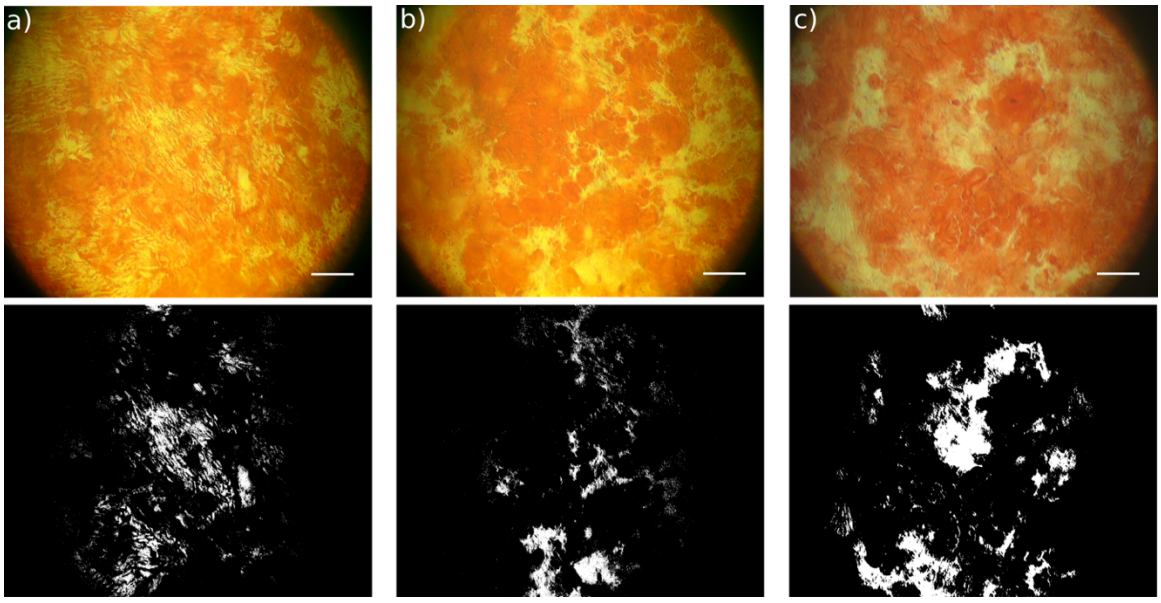

Figure 4.11 Representative images of mesenchymal stem cells (hMSCs) osteogenic differentiation. Untreated hMSCs were used as a control (a). Cells modified with [scGFP_PIGF2][S] (b) and [scGFP_PIGF2] (c) were cultured for 21 days in osteogenic differentiation medium, then assessed for calcium deposits with Alizarin red S stain. A mean threshold was applied to achieve discrete sections. Pixel count at the bottom of the image was used to identify calcium deposits by measuring the total count of the white area. Scale bar: 500 µm.

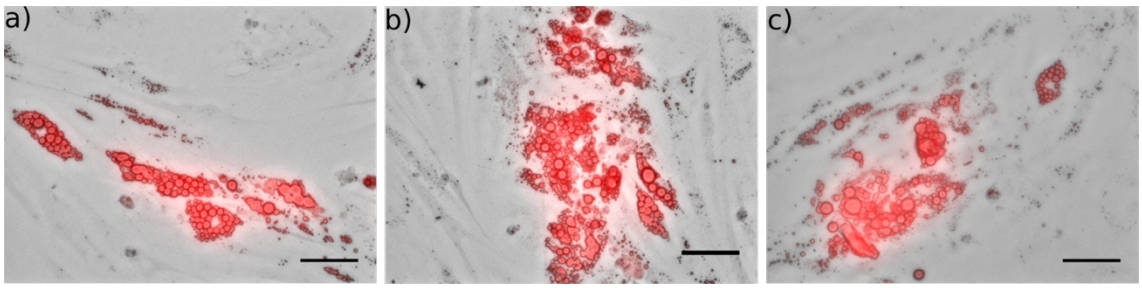

Figure 4.12 Representative images of mesenchymal stem cells adipogenic differentiation. Untreated stem cells were used as a control (a). Cells modified with [scGFP_PIGF2][S] (b) and [scGFP_PIGF2] (c) were cultured for 21 days in adipogenic differentiation medium, then assessed for vacuole formation with Oil red O stain. Scale bar: 50 µm.

Furthermore, chondrogenesis was examined by quantitative PCR (qPCR) experiments to measure the degree of mRNA production from *col1a2* and *col2a1*, the genes responsible for collagen type I and type II production, respectively. Their expression levels were compared to the housekeeping gene *GAPDH*, which is involved in glycolysis and is expressed constitutively[33]. A significant increase in the transcription of the *col2a1* gene was observed in the modified cells with [scGFP_PlGF2][S] (Figure 4.13).

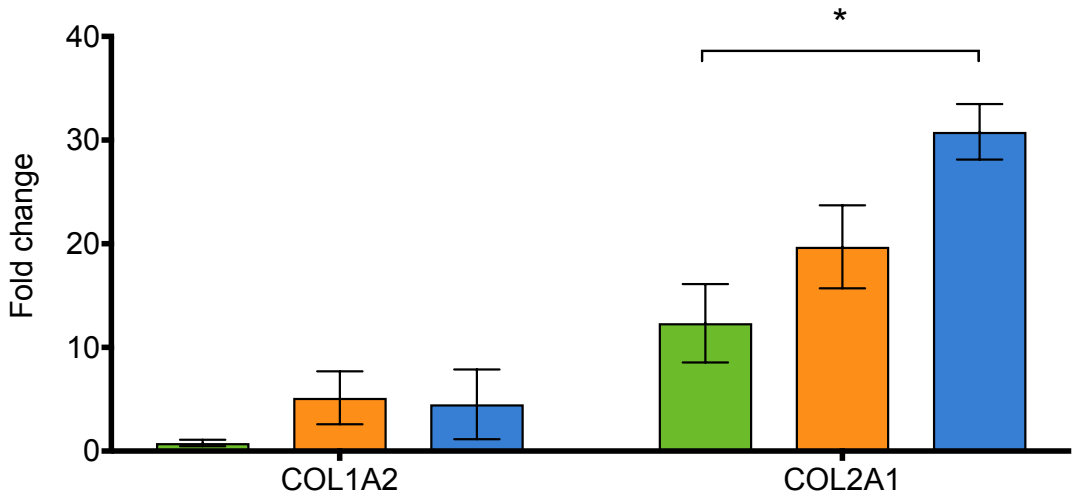

Figure 4.13 Quantitative PCR results for chondrogenesis differentiation. qPCR data comparing variations in mRNA expression relative to housekeeping gene *GAPDH* in undifferentiated human mesenchymal stem cells (hMSCs). Equal amounts of hMSCs were modified with [scGFP_PlGF2] (orange), [scGFP_PlGF2][S] (blue) and unmodified cells were used as a control (green). All samples were treated with chondrogenic medium for three weeks under a 5% CO_2 atmosphere at 37°C. N=3 different patients hMSCs. Mean and standard deviation are reported; *: $p<0.05$.

There are various parameters that can affect the differentiation pathway in stem cells, such as rearrangement of the cell cytoskeleton caused by mechanical forces[34], physicochemical change on the cell surface or oxygen tension[35]. It has been demonstrated that genetic changes can be seen after 24 h of starting differentiation[36], which is within the time frame that [scGFP_PlGF2][S] persists anchored to the cell membrane. For instance, Mcbeath et al. reported that the

rearrangement of the actin cytoskeleton is crucial during the first 48 h after differentiation has started because disruption in this period may decrease osteogenesis[37]. It has also been reported that a decrease in the actin cytoskeletal structure favours chondrogenic and adipogenic differentiation[38]. In the same manner, reduction in the stiffness of the hMSCs has been associated with an increase in chondrogenesis and adipogenesis while osteogenesis is favoured by an increase in stiffness[39]. The above experiments revealed no visual difference in the level of osteogenic differentiation between modified and unmodified cells (Figure 4.11), suggesting that a change in the mechanical properties of the actin cytoskeleton is unlikely to result from cell modification with [scGFP_PlGF2] or [scGFP_PlGF2][S].

The oxidised IGEPAL-co890 used to build [scGFP_PlGF2][S] contains at least 39 polyethylene glycol units (PEG). Studies of polyethylene glycol surfactant have elucidated its low toxicity[40], biocompatibility, and, more recently its ability to interact with biomolecules to form conjugates with other proteins[41]. It has been demonstrated that this polymer facilitates the crossing of reagents through cell membranes by endocytosis[42], as it has been hypothesised that it can lower the surface tension of the membrane to improve transport of metabolites in mammalian cells[43]. Another hypothesis is that the polyethylene glycol chains could be sequestering nutrients present in the cell medium, and then internalised them into the cell when endocytosis occurs within the first 24 hours.

Finally, hypoxia has been suggested as a factor to drive chondrogenesis in stem cells[30,35]. In light of this, it is possible that the polymer surfactant impedes oxygen transfer during the first 12 hours whilst [scGFP_PlGF2][S] is retained on the cell membrane.

4.3 Chapter conclusions

In this chapter the ability of the nanobiohybrid constructs to interact with the stem cell membrane was evaluated. Cytotoxicity assays demonstrated that the working concentration of 4 μM of [scGFP_PlGF2] and [scGFP_PlGF2][S] did not cause significant damage to cell metabolism or proliferation rates. Flow cytometry experiments revealed that hMSCs labelled with [scGFP_PlGF2] have a higher mean fluorescence than [scGFP_PlGF2][S]. This could be due to the rapid internalisation of the protein molecules into the cell, making the overall quantity of protein higher than [scGFP_PlGF2][S], since this only covers the outer cell membrane at the time when the fluorescence measurements were taken.

The surface modification of the cell did not negatively affect multilineage differentiation into osteoblasts, adipocytes and chondrocytes. Conversely, it was shown that the construct can upregulate the transcription of *co2la1* during chondrogenesis. The change in collagen II transcription is due to the surface modification of the cell with [scGFP_PlGF2][S] during the first 12 hours. This might be due to the polyethylene glycol chains in the polymer surfactant facilitating the transport of important nutrients across the cell membrane, and the saturation of the membrane with the nanobiohybrid leading to a hypoxic environment, therefore promoting differentiation.

4.4 Further work

There are a great number of experiments that have not been explored thus far. It would be important to determine the exact mechanism that decrease cell viability on modified cells, as this could lead to the fate and interaction of [scGFP_PlGF2] and [scGFP_PlGF2][S] with cells. It could be useful to know the path of the cell death, since it can occur by apoptosis, autophagy or necrosis, which could be done by treating the cells with different markers for colorimetric or flow cytometry assays. It was shown that both [scGFP_PlGF2] and [scGFP_PlGF2][S] are fully internalised by the cells, however, it would be useful to know if [scGFP_PlGF2][S] is endocytosed as a whole entity or if the oxidised IGEPAL co-890 is left outside the cell membrane. In this case, a surfactant with a fused fluorescent probe to act as a marker could be useful to observe localisation through time.

Corelated light electron microscopy is a technique that makes use of both transmitted electron and fluorescence microscopy to identify co-localisation and identify changes in cells. This method could be used to measure the thickness of the layer deposited on the cell membrane, as the fluorescent protein could be seen by light microscopy.

Furthermore, exploring the change on the surface membrane after modification is of great importance, since changes in the stiffness and surface area of the cell have a major impact on cell differentiation and interaction with its environment. Atomic force microscopy has been used for these findings in the past to map the topographic surface at the cell membrane[44]. More experiments could be carried out to fully investigate the quality of the chondrocytes with qPCR technology to elucidate any pathways that are favoured as a result of cell modification, as this could have major implications in cell therapies. Finally, it is essential to evaluate

the extent of the effect of the polyethylene glycol chains in chondrogenic differentiation. This could be done by varying the polyethylene glycol chain length in IGEPAL co-890 or by conjugating [scGFP_PIGF2] with different surfactants that lack polyethylene glycol repeating units.

4.5 Bibliography

1. Overton, E. The probable origin and physiological significance of cellular osmotic properties. *Biol. Membr. Struct.* **44,** 88–135 (1968).

2. Singer, S. J. & Nicolson, G. L. The Fluid Mosaic Model of the Structure of Cell Membranes. *Source Sci. New Ser.* **175,** 720–731 (1972).

3. Tanford, C. The hydrophobic effect and the organization of living matter. *Science (80-.).* **200,** 1012–1018 (1978).

4. Encyclopedia Britannica. cell membrane | biology | Britannica.com. (2015). Available at: https://www.britannica.com/science/cell-membrane. (Accessed: 3rd March 2019)

5. Edidin, M. Lipids on the frontier: A century of cell-membrane bilayers. *Nat. Rev. Mol. Cell Biol.* **4,** 414–418 (2003).

6. Reitsma, S., Slaaf, D. W., Vink, H., van Zandvoort, M. A. M. J. & oude Egbrink, M. G. A. The endothelial glycocalyx: composition, functions, and visualization. *Pflügers Arch. - Eur. J. Physiol.* **454,** 345–359 (2007).

7. Wei, X. *et al.* Mesenchymal stem cells: A new trend for cell therapy. *Acta Pharmacologica Sinica* **34,** 747–754 (2013).

8. Nowakowski, A., Andrzejewska, A., Janowski, M., Walczak, P. & Lukomska, B. Genetic engineering of stem cells for enhanced therapy. *Acta Neurobiol. Exp. (Wars).* **73,** 1–18 (2013).

9. Winslow, T. Use of genetically sodified stem cells in experimental gene therapies. *Regen. Med.* **1,** 45–52 (2006).

10. Martin, D. D. O. *et al.* Rapid detection, discovery, and identification of post-translationally myristoylated proteins during apoptosis using a bio-orthogonal azidomyristate analog. *FASEB J.* **22,** 797–806 (2008).

11. Krauss Juillerat, F. *et al.* Functionalization of microstructured open-porous bioceramic scaffolds with human fetal bone cells. *Bioconjug. Chem.* **23,** 2278–2290 (2012).

12. Lo, C. Y. *et al.* The use of surface immobilization of P-selectin glycoprotein ligand-1 on mesenchymal stem cells to facilitate selectin mediated cell tethering and rolling. *Biomaterials* **34,** 8213–8222 (2013).

13. Rabuka, D., Forstner, M. B., Groves, J. T. & Bertozzi, C. R. Noncovalent cell surface engineering: Incorporation of bioactive synthetic glycopolymers into cellular membranes. *J. Am. Chem. Soc.* **130,** 5947–5953 (2008).

14. Stephan, M. T. & Irvine, D. J. Enhancing cell therapies from the outside in: Cell surface engineering using synthetic nanomaterials. *Nano Today* **6,** 309–325 (2011).

15. Doyle, R. J., Chaloupka, J. & Vinter, V. Turnover of Cell Walls in

Microorganisms. *Microbiol. Rev.* **52,** 554–567 (1988).

16. Armstrong, J. P. & Perriman, A. W. Minireview Strategies for cell membrane functionalization. *Exp. Biol. Med.* **241,** 1098–1106 (2016).

17. Kim, S. A. & Peacock, J. S. The use of palmitate-conjugated protein A for coating cells with artificial receptors which facilitate intercellular interactions. *J. Immunol. Methods* **158,** 57–65 (1993).

18. Dennis, J. E., Cohen, N., Goldberg, V. M. & Caplan, A. I. Targeted delivery of progenitor cells for cartilage repair. *J. Orthop. Res.* **22,** 735–741 (2004).

19. Zheng, G. *et al.* Induction of antitumor immunity via intratumoral tetra-costimulator protein transfer. *Cancer Res.* **61,** 8127–8134 (2001).

20. Riss, T. L. *et al. Cell Viability Assays*. *Assay Guidance Manual* **740,** (2004).

21. Hillaireau, H. & Couvreur, P. Nanocarriers' entry into the cell: Relevance to drug delivery. *Cell. Mol. Life Sci.* **66,** 2873–2896 (2009).

22. Lambert, G., Fattal, E., Brehier, A., Feger, J. & Couvreur, P. Effect of polyisobutylcyanoacrylate nanoparticles and Lipofectin® loaded with oligonucleotides on cell viability and PKCα neosynthesis in HepG2 cells. *Biochimie* **80,** 969–976 (1998).

23. Jones, M. N. Surfactants in membrane solubilisation. *International Journal of Pharmaceutics* **177,** 137–159 (1999).

24. McNaughton, B. R., Cronican, J. J., Thompson, D. B. & Liu, D. R. Mammalian cell penetration, siRNA transfection, and DNA transfection by supercharged proteins. *Proc. Natl. Acad. Sci.* **106,** 6111–6116 (2009).

25. Tower, J. Stress and stem cells. *Wiley Interdiscip. Rev. Dev. Biol.* **1,** 789–802 (2012).

26. Lee, K. D., Hong, K. & Papahadjopoulos, D. Recognition of liposomes by cells: In vitro binding and endocytosis mediated by specific lipid headgroups and surface charge density. *BBA - Biomembr.* **1103,** 185–197 (1992).

27. Schiffelers, R. M. *et al.* Cancer siRNA therapy by tumor selective delivery with ligand-targeted sterically stabilized nanoparticle. *Nucleic Acids Res.* **32,** (2004).

28. Huang, M., Ma, Z., Khor, E. & Lim, L. Y. Uptake of FITC-chitosan nanoparticles by A549 cells. *Pharm. Res.* **19,** 1488–1494 (2002).

29. Cronican, J. J. *et al.* Potent delivery of functional proteins into Mammalian cells in vitro and in vivo using a supercharged protein. *ACS Chem. Biol.* **5,** 747–52 (2010).

30. Armstrong, J. P. K. *et al.* Artificial membrane-binding proteins stimulate oxygenation of stem cells during engineering of large cartilage tissue. *Nat. Commun.* **6,** 7405 (2015).

31. Thompson, D. B., Villaseñor, R., Dorr, B. M., Zerial, M. & Liu, D. R. Cellular uptake mechanisms and endosomal trafficking of supercharged proteins. *Chem. Biol.* **19,** 831–843 (2012).

32. Chamberlain, G., Fox, J., Ashton, B. & Middleton, J. Concise Review: Mesenchymal Stem Cells: Their Phenotype, Differentiation Capacity, Immunological Features, and Potential for Homing. *Stem Cells* **25,** 2739–2749 (2007).

33. Kozera, B. & Rapacz, M. Reference genes in real-time PCR. *Journal of Applied Genetics* **54,** 391–406 (2013).

34. Kelly, D. J. & Jacobs, C. R. The role of mechanical signals in regulating chondrogenesis and osteogenesis of mesenchymal stem cells. *Birth Defects Research Part C - Embryo Today: Reviews* **90,** 75–85 (2010).

35. Shang, J., Liu, H., Li, J. & Zhou, Y. Roles of Hypoxia During the Chondrogenic Differentiation of Mesenchymal Stem Cells. *Curr. Stem Cell Res. Ther.* **9,** 141–147 (2014).

36. Liu, E., Gordonov, S., Treiser, M. D. & Moghe, P. V. Parsing the early cytoskeletal and nuclear organizational cues that demarcate stem cell lineages. *Cell Cycle* **9,** 2108–2117 (2010).

37. McBeath, R., Pirone, D. M., Nelson, C. M., Bhadriraju, K. & Chen, C. S. Cell shape, cytoskeletal tension, and RhoA regulate stem cell lineage commitment. *Dev. Cell* **6,** 483–95 (2004).

38. Titushkin, I. & Cho, M. Regulation of cell cytoskeleton and membrane mechanics by electric field: Role of linker proteins. *Biophys. J.* **96,** 717–728 (2009).

39. Darling, E. M., Topel, M., Zauscher, S., Vail, T. P. & Guilak, F. Viscoelastic properties of human mesenchymally-derived stem cells and primary osteoblasts, chondrocytes, and adipocytes. *J. Biomech.* **41,** 454–464 (2008).

40. Forrest, M. L., Koerber, J. T. & Pack, D. W. A degradable polyethylenimine derivative with low toxicity for highly efficient gene delivery. *Bioconjug. Chem.* **14,** 934–940 (2003).

41. Khandare, J. & Minko, T. Polymer-drug conjugates: Progress in polymeric prodrugs. *Progress in Polymer Science (Oxford)* **31,** 359–397 (2006).

42. Damodaran, V. B. Protein PEGylation Process: An overview of chemistry. *Eur. Pharm. Rev.* **15,** 1–18 (2010).

43. Shintani, Y., Iwamoto, K. & Kitano, K. Polyethylene glycols for promoting the growth of mammalian cells. *Appl. Microbiol. Biotechnol.* **27,** 533–537 (1988).

44. Mathieu, P. S. & Loboa, E. G. Cytoskeletal and Focal Adhesion Influences on Mesenchymal Stem Cell Shape, Mechanical Properties, and Differentiation Down Osteogenic, Adipogenic, and Chondrogenic Pathways. doi:10.1089/ten.teb.2012.0014

Chapter 5

The Effect of Membrane Engineering on Mesenchymal Stem Cell Adhesion

5.1 Introduction

5.1.1 The cartilage and the extracellular matrix

Cartilage tissue can be found throughout the human body in the form of elastic, hyaline, and fibrocartilage[1]. Hyaline articular cartilage provides a smooth gliding surface for articulation and enables the transmission of loads to protect the ends of the bones in diarthroidal joints[1]. This type of tissue is avascular, aneural and alymphatic[2]. It contains one type of highly specialised cells, chondrocytes, which secrete the extracellular matrix (ECM).

The cartilage ECM is mainly comprised of water, collagen II and proteoglycans, which confer to cartilage the shape and compressive strength[3,4]. The ECM is formed of fibres varying from 50 to 500 nm in diameter[5]. Particularly, the collagen fibres in the superficial zone of the cartilage are densely packed and are arranged in parallel to the articular surface[1].

Within the articular cartilage, there are three zones based on their distance to the chondrocytes: pericellular, territorial and interterritorial matrix[6]. The pericellular matrix contains glycoproteins, proteoglycans and other non-collagenous molecules. It is the closest in proximity to the chondrocytes, surrounding the cell membrane[7]. The territorial matrix encapsulates the pericellular matrix and contains fine collagen fibrils forming a network around the cells[6].

5.1.2 Cell-extracellular matrix interactions

Cell-ECM interactions are not only responsible for the arrangement, morphogenesis, phenotype acquirement and maintenance of the cells, but also play an important role in wound healing[8]. These interactions allow cells to bind to the ECM through focal adhesions and promote direct communication between the

cells and ECM[8]. These interactions also prompt a change in the cytoplasmic domain of the integrin receptor, which associates with the cytoskeleton at focal adhesion sites, and regulates the response of the cells as a consequence of ECM adhesion[9].

The cell surface possesses two kinds of receptors for the attachment to ECM: non-integrin and integrin receptors[10]. Integrins are heterodimeric cell transmembrane proteins, that enable cell-ECM adhesion[11]. Once cells have approached the substrate surface and commenced the attachment process, the spreading phase of adhesion is induced by integrins (Figure 5.1). As the integrins on the cell surface bind to certain sequences on the ECM, they cluster on the surface of the cell membrane associating with the cytoskeleton and promote the production of actin filaments[11].The association of integrin receptors with the actin cytoskeleton may also induce the rearrangement of the matrix[9] and modify the ability of cells to proliferate and differentiate[12].

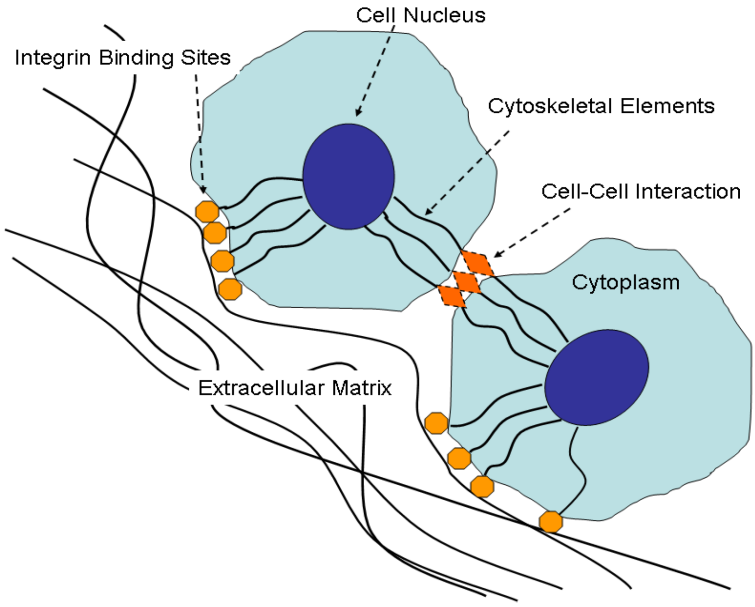

Figure 5.1 Schematic representation of cell-extracellular matrix interactions. Integrin receptors bind to extracellular matrix proteins. Reproduced from[13].

The ECM is also able to interact with proteins including growth factors. In fact, they have been used as agents to improve wound healing[14]. Due to the innate ability of growth factors to bind to ECM, their binding moieties have been isolated such as those that interact with the heparan sulphate proteoglycans on the ECM[15]. For instance, the sequence from 123 to 144 in placenta growth factor 2 (PlGF2_123–144) has high affinity for the main proteins on the ECM such as fibronectin, fibrinogen, and vitronectin[14].

Stem cells, due to their capacity for proliferation and differentiation, are a promising tool for minimally invasive tissue engineering approaches. Accordingly, there has been significant interest in the development of injectable cell therapy approaches to treat cartilage damage. For example, Murphy et al. showed the therapeutic benefit after injecting stem cells into an osteoarthritic caprine animal model, delaying the progression of OA. Saulnier et al. also reported on the inhibition of metalloproteinases after injecting mesenchymal stromal stem cells into the knee joints of rabbits[16]. However, one of the major challenges associated with these approaches is directing the cells to the desired locations in sufficient numbers without off-target effects. For example, Adachi et al. reported the generation of scar tissue free-bodies after the transplantation of stem cells in the knee due to the excess and free movement of the cells[17].

A possible solution would be the rational modification of hMSC membranes to enhance their adhesion, engraftment, and integration in place. Accordingly, in this chapter, the interaction of [scGFP], [scGFP_PlGF2] and [scGFP_PlGF2][S] modified hMSCs with ECM protein components and bovine articular cartilage explants is explored. First, the adhesion of the modified cells was investigated on a controlled surface with collagen I and collagen II. Then, the cell adhesion in a

dynamic environment was examined using microfluidics over a rage of shear stresses. Bovine ex vivo explants were also used as a substrate to evaluate the degree of mesenchymal stem cell association in a living ECM. Finally, the interaction of aqueous dispersions of nanobiohybrids with bovine cartilage was assessed.

5.2 Results and discussion

5.2.1 Static affinity assay

The stability of the nanobiohybrids on the surface of human mesenchymal stem cells (hMSCs) was evaluated on Chapter 4. The viability, proliferation rate and multilineage differentiation were not inhibited after hMSC membrane modification with [scGFP_PlGF2] and [scGFP_PlGF2][S]. Additionally, it was found that [scGFP_PlGF2][S] could persist on the surface membrane for up to 12 hours after modification, and be completely removed from the cell after 12 days. Accordingly, in this chapter, the affinity of the modified hMSCs for extracellular matrix (ECM) proteins is explored.

Collagen II is the predominant collagen secreted by chondrocytes, and it comprises 95% of articular cartilage[18]. Although collagen I is a minor constituent of normal articular cartilage[19], it has also been found in osteoarthritic cartilage[20] and fibrocartilage[21]. Furthermore, collagen III, IV, V, VI, IX, and XI are all present in the cartilage ECM[19] in low quantities.

To quantify the affinity of modified hMSCs for ECM components, plate-wells coated with collagen I, collagen II, or bovine serum albumin (BSA) were exposed to suspensions of hMSCs modified with either [scGFP], [scGFP_PlGF2], or [scGFP_PlGF2][S], as described in section 2.8. The number of hMSCs was calculated by measuring the DNA content in each well (Figure 5.2).

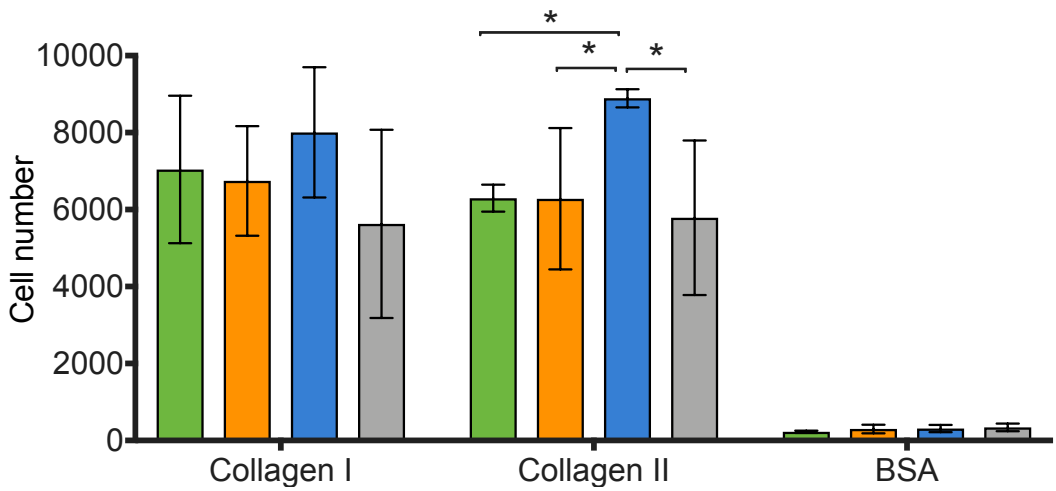

Figure 5.2 Static affinity assay. Human mesenchymal stem cells (hMSCs) were used untreated as a control (green), or treated for 15 minutes with [scGFP_PlGF2] (orange), [scGFP_PlGF2][S] (blue), or [scGFP] (grey). hMSCs were suspended in DMEM phenol free media without any supplements and plated into wells pre-coated with collagen type I (0.2 mg·mL^{-1}), collagen type II (0.2 mg·mL^{-1}) or bovine serum albumin (BSA) (10 mg·mL^{-1}). The hMSCs were incubated on the wells for four hours at 37°C in a 5% CO_2 atmosphere. Cell attachment was measured by DNA quantification. N=4 different patient's hMSCs. Mean and standard deviation are reported; *: p<0.05.

Figure 5.2 shows that there is a significant difference in the cell affinity between surfaces coated with collagens and BSA, since hMSCs are naturally adherent to surfaces coated in collagen type I[22] or II[23]. For the substrate coated with collagen I, hMSCs modified with [scGFP_PlGF2] did not show a significant difference when compared with the unmodified hMSC control. The treatment with [scGFP_PlGF2][S] appeared to show an increased in the number of cells attached onto the substrate, however, this change was not significant. The number of cells attached when modified with [scGFP] was not different between collagen I and collagen type II.

Importantly, the presence of both PlGF2_123–144 peptide and surfactant IGEPAL co-890 ([scGFP_PlGF2][S]) had a significant impact on the cell affinity for collagen type II when compared to [scGFP], [scGFP_PlGF2], and the unmodified hMSCs. This could be attributed to the longer persistence of the conjugates on the cell

membrane surface (Chapter 4, section 4.2.3). Alternatively, the increased affinity for collagen type II may have resulted from the orientation and display of the peptide in the fusion when membrane binding was via hydrophobic tail insertion. With respect the difference in the adhesion between the collagens, it has previously been determined that the fibrils of collagen I and collagen II pack differently, with collagen I exhibiting less space between the fibres[24], which might reduce cell binding due to a lower surface area for interaction.

Martino and colleagues demonstrated that the PlGF2_123–144 domain, present in placenta growth factor 2, has affinity for heparan sulphate, vitronectin, and fibrinogen, poor binding to collagen I, but did not do assays against collagen type II[14]. This was not unexpected given that a binding site for collagen I to growth factors has not yet been found[14].

5.2.2 Dynamic affinity assays

Due to the inherent adhesion of hMSCs to collagen I and collagen II, adhesion experiments were performed under flow. This not only provides a more effective method for separating highly adhesive cells, but also valuable information on how the modified cells would perform when shear stress is present (Figure 5.3). Shear stress is the result of the friction caused by the fluid flow against a capillary surface, in this case, the human body[25]. For instance, 2 dyne·cm^{-2} is approximately the shear stress in human arteries *in vivo*[26], and in large arteries this range can be as high as 10 to 40 dyne·cm^{-2} [27,28]. Since there was no significant difference between the groups in the collagen I substrate assays, the dynamic affinity assays were only carried out using a collagen II substrate.

For this experiment, a biochip was coated with collagen type II and hMSCs were modified with either [scGFP_PlGF2] or [scGFP_PlGF2][S]. Unmodified cells were

used as a control. Flow rates of 0.75, 1.0 and 1.5 dyne·cm^{-2} were utilised, which are in the vicinity of the a physiologically relevant flow in the synovium (0.5 dyne·cm^{-2}) [29–31], and cell adhesion quantified in five different positions of the channel (Figure 5.3). Importantly, the hMSCs modified with [scGFP_PlGF2][S] exhibited a significantly increased affinity for collagen II, even at the fastest flow rate tested of 1.5 dyne·cm^{-2}. A negative control was also performed whereby the biochip was coated with only BSA, which resulted in negligible cell adhesion (Figure 5.3 a).

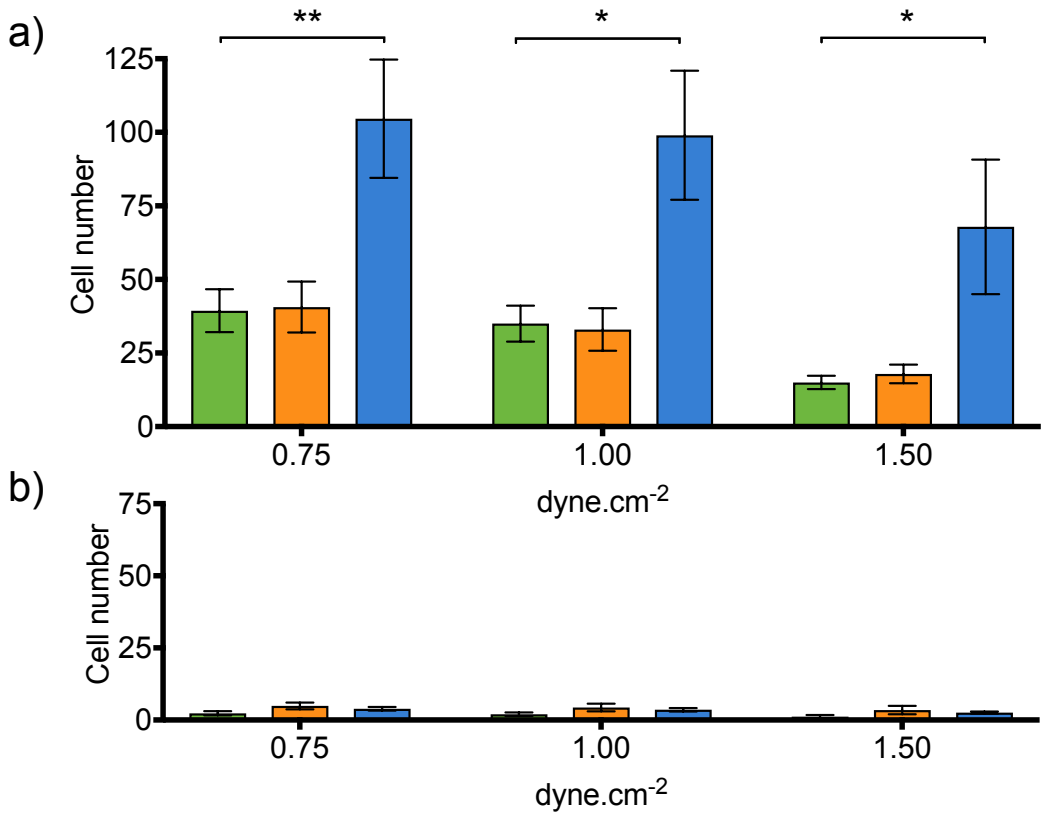

Figure 5.3 Dynamic affinity assays. Human mesenchymal stem cells (hMSCs) were treated for 15 minutes with [scGFP_PlGF2] (orange) and [scGFP_PlGF2][S] (blue) compared to untreated cells as a control (green) at a density of 1×10^6 cells per mL in a serum-free medium. The cells were added to a reservoir in a VenaFluoro8 biochip coated with a) collagen type II (0.2 mg·mL^{-1}), and b) bovine serum albumin (BSA) (0.1 mg·mL^{-1}). N=3 different patients hMSCs. Mean and standard deviation are reported; *: p<0.05, **: p<0.01.

This result is an indication of the greater binding affinity that is provided to the cells after modification with [scGFP_PlGF2][S], which supports the hypothesis that the surfactant-modified construct effectively presented the collagen II binding motif in a conformation that was not sterically hindered and for long enough periods for binding.

5.2.3 Adhesion assays on bovine cartilage ex vivo explants

After having verified that the engineered hMSCs with [scGFP_PlGF2] and [scGFP_PlGF2][S] were able to bind to and be retained on ECM proteins in a coated substrate, it was necessary to determine whether delivering these cells could express the same strong association for bovine ex vivo explants. Accordingly, bovine articular cartilage discs were taken from the lateral and patellar groove from 6 to 8-week-old calves, 8 hours after slaughter (section 2.13). Bovine calves' joints are rich in collagen II, and similar to the human knee joint.

hMSCs were resuspended, modified with [scGFP_PlGF2] or [scGFP_PlGF2][S], and then added to ex vivo explants. After four hours, the unbound cells were washed with phosphate buffer saline (PBS) and the cartilage was imaged with fluorescent widefield microscope to observe the remaining adhered cells (Figure 5.4).

It was observed that hMSCs were able to attach to the surface of the bovine explant discs. The images suggest that [scGFP_PlGF2][S] was retained on the surface, as the outline of the cells seems clearer.

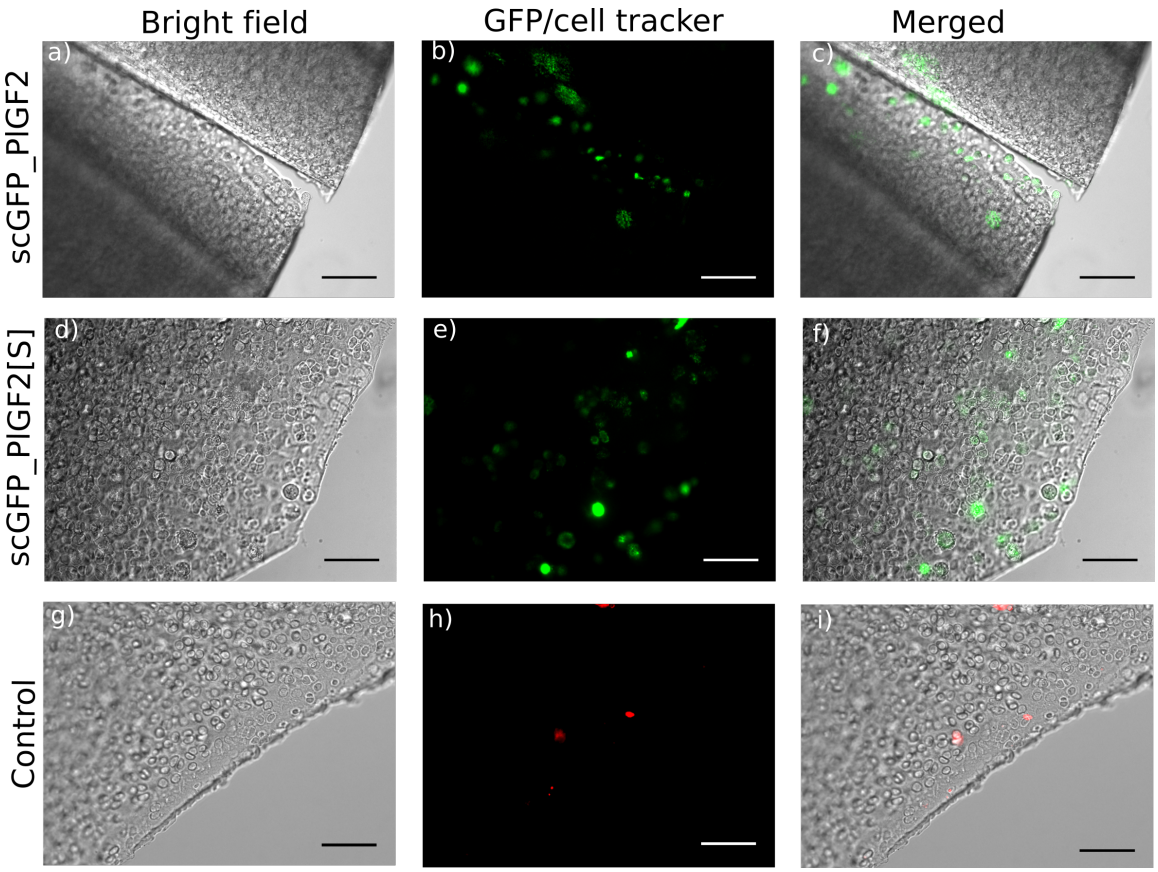

Figure 5.4 Widefield images from modified human mesenchymal stem cells (hMSCs) on cartilage ex vivo explants. hMSCs were treated for 15 minutes with 4 µM of [scGFP_PlGF2] (upper row) and [scGFP_PlGF2][S] (middle row). Untreated cells were used as a control (bottom row). The cells were then added to bovine cartilage discs of 6 mm diameter and were allowed to attach for four hours at 37°C in a 5% CO_2 atmosphere in a serum-free medium. a) transmitted light image of bovine cartilage, b) green fluorescent channel showing modified cells with [scGFP_PlGF2] on surface and c) overlay of the two channels. d) transmitted light image, e) fluorescent channel showing modified cells with [scGFP_PlGF2][S], f) overlay of channels, g) transmitted light image, h) fluorescent red channel showing control cells, i) overlay of channels. Green: [scGFP_PlGF2] and [scGFP_PlGF2][S], red: cell tracker cytoplasm stain. Scale bar: 100 µm.

In order to quantitatively measure the adhesion of hMSCs, confocal fluorescent microscopy was performed on ex vivo explants after the addition of hMSCs modified with [scGFP_PlGF2][S], using unlabelled cells as a control. Calculations were done by image analysis with Fiji (NIH, USA). The modification of mesenchymal stem cells with [scGFP_PlGF2][S] led to a marked increase in

adhesion to the ECM of ex vivo explants when compared to unmodified hMSCs. The numbers correspond to cells per acquired image (Figure 5.5).

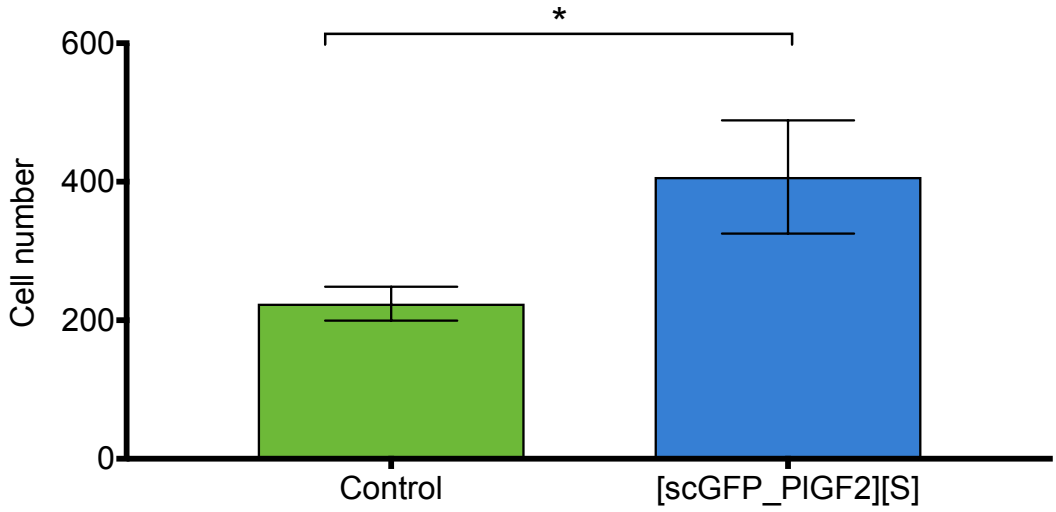

Figure 5.5 Adhesion assay in bovine ex vivo explants. Human mesenchymal stem cells (hMSCs) were treated for 15 minutes with [scGFP_PlGF2][S] (blue), using untreated cells as a control (green). hMSCs were suspended in DMEM phenol-free media without any supplements and added to 96 well plate containing a 6 mm diameter bovine ex vivo explant disc. Cells were allowed to attach for four hours at 37°C in a 5% CO_2 atmosphere. N=6 cartilage discs. Mean and standard deviation are reported; *: p<0.05.

In addition to water and collagens, bovine and human cartilage ECM is also rich in heparan sulphate proteoglycans, which are important for cartilage development[32]. Growth factors, such as fibroblast growth factor, are known to be heparin-binding proteins that also have a high affinity for heparan sulphate proteoglycans[33]. Heparin and heparan sulphate in articular cartilage are structurally related[34]. In light of this, it could be inferred that the heparin-binding peptide (PlGF2_123–144) of placenta growth factor 2 may also bind the heparan sulphate present in the bovine cartilage.

Martino et al. also found that the sticky peptide PlGF2_123–144 could be retained by the ECM *in vivo* when, in a mouse model, the addition of growth factors with the fused peptide induced bone regeneration. This was attributed to the retention

of the growth factors on the damaged bone, which could then recruit stem cells to the site.

In light of this, hMSCs were allowed to adhere for further 24 hours and they were subjected to histological analysis (Figure 5.6). It was observed that when hMSCs were submitted to treatment with [scGFP_PlGF2][S], they displayed adhesion and retention in bovine cartilage explants (Figure 5.6 d-f).

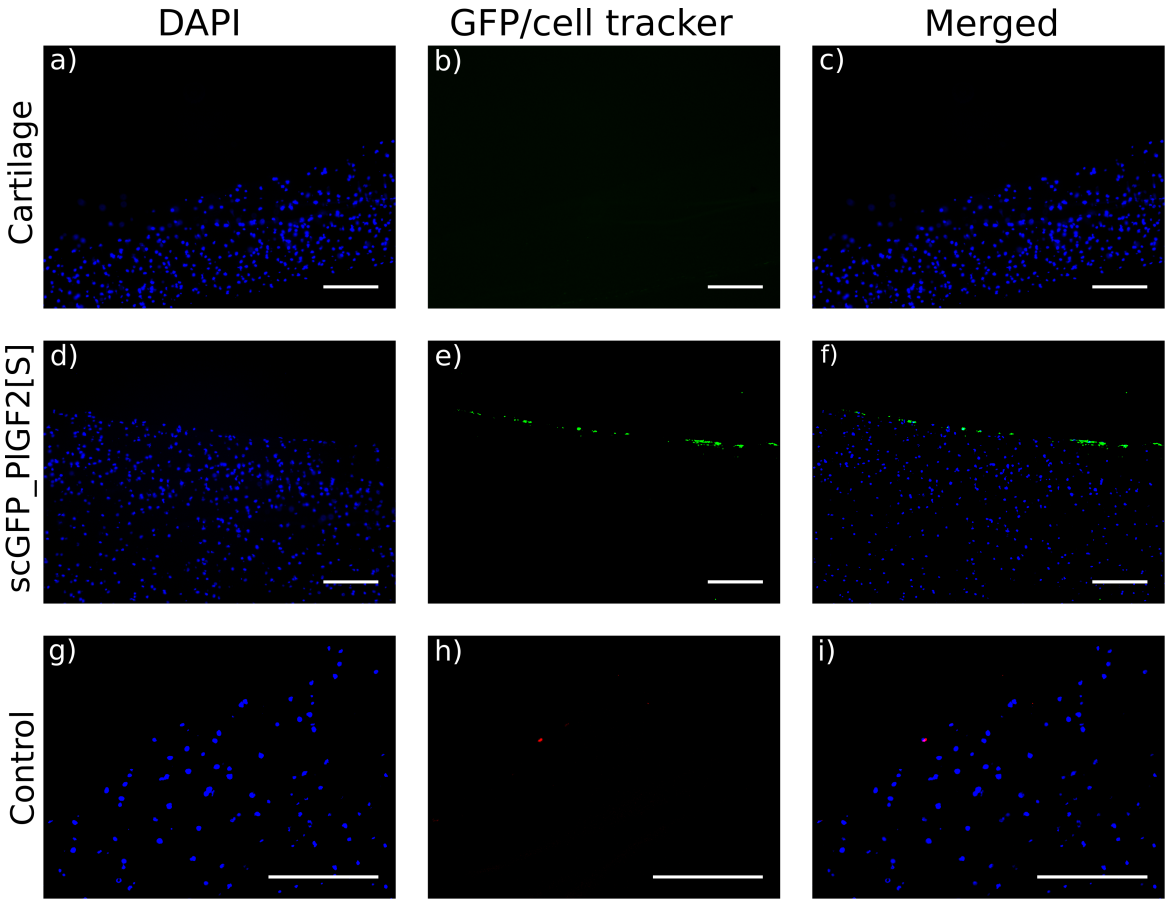

Figure 5.6 Histological fluorescent slices of bovine ex vivo cartilage discs. Human mesenchymal stem cells (hMSCs) were treated for 15 minutes with 4 µM of [scGFP_PlGF2][S] (middle row). Uncoated hMSCs were used as a control (bottom row). The cells were then seeded on bovine cartilage discs of 6 mm diameter and were allowed to attach for 24 hours at 37°C in a 5% CO_2 atmosphere in a serum-free medium. Samples were fixed and stained before being submitted to cryo-sectioning at 10 µm thickness. a, b, c) cartilage without seeded hMSCs. d, e, f) cartilage with seeded hMSCs modified with [scGFP_PlGF2][S]. g, h, i) control hMSCs seeded on ex vivo explants. Blue: DAPI cell nuclei, green: [scGFP_PlGF2][S], red: cell tracker cytoplasm stain. Scale bar: 100 µm.

The untreated hMSCs did not seem to be retained, as it was difficult to locate them on the surface of the cartilage, even at higher magnification. While these three sets of images were not used to calculate adhesion, they gave a strong visual indication of the affinity of the modified hMSCs for bovine cartilage.

Likewise, it was considered appropriate to image the ex vivo explants using scanning electron microscopy to observe the surface of the cartilage (Figure 5.7). There was a large contrast in the observed number of hMSCs after they were modified with [scGFP_PlGF2][S]. Furthermore, it can be observed that the cells are spreading out as a sign of the development of focal adhesion sites.

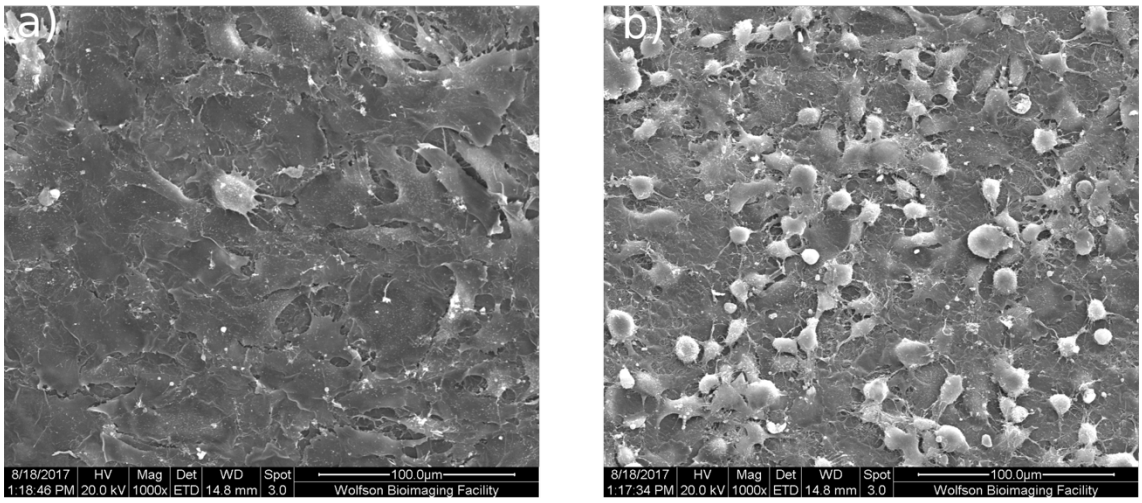

Figure 5.7 Scanning electron microscopy images of modified human mesenchymal stem cells (hMSCs) on bovine explant surface. hMSCs were treated for 15 minutes with 4 µM of [scGFP_PlGF2][S], then seeded on bovine explant discs of 6 mm diameter and allowed to attach for four hours at 37°C in a 5% CO_2 atmosphere in a serum-free medium. Samples were fixed, treated with osmium to improve contrast, dehydrated with ethanol and coated with platinum. a) untreated control hMSCs on bovine cartilage and b) hMSCs treated with [scGFP_PlGF2][S] on bovine cartilage.

5.2.4 Modifying ex vivo explants with acellular nanobiohybrids

Drugs injected into the intraarticular cartilage need to infiltrate the full depth in order to have an influence in the ECM and the residing chondrocytes. Therefore, new delivery procedures have been developed, such as the use of polymeric nanoparticles[35], and polypeptides[36]. These micro-sized carriers might be able to release drugs in a more efficient manner. However, the penetration and retention on the cartilage is still a challenge, especially in the middle and deep cartilage zones, which could be owed to the negative charge present in the ECM[37].

Accordingly, an investigation lead by Grodzinsky et al., has recently given an insight of the interactions between cartilage and charged or neutral small molecules, as this might be used as a platform for drug delivery. The experiments were carried out using variants of supercharged GFP. They coated bovine explants, similar to those used in this project, with neutral GFP, +9 GFP, +15 GFP, +25 and +36 GFP and concluded that the protein-cartilage interaction was dependent on the surface charge of the protein[38].

In order to assess the interaction of the novel nanobiohybrids with cartilage, analogous experiments were carried out. Using the methods from the Grodzinsky group, [scGFP], [scGFP_PlGF2] and the charge neutral [scGFP_PlGF2][S] (described in Chapter 2) were used to coat bovine ex vivo explants[38]. Briefly, bovine cartilage discs were submerged in equal 1 μM solutions of [scGFP], [scGFP_PlGF2] and [scGFP_PlGF2][S]. The solution also contained 1% of BSA to avoid loss of protein due to unspecific binding to the plastic container. After a 24-hour period, the absorbance of the supernatant bath solution was measured at 487 nm, and the number of constructs was normalised to cartilage volume (Figure 5.9 a-c). A similar method for the calculation of cell uptake was used (Figure 5.8).

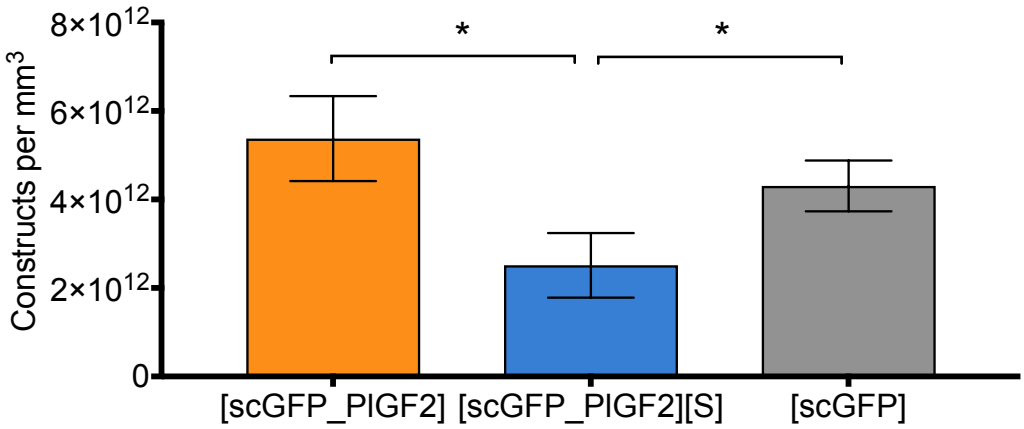

Figure 5.8 24-hour uptake of [scGFP_PIGF2], [scGFP_PIGF2][S] and [scGFP] by bovine cartilage explants. After one day, the supernatant was collected and compared to the initial concentration by measuring the UV absorption at 487 nm. N=3 cartilage discs assuming a uniform volume of 56.6 mm^3. Mean and standard deviation are reported; *: p<0.05.

A comparable result to Grodzinsky was obtained, since after quantification, the uptake of the neutral [scGFP_PIGF2][S] by the cartilage was almost half of the positively charged species [scGFP] and [scGFP_PIGF2]. This could be explained by the numerous amount of negatively charged sulphated glycosaminocans present in the surface of the articular cartilage, which produced a coulombic attraction[38].

In order to identify the location of the nanobiohybrids and [scGFP] after 24 hours incubated in the same bath, confocal microscopy was performed on the cross section of the cartilage discs (Figure 5.9 and Figure 5.10).

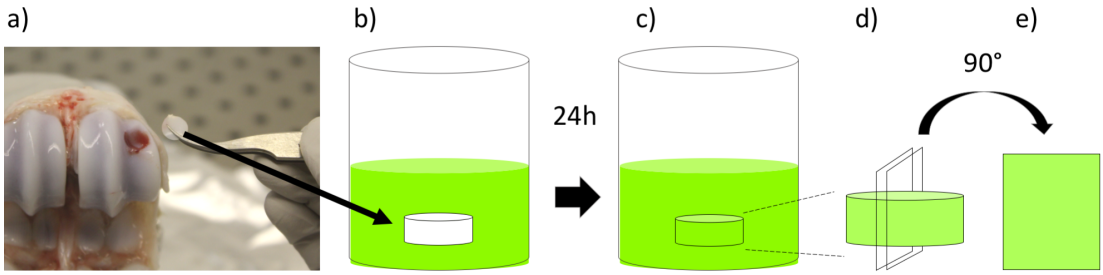

Figure 5.9 Schematic representation of ex vivo explants modification with proteins. a) bovine discs explants were harvested from articular cartilage. b) a 6 mm disc was submerged in a protein bath containing 1% bovine albumin serum and 1 µM of either [scGFP], [scGFP_PIGF2] or [scGFP_PIGF2][S]. c) after 24 hours, the cartilage was removed, d) sectioned and e) the cross-section was imaged. Adapted from[38].

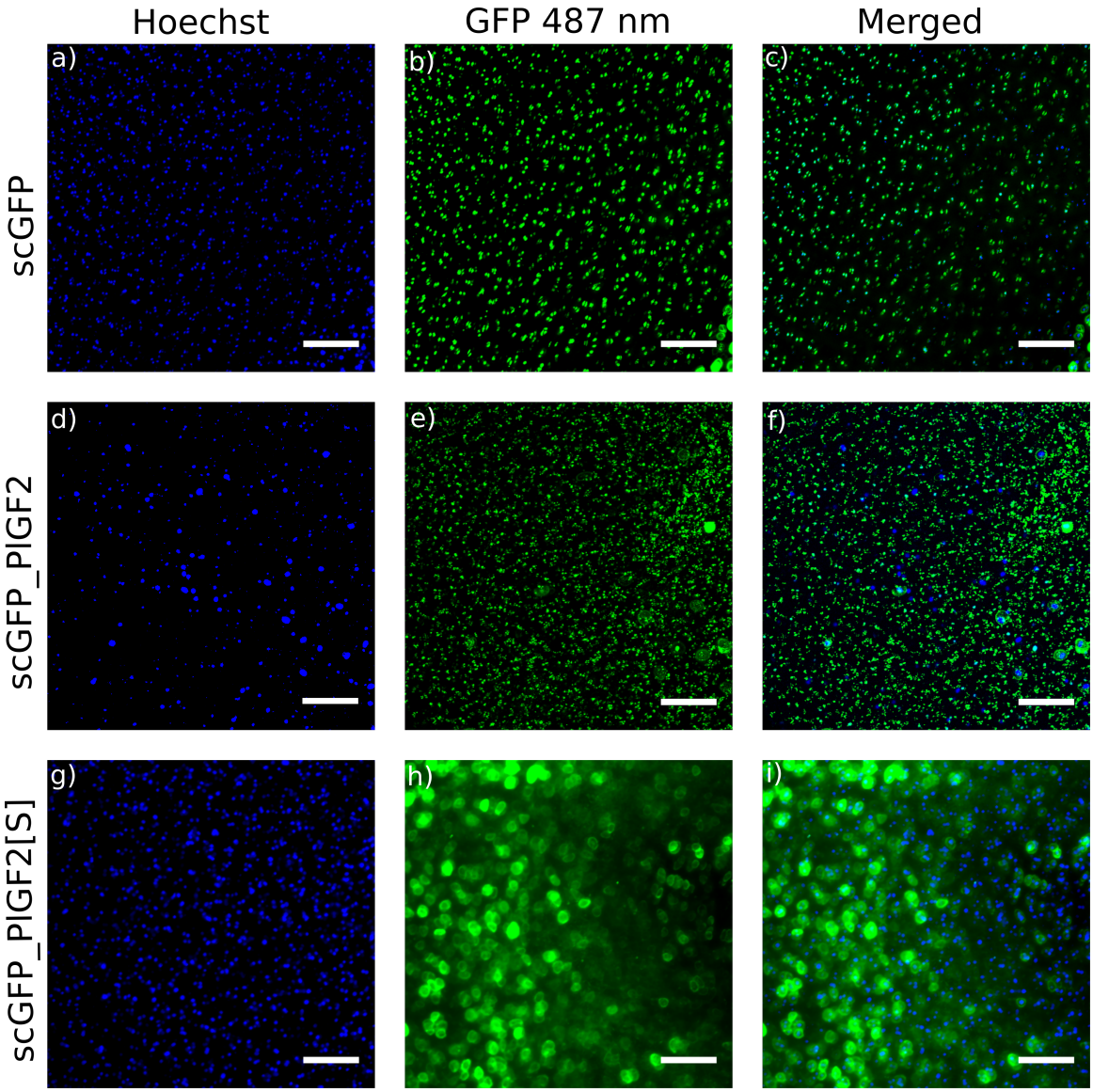

Figure 5.10 Bovine cartilage ex vivo explants exposed to nanobiohybrids. Discs were incubated in 1 µM solutions of [scGFP] (upper rows), [scGFP_PlGF2] (d to f) and [scGFP_PlGF2][S] (g to i) with 1% bovine serum albumin. The cross section was imaged after 24 hours. Green: supercharged proteins, blue: Hoechst nuclei stain. Scale bar: 100 µm.

In bovine cartilage discs exposed to [scGFP] (Figure 5.10 a-c), the protein appears to be localised inside the chondrocytes as the green areas are homogenous and appear to be elliptical in shape, correlating with the cell nuclei (blue channel). Therefore, the [scGFP] may not interacting with the ECM but is instead being captured by the chondrocytes, which agrees with the results obtained by Grodzinsky et al. and the results obtained in Chapter 4.

The bottom right corner of the images shows chondrocytes that are in the process of internalisation and may have interacted with the protein not long before being imaged.

The [scGFP_PIGF2] did not tend to always localise where the cells were. The green patches are not homogenous and appeared to be far more numerous than the nuclei locations. There is a strong possibility that the PIGF2 component was interacting with ECM components, aggregating, and thus preventing the [scGFP_PIGF2] from interacting and entering the chondrocytes.

Finally, [scGFP_PIGF2][S] correlated with the location of the chondrocytes, but in contrast to [scGFP], the protein clearly outlined the cells. This could be an indication of interaction with the ECM at the pericellular matrix or the territorial matrix and thus retained there. The background ‘haziness’ may suggest the [scGFP_PIGF2] is binding to the ECM throughout the cartilage in the interterritorial region. This could be due to the neutrality of the particle not being able to interact electrostatically, and the presence of the PIGF2_123–144 peptide which strongly binds to the ECM.

Additionally, this could serve as an alternative instead of modifying hMSCs, whereby the cartilage is first modified with nanobiohybrids and hMSCs are subsequently added; or the supercharged proteins could be loaded with drugs to enhance delivery deep in to the cartilage.

5.3 Chapter conclusions

Static adhesion assays revealed that human mesenchymal stem cells (hMSCs) are naturally adherent to collagens, as there was not significant difference between treated and untreated cells for collagen I. Importantly, there was a considerable increase in hMSCs affinity for collagen type II in artificially coated wells, when the surface membrane was modified with [scGFP_PlGF2][S], compared to untreated control hMSCs and [scGFP_PlGF2] and [scGFP]. In a similar manner, when hMSCs were modified with the nanobiohybrid [scGFP_PlGF2][S], their ability to adhere to collagen II in a dynamic environment of 0.75 to 1.0 dyne·cm^{-2} shear stress was significantly enhanced. This was attributed to the presence of the peptide PlGF2_123–144 that has a strong affinity for extra cellular matrix proteins (ECM). These data suggest that the peptide is exposed on the outer membrane available to bind collagen II, and that the surfactant IGEPAL co-890 in the nanobiohybrid, served as an anchor to the cell.

Importantly, the proficiency of hMSCs to interact with bovine ex vivo explants was amplified for surface engineered hMSCs with 4 μM [scGFP_PlGF2][S]. Moreover, experiments also demonstrated that [scGFP_PlGF2][S] alone has affinity for bovine cartilage *in vitro*, and were retained on the ECM. These data suggest that modifying the lipidic membrane of hMSCs may be a suitable platform to deliver cells into cartilage ECM.

5.4 Further work

The modification of hMSCs with [scGFP_PlGF2][S] enhanced affinity for ECM proteins, such as collagen II. However, their ability to improve would healing in bovine ex vivo explants needs further investigation. This could be done by measuring the amount of aggrecan and collagen II secreted by the explants before and after the addition of hMSCs at different time points. Importantly, the immunogenicity of the proteins used for these experiments should be measured in order to avoid rejection of the nanobiohybrids.

An attempt to evaluate stem cell differentiation into chondrocytes after adhesion was made (section 2.13.5), nevertheless, the results from such experiments were not conclusive and the data was not shown. It would be interesting to perform adhesion assays whereby the cartilage is first treated with [scGFP_PlGF2] and [scGFP_PlGF2][S] (as in the last figure) and plain hMSCs are then added to see if the adhere to the nanobiohybrid, having an untreated cartilage disc as a control. In order to better understand this technology, it could be necessary to develop in vivo assays in small mammals such as mouse or rabbit. These experiments could be performed by stem cell injection into the defective site and use histology techniques to evaluate the response of the tissue.

5.5 Bibliography

1. Bhosale, A. M. & Richardson, J. B. Articular cartilage: Structure, injuries and review of management. *British Medical Bulletin* **87,** 77–95 (2008).

2. Buckwalter, J. A. & Mankin, H. J. Articular cartilage: tissue design and chondrocyte-matrix interactions. *Instr. Course Lect.* **47,** 477–86 (1998).

3. Mow, V. C., Ratcliffe, A. & Poole, A. R. Cartilage and diarthrodial joints as paradigms for hierarchical materials and structures. *Biomaterials* **13,** 67–97 (1992).

4. Muir, H., Bullough, P. & Maroudas, A. The distribution of collagen in human articular cartilage with some of its physiological implications. *J. Bone Joint Surg. Br.* **52,** 554–63 (1970).

5. Hynes, R. The extracellular matrix: not just pretty fibrils. *Science (80-.).* **11760,** (2009).

6. Sophia Fox, A. J., Bedi, A. & Rodeo, S. A. The basic science of articular cartilage: structure, composition, and function. *Sports Health* **1,** 461–8 (2009).

7. Eggli, P. S., Herrmann, W., Hunziker, E. B. & Schenk, R. K. Matrix compartments in the growth plate of the proximal tibia of rats. *Anat. Rec.* **211,** 246–257 (1985).

8. Barnes, C. P., Sell, S. a, Boland, E. D., Simpson, D. G. & Bowlin, G. L. Nanofiber technology: designing the next generation of tissue engineering scaffolds. *Adv. Drug Deliv. Rev.* **59,** 1413–33 (2007).

9. Chen, C. S., Alonso, J. L., Ostuni, E., Whitesides, G. M. & Ingber, D. E. Cell shape provides global control of focal adhesion assembly. *Biochem. Biophys. Res. Commun.* **307,** 355–361 (2003).

10. Damsky, C. H. & Werb, Z. Signal transduction by integrin receptors for extracellular matrix: cooperative processing of extracellular information. *Curr. Opin. Cell Biol.* **4,** 772–781 (1992).

11. Giancotti, F. G. & Ruoslahti, E. Integrin signaling. *Science* **285,** 1028–32 (1999).

12. Rosso, F., Giordano, A., Barbarisi, M. & Barbarisi, A. From cell-ECM interactions to tissue engineering. *J. Cell. Physiol.* **199,** 174–80 (2004).

13. Sell, S. a. *et al.* The Use of Natural Polymers in Tissue Engineering: A Focus on Electrospun Extracellular Matrix Analogues. *Polymers (Basel).* **2,** 522–553 (2010).

14. Martino, M. M. *et al.* Growth Factors Engineered for Super-Affinity to the Extracellular Matrix Enhance Tissue Healing. *Science (80-.).* **343,** 885–888 (2014).

15. Macri, L. & Silverstein, D. Growth factor binding to the pericellular matrix and its importance in tissue engineering. *Adv. Drug Deliv. Rev.* **59,** 1366–1381 (2007).

16. Saulnier, N. *et al.* Intra-articular administration of xenogeneic neonatal Mesenchymal Stromal Cells early after meniscal injury down-regulates metalloproteinase gene expression in synovium and prevents cartilage degradation in a rabbit model of osteoarthritis. *Osteoarthr. Cartil.* **23,** 122–133 (2015).

17. Adachi, N. *et al.* Mobilization of bone marrow-derived mesenchymal stem cells into the injured tissues after intraarticular injection and their contribution to tissue regeneration. *Knee Surgery, Sport. Traumatol. Arthrosc.* **14,** 1307–1314 (2006).

18. Cheah, K. S., Stoker, N. G., Griffin, J. R., Grosveld, F. G. & Solomon, E. Identification and characterization of the human type II collagen gene (COL2A1). *Proc. Natl. Acad. Sci. U. S. A.* **82,** 2555–9 (1985).

19. Hagiwara, Y. *et al.* Expression of collagen types i and II on articular cartilage in a rat knee contracture model. *Connect. Tissue Res.* **51,** 22–30 (2010).

20. Nerlich, A. G., Wiest, I. & Von Der Mark, K. *Virchows Archiv B Immunohistochemical analysis of interstitial collagens in cartilage of different stages of osteoarthrosis*. *Virchows Archiv B Cell Pathol* **63,** (1993).

21. Miosge, N. *et al.* Light and electron microscopic in-situ hybridization of collagen type I and type II mRNA in the fibrocartilaginous tissue of late-stage osteoarthritis. *Osteoarthr. Cartil.* **6,** 278–285 (1998).

22. Mawrie, D. *et al.* Collagen Promotes Higher Adhesion, Survival and Proliferation of Mesenchymal Stem Cells. *PLoS One* **10,** e0145068 (2015).

23. Ragetly, G. R., Griffon, D. J., Lee, H. B. & Chung, Y. S. Effect of collagen II coating on mesenchymal stem cell adhesion on chitosan and on reacetylated chitosan fibrous scaffolds. *J. Mater. Sci. Mater. Med.* **21,** 2479–2490 (2010).

24. Grynpas, M. D., Eyre, D. R. & Kirschner, D. A. Collagen type II differs from type I in native molecular packing. *BBA - Protein Struct.* **626,** 346–355 (1980).

25. Paszkowiak, J. J. & Dardik, A. Arterial wall shear stress: Observations from the bench to the bedside. *Vasc. Endovascular Surg.* **37,** 47–57 (2003).

26. Franke, R.-P. *et al.* Induction of human vascular endothelial stress fibres by fluid shear stress. *Nature* **307,** 648–649 (1984).

27. Resnick, N. *et al.* Fluid shear stress and the vascular endothelium: For better and for worse. *Progress in Biophysics and Molecular Biology* **81,** 177–199 (2003).

28. Papaioannou, T. G. & Stefanadis, C. Vascular wall shear stress: basic principles and methods. *Hellenic J. Cardiol.* **46,** 9–15 (2005).

29. Nalim, R., Pekkan, K., Sun, H. Bin & Yokota, H. Oscillating Couette flow for in vitro cell loading. *J. Biomech.* **37,** 939–942 (2004).

30. Sun, H. Bin, Nalim, R. & Yokota, H. Expression and activities of matrix metalloproteinases under oscillatory shear in IL-1-stimulated synovial cells. *Connective Tissue Research* **44,** 42–49 (2003).

31. Pekkan, K., Nalim, R. & Yokota, H. Computed Synovial Fluid Flow in a Simple Knee Joint Model. *Proc. 4th ASME/JSME Jt. Fluids Eng. Conf.* 1–5 (2003). doi:10.1115/FEDSM2003-45430

32. Farach-Carson, M. C., Hecht, J. T. & Carson, D. D. Heparan Sulfate Proteoglycans: Key Players in Cartilage Biology. *Crit. Rev. Eukaryot. Gene Expr.* **15,** 29–48 (2005).

33. Ornitz, D. M. FGFs, heparan sulfate and FGFRs: Complex interactions essential for development. *BioEssays* **22,** 108–112 (2000).

34. Capila, I. & Linhardt, R. J. Heparin - Protein interactions. *Angewandte Chemie - International Edition* **41,** 390–412 (2002).

35. Rothenfluh, D. A., Bermudez, H., O'Neil, C. P. & Hubbell, J. A. Biofunctional polymer nanoparticles for intra-articular targeting and retention in cartilage. *Nat. Mater.* **7,** 248–254 (2008).

36. Shamji, M. F. *et al.* Development and characterization of a fusion protein between thermally responsive elastin-like polypeptide and interleukin-1 receptor antagonist: Sustained release of a local antiinflammatory therapeutic. *Arthritis Rheum.* **56,** 3650–3661 (2007).

37. Bajpayee, A. G. & Grodzinsky, A. J. Cartilage-targeting drug delivery: can electrostatic interactions help? *Nat. Rev. Rheumatol.* **13,** 183–193 (2017).

38. Krishnan, Y. *et al.* Green fluorescent proteins engineered for cartilage-targeted drug delivery: Insights for transport into highly charged avascular tissues. *Biomaterials* **183,** 218–233 (2018).

Chapter 6

Conclusions and Future Opportunities

6.1 Overview

The global aim of this project was to develop an approach to improve OA-based stem cell therapies. In practice, this involved re-engineering the plasma membrane of human mesenchymal stem cells (hMSCs) with a novel nanobiohybrid construct. This modification was designed to enhance adhesion to the natural extracellular matrix (ECM) in articular cartilage.

The designer nanobiohybrid [scGFP_PlGF2][S] consists of a polymer surfactant (S) conjugated supercharged green fluorescent protein (scGFP)[1] fused to a heparin binding domain found in placenta growth factor 2 (PlGF2_123-144)[2]. Here, the solvent-exposed positive residues in scGFP would be electrostatically conjugated with anionic polymer surfactant comprised of a polyethylene glycol (PEG) containing a nonylphenyl tail. Significantly, it was hypothesised that the hydrophobic tail would penetrate into hydrophobic bilayer of the cell membrane, anchoring the nanohybrid construct to the cell surface.

6.2 Outcomes from the study

Overall, study yielded a host of exciting new results which are summarised below. The *scgfp-plgf2_123-144* gene was designed by adding the *plgf2_123-144* peptide sequence to the C-terminal of the *scgfp* gene, then incorporating an N-terminal hexahistidine tag. Then, the plasmid carrying the *scgfp-plgf2_123-144* was successfully transfected into *Escherichia coli* (*E. coli)* for protein expression. The hexa-histidine tag in the expressed protein [scGFP_PlGF2] facilitated protein isolation with immobilised metal affinity chromatography. The purification of [scGFP_PlGF2] was evaluated by sodium dodecyl sulphate polyacrylamide gel electrophoresis (SDS-PAGE) and matrix assisted laser desorption ionisation mass spectrometry, indicating a highly pure isolate. UV spectroscopy was also used to

establish the purity of the protein by utilising the ratio between its two extinction coefficients values at 280 and 487 nm.

The isolation of the pure [scGFP_PlGF2] protein was followed by conjugation with the anionic oxidised IGEPAL co-890, by continuous stirring at 4°C to form [scGFP_PlGF2][S]. The presence of the surfactant corona was confirmed by dynamic light scattering (DLS) and zeta potential measurements by an increase in hydrodynamic diameter attributed to the surfactant corona around the protein. Circular dichroism showed that the secondary structure of the native protein was not compromised after surfactant conjugation.

Further characterisation included other spectroscopic techniques, such as UV-vis and fluorimetry, from which it was determined that [scGFP_PlGF2] and [scGFP_PlGF2][S] shared similar optical characteristics. UV spectroscopy was used to ascertain the extent of the electrostatic conjugation with the surfactant. The emission and excitation maxima were found in the same wavelength regardless the addition of the surfactant, further suggesting that the folding of the β-barrel structure of scGFP and chromophore were not perturbed, and that the protein was not denatured. DLS confirmed the protein did not aggregate in solution, and that conjugation lead to an increase in the hydrodynamic diameter.

Small-angle X-ray scattering (SAXS) validated the β-barrel tertiary structure of the protein [scGFP] and the flexibility of the fused peptide [scGFP_PlGF2]. SAXS also supported data obtained from DLS and mass spectrometry with respect to the size and molecular mass, respectively.

After the biophysical characterisation of [scGFP_PlGF2] and [scGFP_PlGF2][S], experiments were carried out to explore the affinity of the constructs for the cell membrane of human mesenchymal stem cells (hMSCs). First, the viability of stem

cells was correlated to the ability of the cells to maintain their metabolic rate after being treated with various concentrations of the nanobiohybrid. hMSCS were exposed to increasing concentrations of [scGFP_PlGF2] and [scGFP_PlGF2][S]. Significant toxicity was observed when hMSCs were exposed to 12 μM of native protein or surfactant conjugate. All subsequent experiments were carried out at a concentration of 4 μM where no cytotoxicity was observed. Secondly, the proliferation of the modified hMSCs was assessed by manually counting the cell population every seven days for 14 days. The population doubling time remained stable after modification.

The affinity of the nanoconstructs for the hMSC membrane was evaluated with flow cytometry. All hMSCs were successfully labelled with the constructs [scGFP_PlGF2] and [scGFP_PlGF2][S], as they showed an increase in fluorescence in the GFP region, though it was observed that the fluorescent intensity was greater in cells labelled with [scGFP_PlGF2]. It was hypothesised that this was due to the number of constructs deposited on the cell surface. In the future, the use of correlated light electron microscopy and atomic force microscopy could assist in the measuring of the thickness of the layer of nanoconstructs on the cell membrane and the roughness of the engineered membrane, respectively. Subsequent experiments were carried out to determine the number of constructs on the hMSC surface. As a result, it was quantified that hMSCs carried approximately twice the amount of [scGFP_PlGF2] than [scGFP_PlGF2][S]. It was hypothesised to be the result of rapid internalisation of [scGFP_PlGF2] by the cells, as it has been demonstrated before that scGFP can be internalised by mammalian cells[3,4] via clatherin derived endocytosis.

Live cell imaging confirmed that [scGFP_PIGF2][S] was associated with the hMSC membrane, as it appears to surround the entire cell, and it was not found within the cell cytoplasm or the nucleus, when cells were imaged immediately after exposure. Similarly, time-lapse microscopy was performed to trace the fate of the nanobiohybrids once it was added onto the cell membrane. It was observed that [scGFP_PIGF2] was rapidly internalised by the cells. This event has been observed before for positively charged molecules[5], as they are electrostatically attracted to the negatively charged proteoglycans in the cell surface and induce internalisation[6]. In contrast, the conjugate was retained on the surface of the hMSCs membrane. This is likely due to the nonylphenyl tail of the surfactant serving as a hydrophobic anchor to cell membrane. Both constructs were fully internalised after 24h, however, future experiments should be performed to determine if the surfactant is internalised together with the protein as one entity, or if the surfactant stays anchored on the cell membrane.

Further assessment with flow cytometry was used to evaluate the persistence of [scGFP_PIGF2] and [scGFP_PIGF2][S] would be completely removed from the hMSCs. After 12 days all exogenous fluorescence was removed.

Significantly, the multipotency of the mesenchymal stem cells was not inhibited by the modification of the cell membrane. Osteogenesis and adipogenesis did not show an observable difference versus the untreated control. Nevertheless, chondrogenesis differentiation seemed to be improved for hMSCs modified with [scGFP_PIGF2][S]. It might possible that the anchored polymer surfactant reduced the oxygen transport into the cells, by saturating the membrane surface, i.e., hypoxic environments are often associated with the induction of chondrogenesis. The change in chondrogenesis could also be owed to the presence of the PEG

chains in the surfactant, as it has been suggested that PEG facilitates the transport of nutrients to inside of the cell[7]. However, this has yet to be elucidated for the surfactant used in this project (oxidised IGEPAL co-890).

After the stability of [scGFP_PlGF2][S] on the cell membrane was evaluated, the adhesion properties of the modified hMSCs was tested in wells coated with collagen type I and II, and bovine cartilage ex vivo explants. The cells modified with [scGFP_PlGF2][S] demonstrated superior affinity to collagen II in a static and a physiologically relevant dynamic environment. Importantly, when the modified cells with [scGFP_PlGF2][S] and control cells were seeded in bovine ex vivo explants, the number of modified cells found in the cartilage was greater than that of unlabelled control cells.

Using a different approach, bovine cartilage explants were exposed to [scGFP_PlGF2][S], [scGFP_PlGF2] or [scGFP]. The nanobiohybrid [scGFP_PlGF2][S] was found distributed on the cartilage ECM unlike [scGFP_PlGF2] or [scGFP], which appeared to be internalised by the residing chondrocytes. Further hMSC adhesion studies on the modified cartilage would be needed in order to explore the idea that this could be used as a platform to attract hMSCs. Moreover, *in vivo* studies need to be performed in order to assess adhesion and cell engraftment, and the immune response after *in vivo* injection of supercharged GFP, as well as differentiation capacity in a damaged cartilage model. Taken together, all these findings suggest that mesenchymal stem cell membrane modification with [scGFP_PlGF2][S] is able to improve cell adhesion to cartilage, which is of crucial importance for regenerative therapies to treat diseases such as osteoarthritis.

6.3 Bibliography

1. Lawrence, M. S., Phillips, K. J. & Liu, D. R. Supercharging proteins can impart unusual resilience. *J. Am. Chem. Soc.* **129,** 10110–2 (2007).

2. Martino, M. M. *et al.* Growth Factors Engineered for Super-Affinity to the Extracellular Matrix Enhance Tissue Healing. *Science (80-.).* **343,** 885–888 (2014).

3. Schiffelers, R. M. *et al.* Cancer siRNA therapy by tumor selective delivery with ligand-targeted sterically stabilized nanoparticle. *Nucleic Acids Res.* **32,** (2004).

4. McNaughton, B. R., Cronican, J. J., Thompson, D. B. & Liu, D. R. Mammalian cell penetration, siRNA transfection, and DNA transfection by supercharged proteins. *Proc. Natl. Acad. Sci.* **106,** 6111–6116 (2009).

5. Huang, M., Ma, Z., Khor, E. & Lim, L. Y. Uptake of FITC-chitosan nanoparticles by A549 cells. *Pharm. Res.* **19,** 1488–1494 (2002).

6. Cronican, J. J. *et al.* Potent delivery of functional proteins into Mammalian cells in vitro and in vivo using a supercharged protein. *ACS Chem. Biol.* **5,** 747–52 (2010).

7. Khandare, J. & Minko, T. Polymer-drug conjugates: Progress in polymeric prodrugs. *Progress in Polymer Science (Oxford)* **31,** 359–397 (2006).

Appendix A: Protein sequence information

scGFP Amino Acid Sequence (238)

ASKGERLFRGKVPILVELKGDVNGHKFSVRGKGKGDATRGKLTLKFICTTGKLP
VPWPTLVTTLTYGVQCFSRYPKHMKRHDFFKSAMPKGYVQERTISFKKDGKYK
TRAEVKFEGRTLVNRIKLKGRDFKEKGNILGHKLRYNFNSHKVYITADKRKNGIK
AKFKIRHNVKDGSVQLADHYQQNTPIGRGPVLLPRNHYLSTRSKLSKDPKEKR
DHMVLLEFVTAAGIKHGRDERYK

scGFP Nucleotide Sequence (714)

GCT TCG AAA GGT GAA CGC CTG TTT CGC GGT AAA GTT CCG ATT CTT
GTG GAA CTG AAA GGC GAT GTG AAC GGA CAC AAA TTT TCG GTA CGT
GGG AAA GGT AAA GGC GAT GCA ACC CGC GGA AAA CTG ACC CTC AAA
TTC ATT TGC ACC ACT GGC AAG CTG CCC GTT CCA TGG CCA ACC TTA
GTG ACA ACC TTG ACC TAT GGC GTT CAG TGC TTC TCT CGT TAT CCG
AAA CAC ATG AAA CGT CAT GAC TTC TTT AAA TCC GCG ATG CCG AAA
GGC TAT GTG CAG GAA CGC ACG ATC AGC TTT AAG AAA GAC GGC AAA
TAC AAG ACT CGC GCG GAA GTC AAG TTT GAA GGA CGT ACG CTT GTG
AAT CGC ATC AAA CTG AAA GGG CGC GAT TTC AAA GAG AAA GGC AAC
ATT CTG GGC CAC AAA TTA CGG TAC AAC TTT AAC AGT CAC AAG GTC
TAC ATT ACG GCC GAT AAA CGG AAG AAT GGC ATC AAA GCG AAA TTC
AAA ATT CGT CAC AAT GTG AAG GAT GGT AGC GTT CAA CTG GCC GAT
CAT TAC CAG CAG AAT ACG CCC ATT GGT CGT GGT CCG GTA TTG TTA
CCG CGG AAC CAT TAT CTG AGT ACA CGC TCA AAA CTG AGC AAA GAC
CCG AAA GAA AAG CGC GAT CAT ATG GTA CTG CTG GAA TTT GTC ACT
GCA GCT GGG ATC AAG CAT GGT CGC GAT GAG CGC TAT AAA

PlGF-2$_{123-144}$ Amino Acid Sequence (21)

RRPKGRGKRRREKQRPTDCHL

PlGF-2$_{123-144}$ Nucleotide Sequence (63)

CGC CGC CCT AAA GGC CGT GGT AAA CGT CGT CGT GAG AAA CAA CGC
CCT ACC GAC TGT CAT CTC

Synthetic Gene Amino Acid Sequence (259)

ASKGERLFRGKVPILVELKGDVNGHKFSVRGKGKGDATRGKLTLKFICTTGKLP
VPWPTLVTTLTYGVQCFSRYPKHMKRHDFFKSAMPKGYVQERTISFKKDGKYK
TRAEVKFEGRTLVNRIKLKGRDFKEKGNILGHKLRYNFNSHKVYITADKRKNGIK

AKFKIRHNVKDGSVQLADHYQQNTPIGRGPVLLPRNHYLSTRSKLSKDPKEKR
DHMVLLEFVTAAGIKHGRDERYKRRPKGRGKRRREKQRPTDCHL

Synthetic Gene Nucleotide Sequence (777)

GCT TCG AAA GGT GAA CGC CTG TTT CGC GGT AAA GTT CCG ATT CTT
GTG GAA CTG AAA GGC GAT GTG AAC GGA CAC AAA TTT TCG GTA CGT
GGG AAA GGT AAA GGC GAT GCA ACC CGC GGA AAA CTG ACC CTC AAA
TTC ATT TGC ACC ACT GGC AAG CTG CCC GTT CCA TGG CCA ACC TTA
GTG ACA ACC TTG ACC TAT GGC GTT CAG TGC TTC TCT CGT TAT CCG
AAA CAC ATG AAA CGT CAT GAC TTC TTT AAA TCC GCG ATG CCG AAA
GGC TAT GTG CAG GAA CGC ACG ATC AGC TTT AAG AAA GAC GGC AAA
TAC AAG ACT CGC GCG GAA GTC AAG TTT GAA GGA CGT ACG CTT GTG
AAT CGC ATC AAA CTG AAA GGG CGC GAT TTC AAA GAG AAA GGC AAC
ATT CTG GGC CAC AAA TTA CGG TAC AAC TTT AAC AGT CAC AAG GTC
TAC ATT ACG GCC GAT AAA CGG AAG AAT GGC ATC AAA GCG AAA TTC
AAA ATT CGT CAC AAT GTG AAG GAT GGT AGC GTT CAA CTG GCC GAT
CAT TAC CAG CAG AAT ACG CCC ATT GGT CGT GGT CCG GTA TTG TTA
CCG CGG AAC CAT TAT CTG AGT ACA CGC TCA AAA CTG AGC AAA GAC
CCG AAA GAA AAG CGC GAT CAT ATG GTA CTG CTG GAA TTT GTC ACT
GCA GCT GGG ATC AAG CAT GGT CGC GAT GAG CGC TAT AAA CGC CGC
CCT AAA GGC CGT GGT AAA CGT CGT CGT GAG AAA CAA CGC CCT ACC
GAC TGT CAT CTC

Vector

pOPINF (https://www.addgene.org/26042/)

Fusion Tag; MAHHHHHHSSGLEVLFQ🕐GP…tag

Forward Primer Sequence
AAG TTC TGT TTC AGG GCC CG

Reverse Primer Sequence
ATG GTC TAG AAA GCT TTA GAG ATG ACA GTC GGT AGG (reverse complimented (olive green))

Eurofins Login
https://ecom.mwgdna.com/register/index.tcl

Appendix B: Protein sequence

Protein calculator results:

Accepted Sequence

```
MAHHHHHHSS GLEVLFQGPA SKGERLFRGK VPILVELKGD VNGHKFSVRG KGKGDATRGK  60
LTLKFICTTG KLPVPWPTLV TTLTYGVQCF SRYPKHMKRH DFFKSAMPKG YVQERTISFK  120
KDGKYKTRAE VKFEGRTLVN RIKLKGRDFK EKGNILGHKL RYNFNSHKVY ITADKRKNGI  180
KAKFKIRHNV KDGSVQLADH YQQNTPIGRG PVLLPRNHYL STRSKLSKDP KEKRDHMVLL  240
EFVTAAGIKH GRDERYKRRP KGRGKRRREK QRPTDCHL                          278
```

Amino Acid Count

Residue			Number Found
A	Ala	Alanine	10
R	Arg	Arginine	27
N	Asn	Asparagine	9
D	Asp	Aspartate	12
Q	Gln	Glutamine	7
E	Glu	Glutamate	11
G	Gly	Glycine	26
H	His	Histidine	17
I	Ile	Isoleucine	10
L	Leu	Leucine	22
K	Lys	Lysine	39
M	Met	Methionine	4
F	Phe	Phenylalanine	13
P	Pro	Proline	13
S	Ser	Serine	12
T	Thr	Threonine	16
Y	Tyr	Tyrosine	9
V	Val	Valine	17
W	Trp	Tryptophan	1
C	Cys	Cysteine	3
U	SeC	Selenocysteine	0

Atom Count

Type	Number Found
Carbon	1434
Nitrogen	449
Oxygen	378
Sulphur	7
Hydrogen	2315

Isotopically Averaged Molecular Weight = 32118.2656

Estimated pI = 10.58

WARNING: pI estimate assumes all residues have pKa values that are equivalent to the isolated residues. For a folded protein this is **not** valid. However, this rough value can be useful for planning protein purfications. pKa values for the individual amino acids from Stryer Biochemistry, 3rd edition.

Estimated charge at pH 7.00 = 46.9

WARNING: pI estimate assumes all residues have pKa values that are equivalent to the isolated residues. For a folded protein this is **not** valid. However, this rough value can be useful for planning protein purfications. pKa values for the individual amino acids from Stryer Biochemistry, 3rd edition.

Extinction Coefficient

Extinction coefficient estimated by the method of Gill and von Hippel (*Analytical Biochemistry*, **182**:319-326,1989) where lyophilized proteins were used to establish an absorbance curve based on the number of tyrptophans, tyrosines, and disulfide bonds. Units are in M^{-1} cm^{-1}.

Wavelength	Molar Extinction w/o Disulfides	Molar Extinction w/ All Disulfides
278	18200	18327
279	17765	17885
280	17210	17330
282	16400	16500

Extinction Coefficient

Extinction coefficient estimated by the method of Gill and von Hippel (*Analytical Biochemistry*, **182**:319-326,1989) where lyophilized proteins were used to establish an absorbance curve based on the number of tyrptophans, tyrosines, and disulfide bonds. Units are in $(mg/mL)^{-1}$ cm^{-1}.

Wavelength	Molar Extinction w/o Disulfides	Molar Extinction w/ All Disulfides
278	0.5667	0.5706
279	0.5531	0.5568
280	0.5358	0.5396
282	0.5106	0.5137

Last Updated: May 13, 2013
http://protcalc.sourceforge.net/cgi-bin/protcalc

Appendix C: Amino acids

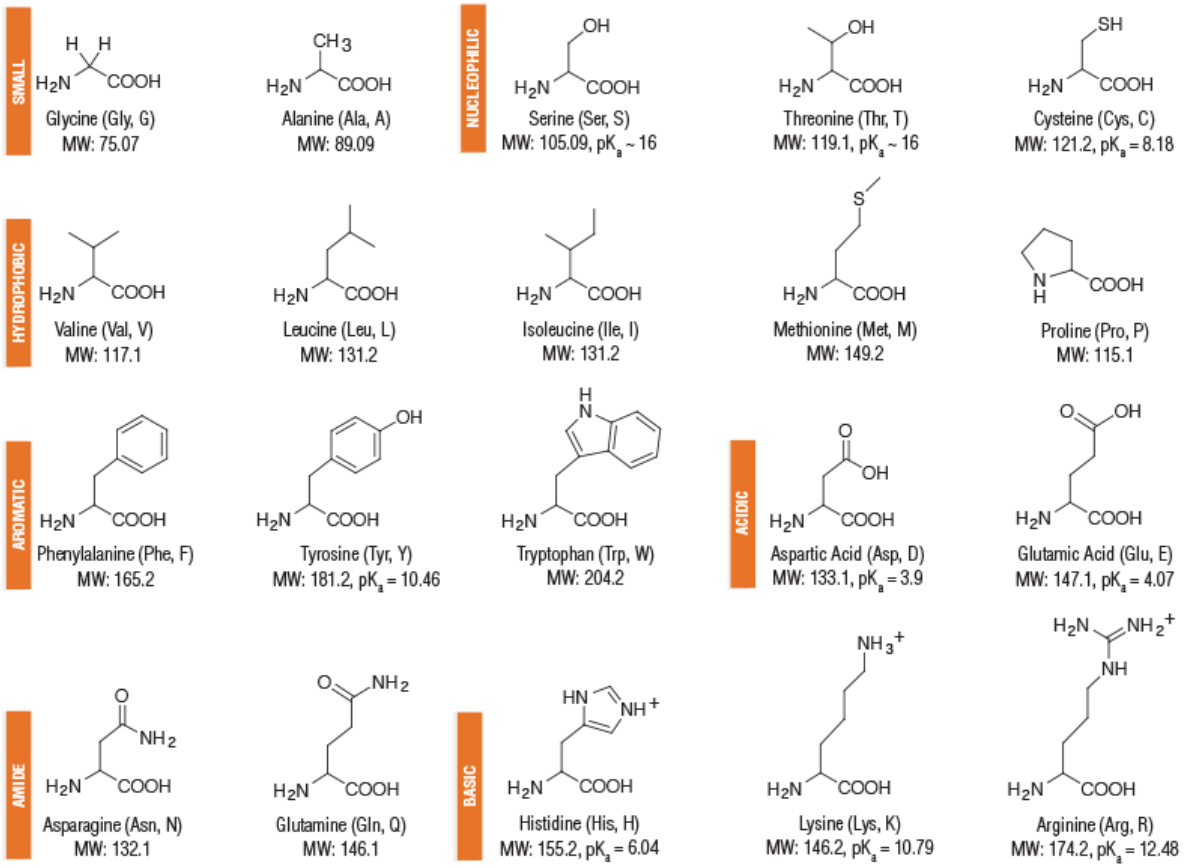

Reproduced from:

https://www.neb.com/tools-and-resources/usage-guidelines/amino-acid-structures

Appendix D: Oxidation of IGEPAL co-890

The oxidation reaction of IGEPAL co-890 was carried out as previously reported[1] and section 2.4. An oxidation was carried out on the alcohol group into a carboxylic acid in order to make it an anionic surfactant. In the surfactant structure, hydrophilic head group is followed by an amphiphilic polyethylene glycol (n=39) and a hydrophobic nonyl phenyl tail group (Figure 1).

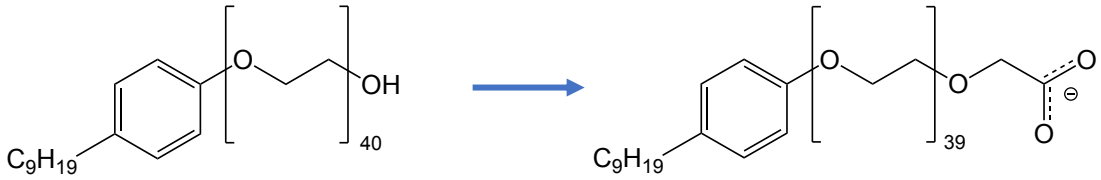

Figure 1 IGEPAL co-890 oxidation. The native surfactant IGEPAL co-890 (left) is oxidised to obtain the oxidised version presenting a carboxylic acid at the end (right). The reaction is carried out on the presence of TEMPO, NaClO and NaBr in a basic pH of 11.

Fourier transformed infrared spectroscopy was performed in order to ensure the addition of the carboxylic group (Figure 2). It was possible to see the appearance of the carboxylic group stretch band at 1760 cm^{-1}, which is expected for a carbonyl stretch between[2] , This value corresponded to the C=O bond stretch in a saturated carboxylic acid, which is not present when the spectrum is taken from the neat polymer. Other relevant peaks on the spectrum are O-C-O asymmetrical stretch between 1180 and 1290 cm^{-1}, and C-OH at approximately 3000 cm^{-1} [3].

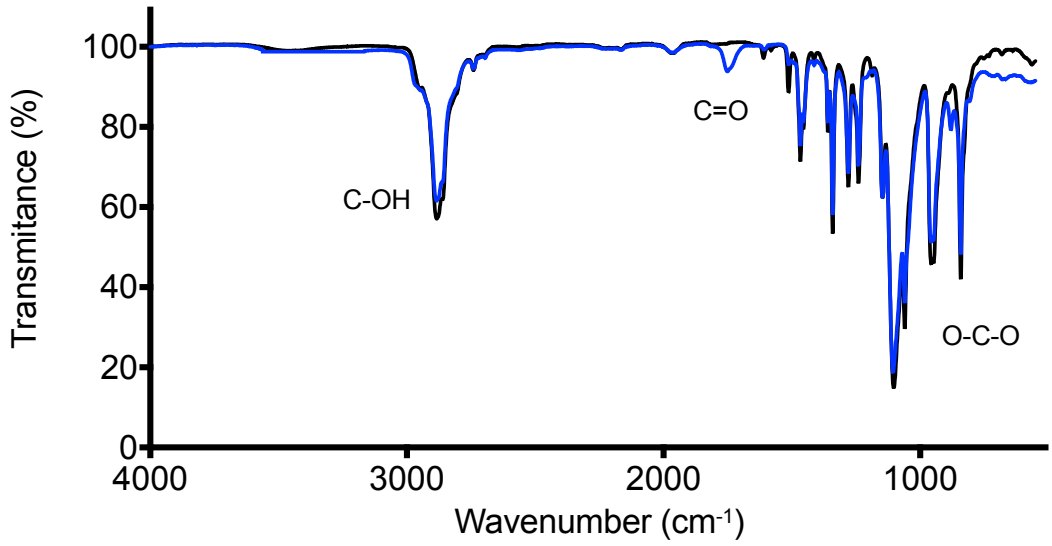

Figure 2 FTIR spectrum from native and oxidised surfactant. IGEPAL co-890 (red line) and IGEPAL co-890 (black line) after oxidation showing the carbonyl stretch C=O between 1600 and 1800 cm^{-1}, O-C-O asymmetrical stretch between 1180 and 1290 cm^{-1}, and C-OH at approximately 3000 cm^{-1}.

An acid-base titration was carried out with sodium hydroxide (NaOH) in order to quantify the oxidation of IGEPAL co-890 (Figure 3).

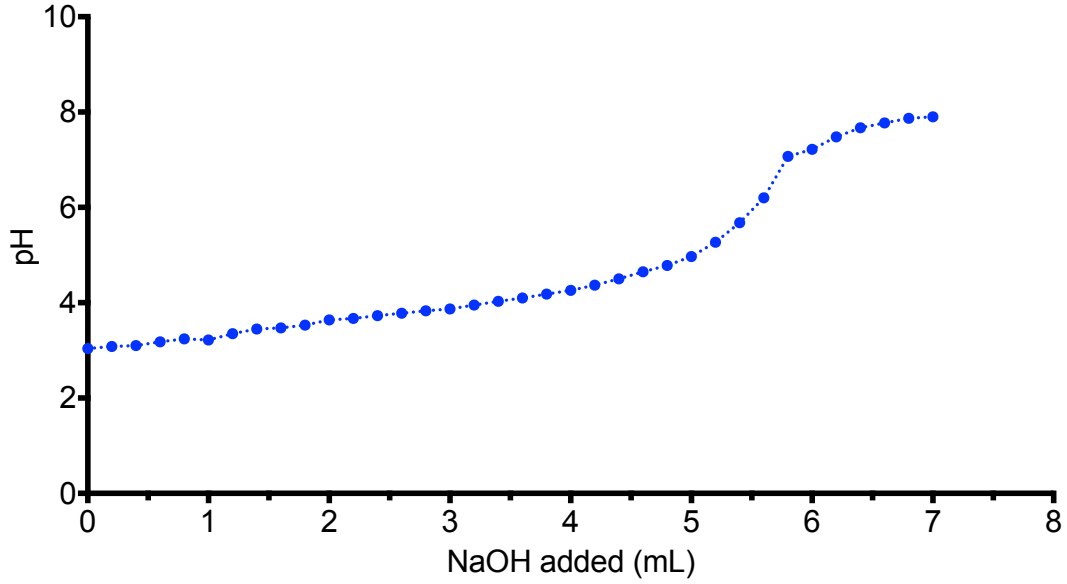

Figure 3 Titration curve of oxidised IGEPAL co-890 against sodium hydroxide added. The neutralisation point was determined to calculate surfactant purity. Aliquots of 200 µL were added and the pH was measured every time until stability was reached.

The neutral pH 7 was reached when 5.8 mL of 2.5 mM NaOH are added to the solution. The ratio between carboxylic acid and sodium hydroxide (NaOH mol / COOH mol) was determined to be 1.03, meaning that a 100% of the surfactant was oxidised to have a carboxylic acid ending.

MALDI-TOF mass spectrometry was performed in both samples IGEPAL co-890 and the oxidised version. A shift in the molecular weight of 14 Da is observed due to the addition of the oxygen at the end of the chain, along with the periodicity of 44 Da from the polyethylene glycol chain (Figure 4).

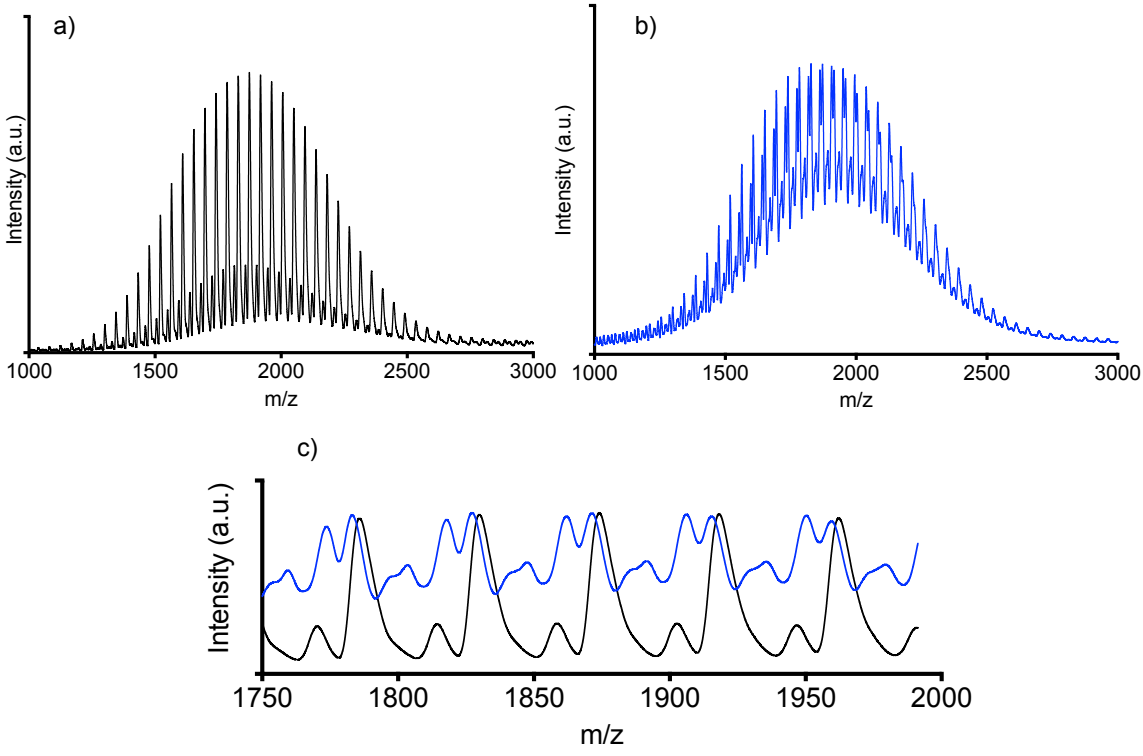

Figure 4 MALDI-TOF mass spectrometry of polymers. a) spectrum from IGEPAL co-890 from sigma (black) and b) oxidised IGEPAL co-890 (blue). c) Reduced range demonstrated the peak shift on the mass of the oxidised polymer (blue) as well as 44 Da periodicity of polyethylene glycol chain.

In order to determine the extinction coefficient of the surfactant, a UV-vis absorbance measurement was made with a known surfactant concentration (Figure 5).

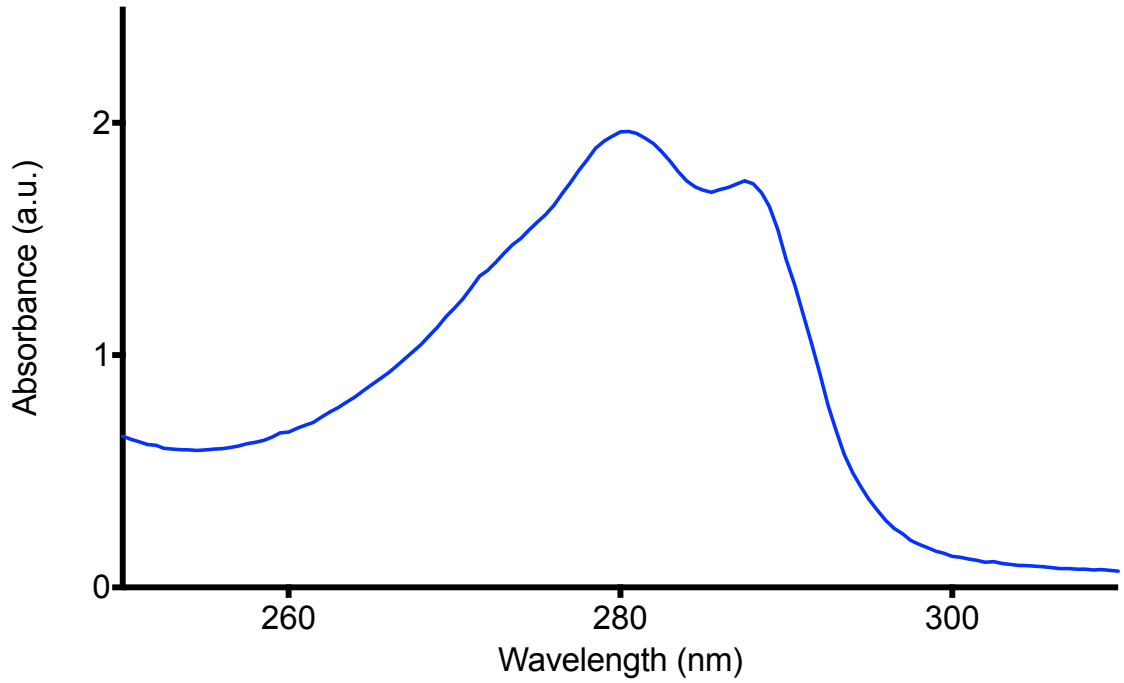

Figure 5 UV-vis spectrum from oxidised IGEPAL co-890. This was performed at room temperature in buffer 20 mM Tris.HCl with 400 mM NaCl at pH 7.5.

Using Beer-Lambert equation it was possible to calculate the extinction coefficient to be 1563.4 when the surfactant was dissolved in buffer 20 mM Tris.HCl with 400 mM NaCl at pH 7.5.

The critical micellar concentration (CMC) of oxidised IGEPAL co-890 was obtained in the buffer to be used for protein conjugation, as this could vary depending on the solvent used. This experiment was carried out by mixing a known surfactant concentration and 1,6-diphenyl-1,3,5-hexatriene (DPH). The CMC was found to be in between 0.5 and 1 $mg \cdot mL^{-1}$, when the fluorescence was positive, which is consisted with the previously reported value[1] of 0.8 $mg \cdot mL^{-1}$. (Figure 6).

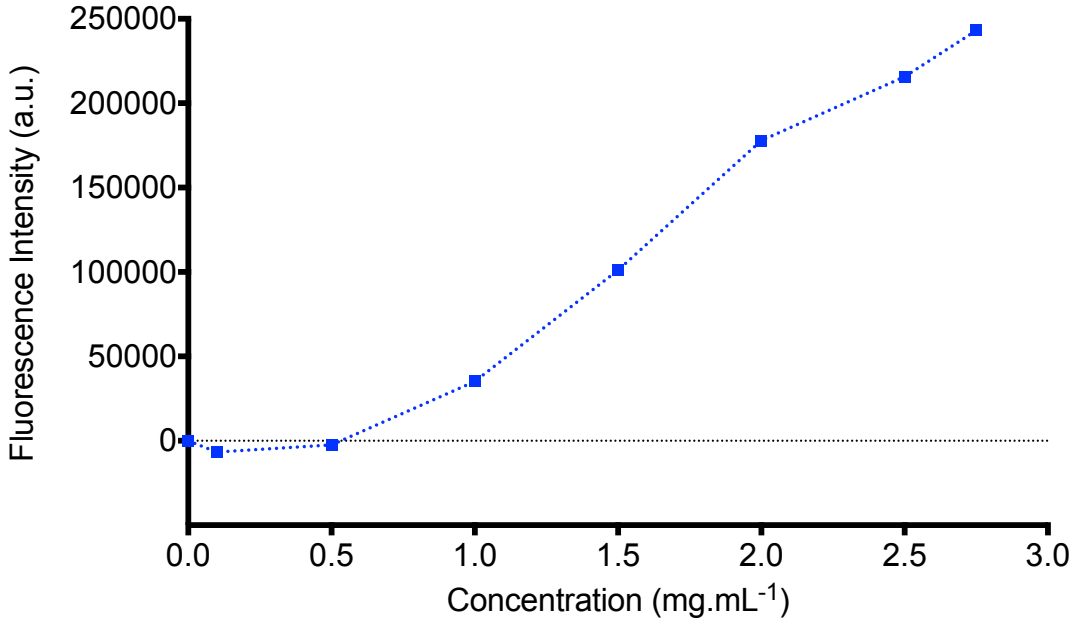

Figure 6 Critical micellar concentration of oxidised IGEPAL co-890. Data was obtained in buffer 20 mM Tris.HCl and 400 mM NaCl at pH 7.5.

Bibliography

1. Armstrong, J. P. K. *et al.* Artificial membrane-binding proteins stimulate oxygenation of stem cells during engineering of large cartilage tissue. *Nat. Commun.* **6,** 7405 (2015).

2. Ojamäe, L., Aulin, C., Pedersen, H. & Käll, P. O. IR and quantum-chemical studies of carboxylic acid and glycine adsorption on rutile TiO2nanoparticles. *J. Colloid Interface Sci.* **296,** 71–78 (2006).

3. Talari, A. C. S., Martinez, M. A. G., Movasaghi, Z., Rehman, S. & Rehman, I. U. Advances in Fourier transform infrared (FTIR) spectroscopy of biological tissues. *Applied Spectroscopy Reviews* **52,** 456–506 (2017).